Analysis and reduction of chemical kinetics for combustion applications

Quentin Cazeres

THÈSE

En vue de l'obtention du

DOCTORAT DE L'UNIVERSITÉ DE TOULOUSE

Délivré par :

Institut National Polytechnique de Toulouse (Toulouse INP)

Discipline ou spécialité :

Energétique et Transferts

Présentée et soutenue par :

M. QUENTIN CAZERES

le mardi 13 juillet 2021

Titre :

Analysis and reduction of chemical kinetics for combustion applications

---

Ecole doctorale :

Mécanique, Energétique, Génie civil, Procédés (MEGeP)

Unité de recherche :

Centre Européen de Recherche et Formation Avancées en Calcul Scientifique (CERFACS)

Directrices de Thèse :

MME BENEDICTE CUENOT

MME ELEONORE RIBER

Rapporteurs :

M. EPAMINONDAS MASTORAKOS, UNIVERSITE DE CAMBRIDGE

M. MARCO MEHL, POLITECNICO DE MILAN

Membres du jury :

M. PIERRE-ALEXANDRE GLAUDE, UNIVERSITÉ LORRAINE, Président

MME BENEDICTE CUENOT, CERFACS, Membre

MME PERRINE PEPIOT, CORNELL UNIVERSITY EU, Invitée

M. PATRICK LECLERCQ, UNIVERSITAT STUTTGART, Invité

Abstract

Combustion of fossil fuels has been used for decades for all kinds of purposes, from generating electricity to make air planes fly but they are also the main source of pollution leading to climate change. New sustainable, less polluting fuels must be studied in order to diminish as much as possible the human impact on the planet. Combustion is a very complex process combining fluid dynamics, thermodynamics and chemistry with hundreds of species involved. In order to be able to use all the tools the numerical simulation has to offer with increasing complexity, from canonical cases to 3D Large Eddy Simulations (LES) with two-phase flows, analysing the relevant chemical pathways and reducing the reaction mechanisms describing this chemistry is necessary. Analytically Reduced Chemistry (ARC) is a way of reducing the size and the complexity of chemical mechanisms where only the species and reactions relevant to given conditions are kept while keeping a physically coherent mechanism. ARC lies among several methodologies for the reduction of kinetics but with the increasing complexity of the fuels and configurations that need to be studied in the future years, it is now more and more interesting. The first objective of this work is to develop a fully automatic procedure for developing ARC mechanisms that do not require and expert knowledge on kinetics and can be adapted to any kind of conditions to be as versatile as possible. This objective has been fulfilled by the creation of the code ARCANE and the second objective was to assess its performances in two different configurations. The first configuration consists in the combustion of premixed hydrogen-enriched methane/air in a swirled combustor with 2 levels of enrichment in the solver AVBP. The ARC mechanism has been derived with the prediction of NO_x and the addition of the chemiluminescent species OH^*. The fully automatic reduction of this mechanism is proven to capture well the experimental results and the effect of the enrichment level on the flame structure. The presence of OH^* in the mechanism allows for more direct comparison with experiments and is the start of a discussion about the actual identification of the flame structure. Numerical simulation is also used in this case for the prediction of the NO_x emissions and how it is affected by the hydrogen enrichment. The second configuration consists in the reduction of 3 aviation fuels (conventional kerosene, sustainable aviation fuel (SAF) and high-aromatic content kerosene) described by 3-components surrogates. The reduction of each fuel is then used in canonical configurations of liquid droplets combustion. The discrete evaporation model implemented in AVBP allows to observe the effects of the preferential evaporation on the flame structure. Finally, the different fuels are compared to one another to identify their particularities and assess the benefits of the multi-component approach.

Résumé

La combustion de carburants fossiles est utilisée depuis des décennies pour nombre d'applications, de la génération d'électricité au fonctionnement des moteurs d'avions, mais c'est également une des raisons principales du dérèglement climatique. De nouveaux carburants, durables et moins polluants, doivent être étudiés afin de diminuer l'impact humain sur notre planète. La combustion est un procédé complexe alliant mécanique des fluides, thermodynamique et chimie avec des centaines d'espèces impliquées dans celle-ci. Afin de pouvoir utiliser les outils de la simulation numérique pour représenter des phénomènes de plus en plus complexes, des cas canoniques jusqu'à des Simulations aux Grandes Échelles (SGE), l'analyse des chemins chimiques prépondérants et la réduction des mécanismes réactifs est nécessaire. La Chimie Analytiquement Réduite (CAR) est une méthode pour réduire la taille et la complexité des mécanismes chimiques dans laquelle seules les espèces et les réactions cohérentes avec les conditions opératoires sont gardées. La CAR n'est qu'une méthode parmi les nombreuses méthodologies pour la réduction de la cinétique chimique mais avec la complexité grandissante des carburants qui devront être étudiés dans les prochaines années, elle se distingue plus que jamais. Le premier objectif de ce travail est de développer une procédure entièrement automatique pour le développement de CAR sans demander à l'utilisateur une expertise poussée de la réduction et d'une manière adaptable au plus de conditions possibles dans un but de versatilité. Ce premier objectif a été rempli par la création du code ARCANE dont les performances sont démontrées sur 2 configurations. La première configuration consiste en une flamme swirlé de méthane/air prémélangée avec 2 niveaux d'enrichissement à l'hydrogène calculée avec le solveur AVBP. Le mécanisme CAR a été réduit en incluant les NO_x et l'espèce chimiluminescente OH^*. La réduction capture correctement les résultats expérimentaux et les effets de l'enrichissement sur la structure de flamme. La présence d'OH^* dans le mécanisme permet une comparaison plus directe entre la simulation numérique et les expériences. La simulation numérique est aussi utilisée de manière prédictive pour identifier l'effet de l'enrichissement sur les émissions de NO_x. La seconde configuration comporte la réduction de 3 carburants pour l'aviation (du kérosène conventionnel, un kérosène de synthèse renouvelable et un kérosène riche en aromatiques) décrits par des modèles à 3 composants. Les schémas réduits obtenus ont ensuite été utilisés dans des cas canoniques de combustion diphasique. Le modèle d'évaporation multi-composants discret implémenté dans AVBP permet d'observer les effets de l'évaporation préférentielle sur la structure de flamme. Enfin, les différents carburants sont comparés pour identifier leurs particularités et déterminer les avantages de l'approche multi-composants.

Acknowledgements

I want to sincerely thank Professor Epaminondas Mastorakos and Professor Marco Mehl for agreeing to read and review this manuscript, your feedback was really important and insighful. I also thank the members of my jury Pierre-Alexandre Glaude, Patrick Leclercq, Perrine Pepiot and Stephan Zurbach for their questions and their views on my PhD work. This PhD thesis took place in the context of the JETSCREEN project that I would like to thank for the opportunity of working on such an important matter. It also allowed me to meet great people involved in the research community.

Je souhaite ensuite remercier mes encadrantes, Bénédicte et Eléonore, qui m'ont fait confiance pour réaliser cette thèse et qui m'ont aidé à partir dans les bonnes directions en me laissant de la liberté dans mon travail et des responsabilités très formatrices. J'ai beaucoup apprécié travailler avec vous, toujours dans la bonne humeur et avec juste ce qu'il faut de sérieux. Dans mon encadrement officieux, je remercie Perrine de m'avoir initié aux arcanes de la cinétique chimique lors de mon arrivée au CERFACS et tout au long de la thèse. Je suis très heureux d'avoir pu continuer le travail démarré avec YARC pour en faire ARCANE.

Le CERFACS ne serait rien sans l'équipe CSG qui nous permet de toujours travailler dans d'excellentes conditions et qui fait preuve d'une efficacité à toute épreuve, alors merci à Fred, Gérard, Fabrice, Isabelle et Patrick. Il ne serait rien non plus sans l'aide de l'administration alors je me dois de remercier Michèle, Marie, Jade et Chantal pour leur aide et leur bonne humeur.

Un grand merci à tous les collègues du CERFACS, stagiaires, thésards, post-docs et seniors qui font de ce laboratoire un lieu si agréable. Mention spéciale pour la team chimie; Jonathan, Antoine, Théo et Thomas le nouveau venu qui m'ont aidé et m'aideront encore je l'espère, à faire grandir mon bébé.

On passe ensuite à ceux qui de collègues sont devenus rapidement de très bons amis, Simon, Etienne, Julien, Léa, Thomas, Adèle, Soizic, Arthur, Fabien, Fred et Maël avec qui de nombreuses soirées ont été passées (Salma et Biéro sisi) et de nombreux blocs essayés (parfois réussis). Ami, binôme et ensuite collège (sans faire exprès), merci Paul pour ces 8 ans passés à étudier, ne pas étudier, travailler et ne pas travailler ensemble. A mes amis non-scientifiques Macha, Baba, Manu, Mathilde, Coco, Audrey, Lucien qui ont supporté des discussions de thèse maintes fois jusqu'à épuisement, merci et un peu désolé aussi.

Parce que le temps passé avec eux est précieux, je remercie ma famille d'être là et d'être telle qu'elle est. C'est toujours un plaisir de se retrouver pour partager un bon repas gersois.

Évidemment, je tiens à remercier mes parents pour leur amour et leur éducation qui m'a permis de devenir la personne que je suis aujourd'hui. Vous êtes les meilleurs parents que l'on puisse rêver d'avoir et toutes mes qualités viennent de vous. Merci également pour votre accueil sans faille lors de tous les traditionnels kayak-BBQ. Malgré vos inquiétudes initiales, je pense qu'on est d'accord pour dire que je ne me suis pas lassé des études longues ...

Et enfin, merci à toi Clémentine. Merci de m'avoir soutenu et aidé sur cette fin de thèse. Merci d'être présente dans ma vie.

Part of the journey is the end.
- Tony Stark

Contents

Nomenclature

Roman Symbols

A	Pre-exponential factor	$mol^{(1-order_j)}.m^{-3(1-order_j)}$
B_M	Mass Spalding transfer number	
B_T	Temperature Spalding transfer number	
$\dot{c}_j$	Reaction rate of reaction j	$mol.m^{-3}.s^{-1}$
C	Molar concentration	$mol.m^{-3}$
c	Progress variable	-
$\mathcal{C}_D$	Drag coefficient	-
$\dot{c}$	Production rate	$mol.m^{-3}.s^{-1}$
c_p	Isobaric molar heat capacity	K
C_v	constant volume heat capacity	$J.mol^{-1}.K^{-1}$
Da	Damköhler number	-
ΔQ_j	Heat of reaction	$K.mol^{-1}$
ΔV	Local control volume	m^3
D_k	Molecular diffusion coefficient of species k	$m^2.s^{-1}$
d_p	Particle diameter	m
dt	Computation timestep	s

D_{th}	Thermal diffusivity	$m^2.s^{-1}$
E	Mass energy	$J.kg^{-1}$
E_a	Activation energy	$J.mol^{-1}$
$F_{p,i}^{ext}$	Momentum phase exchange source term	$J.s^{-1}$
$F_{p,i}^{ext}$	Momentum phase exchange source term	$kg.m^{-2}.s^{-2}$
$F_{p,i}^{ext}$	Momentum phase exchange source term	$kg.s^{-1}$
H	Standard enthalpy	$J.mol^{-1}$
$\Delta h_{f,k}^0$	Species k enthalpy of formation	$J.mol^{-1}$
h_k	Species k total enthalpy	$J.mol^{-1}$
$h_{s,k}$	Species k sensible enthalpy	$J.mol^{-1}$
$h_{s,p}$	Latent heat of vaporisation at the droplet temperature	$J.kg^{-1}$
k	Rate constant	$mol^{(1-order_j)}.m^{-3(1-order_j)}.s^{-1}$
Ka	Karlovitz number	-
Le_k	Lewis number of species k	-
l_T	Integral length scale	m
N	Total number of entities	-
n	Number of entities	-
$n_{\frac{N_2}{O_2}}$	Air nitrogen/oxygen molar ratio	-
N_p	Number of particles	-
N_r	Total number of reactions in the mechanism	-
N_s	Total number of species in the mechanism	-
Nu	Nusselt number	-
P	Pressure	Pa

P_{atm}	Atmospheric pressure	$1.01325e^5 \quad Pa$
Pr	Prandtl	-
$\mathcal{P}$	Product	
$\dot{Q}$	Heat release rate	$J.m^{-3}.s^{-1}$
q_i	Energy flux in direction i	$W.m^{-2}$
R	Universal gas constant	$8.31446 \quad J.K^{-1}.mol^{-1}$
$\mathcal{R}$	Reactant	
Re	Reynolds number	-
ρ	Density	$kg.m^{-3}$
r_p	Particle radius	m
r	Direct relation graph coefficient	$kg.mol^{-1}$ / $J.m^{-3}.s^{-1}$
$[S]$	Molar concentration of species S	$mol.m^{-3}$
S	Standard entropy	$J.K^{-1}$
Sc_k	Schmidt number of species k	-
Sh	Sherwood number	-
s_l	Laminar flame speed	$m.s^{-1}$
s_X	Molar stoichiometric ratio	-
s_Y	Mass stoichiometric ratio	-
s_{Y,O_2}	Mass stoichiometric ratio with oxygen only as oxidiser	-
T	Temperature	K
t	Time	s
T_{ad}	Adiabatic flame temperature	K
T_b	Burnt gases temperature	K

T_f	Fresh gases temperature	K
$\mathcal{F}$	Thickening factor	-
$\mathcal{M}$	Third body	
u, v, w	Velocity components	$m.s^{-1}$
U_k	species k internal energy	J
u_K	Kolmogorov velocity scale	$m.s^{-1}$
u_T	Turbulent velocity fluctuations	$m.s^{-1}$
V_i^c	Correction velocity in the direction i	$m.s^{-1}$
$V_{k,i}$	Diffusion velocity of the species k in the direction i	$m.s^{-1}$
W	Molecular weight	$kg.s^{-1}$
X	Mole fraction	-
x, y, z	Spacial coordinates	
X_{H_2}	Hydrogen mole fraction in the fuel (Enrichment level)	-
$\tilde{X}_{H_2}$	Equivalent enrichment ratio	-
Y	Mass fraction	-
Z	Mixture fraction	-

Greek Symbols

β	Temperature exponent	-
χ	Scalar dissipation rate	s^{-1}
δ	Diffusive flame thickness	m
δ_l	Thermal flame thickness	J
ϵ	Efficiency function	-
ϵ	Turbulent dissipation rate	$m^2.s^{-3}$

η_K	Kolmogorov length scale	m
λ	Thermal conductivity	$W.m^{-1}.K^{-1}$
μ	Dynamic viscosity	$Pa.s$
μ	Gibbs free energy	J
ν	Kinematic viscosity	$m^2.s^{-1}$
ν	stoichiometric coefficient of the species	-
$\dot{\omega}_j$	Mass reaction rate of reaction j	$kg.m^{-3}.s^{-1}$
$o\tau_{chem}$	Chemical timescale order of magnitude	-
ϕ	Equivalence ratio	-
ϕ_{eff}	Effective equivalence ratio	
ϕ_g	Gaseous equivalence ratio	
ϕ_l	Liquid equivalence ratio	
ϕ_{tot}	Total equivalence ratio	
Ψ_p	Inverse distance interpolation function	
σ_{ij}	Stress tensor	$N.m^{-2}$
τ	Timescale	s
τ_c	Flame characteristic timescale	s
τ_{chem}	Chemical timescale	s
τ_{ij}	Reynolds stress tensor	$N.m^{-2}$
τ_K	Kolmogorov time scale	s
τ_T	Integral timescale of the turbulence	s
$\dot{\omega}$	Mass production rate	$kg.m^{-3}.s^{-1}$

Superscripts

.	Time derivative $\frac{d}{dt}$
$-$	Spatial filter
order	Order of the species or reaction
$\prime$	Reactants side of a reaction equation
$\prime\prime$	Products side of a reaction equation
sgs	sub-grid scale

Subscripts

backward	Right to left direction in a reversible reaction
dim	Number of dimensions of the considered space
eq	Equilibrium value of the quantity
$forward$	Left to right direction in a reversible reaction
g	Gaseous phase
∞	Far-field
j	Reaction index in the mechanism / iterative index
k	index of the species in the mechanism
l	Liquid phase
mass	Mass formulation of the quantity
$\mathcal{K}$	Evaporating species (either present in liquid or gaseous phase)
mixture	Value for the whole gaseous mixture
net	Forward contribution - backward contribution
p	Particle
ζ	Droplet surface

Acronyms / Abbreviations

A1 Jet-A1 surrogate

ARC Analytically Reduced Chemistry

B1 ATJ-SPK surrogate

C1 High-aromatic content kerosene surrogate

CFD Computational Fluid Dynamics

CFL Courant–Friedrichs–Lewy number

CSP Computational Single Perturbation

DNS Direct Numerical Simulation

DRG Direct Relation Graph

DRGEP Direct Relation Graph with Error Propagation

GRC Globally Reduced Chemistry

IRZ Inner Recirculation Zone

LES Large Eddy Simulation

LHS Left Hand Side

LIP Laser Induced Phosphorescence

LOI Level Of Importance

LW Lax-Wendroff scheme

ORZ Outer Recirculation Zone

PFA Path Flux Analysis

PIV Particle Imagery Velocity

PLIF Planar Laser Induced Fluorescenc

PSR Perfectly Stirred Reactor

QSSA Quasi-Steady State Assumption

QSS Quasi-Steady State

RANS Reynolds-Averaged Navier Stokes

RHS Right Hand Side

SA Sensitivity Analysis

TI Takeno Flame Index

TTGC Two-step Taylor Galerkin scheme

Chapter 1

Introduction and Context

Contents

The fight against global warming is undeniably the most ambitious and critical challenge of the next few years. The emissions of greenhouse gases by human activity creates atmospheric forcing resulting in a rise of the average temperature. Already observed in the last decades, it considerably modifies our planet ecosystem. The consequences of the climate change are various and all the more worrying.

- The most obvious consequence from a strictly semantic aspect is an increase of the global median temperature causing a disruption of the world's climate. An increase in the intensity and frequency of heat waves around the globe has been observed [Perkins-Kirkpatrick and Lewis, 2020][Vogel et al., 2020] that can threaten human survival [Ahima, 2020]. This is also believed to be more generally the cause of the recent increase of extreme weather conditions in the northern hemisphere in the last few years [Risser and Wehner, 2017].
- The Arctic is a visible indicator of the global change as it is warming at double

the rate of other regions in the world [Jorgenson and Jorgenson, 2021]. At this location, the ice faces an important decline, specifically in Greenland [Yadav et al., 2020][Kumar et al., 2020] and will certainly rise the sea level leading to increasing coastal floods [Taherkhani et al., 2020] and ultimately to population migration [Hauer et al., 2020]. The melting, having an effect on the planet albedo, might also contribute to a positive feedback on the atmosphere median temperature worsening its warming on an intermediate to long timescale [Wunderling et al., 2020].

- Without even considering the destruction of wild animals and plants habitat, the global change induces modifications in life forms behaviours and may even lead to the extinction of some species [Root et al., 2003][Kubisch et al., 2015][García-Robledo et al., 2016].

Because the earth population is still increasing hence an increasing demand in energetic resources, the economical concept of degrowth, which implies less energy demand by less consuming, seems utopian. Other solutions must be found in order to decrease the global emissions and avoid catastrophic consequences in the future years, as highlighted in the special report of the International Panel on Climate Change (IPCC) on the global warming of 1.5°C compared to preindustrial era [Masson-Delmotte et al.,].

The Paris agreement [1], signed by almost all countries recognised by the United Nations [2], has fixed several objectives in an attempt to fall below the 2 degrees rise in global temperature projected for 2030. In order to reach these objectives, the energy sector must operate a radical change to turn away from fossil fuels towards renewable and decarbonated sources.

1.1 Energetic turnover to reduce global emissions

A complete shift in the energy production from combustion to electricity does not seem a viable strategy in the short to medium term as it would require an energy

[1] Official website: https://unfccc.int/process-and-meetings/the-paris-agreement/the-paris-agreement/key-aspects-of-the-paris-agreement

[2] Only the Vatican City stands in the non-signatories because of the incapacity to do so as it is not yet a member of the United Nations Framework Convention on Climate Change.

production that is not yet reachable with renewable energy only given the current state of the worldwide production [3]. Because combustion represents an important part of the world energy production, the smoothest, most affordable and most reasonable energetic transition path to decrease human impact on the planet is to adapt or replace the fossil fuels presently used in combustion processes by more sustainable fuels.

Energy production from combustion processes is mainly composed of ground-based gas turbines burning either natural gas or coal. Despite attempts to control the pollution of the latter [You and Xu, 2010], its decarbonation is difficult by nature. Natural gas is composed primarily of methane with a percentage between 85 and 95 percents in volume [Faramawy et al., 2016]. Less polluting than coal, natural gas is however a fossil fuel, with a risk of shortage. In the past few years, a growing interest has appeared for blends of natural gas with hydrogen, which can be produced by sustainable processes, in order to both lower the carbon content of the fuel and increase the performances of the combustion process. This subject will be discussed more in Chapter 6.

Besides power generation, transportation is also a key element of the energetic transition. Electrical engines sound like a good choice for personal vehicles [Buekers et al., 2014][Requia et al., 2018] depending on the local electricity production source. But in the case of heavier transportation vehicles, it is way more complicated. For cargo ships, this transition seems very difficult [Koumentakos, 2019] and despite several projects of electrically powered planes [4] it seems also unlikely for the aeronautical sector that electricity will be a viable solution. Hydrogen as a fuel is more realistic, in particular for land transportation but also for commercial planes as promoted in recent projects [5]. However hydrogen raises many yet unsolved technical questions and requires intensive research and development. Note that in the case of planes, any technical change takes about 25 years to be implemented in the whole fleet around the world .

Because of the advantages in terms of power and storing, in particular in the case of aviation, alternative kerosene fuels originating from sustainable sources seem to be

[3] IEA, Electricity generation by fuel and scenario, 2018-2040, IEA, Paris https://www.iea.org/data-and-statistics/charts/electricity-generation-by-fuel-and-scenario-2018-2040

[4] Airbus electrical flight project https://www.airbus.com/innovation/zero-emission/electric-flight.html

[5] Airbus hydrogen plane https://www.airbus.com/innovation/zero-emission/hydrogen.html

the most reasonable road toward a cleaner aviation in the short-run. Indeed, even if their properties are close to the current standard kerosene (with all the detrimental emissions it implies), alternative fuels have two main advantages :

- as they do not differ much in terms of combustion, they can be directly used in the existing aircrafts and engines. This explains why they are named drop-in fuels.
- as part of their composition does not come from the soils but from organic matter, the overall life cycle of the fuels lead to lower overall detrimental emissions.

Several European collaborations such as the JETSCREEN project (further detailed in Chapter 10) have worked on the capabilities of alternative jet fuels to replace existing fossil fuels in aeronautical engines. Very recently, Airbus, DLR and Rolls-Royce launched the Emission and Climate Impact of Alternative Fuels (ECLIF3) [6] program which will directly assess the impact on pollutants and performances of an aircraft flying with 100% of sustainable aviation fuels (SAF).

1.2 Detailed chemistry expanding the range of possible fuels in combustion

From the previous depiction of what the future will need from the scientific community, it is clear that combustion processes will rise in complexity and with it, their chemical description.

The detailed description of combustion chemical kinetics has been an important focus of the combustion community for almost 30 years and is now, more than ever, a necessary foundation in the construction of accurate and reliable studies for combustion.

An extensive review of all the work associated with the construction of these chemical kinetics mechanisms has been made by [Curran, 2019] and because chemical

[6] https://www.airbus.com/newsroom/press-releases/en/2021/03/aviation-leaders-launch-first-inflight-100-sustainable-aviation-fuel-emissions-study-on-commerc
html

processes are being developed regularly, the possibilities offered by these models are constantly increasing.

These detailed models of combustion chemistry providing important information about the microscopic interactions between the molecules, need to be coupled to the description of transport phenomena with Computational Fluid Dynamics (CFD) solvers in order to study the behaviour of real burners and combustion chambers.

1.3 Numerical simulation to tackle the energy crisis

Numerical simulation is a powerful tool allowing to consider phenomena which would be too hard to measure in experiments, especially when dealing with complex chemistry. It needs to work as a complement of experiments in order to assess its accuracy and predictive capacities.

From the number of abstracts in the last International Conference on Numerical Combustion in Aachen, Germany [7], it is clear that numerical simulation of combustion is a flourishing domain which will play an important role in the scientific challenges ahead.

The Large Eddy Simulation (LES) approach especially [8] has allowed to better understand combustion and helped the industry in their design of more efficient and less polluting engines [Franzelli et al., 2012a, Bulat et al., 2014, Jaravel et al., 2017a, Collin, 2019a, Gallen et al., 2019].

1.4 Objectives and structure of the manuscript

CERFACS has developed over the past 30 years a strong expertise in Computational Fluid Dynamics (CFD), based on Large Eddy Simulation (LES) implemented in

[7] List of abstracts of the 17^{th} International Conference on Numerical Combustion https://www.nc19.itv.rwth-aachen.de/bookOfAbstracts.pdf

[8] A non-exhaustive list of Large Eddy Simulations between 2000 and 2017 can be found in the PhD of [Felden, 2017]

its in-house solver AVBP. It has led to a vast amount of studies in the context of reactive flows REFS. The present work closely follows [Felden, 2017] and [Jaravel, 2016] theses which demonstrated the feasibility of using realistic chemistry in CFD and in particular implemented first Analytically Reduced Chemistry (ARC, described in Chapter 3) mechanisms in AVBP.

Considering everything said earlier, the complexity of the cases which must be studied in order to go forward both from an industrial and an academic point of view requires increasingly complex chemistry description and thus affordable methods to compute them. The first objective of this PhD thesis is therefore to extend the available tools for the reduction of detailed chemical kinetics mechanisms into Analytically Reduced Chemistries (ARC) to make their derivation fully automatic and accessible to non-experts. Part I describes in length the ARC methodology and the ARCANE code which is a major achievement of this work. The code provides a user-friendly environment for researchers interested in reducing a detailed mechanism to an ARC for almost every kind of mixture and in any operating conditions. The code is detailed in Chapters 4 and 5.

The following parts present the application of the reduction process based on academic configurations with non-standard conditions. They aim to demonstrate the robustness and usefulness of the current methodology for the study of cases where the chemical description are critical and where analytical reduction was previously difficult to attain.

Part II presents the specificity of the reduction for hydrogen-enriched methane gaseous premixed flames and its performances on the VALOGAZ academic combustor in the prediction of the flame structure and NO_x emissions.

Part III focuses on the description of kerosene surrogate and 2 alternative jet fuels in conditions of forced ignition of liquid droplets. The fuel is represented by multi-component surrogates exhibiting preferential evaporation. This effect is assessed on zero- and one-dimensional configurations, also comparing the effects of the fuel composition on combustion behaviour.

PART I: Analytically Reduced Chemistry

Part I

Analytically Reduced Chemistry

Chapter 1

Combustion chemistry

Contents

1.1 Introduction

As said by [Curran, 2019], "combustion is the ultimate interdisciplinary field; it requires knowledge of chemistry, physics, fluid dynamics, thermodynamics, mathematics and computer science". Even for the simplest combustion system being the oxy-combustion of hydrogen that can be described by the global reaction $H_2 + 0.5\ O_2 \rightarrow H_2O$, several chemical species are involved and this process must be decomposed into smaller reaction steps, called elementary reactions, in order to accurately describe the evolution of the chemical system both in term of chemical composition and thermodynamic state.

A thorough presentation of the combustion chemistry can be found in the book of [Gardiner, 2012], among others, and its basic principles will be recalled here.

The combustion of any type fuel is driven by the presence of *radicals* that are compounds with unfilled outer electron configuration. This electron craving makes those species highly reactive and will often react shortly after they are produced. OH, O and H are radicals that are of great importance in most combustion systems and the reaction $H + O_2 \rightarrow OH + O$ is often considered as the most important reaction of combustion at high temperatures, as it gives the pace to the whole system.

The characteristic of combustion among other chemical processes is that combustion mechanism is composed of chain reactions. The radicals mentioned earlier, or free radicals, will serve as indicators of the evolution of the chain reaction and elementary reactions will be classified according to the number of radicals in the reactants and the products (that will be noted $N_{radicals,reactants}$ and $N_{radicals,products}$):

- **Chain initiation reactions** are reactions that will produce free radicals starting from stable species. They can be summarised as $N_{radicals,reactants} = 0$, $N_{radicals,products} > 0$.

  The mechanisms leading to chain initiation are:

  - *Homolysis*, which is a dissociation process where a stable molecule breaks to give fragments, each retaining the one electron of the broken bond. At high temperatures, homolysis is called *pyrolysis* because it needs a higher activation energy that is typically given by a flame or an energy source. This mechanism constitutes a unimolecular initiation step.

  - *Hydrogen atom abstraction* or *H abstraction*, in which an O_2 molecules removes and hydrogen atom from a molecule. This constitutes a bimolecular initiation step.

- **Chain propagation reactions** are reactions where a free radical interacts with a stable species to form another radical. They can be summarised as $N_{radicals,reactants} = N_{radicals,products}$.

  Chain propagation reactions include:

  - *Metathesis* or *H abstraction*, in which a free radical removes and hydrogen atom from a molecule creating another free radical.
  - *Dissociation*, where a molecular bond is broken to produce smaller radicals. A special dissociation is *β-scission* that produces a free radical and an unsaturated molecule.
  - *Addition* where two molecules combine to form one.
  - *Izomerisation* where the atoms inside a molecule rearrange to form an isomer. The isomer possesses the same chemical formula as the initial molecule but due to its different geometry, its thermodynamic behaviour is changed.
  - *Dissociation* where similarly to homolysis, a bond breaking result in the production of smaller species. The difference being that the initial molecule is often an intermediate species or a radical.

- **Chain branching reactions** are reactions where a free radical with interact with a stable species to form more radicals. This type of reaction, to which $H + O_2 \rightarrow OH + O$ belongs to, is critical to predict the correct combustion behaviour as a succession of them will rapidly amplify the radical concentration. They can be summarised as $N_{radicals,reactants} < N_{radicals,products}$.

  The mechanisms of branching are the same as the propagation with a different number of radicals as products. Chain branching reactions that go through a stable molecule are called *degenerated branching*.

- **Chain termination reactions**, also called recombination reactions, are reactions that will terminate the chain reaction by forming stable species from free radicals. They can be summarised as $N_{radicals,reactants} > 0$, $N_{radicals,products} = 0$.

  Termination is reached through two mechanisms.

  - *Combination*, where radicals react together to only form stable molecules

– *Disproportionation*, also called *dismutation*, consisting in an exchange of hydrogen atom between radicals to make them stable.

All those different reactions and the path between them the system will take will be highly dependent on the temperature conditions and the flow features. It is therefore critical to initially study canonical cases as the one presented in the following (Section 2) to fully understand the chemistry before applying it to realistic case.

Accurately capturing all the complexity of a combustion system requires a precise chemistry description given by the detailed chemical kinetics mechanisms and all the necessary equations for the computation of compressible reactive flows of gaseous mixtures that are detailed in the following.

1.2 Species quantity

The simpler way of quantifying a species in a mixture is to simply express it as the number of molecules there is in the whole mixture. The number of moles of species k is written n_k.

It can also be convenient to express the mass of species k written m_k, being :

$$m_k = n_k W_k \tag{1.1}$$

where W_k the molecular weight of species k.

A usual way of quantifying species is to express it relatively to the other species quantities.

The mole fraction X_k of species k, which is a dimensionless quantity, represent how much species k there is in 1 mole of the total mixture.

$$X_k = \frac{n_k}{\sum_{k=1,N_s} n_k} \tag{1.2}$$

It is a normalised value so $\sum_{k=1,N_s} X_k = 1$.

The mass equivalent of that quantity is the mass fraction Y_k of species k which represent the mass of species k there is in 1 kg.

$$Y_k = \frac{m_k}{\sum_{k=1,N_s} m_k} \tag{1.3}$$

with $\sum_{k=1,N_s} Y_k = 1$.

It can be express from the mole fraction as:

$$Y_k = X_k \frac{W_i}{W}, \qquad k = 1, N_s \tag{1.4}$$

where $\overline{W}$ is the mean molecular weight of the mixture expressed as $W = \sum_{k=1,N_s} X_k W_k$

The important quantity for kinetics computation is the molar concentration of species k noted c_k which represent the number of mole of species k in a cubic meter and is not dependent from the other species values. It is expressed as

$$c_k = \rho \frac{X_k}{W} = \rho \frac{Y_k}{W_k}, \qquad k = 1, N_s \tag{1.5}$$

Where ρ is the mixture density (in $kg.m^{-3}$).

When the species is explicitly referenced, for example the concentration of CO_2, the molar concentration is written as $[CO_2]$.

The concentration can also be expressed in term of mass and will represent the mass of species k inside a cubic meter. This quantity $c_{k,mass}$ can also be understood as the species density ρ_k, written:

$$c_{k,mass} = \rho_k = \rho Y_k, \qquad k = 1, N_s \tag{1.6}$$

Once all the species quantifying quantities are defined, the reaction between them

can be studied through the chemical kinetics equations described in the following sections.

1.3 Reaction rates

For a given reaction j in the general form $\mathcal{R} \rightarrow \mathcal{P}$, called in the following elementary reaction, the reaction rate $\dot{c}_j$ represents the speed at which the reactants $\mathcal{R}$ are transformed into the products $\mathcal{P}$.

This reaction rate of reaction j (in $mol.m^{-3}.s^{-1}$) is expressed as:

$$\dot{c}_j = k_j \prod_{k=1}^{N_s} c_k^{order_{k,j}}, \qquad j = 1, N_r \tag{1.7}$$

with k_j the rate constant of the reaction and $order_{k,j}$ the reaction order of species k in reaction j.

According to fundamental chemistry, the reaction order can be any positive value and is determined via experiment or by studying the role of the species in a reaction. In bio-chemistry, some reactions such as $C_2H_5OH \rightarrow CH_3CHO$ (producing liver enzymes) actually have a zero overall order meaning that the reaction rate does not depend on the reactants concentration [Tinoco and Jaworski, 2014].

For combustion, complex chemical kinetics schemes are constructed with the mass action law [Waage and Gulberg, 1986] formulated in 1864, stating that for ideal conditions the reaction order of a species depends only on its concentration with no consideration about its size or functionality hence the reaction order of a species equals its stoichiometric coefficient, changing the above equation into:

$$\dot{c}_j = k_j \prod_{k=1}^{N_s} c_k^{\nu'_{k,j}}, \qquad j = 1, N_r \tag{1.8}$$

with $\nu'_{k,j}$ the stoichiometric coefficient of species k in reaction j. The overall reaction order $order_j$ is then $\sum_{k=1}^{N_s} \nu'_{k,j}$.

In order to consistently keep the same unit for the reaction rate, the rate constant unit is dependent on the overall reaction rate and is $mol^{(1-order_j)}m^{-3(1-order_j)}s^{-1}$.

However, in some mechanisms ($CRECK\_2003\_TOT\_HT\_LT\_SOOT$ [1] for example [Ranzi et al., 2014] [Ranzi et al., 2015] [Pejpichestakul et al., 2019]), zero order can be applied to hydrogen atoms in soot formation because of their negligible size compared to soot particles making their impact negligible.

As mass is the variable that is conserved when the reaction takes place, it can be interesting to express the reaction rate in term of mass as:

$$\dot{\omega}_j = \dot{c}_j * W_k, \qquad j = 1, N_r \tag{1.9}$$

The rate constant previously introduced is generally written as temperature dependant equation known as Arrhenius equation:

$$k_j(T) = A_j T^{\beta_j} e^{\frac{-E_{a,j}}{RT}}, \qquad j = 1, N_r \tag{1.10}$$

with T the temperature, A the pre-exponential exponent, β the temperature exponent, E_a the activation energy and R the universal gas constant ($= 8.31446 \quad J.K^{-1}.mol^{-1}$).

The activation energy E_a (in $J.mol^{-1}$) is the kinetic energy of colliding molecules required for the reaction to happen and divided by the perfect gas constant R, can be seen as an activation temperature T_a.

The pre-exponential factor A can be seen as a quantification of the reaction reactivity compared to other reactions. To be consistent with the rate constant, its unit is $mol^{(1-order_j)}m^{-3(1-order_j)}s^{-1}K^{-1}$.

As explained in [Laidler, 1984], the temperature exponent β is a correction of the pre-exponential coefficient allowing to cover a wider range of temperature (which is particularly important when dealing with combustion).

[1] http://creckmodeling.chem.polimi.it/menu-kinetics/menu-kinetics-detailed-mechanisms/107-category-kinetic-mechanisms/407-mechanisms-1911-tot-ht-lt-soot

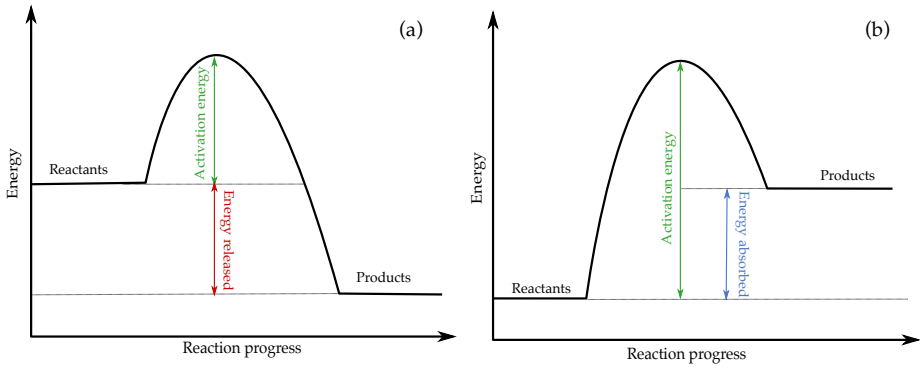

Figure 1.3.1: Energy profile of an exothermic (a) and an endothermic (b) reaction

1.3.1 Reversible reactions

A majority of reactions does not go only one way and depending on the local conditions, the products of the equation can become reactants. This type of reaction called reversible (as opposed to irreversible) are written $\mathcal{R} \leftrightarrow \mathcal{P}$. The reaction rate c_j for such reactions, called the net reaction rate, is then the contribution of both the left to right and the right to left reactions:

$$\dot{c}_j = k_{forward,j} \prod_{k=1}^{N_s} c_k^{\nu'_{k,j}} + k_{backward,j} \prod_{k=1}^{N_s} c_k^{\nu''_{k,j}}, \qquad j = 1, N_r \tag{1.11}$$

$$\dot{c}_{net,j} = \dot{c}_{forward,j} + \dot{c}_{backward}j, \qquad j = 1, N_r \tag{1.12}$$

The subscripts $forward$ and $backward$ indicating the direction of the reaction, respectively $\mathcal{R} \rightarrow \mathcal{P}$ and $\mathcal{P} \rightarrow \mathcal{R}$. The forward and backward rate constants are related through the equilibrium constant $k_{equilibrium,j}$ which writes :

$$k_{equilibrium,j} = \frac{k_{forward,j}}{k_{backward,j}}, \qquad j = 1, N_r \tag{1.13}$$

$$k_{equilibrium,j} = \left(\frac{P_{atm}}{RT}\right)^{\sum_{k=1}^{N_s} \nu_{k,j}} e^{\sum_{k=1}^{N_s} \nu_{k,j} \frac{\mu_k}{RT}}, \qquad j = 1, N_r \tag{1.14}$$

where P_{atm} is the atmospheric pressure and μ_k the Gibbs free energy of species k defined as $\mu_k = H_k - S_k T$, H_K being species k standard enthalpy and S the standard entropy at the given temperature and pressure.

Unless clearly specified, all reactions of a specified kinetic system will be expressed as elementary reactions in the following equations, meaning that all reversible reactions will be split into two irreversible reactions linked through the relation of their rate coefficients given by Eq. 1.13.

1.3.2 Third body reactions

For specific reactions to happen, a collision partner is sometimes necessary, meaning an inert species in the reaction that will carry some of the reaction energy to make the reaction stable. Such reactions, called third body reaction, are written as $\mathcal{R} + \mathcal{M} \rightarrow \mathcal{P} + \mathcal{M}$ with $\mathcal{M}$ symbolizing collision partners. The reaction rates then becomes:

$$\dot{c}_j = k_j M_j \prod_{k=1}^{N_s} c_k^{\nu'_{k,j}}, \qquad j = 1, N_r \tag{1.15}$$

with M_j the concentration of the collision partner defined as $M_j = \sum_{k=1}^{N_s} z_{k,j} c_k$ with $z_{k,j}$, called the catalytic efficiency, a coefficient weighting the effectiveness of each species being a collision for the reaction j.

1.3.3 Pressure dependent reactions

As explained in [Peters, 1992], some reaction exhibit a three body reaction behaviour at low pressures ($\mathcal{R} + \mathcal{M} \rightarrow \mathcal{P} + \mathcal{M}$) and a elementary reaction behaviour at high pressures ($\mathcal{R} \rightarrow \mathcal{P}$).

This change in behaviour is explained by the differences in collision partners concentrations order of magnitude when the pressure changes. At high pressures, concentrations are higher meaning that more species are available for taking away the reaction energy. The reaction rate then does not depend on other species concentrations because the concentration will always be high enough. For low pressures, the concentrations are also lower so the collision partners concentration becomes critical

to the reaction rate. Between those high and low pressures limits yields the fall-off regime which gives its name to this type of reactions, fall-off reactions.

For this type of reactions, two sets of Arrhenius equation parameters are defined resulting in two rate constants k_0 and k_{inf} respectively for the low pressure and the high pressure limit.

The final rate constant for the reaction is defined as :

$$k_j = k_{inf}\left(\frac{P_r}{P_r+1}\right), \qquad j = 1, N_r \tag{1.16}$$

with P_r called the reduced pressure expressed as $\frac{k_0 M_j}{k_{inf}}$.

Most formulations introduce a broadening factor F (also called fall-off function) in order to describe more accurately the transition regime, the previous equation becomes:

$$k_j = k_{inf}\left(\frac{P_r}{P_r+1}\right)F(P_r,T), \qquad j = 1, N_r \tag{1.17}$$

$F(P_r,T)$ can be described for example with the Troe formulation [Gilbert et al., 1983] or the SRI formulation [Stewart et al., 1989].

1.4 Production rates

The first quantity of interest when looking at the evolution of a chemical system is the behaviour of species concentrations as it will tell from a macroscopic point of view which chemical processes are happening. From the previous equations, the temporal evolution of species k concentrations $\frac{dc_k}{dt}$ (in $mol.m^{-3}.s^{-1}$), written for simplicity as $\dot{c}_k$, is expressed as:

$$\dot{c}_k = \sum_{j=1}^{N_R} \nu_{k,j}\dot{c}_j, \qquad k = 1, N_s \tag{1.18}$$

As the total mass should be conserved, this equation ensures that $\sum_{k=1}^{N_s} \dot{c_k} = 0$.

This production rate (sometimes called the net production rate to avoid confusion) can be split into a destruction part and a creation part written as:

$$Destruction_k = -\sum_{j=1}^{N_R} \nu'_{k,j} \dot{c}_j, \qquad k = 1, N_s \tag{1.19}$$

$$Creation_k = \sum_{j=1}^{N_R} \nu''_{k,j} \dot{c}_j, \qquad k = 1, N_s \tag{1.20}$$

As mass is the quantity conserved throughout the combustion, the chemical source term is often written $\dot{\omega_k}$ (in $kg.m^{-3}.s^{-1}$), expressed as:

$$\dot{\omega_k} = \sum_{j=1}^{N_R} \nu_{k,j} \dot{\omega_j} = \dot{c_k} * W_k, \qquad k = 1, N_s \tag{1.21}$$

This term will be used as a source term in the species transport equation that will be detailed in 1.7.

1.5 Thermochemistry

Chemical species carry chemical energy within their electronic bond, it means that any transformation from a set of molecules to another will lead into the release or absorption of energy. Equations describing the thermodynamic evolution of the system are crucial especially in combustion.

1.5.1 Chemical equilibrium

Any given thermodynamic system possesses an equilibrium state at which the Gibbs free energy of the system $\mu = \sum \mu_k$ is minimum.

Starting from a standard state and solving this minimization problem, one can define the equilibrium state of the mixture given that two thermodynamic variables are fixed. This equilibrium state depends only on the initial thermodynamic state and not on the kinetics. It can be seen as the state of the mixture if a infinite time passes.

For an adiabatic process, the equilibrium temperature of the mixture is called the *adiabatic flame temperature* written T_{ad} and the equilibrium species quantities are written with an *eq* superscript.

1.5.2 Heat release

Combustion process is characterised among other chemical processes by its speed and an important production of heat. The amount of heat produced by the combustion rely on the difference of enthalpy between the reactants and the product. The chemical systems aims to achieve chemical equilibrium by rearranging the molecular bonds to create a less energetic mixture. The reactions of chemical system describe that change in molecule structure and dictate the heat that is released (or absorbed) as shown in Fig. 1.3.1.

The total amount of heat ΔQ released during a reaction j (in $J.mol^{-1}$) is defined as the difference between the reactants and the products enthalpy:

$$\Delta Q_j = \sum_{k=1}^{N_s} \nu'_{k,j} h_k - \sum_{k=1}^{N_s} \nu''_{k,j} h_k \tag{1.22}$$

With h_k the total enthalpy of species k for a specific temperature, written:

$$h_k(T) = h_{s,k}(T) + \Delta h^0_{f,k}(T) = \int_{T_0}^{T} c_{p,k}\, dT + \Delta h^0_{f,k} \tag{1.23}$$

With T_0 the reference temperature taken here as $298K$ and $C_{p,k}$ the isobaric molar heat capacity, $h_{s,k}$ the sensible enthalpy of species k and $\Delta h^0_{f,k}$ the enthalpy of formation of species k.

The enthalpy of formation of a species is defined as *the heat released from the*

creation of one mole of molecule from its constituting elements at that same temperature. From that definition, it is deduced that atomic species have a null enthalpy of formation as well as stable[2] mono-atomic molecules (O_2 and N_2 for example). The reference temperature as been widely chosen to be $298K$ in order to determine experimentally thermodynamic quantities more easily.

As said earlier, the specificity of combustion among other chemical processes is that this total amount of heat is released instantaneously for the human perception of time. The heat release rate $\dot{Q}$ (in $J.m^{-3}.s^{-1}$) is the quantity of interest for the characterisation of combustion.

The heat release rate of the reaction j is simply the total amount of heat produced by the reaction multiplied by its reaction rate:

$$\dot{Q_j} = -\dot{c_j} * \Delta Q_j \tag{1.24}$$

Also a heat release rate can be defined on a per species base, written as:

$$\dot{Q_k} = -\dot{c_k} * h_k \tag{1.25}$$

The overall heat release rate (sometimes written ω_T) then writes:

$$\dot{Q} = \sum_{j=1}^{N_r} \dot{Q_j} = \sum_{k=1}^{N_s} \dot{Q_k} \tag{1.26}$$

The partial heat release forms (per reaction or per species) are particularly useful for detailed mechanisms where endothermic and exothermic processes are competing in order to identify the dominant reaction pathways.

[2]This criterion is important as ozone (O_3) for example, despite being constituted of only oxygen atoms, has a non-zero enthalpy of formation ($\Delta h^0_{f,k} = 142,12kJ/mol$)

1.6 Conservation equations of reacting flows

When applying chemical kinetics to dimensional cases, the temporal evolution is not sufficient to describe the behaviour of the chemical system and one must introduce an advection-diffusion equation to represent the spatial displacement of chemical species.

In that case, compressible reactive Navier-Stokes equation are applied and writes as $5 + N_s$ equations for the conservation of mass, momentum (one per dimension of the problem N_{dim}), energy and one for each species [Poinsot and Veynante, 2012].

The mass conservation equation writes:

$$\frac{\partial \rho}{\partial t} + \frac{\partial \rho u_i}{\partial x_i} = 0 \qquad i = 1, N_{dim} \tag{1.27}$$

Where t is the time, u_i the i-th velocity and x_i the i-th spatial coordinate.

The momentum conservation equation writes:

$$\frac{\partial \rho u_i}{\partial t} + \frac{\partial \rho u_i u_j}{\partial x_i} = \frac{\partial \sigma_{ij}}{\partial x_i} + \rho \sum_{k=1}^{N_s} Y_k f_{k,j} \qquad i, j = 1, N_{dim} \tag{1.28}$$

Where $f_{k,j}$ is the volumetric forces applied on species k in the direction j and the stress tensor σ_{ij} written for a Newtonian fluid as:

$$\sigma_{ij} = -P\delta_{ij} + \tau_{ij} \qquad i, j = 1, N_{dim} \tag{1.29}$$

with

$$\tau_{ij} = 2\mu(S_{ij} + D_{ij}) \tag{1.30}$$

$$D_{ij} = -\frac{1}{3}\left(\sum_{k}^{N_{dim}} \frac{\partial u_k}{\partial x_k}\right)\delta_{ij} \tag{1.31}$$

$$S_{ij} = \frac{1}{2}\left(\frac{\partial u_i}{\partial x_j} + \frac{\partial u_j}{\partial x_i}\right) \tag{1.32}$$

Where P is the pressure, τ_{ij} the Reynolds stress tensor with D_{ij} and S_{ij} the volumetric stress tensor and the deviator tensor respectively, μ the dynamic viscosity and δ_{ij} the Kronecker symbol ($\delta_{ij} = 1$ if $i = j$, 0 otherwise).

The species k mass conservation equation writes:

$$\frac{\partial \rho Y_k}{\partial t} + \frac{\partial \rho (u_i + V_{k,i}) Y_k}{\partial x_i} = \dot{\omega}_k \qquad i, j = 1, N_{dim}, k = 1, N_s \tag{1.33}$$

Where $V_{k,i}$ is species k diffusion velocity in the direction i which will be detailed in 1.7.1.

The energy conservation equation writes:

$$\frac{\partial \rho E}{\partial t} + \frac{\partial}{\partial x_i}\left(\rho E u_i\right) = -\frac{\partial}{\partial x_i}\left(u_j \sigma_{ij} + q_i\right) + \dot{Q} \qquad i, j = 1, N_{dim}, k = 1, N_s \tag{1.34}$$

Where E is the energy and q_i the energy flux. The energy flux can be decomposed into conductive term and a term due to the energy transported by species diffusion, the energy flux the writes:

$$q_i = -\lambda \frac{\partial T}{\partial x_i} + \sum_{k=1}^{N_s} \rho V_{k,i} Y_k h_{s,k} + p \sum_{k=1}^{N_s} \kappa_k^T V_{k,i} \qquad i, j = 1, N_{dim}, k = 1, N_s \tag{1.35}$$

where λ is the heat conduction coefficient and κ_k^T the thermal diffusion ratio. The first term of the right hand side (RHS) of this equation is the heat conduction term, the second represent the heat flux coming from the species diffusion and the last one, called the Dufour effect, represent the temperature rise due to species diffusion. Comparatively to the other heat flux terms, Dufour effect has been found to have a weak influence on the total heat flux [García-Ybarra et al., 1984] and is therefore neglected in the present study, finally writing the energy flux as

$$q_i = -\lambda \frac{\partial T}{\partial x_i} + \sum_{k=1}^{N_s} \rho V_{k,i} Y_k h_{s,k} \qquad i,j = 1, N_{dim}, k = 1, N_s \tag{1.36}$$

Finally, this system is closed considering the equation of state for an ideal gas:

$$P = \rho r T, \qquad r = R/W \tag{1.37}$$

with r the specific gas constant depending on the local mixture.

1.7 Transport modelling

From previous equations, several quantities must be specified. The quantities than will be detailed in the following are subject to modelling as their exact expression is either not known or too complex to be actually used.

1.7.1 Diffusion velocity

The species diffusion velocities $V_{k,i}$ which determines the velocity at which species will move relatively from one another under the local thermodynamic conditions. This velocity is expressed as follow:

$$V_{k,i} = -\frac{1}{X_k} \sum_{l=1}^{N_s} \frac{W_k}{W} D_{kl} d_{l,i} - \frac{\kappa_k^T}{\rho Y_k} \frac{1}{T} \frac{\partial T}{\partial x_i} \qquad i = 1, N_{dim}, k, l = 1, N_s \tag{1.38}$$

Where $D_{k,l}$ is the diffusion coefficient of species k into species l and $d_{k,i}$ is the diffusion driving force of species k in the direction i. The second term on the RHS is called the Soret effect (written SE in the following equations) and represents the diffusion of species due to thermal gradients, is is the reciprocal of the Dufour effect introduced in 1.36. The diffusion driving force term is a complex term written as:

$$d_{k,i} = \frac{\partial X_k}{\partial x_i} + (X_k - Y_k)\frac{1}{P}\frac{\partial P}{\partial x_i} + \frac{\rho}{P}\sum_{l=1}^{N_s} Y_k Y_l (f_{l,i} - f_{k,i}) \qquad i = 1, N_{dim}, k, l = 1, N_s \tag{1.39}$$

From this equation, the different diffusion driving mechanisms are the local composition gradients (first term of the RHS), the pressure gradients (second term of the RHS) and the volumetric forces (third term of the RHS).

The pressure forces are only relevant for compressibility effects dominated flows which is not the case for the applications in this work. Also volumetric forces are negligible as gravity does not have a significant effect considering the mass of the particles and no electro-magnetic forces (relevant for ionised gases for example) are considered in this work.

Thus Eq. 1.38 becomes:

$$V_{k,i} = -\frac{1}{X_k}\sum_{l=1}^{N_s}\frac{W_k}{W} D_{kl}\frac{\partial X_k}{\partial x_i} - SE \qquad i = 1, N_{dim}, k, l = 1, N_s \tag{1.40}$$

1.7.2 Mixture-averaged transport model

This previous formulation (referred as multi-component transport) is still expensive to compute for CFD codes.

A simplification of that expression is the *Hirshfelder and Curtis approximation* [Hirshfelder and Curtiss, 1954] giving a mixture-averaged expression of the diffusion velocity written as:

$$V_{k,i} = -\frac{1}{X_k} D_k \frac{\partial X_k}{\partial x_i} - SE \qquad i = 1, N_{dim}, k = 1, N_s \tag{1.41}$$

Where $D_k = \frac{1-Y_k}{\sum_{l=1, l\neq k}^{N_s} \frac{X_l}{D_{lk}}}$ is the diffusion coefficient of species k into the mixture.

To ensure mass balance, one needs to ensure that $\sum_{l=1}^{N_s} Y_k V_{k,i} = 0$ which is not

the case with the previous formulation. A correction velocity V_i^c is then introduced as

$$V_i^c = \sum_{k=1}^{N_s} \frac{W_k}{W} D_k \frac{\partial X_k}{\partial x_i} \qquad i = 1, N_{dim} \tag{1.42}$$

The diffusion velocity finally writes

$$V_{k,i} = -\left(\frac{1}{X_k} D_k \frac{\partial X_k}{\partial x_i} - V_i^c \right) - SE \qquad i = 1, N_{dim}, k = 1, N_s \tag{1.43}$$

The aforementioned formulation that will be referenced as *mixture-averaged transport* will be the one used throughout the current work when computing one dimensional cases with the chemical solver Cantera [Goodwin et al., 2017].

According to [Giovangigli, 2015], the Soret effect is only relevant for combustion of very light species, specifically H and H_2, and is neglected for hydrocarbons. For that reason, the Soret effect influence is neglected throughout this manuscript unless specifically addressed.

Expressing the transport properties according the global mixture is also the strategy used for the computation of the dynamic viscosity μ through the Wilke formula [Wilke, 1950] which writes

$$\mu = \sum_{k=1}^{N_s} \frac{\mu_k X_k}{\sum_{l=1}^{N_s} X_l \Phi_{kl}} \tag{1.44}$$

where

$$\Phi_{kl} = \frac{1}{8} \left(1 + \frac{W_k}{W_l} \right)^{-\frac{1}{2}} \left[1 + \left(\frac{\mu_k}{\mu_l} \right)^{-\frac{1}{2}} \left(\frac{W_l}{W_k} \right)^{\frac{1}{4}} \right]^2 \tag{1.45}$$

The thermal conductivity for the mixture, introduced in 1.36 can also be expressed as mixture-averaged [Mathur and Saxena, 1967]:

$$\lambda = \frac{1}{2}\left(\sum_{k=1}^{N_s} X_k \lambda_k + \frac{1}{\sum_{k=1}^{N_s} X_k \lambda_k^{-1}}\right) \tag{1.46}$$

1.7.3 Simplified transport in AVBP

The computation of those transport coefficients are still expensive for an LES solver as it involves complex formulas for the species individual coefficients relying on the species Lennard-Jones potentials.

Because combustion takes place in an environment with a large amount of air, viscosity is considered independent from the mixture composition and close to air, which allows to express it either as a Sutherland law

$$\mu = \alpha_1 \frac{T^{3/2}}{T + \alpha_2} \frac{T_{ref} + \alpha_2}{T_{ref}^{3/2}} \tag{1.47}$$

or as a simpler power law

$$\mu = \alpha_1 \left(\frac{T}{T_{ref}}\right)^b \tag{1.48}$$

with T_{ref} a reference temperature typically taken as $300K$ and α_1, α_2 and b parameters obtain from fitting the mixture averaged value of μ on a temperature range.

For the determination of the heat conductivity λ and the species diffusion coefficients D_k, several non-dimensional numbers must be introduced.

The Schmidt number of a species k is the ratio between the momentum diffusivity of the mixture and the molecular mass diffusivity of this species inside the mixture. It is expressed as

$$Sc_k = \frac{\nu}{D_k} \frac{\mu}{\rho D_k} \tag{1.49}$$

The Prandtl number of the mixture is defined as the ratio between momentum diffusivity of the mixture and the the thermal diffusivity. It is expressed as

$$Pr = \frac{\nu}{D_{th}} = \frac{\mu C_{p,mixture}}{\lambda} \tag{1.50}$$

with $D_{th} = \frac{\lambda}{\rho C_{p,mixture}}$ the mixture thermal diffusivity.

Finally, the Lewis number represents the ratio between thermal diffusivity and molecular mass diffusivity and writes

$$Le_k = \frac{\lambda}{\rho C_{p,mixture} D_k} = \frac{S_{c,k}}{Pr} \tag{1.51}$$

Considering the Lewis number of each species constant in the domain is a reasonable assumption considering the very low variation of the Lewis number value across a flame shown in Fig. 1.7.1. The assumption will be referred to as the *constant Lewis assumption* in the following.

From this assumption, the thermal conductivity λ can be computed as

$$\lambda = \frac{\mu C_{p,mixture}}{Pr} \tag{1.52}$$

and the diffusion coefficients D_k can be computed with

$$D_k = \frac{\mu}{\rho S_{c,k}} \tag{1.53}$$

The values of Schmidt numbers and Prandtl number are selected from gaseous states that are representative of the chosen CFD calculations, the selection strategy will be detailed in 5.4.

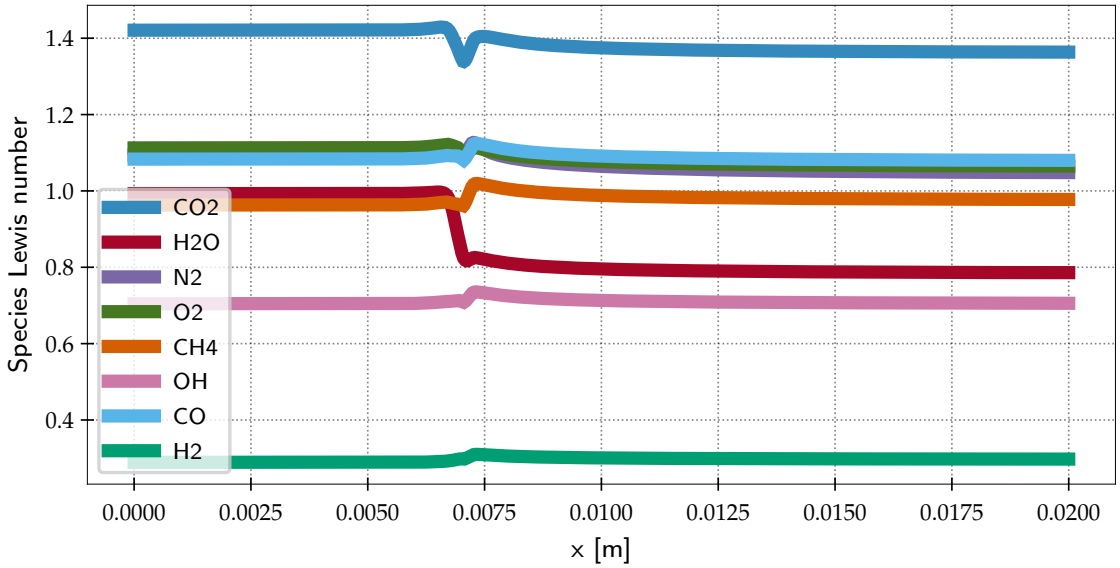

Figure 1.7.1: Lewis number across a laminar freely propagating premixed flame for several import species. This flame corresponds to the stoichiometric combustion of methane/air at 300 K and 1 bar.

1.8 Definition of stoichiometry

The basic definition of combustion is *the exothermic transformation of a fuel and an oxidiser into burnt products*. The relative proportion of fuel and oxidiser species is a crucial parameter in the characterisation of the combustion process. This process can be simplified into a global reaction used to assess the mass balance, written

$$Fuel + Oxidiser = Products \tag{1.54}$$

For a vast majority of combustion processes, this equation can be detailed as:

$$C_xH_y + s_X(O_2 + n_{\frac{N_2}{O_2}}N_2) = xCO_2 + \frac{y}{2}H_2O \tag{1.55}$$

Where x,y and z are respectively the number of carbon, hydrogen and oxygen atoms in the fuel, s_X, called the molar stoichiometric ratio, is the number of mole

required for a complete consumption of both fuel and oxidiser, $n_{\frac{N_2}{O_2}}$ is the molar ratio between nitrogen and oxygen species ($n_{\frac{N_2}{O_2}} 3.76$ for air and 0 for pure oxygen). Combustion with other species as oxidiser and diluent are not considered in this work.

From this atomic balance equation, the molar stoichiometric ratio s_X is defined as

$$s_X = x + \frac{y}{4} \tag{1.56}$$

The equivalence ratio ϕ is introduced to represent if the initial proportions of fuel and oxidiser present an excess of fuel (rich regime) or an excess of oxidiser (lean regime). This variable is expressed as

$$\phi = \frac{X_{fuel}}{X_{oxidiser}} \left(\frac{X_{oxidiser}}{X_{fuel}} \right)_{st} = s_X \frac{X_{fuel}}{X_{oxidiser}} \tag{1.57}$$

The equivalence ratio can be introduced in the element balance equation as follow

$$\phi C_x H_y + s_X (O_2 + n_{\frac{N_2}{O_2}} N_2) = x CO_2 + \frac{y}{2} H_2 O \tag{1.58}$$

It can also be expressed in mass with

$$\phi = \frac{Y_{fuel}}{Y_{oxidiser}} \left(\frac{Y_{oxidiser}}{Y_{fuel}} \right)_{st} = s_Y \frac{Y_{fuel}}{Y_{oxidiser}} = s_Y \frac{m_{fuel}}{m_{oxidiser}} \tag{1.59}$$

Where s_Y is the mass stoichiometric ratio which can be expressed as:

$$s_Y = \frac{s_X W_{oxidiser}}{W_{fuel}} \tag{1.60}$$

With $W_{oxidiser} = W_{O_2} + n_{\frac{N_2}{O_2}} W_{N_2}$ ($= 137.28\ kg/mol$ for air with a classical composition of 21% of di-oxygen and 79% of di-nitrogen).

stoichiometric ratio	s_X	s_Y	s_{Y,O_2}
Dihydrogen (H_2)	0.5	34.32	8
Methane (CH_4)	2	17.16	4
Ethanol (C_2H_6O)	3	8.95	2.09
Propane (C_3H_8)	5	15.6	3.64
n-heptane (C_7H_{16})	11	15.12	3.52
n-dodecane ($C_{12}H_{26}$)	18.5	14.92	3.48

Table 1.8.1: Table of molar, mass and oxygen-mass stoichiometric ratios (respectively s_X, s_Y and s_{Y,O_2}) for a series of fuels with air.

The ratio $\frac{m_{fuel}}{m_{oxidiser}}$ is referenced as the Fuel-Air ratio (FAR) for air combustion and is commonly used in aeronautic engineering because it is simpler to compute from fuel and air mass flow rates.

An in-between definition [Poinsot and Veynante, 2012] that can lead to confusion with the previous one, considers the oxidiser to be only the di-oxygen, making the mass stoichiometric ratio the same regardless of the di-nitrogen content. This leads to the formula

$$s_{Y,O_2} = \frac{s_X W_{O_2}}{W_{fuel}} = s_Y - \frac{s_X n_{\frac{N_2}{O_2}} W_{N_2}}{W_{fuel}} \tag{1.61}$$

Table 1.8.1 present the different values of molar and mass stoichiometric ratios for several fuel.

An important aspect of combustion description is the mixing and can be described with a mixture fraction Z that will take a value of 0 when being in pure fuel and 1 in pure oxidiser

$$Z = \frac{\beta - \beta_{oxidiser}}{\beta_{fuel} - \beta_{oxidiser}} \tag{1.62}$$

where β is defined via mass fractions of atomic elements

$$\beta = \sum_{\ell=1}^{N_e} \gamma_e Y_e = \sum_{e=1}^{N_{elements}} \gamma_e \sum_{k=1}^{N_s} \frac{a_{e,k} W_e Y_k}{W_k} \tag{1.63}$$

where the subscript e stands for the atomic elements C, H and O, $a_{e,k}$ the number of atom e in species k and γ_e a weighting parameter.

From Bilger definition [Bilger et al., 1991]

$$\beta = 2\frac{Y_C}{W_C} + \frac{1}{2}\frac{Y_H}{W_H} - \frac{Y_O}{W_O} \tag{1.64}$$

yielding the weighting parameters $\gamma_C = 2/W_C, \gamma_H = 1/2W_H$ and $\gamma_O = -1/W_O$.

Those weighting coefficients are found by ensuring that for a stoichiometric mixture, $\beta_{st} = 0$.

If we verbose the atomic balance of Eq. 1.55, it means that, at stoichiometry, the number of oxygen atoms in the mixture is two times the number of carbon atoms plus the number of hydrogen atoms divide by four, which writes mathematically:

$$n_O = 2(n_C + \frac{1}{4}n_H) \tag{1.65}$$

which gives

$$2n_C + \frac{1}{2}n_H - n_O = 0 \tag{1.66}$$

The number of atom can be expressed as:

$$n_e = m\frac{Y_e}{W_e} \tag{1.67}$$

Injecting this last expression into Eq. 1.66, we obtain:

$$m\left(2\frac{Y_C}{W_C}+\frac{1}{2}\frac{Y_H}{W_H}-\frac{Y_O}{W_O}\right)=0 \tag{1.68}$$

Finally retrieving the Bilger weighting parameters.

From Eq. 1.66, it can easily be seen that for rich conditions, β will be positive whereas being negative in lean conditions.

Finally, the equivalence ratio can be retrieved from the mixture fraction as

$$\phi=\frac{Z}{1-Z}\frac{1-Z_{st}}{Z_{st}} \tag{1.69}$$

The expression of the equivalence ratio using the mixture fraction has the advantage of being usable outside of premixed fresh gases because it does not need the fuel and oxidiser species to stay intact to be computed.

An other local equivalence ratio can be derived from Eq. 1.55 and 1.58. If X is the number of mole of oxidiser in any case such as $X=\frac{s_X}{\phi}$ in Eq. 1.58 and we consider only one mole of fuel in Eq. 1.55 as it is presently written, then trivially the equivalence ratio writes:

$$\phi=\frac{s_X}{X} \tag{1.70}$$

From its definition, s_X is expressed via the number of carbon and hydrogen atoms in the fuel as $s_X=n_{C,fuel}+\frac{1}{4}n_{H,fuel}$. Because of the atomic conservation, it can be expressed in any resulting mixture as $s_X=n_C+\frac{1}{4}n_H$. Because there is 2 atoms of oxygen in the O_2 species, $n_O=2X$ which gives $X=\frac{n_O}{2}$

Injecting these 2 expressions in Eq. 1.70, one obtains:

$$\phi=\frac{n_C+\frac{1}{4}n_H}{\frac{n_O}{2}}=\frac{2n_C+\frac{1}{2}n_H}{n_O} \tag{1.71}$$

Giving the local equivalence ratio based on an atomic budget. This expression will be the one used throughout the manuscript as in is the most generic one because

it does not involve the a-priori knowledge of the fuel composition which is not possible to assess in mixtures with strong fuel composition inhomogeneities.

Chapter 2

Canonical combustion cases

Contents

Previously established equations for multi-species reactive flows (Section 1.6) are often too complex to solve analytically or require an excessive computational power. Fortunately, canonical combustion regimes can be identified and studied in order to better understand complex combustion phenomena and further simplify those equations. The canonical cases represent a dissociation of the temporal and spatial evolution of the combustion process. The temporal evolution is represented as zero-dimensional reactors where the problem is contained in a single point in which the mixture will evolve in time. This configuration allows to study where the time evolution of a isotropic mixture is of interest such as auto-ignition. The spatial evolution is modelled as one-dimensional steady flames on which the mixture will vary spatially. This is useful to study configurations where the transport needs to be accounted for and spatial profiles are of interest. Both configurations and the canonical cases within them will be detailed in the following. For each case, the

underlying theory will be detailed before explaining how it is actually computed in the chemical solver *Cantera* [Goodwin et al., 2017]. *Cantera* is a chemical solver capable of handling a large variety of 0D and 1D canonical cases. This solver will be used throughout the entire manuscript to compute chemical processes in the canonical cases detailed in the following.

2.1 Zero-dimensional cases

This type of case can be visualised as a domain that is homogeneous and isotropic at each time thus removing all spatial components of the equations described in 1.6. This type of case being only time dependant, the species transport is irrelevant allowing very fast computations even with hundreds of species.

2.1.1 Isochoric reactor

For isochoric reactors, the volume of the domain V is set to an arbitrary value as it is represented by the mixture density rho in the state equation 1.37. Taking into account the zero-dimensional assumption, the energy conservation equation can be written in the temperature form as:

$$\rho C_v \frac{dT}{dt} = -\sum_{k=1}^{N_s} \dot{\omega}_k U_k \tag{2.1}$$

with C_v the constant volume heat capacity and U_k species k internal energy.

In *Cantera*, this equation is solved using a stiff ODE solver. The time step of the computation is internally computed in order to satisfy predefined tolerances.

This type of reactor is used to assess an auto-ignition delay time τ_{ig} of a specific mixture that is measured experimentally in tubular flow reactors [Sabia et al., 2013] or shock tube experiments [Herzler and Naumann, 2009].

In this work, the auto-ignition delay time is taken as the time where the heat release rate reaches its maximum.

2.1.2 Reactor networks

In *Cantera*, reactor networks can be created allowing to model a large variety of setups. The different reactors can be modeled with constant volume, constant pressure or with a moving wall to reproduce, for example, apparatus with pistons. They are particularly useful for non-adiabatic computations as heat fluxes can be imposed (this reactor type will be used in 4.5.3 to model a steam cracking process).

2.2 One-dimensional cases

The other interesting simplification of the combustion process is to study the spacial profiles of steady flames. In that case the temporal evolution is not considered and the species transport will play an important role. A complex flame can be described as the combination of two phenomenon: premixed flames and non-premixed flames.

2.2.1 Premixed flames

The premixed flame is the combustion regime where the fuel and the oxidizer are mixed together before burning. The equivalence ratio ϕ (or alternatively the Fuel-Air Ratio in engineering) is the variable describing this premixing.

The premixed flame exhibits three different layers within its structure:

- The *preheat zone* where no heat is released and the fresh gases are heated via thermal diffusion by the high temperatures of the reactive zone.
- The layer where the exothermic reactions occur is called the *inner reaction zone*. It is characterised by a thermal thickness δ_l defined as :

$$\delta_l = \frac{T_b - T_f}{max\left(\left|\frac{\partial T}{\partial x}\right|\right)} \tag{2.2}$$

  where T_b is the burnt gases temperature and T_f the fresh gases temperature.

  Fig. 2.2.1d shows that the vast majority of the species in the chemical scheme are only present in this zone with a peak value of 105 species out of 118 in total.

Looking at the order of magnitude of the characteristic chemical timescale (Fig. 2.2.1e) called $o\tau_{chem}$ computed with Eq. 2.4 ($\tau_{chem} = 1e-10$ gives $o\tau_{chem} = 10$), the lowest timescales are observed in that zone and immediately after it meaning that the stiffness of the chemical kinetics scheme is concentrated in that zone. For those reasons, this zone is the most critical from a numerical point of view and is the one that needs to be carefully resolved in simulations.

$$\tau_{chem,k} = \frac{\partial C_k}{\partial \dot{c_k}} \tag{2.3}$$

$$o\tau_{chem} = \max_{\text{all species k}} -\log_{10}\left(\tau_{chem,k}\right) \tag{2.4}$$

- Finally, the *post-flame* is where the final products are produced from intermediate species and where the mixture will ultimately reach equilibrium. It is the layer were final reaction products like CO and CO_2 will equilibrate and pollutant such as NO will form as seen in Fig. 2.2.1c .

Another key quantifier of the premixed flame is the laminar flame speed S_l. It corresponds to the speed at which the flame propagates in a free stream normal to the flame front towards the fresh gases. For the canonical simulations performed in this work, the laminar flame speed is taken as the inlet velocity of the fresh gases u_0 because the flame is solved in a steady state in the flame front referential.

In Cantera, the premixed flame is solved via a damped Newton solver using the equations described in the solver documentation [1].

2.2.2 Non-premixed flames

The non-premixed flames correspond to a case where the fuel and oxidiser are injected separately and will only mix within the reactive zone. In one dimension, this phenomenon is represented by the fuel and oxidiser inlet facing each other in a configuration called a counter-flow flame.

The fundamental difference with premixed flames lies in the fact that diffusion flames will live only on a stoechiometric line and will not propagate, therefore the thickness of a diffusion flame is only driven by the thermal and molecular diffusion.

[1] https://cantera.org/science/flames.html

Because an equivalence ratio has no meaning in this case and the flame is mainly affected by the flow conditions, the strain rate a is used to characterise diffusion flames. It corresponds to the local velocity gradient that will directly influence the mixing of the reactants; if the strain rate is too low, no mixing will occur thus no reactions, if the strain rate is too high the flame will be quenched. The strain rate of importance for the characterisation is the stoechiometric strain rate a_{st} corresponding to the strain rate at the stoechiometric position within the flame and can be roughly estimated from the global strain rate $a_{global} = \frac{u_{fuel}+u_{oxidiser}}{L}$ where u_{fuel} and $u_{oxidiser}$ respectively the fuel injection velocity and the oxidiser injection velocity (both positive) and L the distance between the two injectors.

Because the diffusion flames are driven by mixing they are generally represented in a mixture fraction space based on the mixture fraction Z defined in 1.62. In the mixture fraction space and under the unity Lewis assumption (giving $D_k = D$), all the information about the flow features are contained within the scalar dissipation rate χ expressed as:

$$\chi = 2D\left(\frac{\partial Z}{\partial x_i}\frac{\partial Z}{\partial x_i}\right) \tag{2.5}$$

with an important quantity being the stoechiometric scalar dissipation rate χ_{st} evaluated on the stoechiometric line.

In complex flames, the distinction between a premixed flame or a diffusion flame and the tendency of a partially premixed flame toward one or the other can be characterised by the Takeno flame index TI [Yamashita et al., 1996] which writes:

$$TI = \frac{\nabla Y_{fuel}.\nabla Y_{oxidiser}}{|\nabla Y_{fuel}.\nabla Y_{oxidiser}|} \tag{2.6}$$

where ∇ is the gradient operator.

This index takes the value -1 when the fuel burns in diffusion flame regime (the fuel and the oxidiser gradients face each other) and 1 when a premixed flame regime is present (local fuel and oxidiser gradients are i the same direction). This index is often conditioned by the heat release rate so that its value is 0 where there is no combustion happening. Also as discussed in [Felden, 2017], the fuel species may

not always be the best candidate to represent the actual species reacting with the oxidiser especially in hot temperature conditions where the fuel undergo pyrolysis before actually burning. Because of that, the species specified as fuel in Eq. 2.6 must be carefully selected and might need to be a combination of several pyrolysis products.

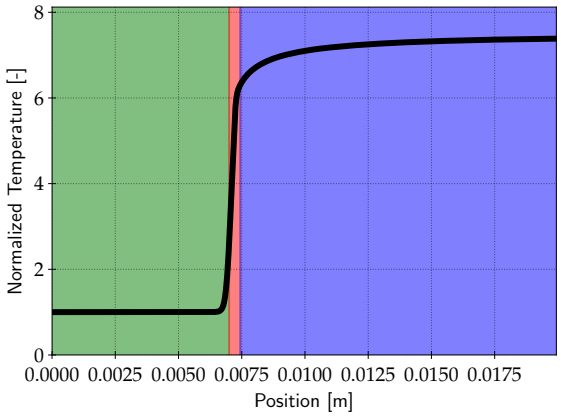

(a) Temperature profile normalised by the inlet value of $300K$

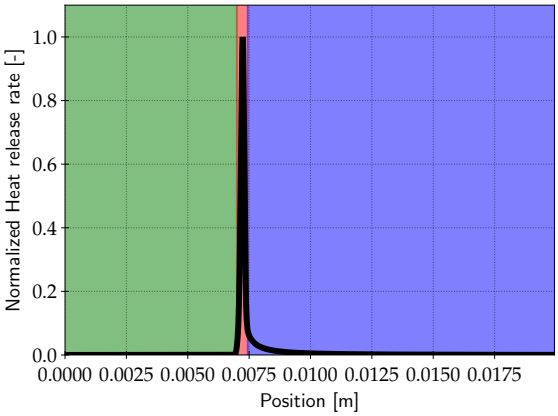

(b) Heat release rate normalised by its maximum value

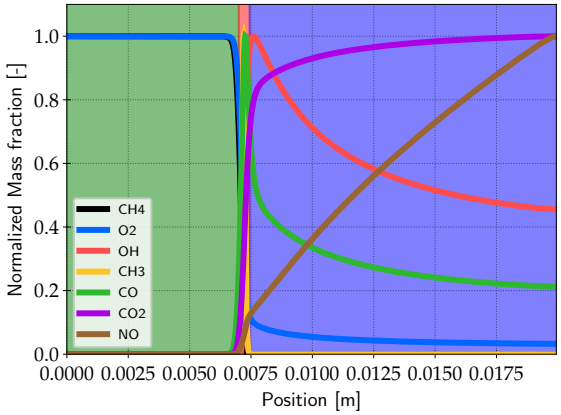

(c) Representative species mass fraction profiles normalised by their maximum values

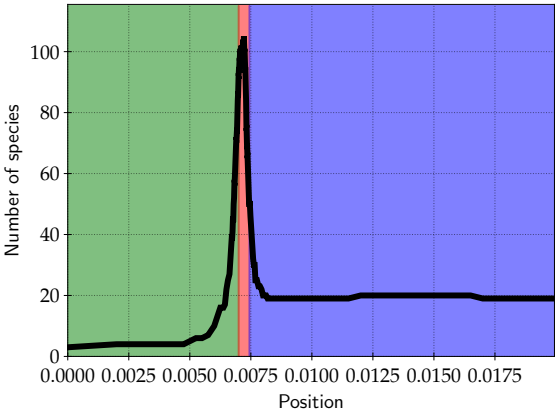

(d) Number of species with $Y_k \geq 1e-9$

(e) Timescales order of magnitude $o\tau_{chem}$

Figure 2.2.1: (a) Normalised temperature, (b) heat release rate and (c) representative mass fraction profiles with (d) number of species and (e) order of magnitude of the timescales involved in the combustion of a premixed stoechiometric methane/air flame at atmospheric conditions.

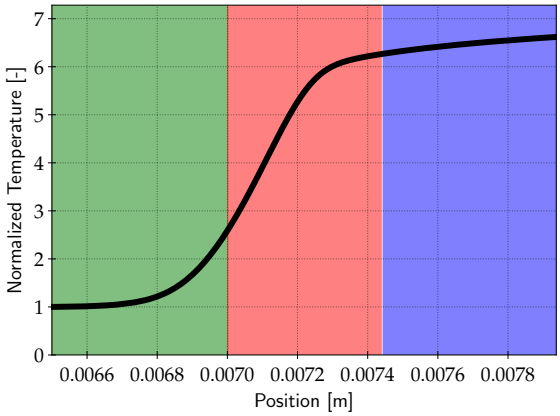

(a) Temperature profile normalised by the inlet value of $300K$

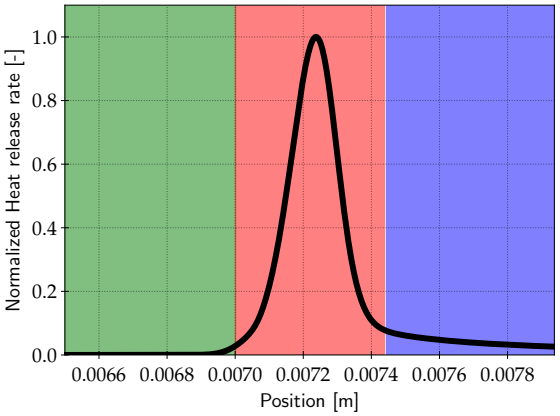

(b) Heat release rate normalised by its maximum value

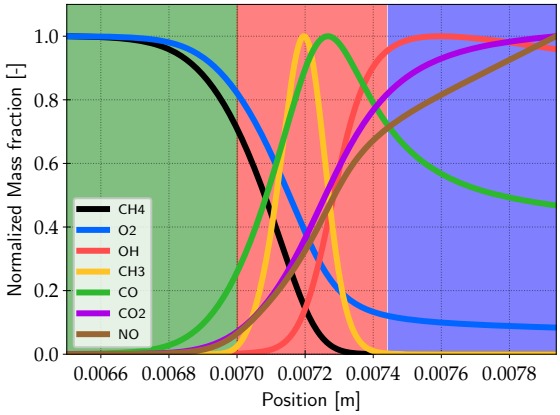

(c) Representative species mass fraction profiles normalised by their maximum values

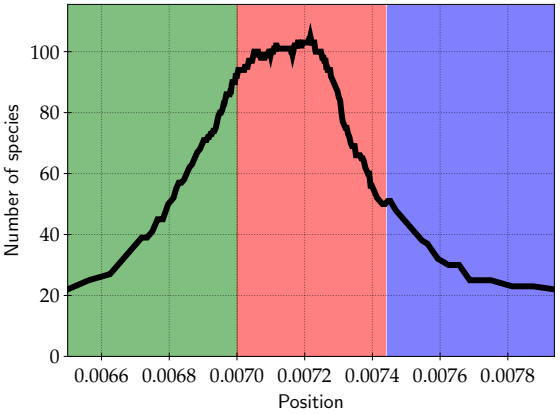

(d) Number of species with $Y_k \geq 1e-9$

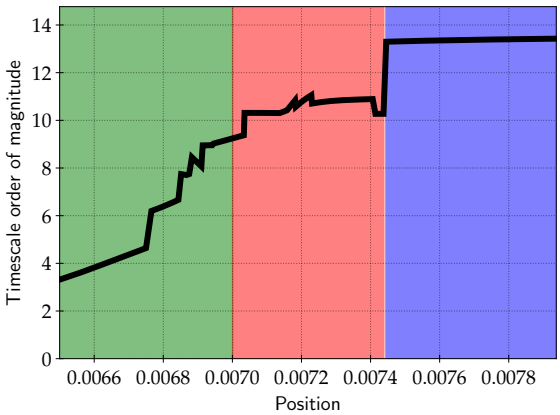

(e) Timescales order of magnitude $o\tau_{chem}$

Figure 2.2.2: (a) Normalised temperature, (b) heat release rate and (c) representative mass fraction profiles with (d) number of species and (e) order of magnitude of the timescales involved in the combustion of a premixed stoechiometric methane/air flame at atmospheric conditions zoomed around the *inner reaction zone*

Chapter 3

Chemistry modelling

Contents

For reactive flows, the description of the chemistry is pivotal as it should be able to capture all the complexity of the flow/flame interactions and all the reactions that can happen in the multitude of thermodynamic states that are living in a reactive case. This chapter will present the modelling approaches that can be found in the literature.

3.1 Detailed chemistry

The development of detailed chemistry derives from a whole different community and scientific field than the one this manuscript belongs to. They come from the association of laboratory experiments and very complex quantum mechanics computations. From a CFD point of view they yield as a reference and are considered as the most accurate we can ever be. In reality, those mechanisms (as every scientific productions) always have room for improvement and face discrepancies between the different research groups depending on which experimental database is used to calibrate the mechanism [Konnov et al., 2018].

Several research groups specialise in the generation of such mechanism, this is the case of the CRECK modelling group from Politecnico di Milano (POLIMI)[1] [Ranzi et al., 2012a][Ranzi et al., 2015][Ranzi et al., 2014][Frassoldati et al., 2010], the Laboratoire Réactions et Génie des Procédés (LRGP)[Battin-Leclerc et al., 2011] or the Lawrence Livermore National Laboratory (LLNL) [2][Mehl et al., 2011][Herbinet et al., 2010] to only cite a few. Mechanisms from POLIMI will be extensively used in this work because of their library structure where a core mechanism will be extended according to the needs of the targeted applications. This methodology is comforting in the philosophy that discarding a part of the mechanism will not affect the global coherence of the mechanism.

Because including detailed kinetic mechanisms directly into CFD solvers is often too expensive, several methods have been developed in order to model the chemical behaviour at a reduced cost.

3.2 Tabulated chemistry

The first method introduced by Peters [Peters, 1984] is based on the **flamelet hypothesis** stating that because the chemical timescales are shorter than the flow timescale, the reaction zone locally behaves as a laminar flame. Thus, an *a priori* correspondence with a canonical laminar flame (such as the ones presented in 2.2.1 and 2.2.2) can be made.

[1] http://creckmodeling.chem.polimi.it/
[2] https://combustion.llnl.gov/mechanisms

The mixture fraction Z introduced in 1.62 is used to describe the initial mixing state of the gas and the spatial evolution of the flame is described by a progress variable c. The progress variable c is a control variable quantifying the progress from fresh gases ($c = 0$) to burnt gases ($c = 1$), it can either be expressed in term of temperature

$$c = \frac{T - T_{fresh}}{T_{burnt} - T_{fresh}} \tag{3.1}$$

or it can be expressed using major products mass fraction

$$c = \frac{Y_c}{Y_c^{eq}} \tag{3.2}$$

where Y_c is a sum of major products mass fraction, typically $Y_c = Y_{CO} + Y_{CO_2} + Y_{H_2O}$ and Y_c^{eq} its equilibrium value as defined in 1.5.1.

This method is employed in the FPI (Flame Propagation of Intrinsic Low-Dimensional Manifold) model proposed by [Gicquel and Darabiha, 2000], the FGM (Flame Generated Manifold) model proposed by [van Oijen et al., 2001] and more recently the F-TACLES (Filtered Tabulated Chemistry for Large Eddy Simulation) model proposed by [Fiorina et al., 2010] which have been intensively used for the simulation of complex systems [Fiorina et al., 2015a][Fiorina et al., 2015b]. Despite their capability to reproduce detailed chemistry at a reasonable cost due to the small number of transport scalars, those methods suffer some limitations in practical combustion systems:

- Most combustion systems promote mixing with swirled highly turbulent flows resulting in strain and curvature effects as well as dilution by burnt gases. When building a lookup table those conditions are generally out of reach because it would require additional dimensions to the table.
- More generally, the multiplicity of combustion regimes such as partial-premixing, local in-homogeneity due to liquid fuel evaporation or multi-fuel configurations may be difficult, unpractical or simply impossible to represent with canonical cases.

- The tabulation methods are based on the assumption that a complex combustion regime will be a linear interpolation of simpler combustion regimes driven by highly non-linear systems which seems unrealistic.
- Furthermore, accounting for additional effects like heat losses, radiations or pollutant emissions [Proch and Kempf, 2015][Ihme and Pitsch, 0008] require more progress variables and more table data, increasing the cost and the complexity of the interpolation process along the number of scalars to transport.

3.3 Global chemistry

The most commonly used chemistry modelling and one of the cheapest method to use is the Globally Reduced Chemistry (GRC) introduced by [Westbrook and Dryer, 1981] which will only consist in a few species and reactions.

In the most common form, a global mechanism consists in two reactions:

$$Fuel + s_X O_2 \rightarrow aCO + bH_2O \tag{3.3}$$

$$CO + 0.5O_2 \leftrightarrow CO_2 \tag{3.4}$$

where a and b are respectively the number of CO and H_2O produced according to stoechiometry.

The first reaction driving the consumption rate of the fuel has its reaction rate built in order to fit an existing laminar flame speed curve as a function of the equivalence ratio. The first reactions rate writes

$$\dot{c}_1 = f_1(\phi) c_{Fuel}^n c_{O_2}^m A_1 T^{\beta_1} e^{\frac{E_{a,1}}{RT}} \tag{3.5}$$

where A_1, β_1 and $E_{a,1}$ are adjusted to match the laminar flame speed and n and m are adjusted to retrieve the correct pressure dependency of the laminar flame speed. In addition, a Pre-Exponential Adjustment (PEA) function $f_1(\phi)$ is added in order to correct the laminar flame speed in the rich mixtures part.

The second reaction aims at representing the CO/CO_2 equilibrium need to obtain a correct prediction of the flame temperature.

This strategy often referred as two-step chemistry has been widely used in industrial applications and is still a valuable method to perform costly computations where the details of the chemistry are not an critical matter []. [Franzelli et al., 2010b] demonstrated for a kerosene surrogate a systematic approach to develop such mechanisms that stay accurate from lean to rich conditions. The methodology was also applied on methane combustion [Franzelli et al., 2012b].

Because of their construction simplicity, the global mechanisms have very narrow ranges of validity and are to guaranteed to work outside of their derivation range because every parameter is optimised and does not yields any physical meaning.

They are also only valid for global quantities such as laminar flame speeds and flame temperature as they do not consider intermediate species. The CO species in this scheme for example does not represent correctly the real species behaviour and is just a buffer species to reach the correct overall behaviour.

3.4 Virtual chemistry

An in between methodology called Virtual Chemistry has been developed by [Cailler et al., 2017] and aims at incorporating the database that could be developed in a Tabulation method into a chemical scheme similar to a Globally Reduced Chemistry.

In that method, virtual species that are not representative of real species, except for the fuel and oxidiser, are created and their thermodynamic characteristics are optimised via genetic algorithm in order to better fit the targeted properties in the database (typically, heat release rate and temperature profiles). This methodology has been successfully used for both simple and complex hydrocarbons [Cailler, 2020] with good results and can be extended with sub-blocks to correctly predict CO, NO and PAH emissions.

This methodology also has limitations because despite its complexity and precise optimisation, it suffers from the intrinsic problem of optimisation methods being their non-generality when exiting the scope in which they have been derived. Also, similarly to the other methods discussed previously, the details about the kinetics

and the path the system is taking are completely lost in the derivation process and do not allow a fine chemical analysis of the processes involved.

This last argument is a good reason to go towards Analytically Reduced Chemistry because the over cost in term of computational resources is balanced by the possibility to understand more precisely the chemical processes involved in practical combustion systems.

3.5 Analytically Reduced Chemistry (ARC)

The detailed mechanisms described earlier are too exhaustive for numerical simulations in which the thermodynamic conditions are often bounded by the operating conditions of the studied system. In that sense, only a sub-part of a detailed mechanism is often needed in order to correctly reproduce a practical system and a lot of superfluous species and reactions can be simply discarded as they do not have a significant impact in the chosen operating conditions.

In that sense, the philosophy of ARC is not to reproduce the consequences of the chemical kinetic system but to identify what are their cause and discard everything that is irrelevant.

3.5.1 Skeletal mechanism

The concept of skeletal mechanism regroups the mechanisms that have been obtained via elimination and compacting of species and reactions without modelling assumption i.e. a skeletal mechanism is only a detailed mechanism trimmed to specialise in a smaller operating range.

Regardless of the methods employed to identify the species and/or reactions to discard from the detailed mechanism that will be discussed in the following, the reduction is only driven by the quantities that are chosen to constrain the reduction. For combustion cases, it is commonly the laminar flame speed and the adiabatic flame temperature as it is the minimal properties needed for a chemical modelling scheme. However, as discussed earlier, this type of modelling should focus on the kinetics elements that are producing those properties, thus one must be able to analyse the

kinetics scheme in depth in order to identify all the chemical paths resulting in the expected global behaviour.

3.5.2 Sensitivity based methods

Several methods exists in the literature aiming at identifying the effect of an entity [3] on a global quantity, the most direct being the sensitivity analysis [Turanyi, 1990]. Because a proper sensitivity analysis requiring an estimation of the sensitivity coefficients using a Taylor series expansion of the solution in the parameter space would require solving complex differential equations, a brute-force approach is often preferred where the chosen case is computed once with the reference detailed mechanism and once with modified parameters. For example, if one is interested in the sensitivity of the laminar flame speed to the reactions of a chemical mechanism, a reference case will be computed with the detailed mechanism as is and one flame will be computed for each reaction with a small modification of its pre-exponential factor. Extracting the targeted laminar flame speed for each case an comparing it to the reference value gives a ranking of the reactions relative importance to this parameter.

This base principle has been adapted into more accurate methods such as Principal Component Analysis (PCA) [Vajda et al., 1985][Turanyi, 1990], Species-Targeted Sensitivity Analysis (STSA) [Stagni et al., 2016] or incorporated into an error-controlled non-linear optimisation [Jaravel et al., 2019].

The main drawback of those methods are mainly their extremely high costs as they demand to perform a lot of slightly different simulations in order to extract the sensitivity coefficients of the entities. Also through a complete reduction process, this analysis must be performed several times because of the rearrangements of the non-linear interactions between the species inside the mechanism, making its application very costly for for big mechanisms.

[3] term that will be used in the following to signify indifferently a species or a reaction

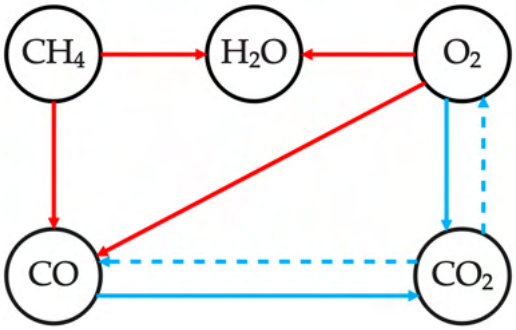

Figure 3.5.1: Kinetic graph for a methane/air global chemistry with red edges representing the oxidation reaction 3.3 and blue edges representing the CO/CO_2 equilibrium reaction 3.4. Full lines represent the forwards reactions while dashed lines represent the backward reactions.

3.5.3 Graph based methods

An other family of methods, called graph based methods looks more precisely at the graph that can be constructed with species as nodes and reactions as links (or edges) between them. The edges have a direction from the reactant to the product. For a global mechanism in the form described in 3.3 with methane (CH_4) as fuel, Figure 3.5.1 represents the associated kinetic graph.

From such representations that becomes more and more complex with the number of species and reactions increasing, a quantification of the edges between the species must be found in order to identify the less significant pathways that can be safely removed from the detailed mechanism.

Path flux analysis

A first method to quantify the importance of graph links is the Path Flux Analysis (PFA).

The basic principle of this method is to follow the atoms present in the reactants through the reactive graph in order to identify the contribution of each path to the

global atomic exchange.

The atomic flux of an element e going from a species k to a species i through reaction j is given by [Frouzakis and Boulouchos, 2000] as:

$$flux(k \rightarrow i)_{e,j} = \frac{\dot{c}_{net,j} n_{e,k} n_{e,i}}{N_{e,j}} \tag{3.6}$$

with $N_{e,j}$ the total number of element e in reaction j.

A $(N_s)^2$ matrix can be constructed at a given point in space and time in the chemical system to give a snapshot of the preferential pathways for the kinetics.

Through integration and normalization of the several path flux matrices that constitute the whole chemical system, a graph representing the whole system can be created. Specifying thresholds values for the total outgoing fluxes for each species, elimination of unimortant species can be performed.

This method has been successfully used for the reduction of methane [Frouzakis and Boulouchos, 2000], kerosene surrogates [Luche et al., 2004] and other liquid fuels [Sun et al., 2010].

One downside of this method is mainly the necessity to impose a threshold on analysed fluxes which can be an arbitrary process. Also, the correct normalization depending on the elements chosen is not trivial and leads again to a priori choices required from the user.

Direct Relation Graph

A more general way of quantifying the interaction between species is given by the Direct Relation Graph (DRG) method proposed by [Lu and Law, 2005]. Here the links between species (arrows in Fig. 3.5.1) represent the contribution of a species B to the production of species A. Similarly to the PFA method, a Direct Interaction Coefficient (DIC) matrix can be constructed to give a quantification of the relation between species A and B and a given point in space and time. Two DIC matrices can be constructed; a species DIC matrix giving the interaction between two species and a reaction DIC matrix giving the interaction between a reaction and a species.

The contribution of species B to the production of species A is given by

$$r_{AB} = \sum_{j=1,n_R} \nu_{j,A} \dot{c}_j \delta_B^j \tag{3.7}$$

where δ_B^j equals 1 if species B is in reaction j and 0 otherwise.

The contribution of reaction j to the production of species A is given by

$$r_{Aj} = \nu_{j,A} \dot{c}_j \tag{3.8}$$

Additionally to an entity impact on a species, their impact can also be quantified on the heat release rate with:

$$r_{HrB} = \sum_{j=1,n_R} \nu_{j,A} \dot{Q}_j \delta_B^j \tag{3.9}$$

as the contribution of species B to the heat release rate.

$$r_{Hrj} = \nu_{j,A} \dot{Q}_j \tag{3.10}$$

as the contribution of reaction j to the heat release rate.

In the following theory of DRG, the heat release rate can be considered as an additional species hence the indices related to species in the following can go up to $N_s + 1$.

An important concept of DRG is the concept of targets. A set of species that are considered important must be selected in order for paths to be drawn inside the kinetic graph. Target species are the end of this paths and are necessary to find entities at their beginning. Once all those paths are drawn the weakest links may be identified and lead to their elimination. Target species should be the species that are absolutely needed for the studied process; for combustion, species target should be at least the heat release rate plus specific species of interest such as CO and NO for exemple if pollutants are of importance.

An improvement of the DRG method has been proposed by [Pepiot-Desjardins and Pitsch, 2008b] that considers the contribution of indirectly linked species called Direct Relation Graph with Error Propagation (DGREP).

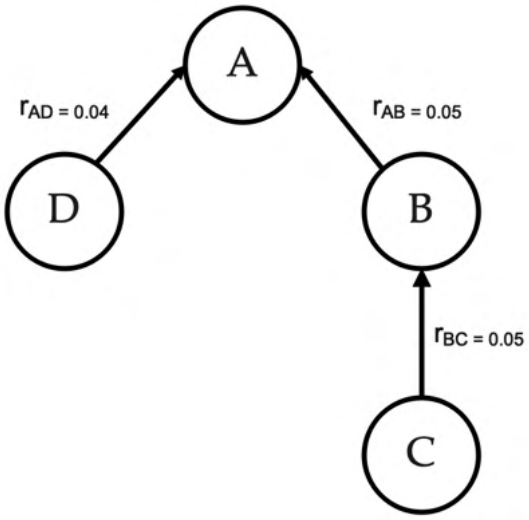

Figure 3.5.2: Part of a directed relation graph involving four species. Although the link between species B and C is not the weakest in the graph, removing C should introduce the smallest error in the prediction of the target A. Adapted from [Pepiot-Desjardins and Pitsch, 2008b]

In Fig. 3.5.2, species A is the target and considering Eq. 3.7, the weakest link is the path from species D to A, thus it should be discarded first. However, there is an indirect contribution of C to A through B, written as :

$$r_{AC} = r_{AB} * r_{BC} \tag{3.11}$$

The contribution of C is significantly lower even though it will influence species B having more significant impact on the target. Species C should be the first species discarded in that case.

The Error Propagation then writes for the general case as:

$$r_{AB,path} = \prod_{i=1,n-1} r_{S_i S_{i+1}} \tag{3.12}$$

where n is the distance between A and B in this specific path, S_1 being species A and S_n species B.

Between all the different possible paths between A and B, only the one with the greater coefficient is retained.

$$R_{AB,path} = \max_{all\ paths} r_{AB,path} \tag{3.13}$$

All the above explanations can be easily adapted to work with reactions and heat release rate as discussed earlier.

The DRGEP method was incorporated inside the the reduction tool YARC [Pepiot, 2008] leading to several publications with successfully reduced mechanisms This method has also been implemented in the automatic reduction code ARCANE that will be described in Chapter 4. Details about practical implementation will be given in the dedicated part 4.2.1.

3.5.4 Chemical lumping

The other component of the skeletal mechanism after elimination is concatenation which will reduce the number of species by assuming that a coherent group of species can be represented by a sole species.

Isomers lumping

The first groups of species that can be modelled as one are the isomer species i.e. a group of species sharing the same molecular formula. As the complexity of a detailed mechanisms increases it is more and more prone to have a large number of isomer species.

Several methods were developed in the literature categorised into two philosophies; the chemical-based approach that proposes to lump species based on their similarity in reactivity and chemical structure [Ranzi et al., 2001] and the mathematically-based approach aiming at finding lumpable species trough the system analysis[Stagni et al., 2014] [Fournet et al., 2000]. The last methodology has found a greater popularity has it does not require an expert knowledge on chemistry to develop systematic approaches to efficient lumping strategies.

According to [Huang et al., 2005], *the crucial issues in this approach are: (i) to determine which species are to be lumped; (ii) to classify how the selected species should contribute to the lumped species, i.e., define the lumping transformation; and (iii) to estimate kinetic parameters for the lumped species.*

The strategy employed in this work is an adaptation of the on from [Pepiot-Desjardins and Pitsch, 2008a], that was previously implemented in the code YARC and implemented in this work into the code ARCANE. The determination of the species to lump *(i)* follows 3 different steps: first, the species with the exact same thermodynamic and transport data are selected and lumped together, then the whole group of isomer species is tested as a lump and finally if that last step fails, the species are selected as couples of thermodynamically similar species. The classification *(ii)* is made by analysing the species contribution inside canonical cases run with the detailed mechanism. Finally, the estimation of the kinetic parameters *(iii)* is done by applying the previously calculated contributions of each species of the lump to the associated Arrhenius-law parameters. Further details will be given in Section 4.2.2.

Hybrid chemistry

Recently, a novel methodology of representing combustion systems has emerged in the context of combustion. In most kinetic mechanism, a core oxidation mechanism can be identified, it contains all the carbonated species and radicals with a number of carbon atoms lesser than 4. The hydrocarbons in this core mechanism (namely butane, ethylene, methane for example) are considered light fuels as opposed to heavy fuels that contain more than 4 carbon atoms in their composition and are generally liquid at room temperature. Those species need the entirety of the core mechanism to be correctly described during their combustion as during oxidation, carbonated radicals can combine and lead to molecules with up to 4 carbons in their structure. Thus the detailed mechanism for butane and methane is the same one. That is not the case for heavy fuel species. Because of their longer carbonated chains, heavier hydrocarbons will undergo a high temperature decomposition step, called pyrolysis. The pyrolysis will result in a decomposition into smaller species, called pyrolysis products, that are contained in the core mechanism.

Based on this observation, [Wang et al., 2018][Xu et al., 2018] proposed to decouple the pyrolysis and oxidation mechanisms of heavy hydrocarbons. This method

called HyChem (for Hybrid Chemistry) is not a proper lumping as the simplified pyrolysis mechanism originates from experimental data. However, because of its idea and structure it will be treated as such. The whole pyrolysis process will be described by the following 7 irreversible reactions:

$$C_mH_n \rightarrow x_1C_2H_4 + x_2C_3H_6 + x_3C_4H_8 + x_4C_6H_6 + x_5C_7H_8 + x_6H + x_7CH_3$$

$$C_mH_n + H \rightarrow H_2 + \Sigma_p$$

$$C_mH_n + CH_3 \rightarrow CH_4 + \Sigma_p$$

$$C_mH_n + OH \rightarrow H_2O + \Sigma_p$$

$$C_mH_n + O_2 \rightarrow HO_2 + \Sigma_p$$

$$C_mH_n + HO_2 \rightarrow H_2O_2 + \Sigma_p$$

$$C_mH_n + O \rightarrow OH + \Sigma_p$$

where

$$\sum_p = y_1C_2H_4 + y_2C_3H_6 + y_3C_4H_8 + y_4C_6H_6 + y_5C_7H_8 + y_6H + y_7CH_3 + y_8CH_4$$

The determination of the x and y coefficients depend on the fuel and their determination method is explained by the authors in [Xu et al., 2018].

The pyrolysis mechanism constructed can then be added to a core mechanism to describe the oxidation of the pyrolysis products in order to describe the combustion of the selected fuel. One advantage of this technique on top of drastically reducing the number of species needed to describe the combustion of heavy fuels is that no surrogate is needed for complex fuel composition such has kerosene as illustrated by Fig 3.5.3. Several mechanisms for different fuels are available on Hai Wang's group website [4]. This methodology and its advantages have been described in the thesis of [Felden, 2017] and will be further discussed in Chapter 11.

[4] https://web.stanford.edu/group/haiwanglab/HyChem/pages/Home.html

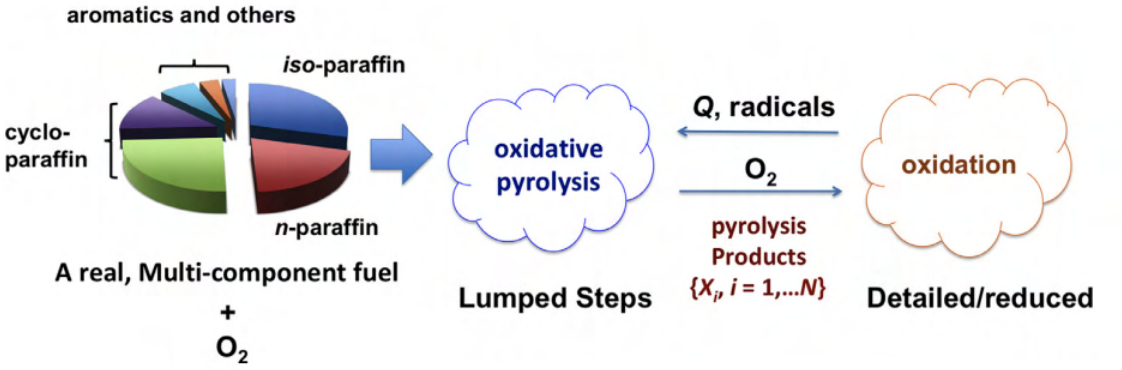

Figure 3.5.3: Schematic of the HyChem approach. Extracted from [Wang et al., 2018]

Pyrolysis lumping

Following the principle of HyChem, [Heberle and Pepiot, 2020a] has developed an automatic methodology to create a pyrolysis mechanism based on the detailed mechanism. Instead of taking experimental data in order to reproduce the chemical behaviour of the pyrolysis step, data extracted from canonical auto-ignition cases are used to find the x and y coefficients previously introduced. A constrained optimization round is also performed to complete the kinetic parameters determination. This methodology has been assessed on both a single component n-dodecane and a mixture of 50% n-dodecane 50% iso-octane and shows a good agreement between the lumped mechanism and the detailed mechanism on auto-ignition and laminar flame speeds predictions.

The implementation of this methodology into ARCANE is an on-going work to extend the code capabilities.

3.5.5 Quasi-Steady State Assumption (QSSA)

The major problem with detailed chemistry, after the number of species to transport, is the numerical stiffness of the chemical system. As already shown in Fig. 2.2.1e and 2.2.2e, the timescales involved in the resolution of the chemical kinetics system are really small compared to the flow convective timescale dictated by the

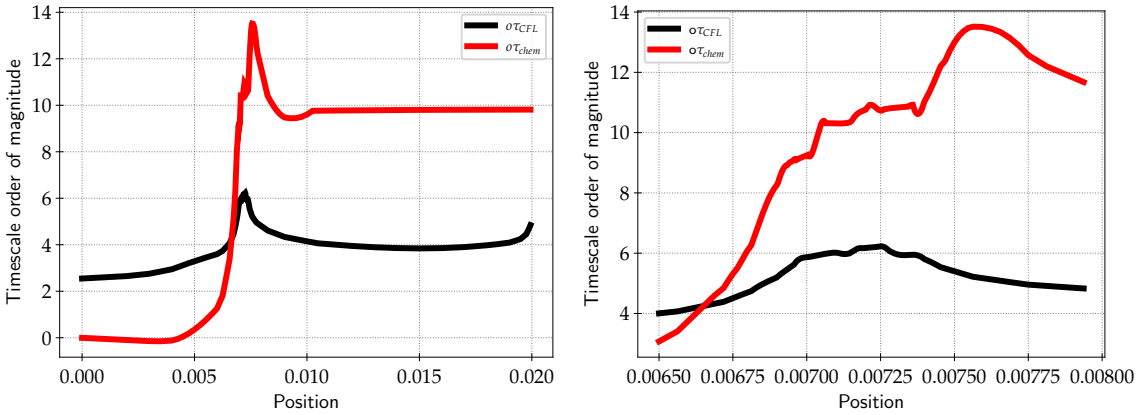

(a) Whole flame (b) Zoom around the *inner reaction zone*

Figure 3.5.4: Order of magnitude of the flow timescale (black) and the chemical timescale (red) along (a) a full premixed stoechiometric methane/air flame at atmospheric conditions and (b) zoomed around the *inner reaction zone*.

Courant–Friedrichs–Lewy (CFL) number written:

$$CFL = \frac{u\Delta t}{\Delta x} \tag{3.14}$$

where u is the flow velocity.

If we take a CFL number of 0.7 which is a classical value for the stability of explicit LES computations, we can determine the flow timescale τ_{CFL} of the premixed flame portrayed in 2.2.1 as:

$$\tau_{CFL} = \frac{0.7\Delta x}{u} \tag{3.15}$$

Similarly to Eq. 2.4 we can determine the timescale order of magnitude $o\tau_{CFL}$.

From Fig. 3.5.4, it is clear that the timestep of an explicit CFD computation will be driven by the chemistry as it is evolving in a whole different range of timescales.

For that reason, stiffness removal techniques have been developed, the more popular being the Quasi-Steady State Assumption (QSSA). Dating back to 1913 and

introduced by one of the founding fathers of the chemical kinetics [Bodenstein, 1913], the Quasi-Steady State Assumption, sometimes called the Bodenstein assumption, states as reformulated by [Lu and Law, 2006] that *A QSS species typically features a fast destruction time scale such that its small or moderate creation rate is quickly balanced by the self-depleting destruction rate, causing it to remain in low concentration after a transient period. The net production rate of the QSS species is therefore negligible compared with both the creation and the destruction rates, resulting in an algebraic equation for its concentration.* Thus the net production rate of a QSS species is written:

$$\dot{c_k} \approx 0 \tag{3.16}$$

For a given system and a given set of QSS species, algebraic equations allowing to directly compute the concentration of those species can be expressed, an example will be given here.

The transported species of the system will be symbolized by $*$ which can be indistinguishably any given species. Considering the following kinetic system comprised of 3 QSS species (QSS_1, QSS_2 and QSS_3):

$$* + QSS_3 \leftrightarrow * + QSS_1$$

$$* + QSS_2 \rightarrow * + QSS_1$$

$$* + QSS_3 \rightarrow * + QSS_2$$

$$* \leftrightarrow * + QSS_1$$

$$* \leftrightarrow * + QSS_3$$

The net production rate of the QSS species is written:

$$\frac{d[QSS_1]}{dt} = k_{1,f}[QSS_3][*] - k_{1,b}[QSS_3][*] + k_2[QSS_2][*] + k_4[*] = 0$$

$$\frac{d[QSS_2]}{dt} = -k_2[QSS_2][*] + k_3[QSS_3][*] = 0$$

$$\frac{d[QSS_3]}{dt} = -k_{1,f}[QSS_3][*] + k_{1,b}[QSS_3][*] - k_3[QSS_3][*] + k_5[*] = 0$$

Factorizing those expressions by the QSS concentrations, one obtain the following system:

$$[QSS_1] - [QSS_2]\frac{k_2[*]}{k_{1,b}[*]} - [QSS_3]\frac{k_{1,f}[*]}{k_{1,b}[*]} = \frac{k_4[*]}{k_{1,b}[*]}$$

$$[QSS_2] - [QSS_3]\frac{k_3[*]}{k_2[*]} = 0$$

$$-[QSS_1]\frac{k_{1,b}[*]}{k_{1,f}[*] + k_3[*]} + [QSS_3] = \frac{k_5[*]}{k_{1,f}[*] + k_3[*]}$$

This factorisation is of course not possible if 2 QSS species or more are present in the reactant side of the reaction equations, it is also the case if on of the species has an exponent different of 1 in the reaction rate expression. Solving those potential quadratic expressions of the QSS species concentrations is doable but is much more computationally consuming than solving a linear system [Lu and Law, 2006][Pantea et al., 2014]. For that reason, quadratic coupling of QSS species is not allowed in this work.

The linear system is better represented in a matricial form written:

$$\begin{pmatrix} 1 & \alpha_{12} & \alpha_{13} \\ 0 & 1 & \alpha_{23} \\ \alpha_{31} & 0 & 1 \end{pmatrix} \begin{pmatrix} [QSS_1] \\ [QSS_2] \\ [QSS_3] \end{pmatrix} = \begin{pmatrix} \beta_1 \\ \beta_2 \\ \beta_3 \end{pmatrix} \tag{3.17}$$

where α_{ij} is called the coupling coefficient between QSS species i and QSS species j and β_i are the uncoupled coefficients.

This system is finally solved with Gauss elimination to retrieve the algebraic expression of the QSS species concentration.

In the previous system, all three species are coupled together as the concentration of one is not independent from the others. For large skeletal mechanism with tenths of QSS species, the resolution of the system can prove to be computationally expensive thus, sub-groups of coupled species are identified and the linear system is reordered to only solve smaller linear systems. This strategy is detailed in [Pepiot, 2008].

Of course, before solving the QSS concentrations, those species need to be identified within the skeletal mechanism. The definition of a QSS species given previously is very generic and more precise identification methods are needed.

Computational Singular Perturbation (CSP)

This technique proposed by [Lam and Goussis, 1994] aims at identifying the different evolution modes of species within the system, through an eigenvalue-eigenvector decomposition of a modified Jacobian matrix. The timescales then computed are ranked from smallest to largest and the species yielding a value smaller than a predefined criterion are considered to have a fast evolution and can thus be chosen as QSS candidates.

This method as been used to investigate detailed mechanisms of methanol oxidation in [Goussis and Lam, 1992]. Systematic identification was also implemented in CSP based algorithm such as S-STEP [Massias et al., 1999] for methane oxidation or ARC-CSP [Lu et al., 2001] for hydrogen and methane oxidation.

However the implementation of such a thorough method requires considerable CPU time and increases in complexity when going to larger detailed mechanisms. Fortunately, other methods based on the species lifetime have been developed which are less demanding in term of computational power.

Level Of Importance (LOI)

[Løvs et al., 2000] proposed a criterion based on a combination of several aspects that might make a species suitable for being put in Quasi-Steady State. The first aspect is the one described earlier, which is a fast timescale quantified by the chemical timescale of each species $\tau_{chem,k}$ (written τ_k for simplicity from now on), introduced in 2.3, at each point of the reference database. From the earlier definition, the species concentration must stay relatively low during the combustion process, the concentration C_k must also be taken into account. The QSSA being an approximation, it induces an error and the quantification of this error is taken into account with the sensitivity $S_{P,k}$ of the parameter P to the species k. Simply combining those quantifying parameters as the single one, the Level Of Importance (LOI) is obtained for each species k:

$$LOI_k = S_{P,k} c_k \tau_k \tag{3.18}$$

The implementation of this criterion is quite easy and it was shown to give similar results compared to CSP [Løvås et al., 2002]. A variation of this formula using the DRGEP coefficients will be presented in 4.2.3 as it was integrated into the ARCANE code.

In the context of saving CPU time, the product of the concentration c_k and the timescale τ_k can also be replaced by the integral of the concentration which is very easy to extract from computations.

None of the previous methods, despite their intensive mathematical and physical backgrounds, is perfect because of an immense complexity emanating from the detailed mechanisms. Because of that, those methods must be integrated into multi-stages reduction codes that will deal with the methods imperfections in order to reduce the mechanisms as much as possible. This last objective is the focal point of the next chapter introducing the development of the automatic multi-stage reduction code ARCANE.

Chapter 4

ARCANE

Contents

This chapter is a transcription of the journal article published in Fuel entitled *A fully automatic procedure for the analytical reduction of chemical kinetics mechanisms*

for Computational Fluid Dynamics applications [Cazères et al., 2021]. Complementary information will be given in Chapter 5.

4.1 Introduction

Prediction and control of combustion processes, be it their efficiency or resulting pollutant emissions, have never been as critical as they are now. Reactive Computational Fluid Dynamics (CFD) has become an essential tool to advance combustion technologies, as numerical approaches allow to investigate broadly customizable configurations unburdened from practical considerations, and may provide better and deeper insight into phenomena that can be difficult to measure and quantify on a test rig. In order to obtain realistic results for complex problems of interest, for example, kerosene spray flames, numerical simulations typically need to combine several physical fields. In the case of turbulent combustion, the two major fields that need to be brought together are fluid dynamics and chemical kinetics of non-homogeneous mixtures. The increasing number of fuels that are considered to either replace fossil fuels (bio-derived fuels) or enhance their performances (hydrogen addition) makes it critical to include accurate chemical kinetics in CFD in order to properly capture fuel effects. The complete description of chemical kinetics for combustion involves a number of molecular species ranging from a few tens (hydrogen combustion) to several thousands (bio-fuels combustion). Three-dimensional simulations with accurate turbulence description and moderately detailed chemical kinetics would require more computing power than is typically available and accessible today. Fortunately, most flames features and characteristics of interest can be accurately captured with a relatively small number of species and reactions. By carefully selecting the relevant pathways within the detailed kinetics model, a smaller mechanism can be extracted, rendering the CFD simulations feasible both in term of time and computational resources. In order to make reduced chemistry accessible to the broader CFD community, who may lack expertise in chemical kinetic modelling, the reduction methodology must be formulated in a fully automatic fashion, the sole required input being the user's specific needs for their CFD simulations. As this holds true not only for combustion but also for all fields using chemical kinetics in CFD solvers, the automatic procedure should be made as versatile and generic as possible.

In this work, the new numerical tool ARCANE for the automatic, robust, and user-friendly reduction of chemical kinetic schemes is presented, and its performance

is assessed. The individual reduction methods used in ARCANE are first briefly summarised, and their efficient implementation and automation described. The code capabilities are then demonstrated through three different applications of increasing complexity. All computations of chemical properties and canonical cases are performed with the chemistry solver Cantera [Goodwin et al., 2017].

4.2 Reduction methods

The reduction strategy used in this work follows the approach described in Lu et al. [Lu and Law, 2009], and is referred here as the Analytically Reduced Chemistry methodology (ARC). In contrast to other, more intrusive methodologies (e.g. [Abou-Taouk et al., 2016, Fiorina et al., 2010, Cailler et al., 2017]), ARC's main advantage is to preserve as much as possible the integrity of the detailed chemical kinetic model: all relevant chemical pathways are included, and there is no kinetic parameter optimisation. Those guiding principles allow for potentially greater robustness in complex simulations and facilitate the chemical interpretation of CFD results.

Reference canonical cases are needed and drive the accuracy of the reduced mechanism with error thresholds applied on specific quantities extracted from those cases. The aforementioned preserved chemical pathways allow for the canonical cases matrix to be quite sparse. Typically, when targeting the evolution of a specific quantity, only a few characteristic points can be selected and not necessarily the whole range. For example, if laminar flame speeds are of interest, only 3 laminar premixed unstrained flames are typically needed (for a given initial temperature and initial pressure): the stoichiometric case and the lean and rich flammability limits, as those 3 cases together will capture all relevant chemical pathways activated at intermediate equivalence ratios.

The three methods combined into ARCANE's multi-step strategy are the Direct Relation Graph with Error Propagation [Pepiot-Desjardins and Pitsch, 2008b] (for both species and reaction reduction), chemical lumping [Pepiot-Desjardins and Pitsch, 2008a], and the Quasi Steady State Approximation [Lu and Law, 2006]. The following sub-sections explain the implementation of the aforementioned methods in ARCANE. The underlying theory is detailed only when the original methods are adjusted for efficiency purposes.

4.2.1 DRGEP

The goal of the first step is to identify the species and the reactions that are not relevant for the set of canonical cases chosen as representative of the target configuration, and can therefore be eliminated from the chemical model with limited loss of accuracy. In this work, DRGEP has been chosen for its generic formulation, which can be applied to a wide range of chemical processes, and for its execution speed compared to other methods (Sensitivity Analysis, or SA, for example [Stagni et al., 2016]).

According to the type of DRGEP reduction, each species or reaction is attributed a coefficient quantifying how strongly it is linked to the targeted quantity of interest. For species, the Direct Interaction Coefficient between a species B and a target A is computed for every composition encountered in the canonical simulation:

$$r_{AB} \equiv \frac{\left|\sum_{j=1,n_\mathrm{R}} \nu_{j,A}\dot{\omega}_j\delta_B^j\right|}{\max\left(P_A, C_A\right)} \tag{4.1}$$

For reactions, the Direct Interaction Coefficient between reaction j and target A is expressed as:

$$r_{Aj} \equiv \frac{|\nu_{j,A}\dot{\omega}_j|}{\max\left(P_A, C_A\right)}\,, \tag{4.2}$$

where n_R is the number of reactions in the mechanism, $\nu_{i,A}$ the stoichiometric coefficient of species A in the reaction j, $\dot{\omega}_j$ the net rate of progress of reaction j, C_A and P_A the consumption and production rates of species A, and δ_B^i equals 1 if B is involved in reaction j, 0 otherwise. This analysis is performed on all canonical cases computed with the detailed kinetic mechanism under consideration. The temporal and spatial grids used for the computations of the canonical cases are constructed by the Cantera solver in order to sufficiently resolve the species gradients and result in non-uniform grid refined around the high gradients zones.

To accelerate the algorithm, it is applied to a user-defined subset of compositions, obtained using box-filtered values of the test case solutions [Pepiot-Desjardins and Pitsch, 2008b]. The final DRGEP coefficient for each species or reaction is the maximum value over all sample points of all test cases and all target quantities:

$$r_i = \max_{\text{samples, cases, targets j}} r_{ij} \tag{4.3}$$

The species/reactions are sorted by their DRGEP coefficients in ascending order and progressively removed from the kinetic mechanism, until the error on the target quantities of the canonical cases, recomputed each time, reaches a predefined tolerance.

4.2.2 Chemical lumping

In many detailed mechanisms, especially when dealing with chemical kinetics for heavy hydrocarbons, isomers species can coexist, that is, species with the same molecular composition but different structure and thus thermodynamic properties. Chemical lumping aims at representing a group of isomers using a single representative species, thereby decreasing the number of species and reactions without significantly changing the reactions dynamics.

Candidate species for lumping are automatically identified based on their molecular composition, and the thermodynamic data and kinetic parameters of the reactions involving lumped species are adjusted to account for the larger concentration of the lumped representative. To do so, the relative contribution (in moles) of each isomer species i to the group of isomers I is first recorded as a function of the temperature, and the resulting dataset is fitted with an Arrhenius law:

$$X_{I,i}(T) = \frac{X_i}{\sum_{i \in I} X_i} = A_i T^{b_i} exp^{\frac{-Ea_i}{RT}}, i = 1, n_I \tag{4.4}$$

where $X_{I,i}(T)$ is the relative mole contribution of isomer i in its isomer group I, and n_I is the number of isomers in the group.

Thermodynamic properties of the lumped isomer, including heat capacity, enthalpy and entropy, are obtained as temperature-dependent, isomer weighted average of the NASA polynomials of each individual isomer. Reaction rates of each reaction involving the lumped representative isomer are also modified to account for the larger concentration of the lumped species, by incorporating the relevant relative mole contributions from Eq. 4.4 directly into the Arrhenius parameters for that reaction. As an example, consider the case of an isomer i being lumped into a group of isomers I. The Arrhenius parameters for a reaction j involving isomer i as the only reactant will be modified as follows:

$$\dot{\omega}_j = A_j T^{b_j} exp^{\frac{-Ea_j}{RT}} (X_i) = A_j T^{b_j} exp^{\frac{-Ea_j}{RT}} (X_{I,i})\, X_I \tag{4.5}$$

where X_I is the mole fraction of the group of isomers I. Using Eq. 4.4, one gets:

$$\dot{\omega}_j = (A_j A_i) T^{b_j+b_i} e^{-\frac{Ea_j+Ea_i}{RT}} X_I \,, \tag{4.6}$$

yielding the following modified reaction coefficient $\tilde{k_j}$:

$$\tilde{k_j} = (A_j A_i) T^{b_j+b_i} e^{-\frac{Ea_j+Ea_i}{RT}} \tag{4.7}$$

with $\tilde{k_j}$ the modified reaction constant of reaction j.

4.2.3 Quasi-Steady State assumptions

From a CFD perspective, the Quasi-Steady State Assumption (QSSA) has two major benefits: it removes species and thus leads to fewer transport equations, and it removes numerical stiffness as Quasi-Steady State species are, by definition, species with short characteristic timescales. To identify QSS candidates among species, a modified Level Of Importance criterion from Løvås et al. [Løvås et al., 2002] is used:

$$LOI_i = S^S_{T_i} c_i \tau_i \,, \tag{4.8}$$

with LOI_i the Level Of Importance of species i, $S^S_{T_i}$ the sensitivity of species i to the temperature T, c_i its concentration and τ_i the timescale of species i. As mentioned in 4.2.1, the sensitivity analysis has not been found to be computer effective and thus an alternative formulation is proposed:

$$LOI_i = r_i c_i \tau_i \tag{4.9}$$

with r_i the DRGEP coefficient computed with Eq. 4.3 and $c_i\tau_i$ computed as follow:

$$c_i \tau_i = \min_{\text{all samples s}} c_{s,i} \frac{\partial c_{s,i}}{\partial \dot{c}_{s,i}} \tag{4.10}$$

which introduces the inverse of the ii component of the Jacobian matrix of the chemical scheme.

4.3 Automatic procedure

The above algorithm can be fully automated to efficiently reduce any detailed chemical mechanism (in standard Arrhenius format) without the need for expert decisions.

The procedure is decomposed into four stages: the number of species is reduced first, followed by a reduction of the number of reactions. Isomer species are then lumped, and Quasi-Steady State assumptions are applied. While each step can be performed independently, the novelty of the ARCANE approach resides in its ability to decide automatically which reduction stage to apply and in which order, thereby delivering *a fully reduced mechanism without requiring any intermediate user input.*

4.3.1 Automation of each step

Species and reactions reduction

The species and reaction reduction steps are quite simple and similar as they both use DRGEP. At each iteration, one species (or reaction) is discarded from the original, or root, mechanism according to the sorting given by Eq. 4.3, and the target cases are computed with the resulting reduced mechanism. Iterations are repeated as long as the error on all target quantities stays below the specified tolerance. It may happen that the error goes above the tolerance and then goes back below it at the next iteration. In that case, the smallest mechanism with all errors below the tolerance is taken as the valid reduced mechanism, but the algorithm continues until it reaches a user-specified threshold (2 times the error tolerance for example). This allows to go slightly further in the reduction. To go even further, and considering that the DRGEP algorithm may misplace some species or reactions in the sorted list, those inducing errors that are too high are kept and the reduction continues until reaching species or reactions that cannot be removed, for example major combustion products.

Lumping species

The lumping of chemically similar species is a more complex step as a group of isomers may not always be replaced by a single representative species. Thus, this step is split into 3 sub-steps. First, a check is performed to identify potential species that are strictly identical in both composition and thermodynamic properties, but appearing under different names. Those species are lumped first, as they typically lead to smaller errors. Then, an attempt to lump the whole isomer group is done, now accounting for potential differences in thermodynamic properties. If this leads to errors above the tolerance, lumping the isomers in pairs is finally attempted.

The pairs are identified by determining thermodynamic properties (heat capacity, enthalpy, and entropy) similarities between isomers. Two species are deemed similar if the relative difference between each of their properties remains below 50% for all temperatures between 300K and 5000K. Note that fuel species are never considered suitable candidates for lumping.

Quasi Steady State assumptions

The final step of the reduction consists in identifying species that can be considered in quasi-steady state (referred as QSS species in the following). This step is similar to the DRGEP species reduction step. According to the modified LOI criterion of Eq. 4.9, species are sorted in a list of QSS species. As explained in [Pepiot, 2008], this step requires to analytically solve a $Ac = b$ linear system with A being the n_{QSS}^2 matrix of coupling coefficients between the QSS species, c the vector of concentrations of the QSS species and b a vector depending only on the transported, non-QSS species concentrations. The matrix A is defined as:

$$A_{ik} = -\left(\frac{\sum_{j=1,n_\mathrm{R}} \nu_{ij}^{'} k_j}{\sum_{j=1,n_\mathrm{R}} \nu_{ij}^{''} k_j}\right)\delta_{ik} \quad i,k = 1, n_{QSS} \tag{4.11}$$

where $\nu_{ij}^{'}$ and $\nu_{ij}^{''}$ are respectively the reactants and products stoichiometric coefficients of species i in reaction j, k_j the rate constant of reaction j and δ_{ik} equals 1 if $\nu_{kj}^{'}$ and $\nu_{ij}^{''}$ are non-zero, i.e., if species k is consumed in reaction j to produce i, else 0.

This set of analytical relations allows to evaluate QSS species concentrations from the non-QSS species concentrations only. The current implementation of the QSS assumption in this work is an extension of the original assumption with an a-posteriori validation. Here, species that do not fit strictly the theoretical concept may be put in quasi-steady state provided that the targeted characteristics are properly predicted. ARCANE generates and compiles the corresponding equations as a dynamic library file, which can be linked to the reactor or flow solver used to integrate the chemistry.

4.3.2 Overall automation

Experience shows that the level of reduction that can be achieved for a given error threshold can be much improved by optimising the sequence of the reduction steps,

including potential repetitions of individual steps. To the knowledge of the authors, the systematic and automatic reduction sequence optimisation has not been proposed or investigated in the literature.

The first sequence in the optimisation procedure concerns the species and reactions DRGEP steps. Indeed, after each iteration removing a species or a reaction, the graph corresponding to the remaining kinetic network is greatly changed, meaning that the DRGEP coefficients become less and less valid. Performing the DRGEP steps several times may become useful, in order to make sure that the final result is based on correct DRGEP coefficients which are re-computed at each step. In ARCANE, species and reaction reduction is done as part of an iterative loop, and repeated alternatively until no further change is observed. The DRGEP loop is illustrated in Fig. 4.3.1.

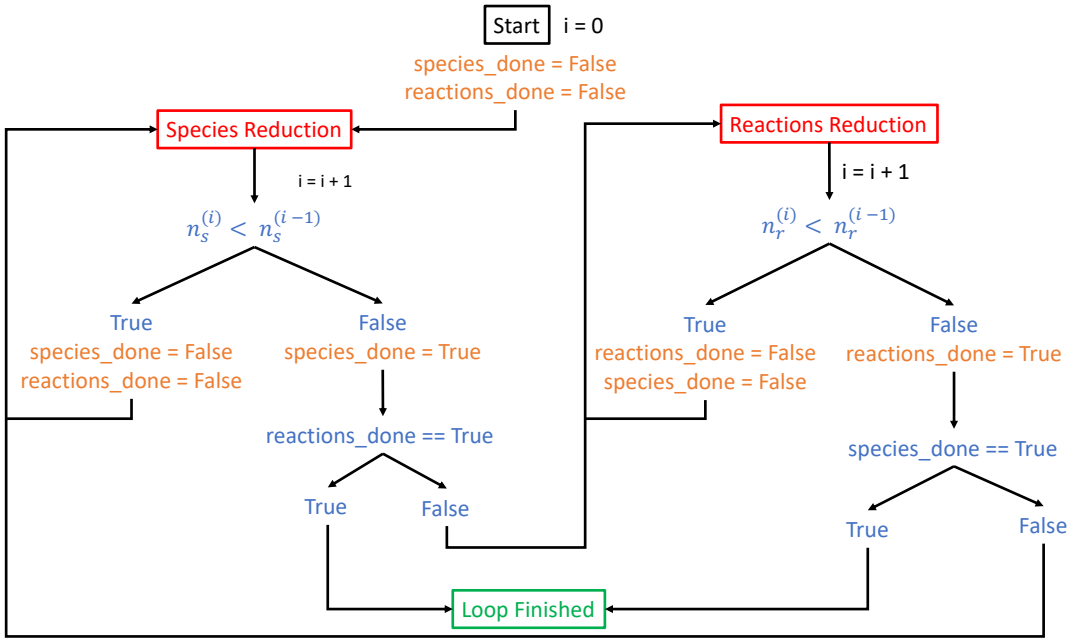

Figure 4.3.1: Schematic of the loop between species reduction and reactions reduction steps with $n_{\mathrm{S}}^{(i)}$ and $n_{\mathrm{R}}^{(i)}$ respectively, the number of species and the number of reactions in the mechanism generated at the i-th reduction iteration

The initial DRGEP loop is followed by a lumping step. Since the lumping does reorganise the kinetic network significantly, the DRGEP loop of Fig. 4.3.1 is repeated

a second time. Once this second loop is done, the QSSA reduction step is finally performed. The reduced mechanism returned by this last step is the final result of the whole reduction process.

4.4 Encapsulating code structure

The automatic reduction algorithm has been implemented in ARCANE (for Analytically Reduced Chemistry: Automatic, Nice and Efficient) which fully exploits the object-oriented nature of Python by revolving around two major objects that contain all the necessary information. The first object, referred as the Case object, is carrying all the operating conditions such as the type of canonical reactor to simulate, the composition of the mixture, and all other parameters necessary for the computation, independently of the mechanism to use. The second object, referred as the Mechanism object, is carrying the information about the mechanism. For each step of the reduction, the reduced Mechanism object is passed to the Case objects to be recomputed and compared to the results with the detailed mechanism. This structure with uncoupled objects allows a great flexibility in the cases that can be computed and the number of mechanisms that can be used. The data resulting from the computation of a case with a given mechanism is stored in a database structured as shown in Figure 4.4.1. The systematic storage of the generated data in a formatted shape allows to re-use already existing data, thereby saving time if restarting a reduction or analysing results. The compositions sampled from the canonical simulation, mentioned in Section 4.2.1, are then used in the reduction steps with each case treated independently with its specific targets, before concatenating the results to obtain the final reduction result.

In principle, ARCANE may use any 0D/1D combustion solver. In its current version, ARCANE is coupled with the open-source software Cantera [Goodwin et al., 2017]. Cantera offers a wide range of options when dealing with chemical kinetics computations, from reactor networks to various one-dimensional flames going from the simplest configurations (freely propagating premixed flames, counter-flow diffusion flames) to more complex ones (ionic premixed burners, or impinging jets).

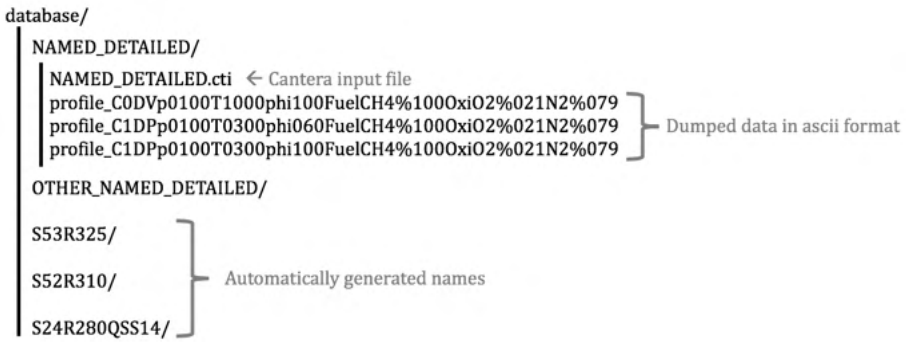

Figure 4.4.1: Structure of the database directory

4.5 Capabilities

Besides complete automation, the other innovation of the method is its versatility resulting from the large variety of canonical computations that may be used to represent real-life processes. The present method has been designed to be able to work with any kind of dataset provided that temperature, pressure, and species concentrations are available. Another flexibility that proved to be useful is the possibility to assign different tolerances for the various quantities targeted in a single case (for example, a 5% error threshold on laminar flame speed and 1% error on maximum temperature can be applied in the same case).

To demonstrate the capabilities of ARCANE, three different case studies are presented in the remainder of this paper. The first one is an unbiquitous configuration in the combustion community: the reduction of a methane/air mechanism with and without NO_x predictions. The purpose of this test case is to serve as a benchmark and demonstrate the performance of the proposed automatic procedure through comparison with literature results. The second case study is the reduction of a three-components surrogate of kerosene, aiming to show the code performance on a complex mechanism with a high number of species and reactions. Finally, the third case study explores a non-combustion configuration, and considers butane steam-cracking. This last case demonstrates the validity and adequacy of the method for any kind of chemical process.

4.5.1 Reduction of Methane/air combustion chemistry

Methane being the simplest hydrocarbon and the major component of natural gas, used in ground-based gas turbines and furnaces, it has been widely studied in the literature. Mainly using GRI-Mech [Smith et al., 1999] as the detailed reference mechanism, numerous chemistry reductions have been proposed (e.g. [Sung et al., 2001, Bahlouli et al., 2014, Gimeno-Escobedo et al., 2019]). Among them, the two reduced mechanisms developed by Lu et al. [Lu and Law, 2008] with and without NO_x predictions are quite popular and as such, were used in [Jaravel et al., 2018] as references to assess the validity of reduced mechanisms obtained with the same techniques as those implemented in ARCANE [Pepiot, 2008]. They are therefore also used here to benchmark the present algorithm.

Methane/air chemistry reduction without NO_x chemistry

The 19 species, 11 QSS species and 184 reactions [1] mechanism of [Lu and Law, 2008] is used here as the reference and referred in the following as Lu19. This mechanism was obtained with an error threshold of 10% in auto-ignition cases and Perfectly Stirred Reactors (PSR). In the present study, different error thresholds are applied depending on the case, as summarised in Table 4.5.1. On every case, the target was chosen to be only the heat release rate.

ARCANE produced a 16 species, 129 reactions and 10 QSS species mechanism. The complete reduction took around 30 minutes on a PC, from which 67 % was spent on the computation of the cases by Cantera. Figure 4.5.1 represents the series of reduction steps followed from the detailed mechanism to the final ARC scheme. For this relatively simple chemistry, the reduction process is straightforward with only one repetition of the species reduction step. The obtained mechanism (referred in the following as Cazeres16) is compared to the detailed mechanism (GRI-Mech 3.0) and Lu19 for laminar flame speeds and ignition delay times over a wide range of conditions. No significant differences can be seen between the three mechanisms, even though the present mechanism Cazeres16 is more reduced than the Lu19.

The difference between Lu19 and Cazeres16 in terms of species is summarised

[1] not to be confused with the 15 steps presented by the authors [Chen, 1997], and representing the number of elemental reactions that do not involve QSS species. Using the same numbering of reactions as in the present work, the mechanism counts 368 irreversible reactions.

Reactor type	0D Isochoric reactor	1D premixed flame
Temperature [K]	1000, 2000	300
Pressure [bar]	1	1
Equivalence ratio	1	0.5, 1, 1.5
Error threshold on Auto-ignition delay time	5 %	/
Error threshold on Laminar flame speed	/	2%
Error threshold on Maximum temperature	1%	1%

Table 4.5.1: Definition of the two considered canonical cases and associated error thresholds applied to various quantities for the methane-air chemistry reduction without NO_x chemistry.

in Table 4.5.2. Interestingly, the present reduction seems less strict for the fastest species, removing some QSS species that are kept in Lu19, and treating as QSS some species that are still transported in Lu19. Note the particular case of CH_2CO, which is transported in Lu19 but removed in Cazeres16, without any degradation of the results.

Species	Status in Lu19	Status in Cazeres16
C_2H_2	transported	QSS
CH_3OH	transported	QSS
CH_2CO	transported	removed
C	QSS	removed
C_2H_3	QSS	removed
HCCO	QSS	removed

Table 4.5.2: Species differences between Lu19 and Cazeres16.

Reduction with NO_x

Adding the prediction of NO_x trough the addition of the NO and NO_2 species as targets, and using the test cases and thresholds of Table 4.5.3 on the GRI-Mech

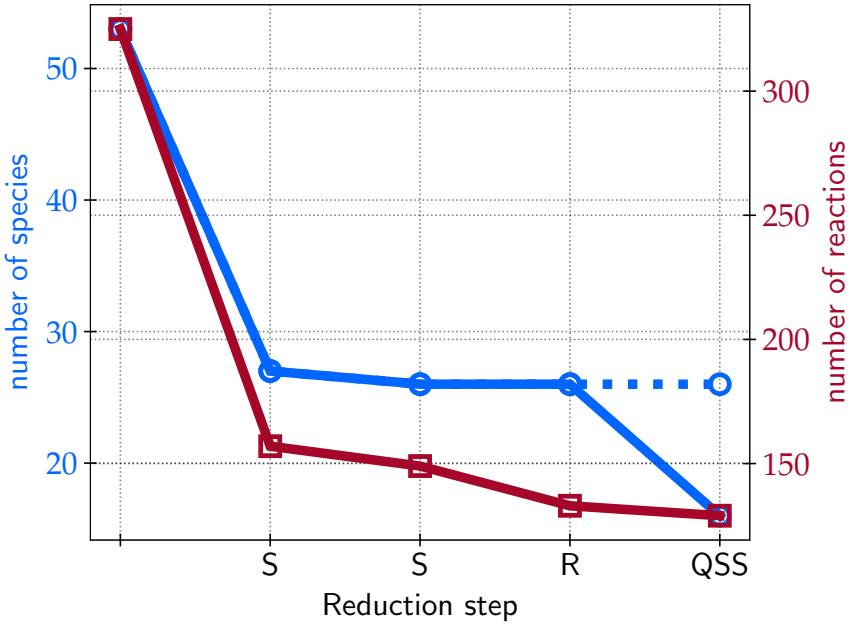

Figure 4.5.1: Graphical representation of the methane/air chemistry without NO_x reduction process: number of species (solid blue line with circles: transported species, dashed blue line with circles: all species) and number of reactions (red line with squares). On the abscissa axis, 'S' stands for species reduction step, 'R' for reactions reduction step and 'QSS' for Quasi-Steady State approximation step.

2.11 detailed mechanism, ARCANE led to a mechanism consisting of 22 transported species, 140 reactions, and 14 QSS species, that is, 6 additional transported species and 4 additional QSS species compared to Cazeres16. This reduction was slightly longer and took 45 minutes on a PC, from which 87 % was devoted to the computation of the flame cases. As shown in Fig. 4.5.3, for this case, several successive repetitions of the same reduction step were necessary, especially for the reduction of reactions which ended in an important number of discarded reactions. Note also the additional species reduction step after the reactions reduction, which allowed a significant further decrease of the species number because of significant changes in the reaction paths graph. This mechanism (referred in the following as Cazeres22) is compared to the detailed mechanism GRI-Mech 2.11. The reason why this mechanism was used instead of the GRI-Mech 3.0 is because it was found to have a better prediction of NO_x emissions in previous studies [Jaravel et al., 2018]. The present

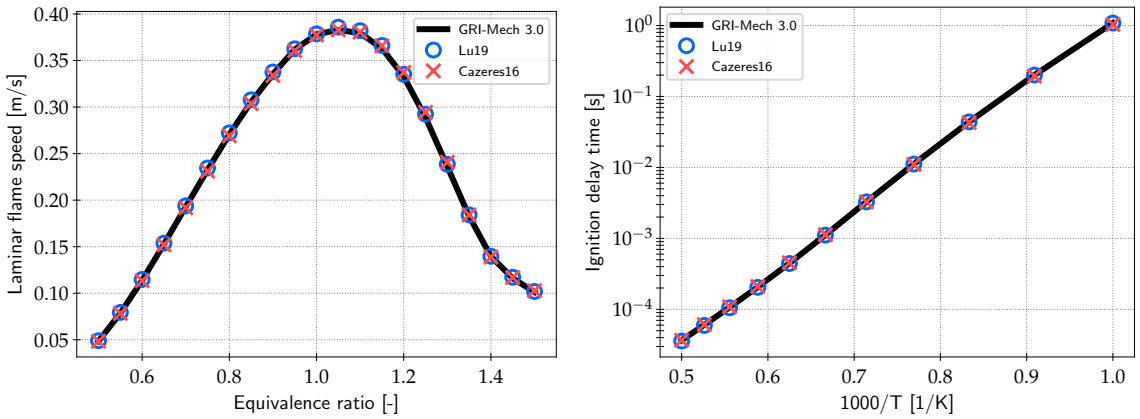

(a) Methane S_l, $T_i = 300K$ (b) Methane τ_{ig} at $\phi = 1$

Figure 4.5.2: Laminar flame speed as a function of the equivalence ratio at 1 bar for (a) methane/air without NO_x flames, and (b) methane/air ignition delay time as a function of $1000/T$ at stoichiometry and 1 bar. Comparison between GRI-Mech 3.0 (black line), Lu19 (blue circles) and Cazeres16 (red crosses).

mechanism was found to be very similar to the latter study, having 4 additional QSS species (C, HCCO, HCNO, NCO) and the same 22 transported species as Cazeres22.

Figure 4.5.5 shows that Cazeres22 recovers all the target quantities across the range of equivalence ratios, as well as the NO_2 mass fraction integral except for the very rich part of the curve. Note that the slight increase in the NO mass fraction integral error occurs in a region where the absolute value of NO is low, and is therefore not overly concerning.

Compared to Cazeres16, there are 6 additional transported species namely NO, NO_2, N_2O, HCN, C_2H_2, CH_3OH. Naturally, NO and NO_2 are kept because they are the species of interest in this case. N_2O and HCN are transported as important species in the NO_x emission process, with an influence on the chemical dynamics too important to be put in quasi-steady state. C_2H_2 and CH_3OH were set in quasi-steady state in Cazeres16 but are now being transported. This indicates that they need to be included to reproduce the correct combustion behaviour, but their correct prediction becomes critical when NO_x are involved. There are 4 more QSS species in Cazeres22 compared to Cazeres16, but this difference is actually an addition of 8 new QSS species with a discarding of 4 former QSS species. The species added are all species with nitrogen atoms directly linked to the NO_x emissions (N, NH, NH_2, NNH,

Reactor type	0D Isochoric reactor	1D premixed flame
Temperature [K]	1000, 2000	300
Pressure [bar]	1	1
Equivalence ratio	1	0.6, 1, 1.4
Error threshold on Auto-ignition delay time	5 %	/
Error threshold on Laminar flame speed	/	2%
Error threshold on Maximum temperature	1%	1%
Error threshold on NO mass fraction integral	5%	5%

Table 4.5.3: Definition of the two canonical cases considered in the study and associated error thresholds applied to various quantities for the methane-air reduction with NO_x chemistry.

HNO, HOCN, HNCO) except for C_2H_3. From the 4 discarded species, C_2H_2 and CH_3OH were moved to the transported species list and CH_2OH and CH_2CHO were completely discarded from the mechanism. The addition of C_2H_3 can be explained by the need for this species to be present to predict C_2H_2 more accurately. The reactions involving CH_2OH and CH_2CHO included in Cazeres16 are reactions consuming O, H, and O_2. When NO_x are involved, those species are predominantly used in NO_x-related pathways, rendering those previous consumption routes negligible and leading to CH_2OH and CH_2CHO being discarded from the mechanism.

4.5.2 Reduction of kerosene combustion using a three-component surrogate

For industrial applications in the domain of aeronautics, accurate prediction of the combustion of kerosene (Jet-A1 more particularly in that case) is required. Kerosene consists in hundreds of hydrocarbons molecules with an exact composition varying from batch to batch. In the literature, surrogates have been formulated in order to represent the composition of such complex fuels. The one used in this study, taken from Humer et al. [Humer et al., 2011], is composed (in volume) of 60% of

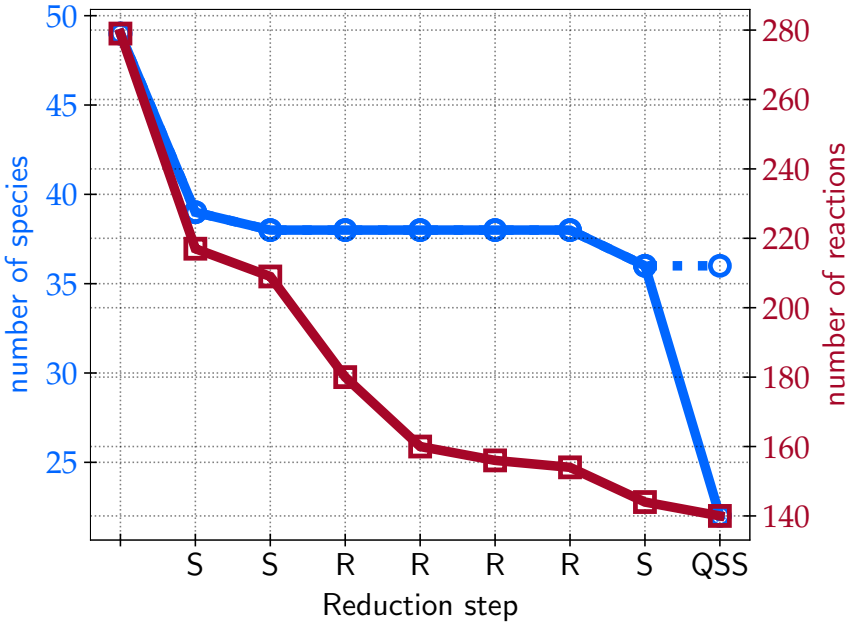

Figure 4.5.3: Graphical representation of the methane/air chemistry with NO_x reduction process: number of species (solid blue line with circles: transported species, dashed blue line with circles: all species) and number of reactions (red line with squares). On the abscissa axis, 'S' stands for species reduction step, 'R' for reactions reduction step and 'QSS' for Quasi-Steady State approximation step.

n-dodecane (n-$C_{12}H_{26}$), 20% of methyl-cyclohexane ($CH_3C_6H_{11}$), and 20% of xylene [2] ($(CH_3)_2C_6H_4$). The detailed mechanism employed in this work is taken from Ranzi et al. [Ranzi et al., 2014] and is available from their website [CRECK,]. This mechanism is labelled CRECK_2003_TOT_HT in the following [3].

The CRECK_2003_TOT_HT mechanism has been designed to incorporate most species involved in jet fuel combustion and is ideally suited to explore kerosene multi-component surrogates, including the 3-component Jet A1 surrogate of interest in this study. It is based on the concept of a palette of fuel components, individually

[2] There is no distinction between xylene isomers (meta-, para-, ortho-xylene) as there is none in the detailed mechanisms

[3] From the detailed mechanisms' authors naming convention, "2003", the mechanism's version, corresponds to March 2020, the latest available update at the time of this study.

$$
\begin{aligned}
CH_2OH + O &\longleftrightarrow CH_2O + OH,\\
CH_2OH + H &\longleftrightarrow CH_2O + H_2,\\
CH_2OH + H &\longleftrightarrow CH_3 + OH,\\
CH_2OH + H &\longleftrightarrow CH_2(S) + H_2O,\\
CH_2OH + O_2 &\longleftrightarrow CH_2O + HO_2,\\
CH_2CHO + O &\longrightarrow CH_2 + CO_2 + H,\\
CH_2CHO + O_2 &\longrightarrow CH_2O + CO + OH,\\
CH_2CHO + O_2 &\longrightarrow 2\,HCO + OH,\\
CH_2CHO + H &\longleftrightarrow CH_3 + HCO,
\end{aligned}
$$

Figure 4.5.4: Reactions involving CH_2OH and CH_2CHO

validated, allowing a variety of surrogates to be simulated. It consists of 368 species among 14,462 reactions. This mechanism does not include low temperature chemistry and is therefore not able to capture the Negative Temperature Coefficient ignition behaviour found at low temperatures. For that reason, only 0D reactors with an initial temperature above 900 K will be computed. For the reduction, heat release rate is targeted along with each individual fuel components. The reduction cases and their relative thresholds are summarised in Table 4.5.4.

Reactor type	0D Isochoric reactor	1D premixed flame
Temperature [K]	1000, 2000	400
Pressure [bar]	1	1
Equivalence ratio	1	0.6, 1, 1.4
Error threshold on Auto-ignition delay time	5 %	/
Error threshold on Laminar flame speed	/	5%
Error threshold on Maximum temperature	1%	1%

Table 4.5.4: Definition of the two canonical cases considered in the study, and associated error thresholds applied to various quantities for the three-component kerosene-air reduction.

The reduced mechanism obtained with ARCANE consists in 39 species, 276 reactions, and 15 QSS species (referred in the following as Cazeres39).

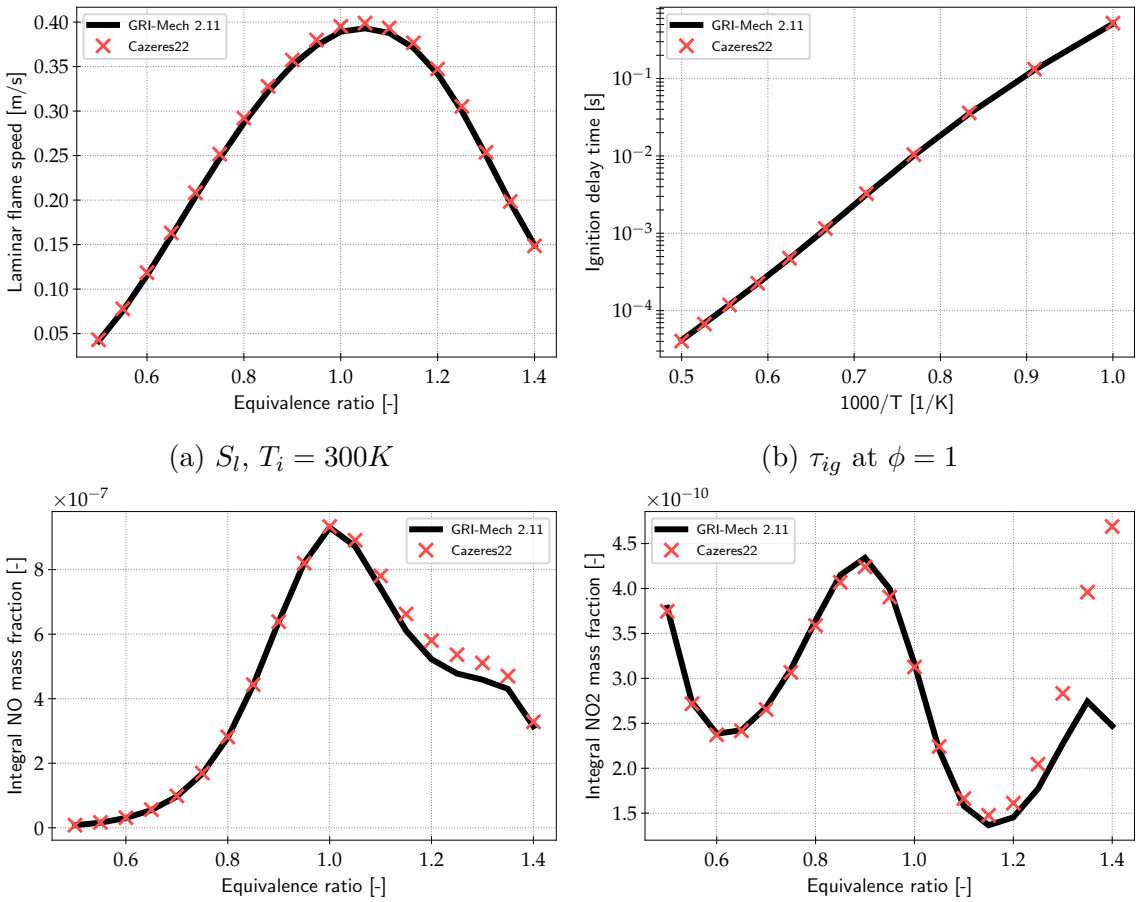

(a) S_l, $T_i = 300K$

(b) τ_{ig} at $\phi = 1$

(c) NO mass fraction integral, $T_i = 300K$

(d) NO_2 mass fraction integral, $T_i = 300K$

Figure 4.5.5: Methane/air combustion at 1 bar: (a) laminar flame speed as function of the equivalence ratio; (b) ignition delay time as a function of $1000/T$ at stoichiometry; (c) total NO, and (d) total NO_2 mass fractions as functions of the equivalence ratio. Comparison between GRI-Mech 2.11 (black line), Cazeres22 (red crosses).

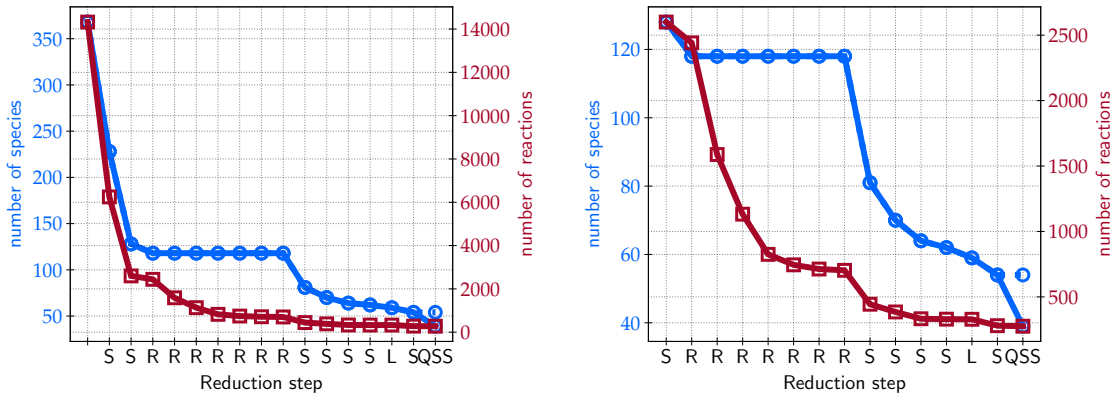

Figure 4.5.6: Graphical representation of the three-component kerosene-air chemistry reduction process: number of species (solid blue line with circles: transported species, dashed blue line with circles: all species) and number of reactions (red line with squares). On the abscissa axis, 'S' stands for species reduction step, 'R' for reactions reduction step, 'L' for lumping step and 'QSS' for Quasi-Steady State approximation step. Left: overall procedure. Right: zoom on the reduction after the first step.

The reduction process is illustrated in Fig. 4.5.6. After the first step, which drastically reduces the number of species and reactions, the reduction continues to progressively decrease the number of reactions, until the reaction graph has sufficiently changed to trigger another decrease of species. This process is similar to the methane-air with NO_x reduction, only more complex. Compared to methane reduction, a lumping step is now present. Because of the higher number of carbon atoms in the fuel, many isomer species can now be found in the chemical pathways. Not all isomer species are lumped together as isomers can have a very different chemical path and cannot be lumped together. In that case, 3 groups of isomers were identified and successfully lumped together, decreasing the number of transported species by 3.

Although it has not been derived based on individual fuel component combustion, results for flame speeds (Fig. 4.5.7) and ignition delay time (Fig. 4.5.8) are shown for the 3-component fuel as well as for the single component fuels.

Results for the 3-component surrogate are in very good agreement with the detailed mechanism, both for laminar flame speed and ignition delay time. For single

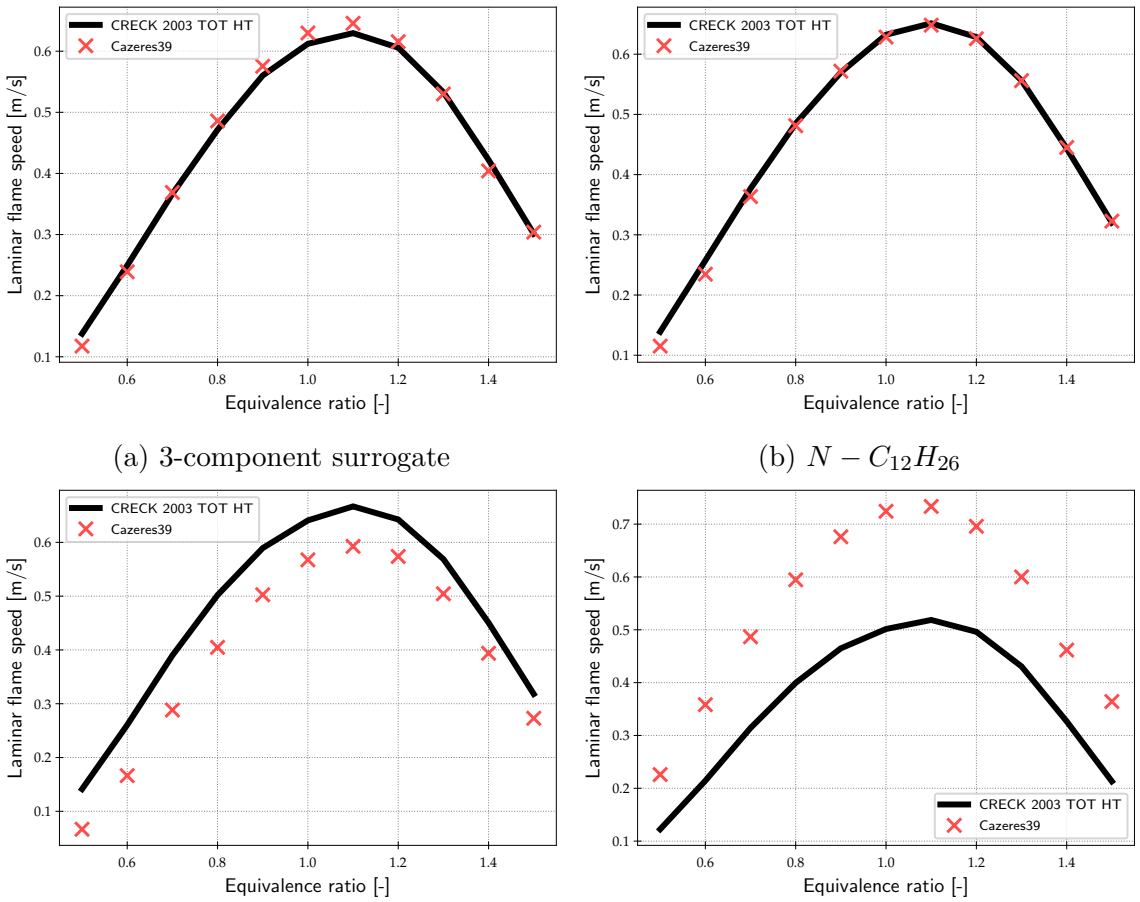

(a) 3-component surrogate

(b) $N - C_{12}H_{26}$

(c) $CH_3C_6H_{11}$

(d) $(CH_3)_2C_6H_4$

Figure 4.5.7: Kerosene combustion at 1 bar and 400K: (a) laminar flame speed as function of the equivalence ratio for the 3-component surrogate, (b) dodecane only, (c) methyl-cyclohexane only, and (d) xylene only. Comparison between CRECK_2003_TOT_HT (black line) and Cazeres39 (red crosses).

component fuels, the agreement between detailed and reduced mechanisms is logically related to its proportion in the surrogate blend that was used for reduction. With a mean error of 115% (maximum of 195%) on ignition delay time, and 27% (maximum of 42%) on laminar flame speed, xylene shows the largest error as it is the least present species in mass in the surrogate (13.7 % in mass). Indeed, its contribution to the overall heat release rate of the surrogate combustion is low and its specific chemical pathways are marginalised during the reduction process, possibly

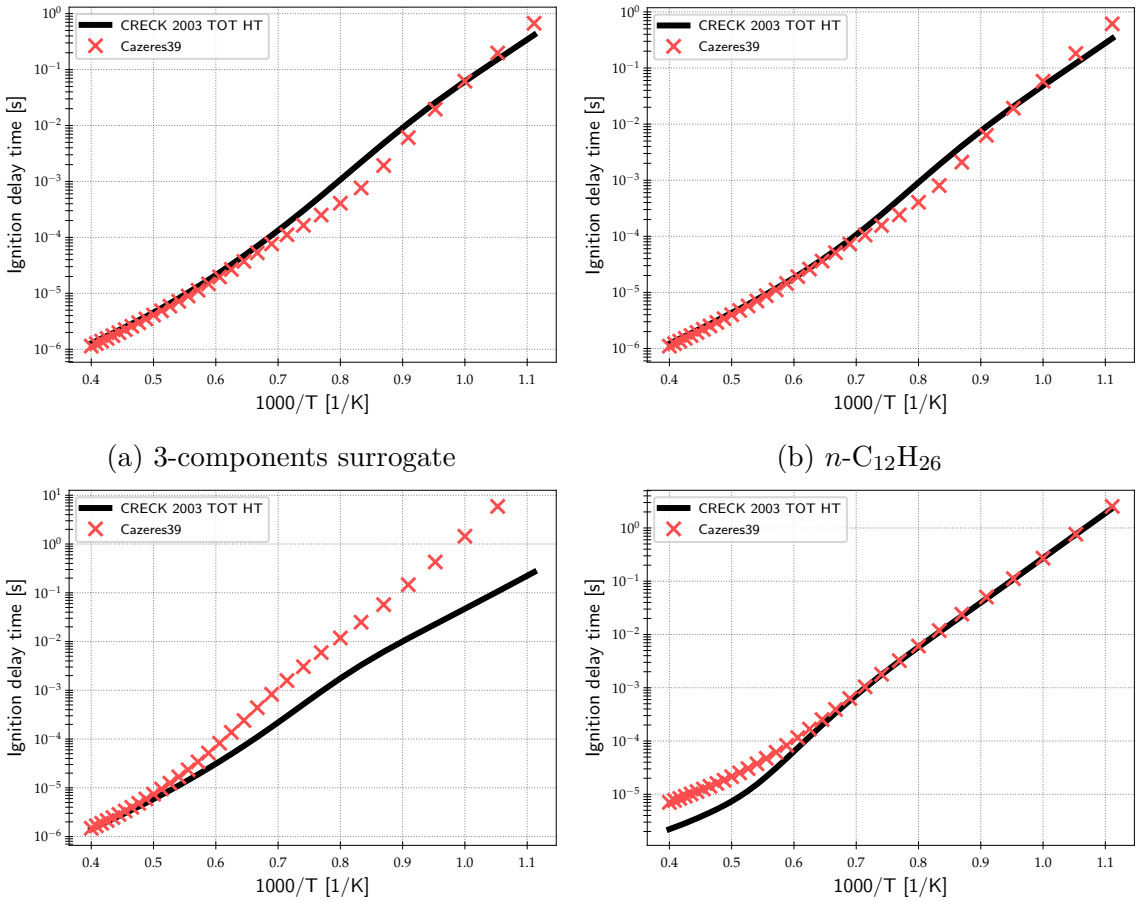

(a) 3-components surrogate

(b) n-$C_{12}H_{26}$

(c) $CH_3C_6H_{11}$

(d) $(CH_3)_2C_6H_4$

Figure 4.5.8: Kerosene combustion at 1 bar and 400K: (a) ignition delay time as a function of $1000/T$ at stoichiometry for the 3-components surrogate, (b) dodecane only, (c) methyl-cyclohexane only, and (d) xylene only. Comparison between CRECK_2003_TOT_HT (black line) and Cazeres39 (red crosses).

removed ultimately. Because the reduction is only constrained by the surrogate characteristics, the overall importance of each of its components will be weighted by their relative mass in the fuel mixture. However minor components may be important, for example in two-phase combustion where preferential evaporation may segregate the vapour components. In such case, single component fuel burning should be added to the target cases for the reduction.

It is here important to highlight the significant gain in computational time brought by reduced chemistry: compared to the detailed mechanism, the Cazeres39 scheme allows to reach a speed-up factor of 363 for the computation of the 3-component stoichiometric freely propagating flame.

4.5.3 Reduction of butane steam cracking

Aside from combustion, the present methodology is suitable for the reduction of kinetic mechanisms applied to any kind of reacting flow process. The simulation of butane steam-cracking, which occurs in high-Reynolds heated pipe flows [Zhu, 2015], is one example of application where the use of reduced chemistry is of high interest. First reduction attempts were presented in [Campet, 2019]. Improved results obtained with ARCANE are presented here.

The detailed mechanism is the same as the one used for kerosene combustion and presented in the previous section, without molecules containing more than 4 carbon atoms, leading to a reference detailed mechanism of 181 species and 5554 reactions. The same steam cracking process studied in [Campet, 2019] is chosen for the present study. It is represented by a zero-dimensional constant pressure reactor, heated via a constant heat flux of 19.38 MW/m^3. The mixture of 69% of butane and 31% of water vapour (in mass fraction) is initially at 909K and 2.3 bar. The simulation is stopped after 0.14s, which is representative of the residence time in butane cracking applications. The main olefins produced by this process are C_2H_4, C_3H_6, and C_4H_6, and are therefore the quantities on which the controlling error is imposed, with a 1% error threshold applied on the value reached at the end of the simulation.

Based on this test case and tolerances, ARCANE allowed to reduce the mechanism down to 24 transported species, 413 reactions, and 12 QSS species (referenced in the following as Cazeres24).

The reduction process illustrated in Fig. 4.5.9 shows a relatively simple procedure, with only one repetition of the species reduction and a lumping step. No reaction reduction was necessary in this case meaning that all the reductions not discarded along species are relevant for this application. Main species profiles shown in Fig. 4.5.10 show a very good agreement between Cazeres24 and the detailed mechanism over the whole simulation, with a maximum deviation of 0.83 % on the peak value of butadiene.

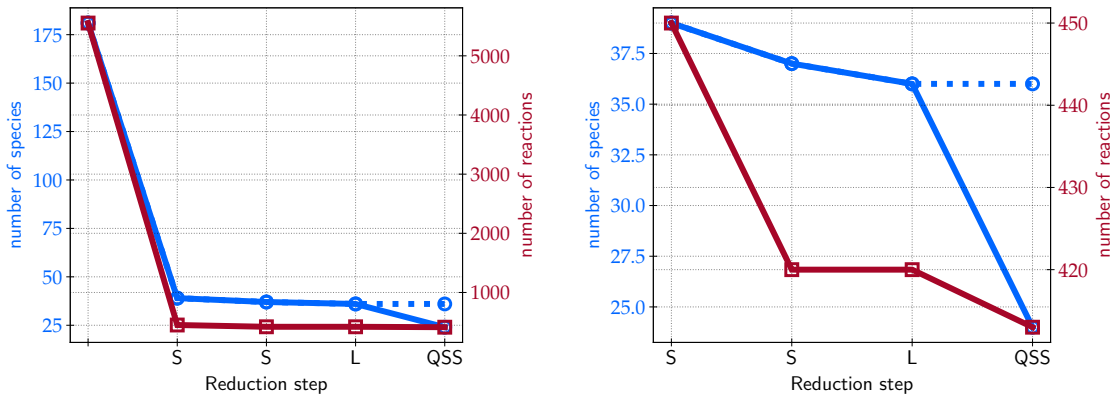

(a) Reduction steps representation

(b) Same graph without the data from detailed mechanism (first point of previous figure)

Figure 4.5.9: Graphical representation of the butane steam-cracking reduction process: number of species (solid blue line with circles: transported species, dashed blue line with circles: all species) and number of reactions (red line with squares). On the abscissa axis, 'S' stands for species reduction step, 'L' for lumping step and 'QSS' for Quasi-Steady State approximation step. Left: overall procedure. Right: zoom on the reduction without the initial.

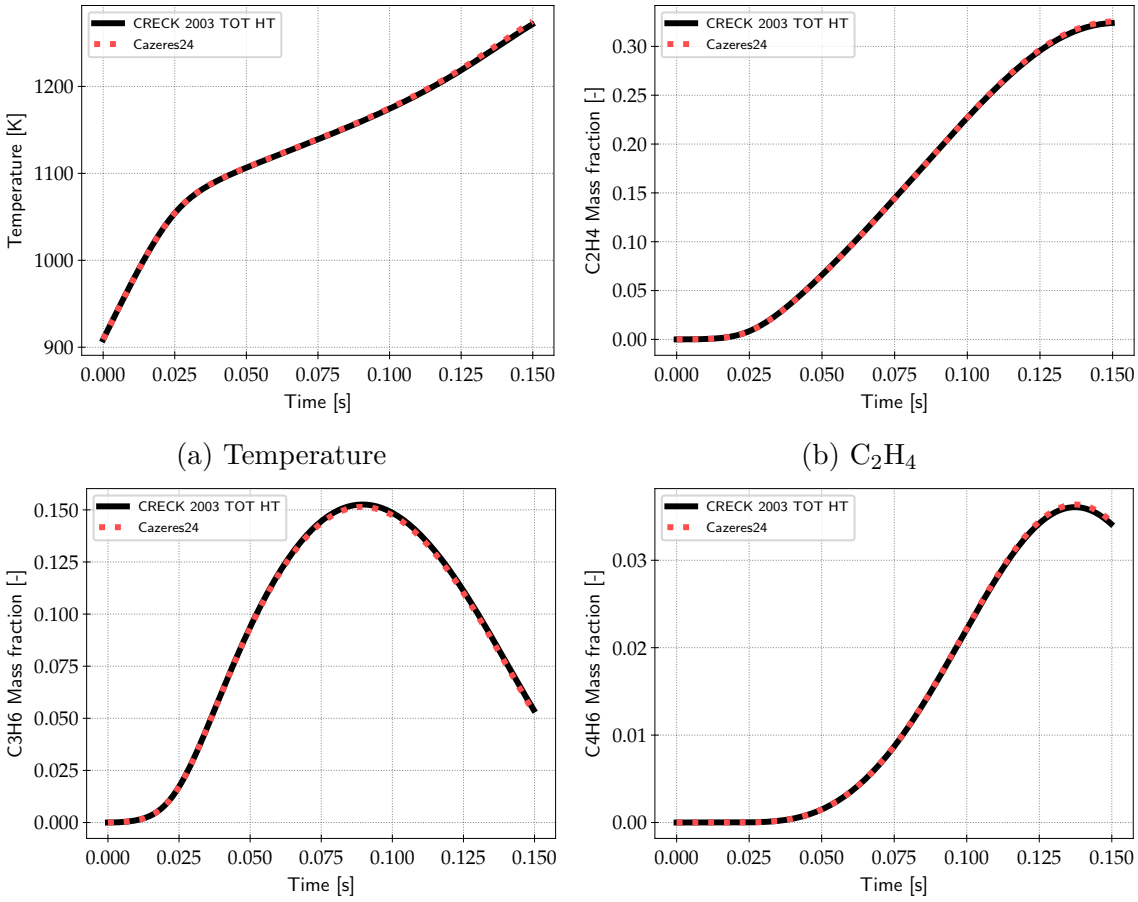

(a) Temperature

(b) C_2H_4

(c) C_3H_6

(d) C_4H_6

Figure 4.5.10: Butane steam-cracking: (a) temperature, (b) ethene, (c) propene, and (d) butadiene mass fractions as functions of time. Comparison between CRECK_2003_TOT_HT (black line) and Cazeres24 (red dots).

4.6 Conclusions

The proposed methodology for the automated reduction of chemical kinetic mechanisms has been shown to be effective on 3 different mechanisms. First, on the GRI-Mech (3.0 and 2.11) with slightly better results than in the literature, both with and without NO_x predictions. It has then shown good performances on the reduction of a Jet A1 3-component surrogate, generating a computationally efficient and affordable 39 species reduced mechanism, despite originating from a 368 species detailed mechanism. Finally, the versatility of the method has been demonstrated on a butane steam-cracking case with perfect agreement between the 24 species reduced mechanism and its 181 species parent mechanism. The implemented algorithm allows to reduce any given chemical mechanism that can be written in elementary reactions following Arrhenius laws, while controlling the error on any user-defined quantity, either directly available in the computation (concentrations, temperature, pressure etc.) or computed with a user-defined function prescribed as an input to the case object. The current implementation also allows for the addition of other reduction and analysis methodologies, for example based on sensitivity coefficients. The reduced mechanisms derived in this work are freely available in Cantera format in the mechanisms database on the CERFACS website (https://chemistry.cerfacs.fr/en/home/) with their associated fortran mechanisms for computation with QSS species. The ARCANE code is available upon request and the procedure for accessing it is detailed on its specific section of the webiste.

Chapter 5

Complementary information about ARCANE

Contents

This chapter will explain in further length what ARCANE is made of, what it is capable of and what are the ongoing development or future applications of the code.

5.1 Code overview

Name of the code: ARCANE
Extended name: Analytically Reduced Chemistry; Automatic, Nice and Efficient
Logo:

Language: Python 3
Release: 1.0
Licence: to be determined
Distribution: private repository hosted on Gitlab
Distribution conditions: access is granted against active participation on the code development
Dependencies: Python 3, Cantera (specific branch), numpy, scipy, matplotlib, pandas, graphviz, networkx, fastdtw
Number of lines: 21 811
Purpose: Automatic reduction of chemical kinetics mechanisms for CFD use and analysis
Keywords: chemical kinetics, reduction, combustion

The code in its current version is not a simple tool but a complete code with an increasing number of capabilities. Python language [Van Rossum and Drake, 2009] has been chosen because it is the easiest to work with when dealing with a broad range of coding needs (from interface with Cantera to writing and reading ascii solution and plotting paper-grade figures). It was designed in the objective of being a long lasting tool with easy implementation of new features that will suit the future researchers and industrial partners in their needs.

5.2 Versatility

Despite being developed with combustion applications in mind, the methods imbued in the code for the reduction process are applicable to any chemical kinetic system with no adaptations to be made as they are all completely defined by the local ther-

modynamic state (temperature, pressure and composition) which is the sole required input for the reduction techniques.

5.2.1 On the applications

As demonstrated in 4.5.3, all kind of applications can be targeted for the reduction of a detailed mechanism. The huge capabilities of Cantera allow to represent a wide variety of canonical cases and to handle the basic computations of the chemical parameters. For the computation of canonical cases, Cantera is not even required by ARCANE as it can take a custom made canonical case as an input. Within the code, the different applications are presented in a demo file in the sources *demo/basic/interface.py* available in Appendix. On top of that, the quantities selected as threshold errors can also be custom made so it suits perfectly the needs of the user. An example of the error handling is presented in the demo file *demo/basic/error.py* available in Appendix.

The only thing required to perform a reduction is a Cantera input file (.cti file) that can be processed in order to generate an initial state. It was already used to derive several reduced mechanisms for methane/hydrogen diffusion flames [Laera et al., 2020], diluted methane flames in flame-wall interaction [Jiang et al., 2021], furnaces applications [Nadakkal-Appukuttan et al., 2020], liquid rocket engines [Blanchard et al., 2021], single component[Collin-Bastiani et al., 2020] [Wirtz et al., 2020] and multi-component [Shastry et al., 2020a] spray flames, and plasma-assisted ethylene/air ignition with a newly implemented method called P-DRGEP[Bellemans et al., 2020].

Future work will try to go towards more complex configuration such as the coupling with CFD codes in order to reduce detailed kinetics on non-canonical cases.

5.2.2 On the required knowledge

As previously said, one of the goals is to provide a reduction code for users that are not necessarily well versed in the intricacies of the chemical kinetics reduction. ARCANE gives great possibilities to each level of user knowledge. An engineer or a beginner just needs to input the basic information that are needed for a reduction

i.e. the detailed mechanism and the list of canonical cases with their associated error thresholds. A complete reduction can be launched in a few lines with no required knowledge about the reduction methods:

```
# Import statements
import ARCANE.cases as cases
import ARCANE.mechanisms as mechanisms
import ARCANE.automatic as automatic

# Create reference mechanism instance
root_mechanism = mechanisms.Mechanism("gri30.cti", name='GRI-Mech 3.0')

# Cases creation
cases_list = []
cases_list.extend(cases.create_case(reactor="0DIsochoric",
                                    mechanism=root_mechanism,
                                    fuel="X/CH4/1",
                                    oxidizer="X/O2/0.21/N2/0.79",
                                    pressure=1e5,
                                    temperature="1000-2000",
                                    phi=1,
                                    targets=["Heat Release"],
                                    error_dict={'tig': 0.05, 'T max': 0.01}))

cases_list.extend(cases.create_case(reactor="1DPremixed",
                                    mechanism=root_mechanism,
                                    fuel="X/CH4/1",
                                    oxidizer="X/O2/0.21/N2/0.79",
                                    pressure=1e5,
                                    temperature=300,
                                    phi="0.5-1-1.5",
                                    targets=["Heat Release"],
                                    error_dict={'Sl': 0.02, 'T max': 0.01}))

# Setup automatic reduction
auto = automatic.Automatic(cases_list, root_mechanism)

# Launching full automatic reduction
mechanisms_list = auto.full_reduction()
```

The above script is everything needed to perform the reduction presented in 4.5.1 with the last object *mechanisms_list* containing the final reduced mechanism along all the intermediate mechanisms obtained at each step of the reduction.

Of course all the reduction methods can be used independently if the user is not satisfied with the result or if another reduction path is to be studied. The object-oriented structure of Python allows for a multitude of ways to use the code and special care as been put in making each structural block as independent as possible so that an experienced user can do as he pleases with the resources available.

The generality of the chosen cases and how the code is written are strongly linked and point towards the objective of being able to use ARCANE on an always increasing number of applications.

5.3 Analysis and post-processing tools

Several methods discussed in 3.5.3 can be used for a-priori or a-posteriori analysis of the kinetic mechanisms and they were integrated to work inside the ARCANE workflow.

Form the data samples extracted from canonical cases, one can obtain a graph similar to Fig. 3.5.1 for a detailed mechanism generated automatically using either PFA or DRGEP as links quantification. Sensitivity analysis can also be performed and even serve for the reduction process coupled with DRGEP with a method called DRGEP-ASA (for DRGEP Aided by Sensitivity Analysis) [Niemeyer et al., 2010].

Different levels of post-processing methods have also been implemented from basic ones such as parametric plots of a quantity over different cases initial values (the laminar flame speed over the equivalence ratio for example) in an automatic fashion with limited inputs. All the chemical kinetics graphs that are presented in this manuscript have been automatically generated with ARCANE.

Timescale analysis can also be performed on the samples database from the cases in order to analyse the stiffness of a given chemical kinetics mechanism in the reference database.

5.4 Towards CFD codes

The prime objective of reducing a chemical kinetic scheme is to implement it into CFD computations that could not have run without reduction.

ARCANE has gathered all the knowledge generated by previous works on ARC in CFD computations to fully automatise even the process of generating the data required by CFD codes.

The CFD code AVBP used in this work (and further detailed in Chapter 8.3) requires the reduction process to not only give a usable chemical kinetics mechanism but also to produce the transport constant required for the Constant Lewis assumption used in the code and described in 1.7.3. The selection process of the Schmidt and Prandtl numbers from a database is embed in ARCANE. In order to stay consistent and possibly compensate the error generated by the reduction, those parameters are chosen as the set extracted from either the fresh or burnt gases of the database flames that minimise the error between the detailed mechanism and the reduced mechanism with simplified transport.

The CFD focused implementation also allows to use different chemical integration techniques compared to classical ones with for example an exponential integration of the chemical source terms that ensures the positivity of the species mass fraction when under-resolving the chemistry in time [Blanchard et al., 2021]. Details about the chemistry integration will be given in 8.4.

Part II

Dual fuel combustion: Methane/Hydrogen blends

Chapter 6

Introduction

Hydrogen is the smallest molecule as it is only composed of one atom and di-hydrogen is then the smallest molecule than can be used as a fuel. Used for a long time in rocket engines, hydrogen as a fuel has grown interest in the last few years, both for the scientific community and the public [1], in the context of the research for cleaner energies.

It has been the subject of a Combustion Webinar [2] given by Heinz Pitch entitled *Hydrogen: A Seemingly Simple Fuel*[3] which highlighted the difficulties of dealing with hydrogen despite its chemical kinetics simplicity. This explains why hydrogen and all its applications are vibrant subjects within the combustion community.

Hydrogen is especially considered as a way to store electric energy produced by renewable sources (solar panels, wind turbines, hydroelectric power plant, etc.). This is achieved through hydrogen production labelled *green hydrogen* via electrolysis of water H_2O which is broken down into H_2 and O_2. The hydrogen then produced can be stored in tanks either at cryogenic conditions (below 20K) or at high pressures around 700 bar. Storing hydrogen energy has the advantage of being more sustainable than the other forms of electrical storage as presented in Fig. 6.0.1, and allows storage of important amounts of energy over a long period. The concept labelled Power to

[1] Google Trends results for "hydrogen" over the past 5 years: https://trends.google.com/trends/explore?date=today%205-y&gprop=news&q=%2Fm%2F02h9byz

[2] https://sun.ae.gatech.edu/combustion-webinar/

[3] https://www.youtube.com/watch?v=h9nQLbJKGFk&t=878s

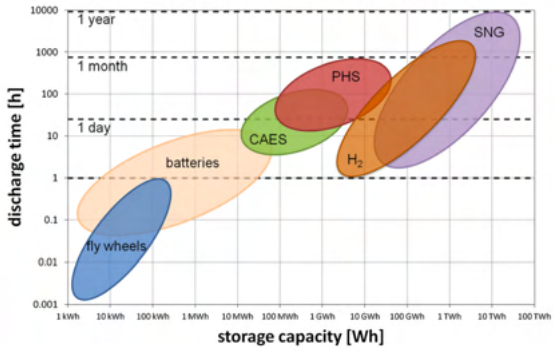

Figure 6.0.1: Charge/discharge period and storage capacity of different electricity storage systems. CAES, compressed air energy storage; PHS, pumped hydro storage; SNG, substitute natural gas. From [Schaaf et al., 2014]

Gas (PtG) is part of several projects focusing on hydrogen with the example of the European Research Council (ERC) project SCIROCCO which joins experiments and numerical simulations and gathers the Institut de Mécanique des Fluides de Toulouse (IMFT) and the CERFACS in France.

Green hydrogen may be then used as a combustible in several ways:

- Hydrogen can power fuel cells mainly used for automotive transportation [O'hayre et al., 2016] allowing cars or trucks to only emit water vapour as an exhaust gas.
- It is also investigated as an alternative fuel for aviation which still relies on thermal energy without any convincing alternative in the near future. Aircraft manufacturers like Airbus have the ambition of developing a hydrogen-powered aircraft by 2035 [4].
- Going full circle, it is also considered for gas turbines which produce today 23.1 % of the world electricity [5]. Depending on the technology, hydrogen can be blended with the natural gas with varying amounts.

In this part, we focus on energy production with hydrogen enrichment of natural

[4] https://www.airbus.com/innovation/zero-emission/hydrogen/zeroe.html

[5] Global share of electricity generation, 2018, International Energy Agency https://www.iea.org/data-and-statistics/charts/global-share-of-electricity-generation-2018

gas. The objective is to demonstrate how the tools for chemistry analysis and reduction developed in the previous part can be used to predict and study the impact of introducing hydrogen in these systems.

The main motivation of using hydrogen enrichment is to lower the CO_2 emissions thanks to the lower hydrocarbon content in the fuel. In addition because hydrogen has a much higher laminar flame speed than hydrocarbons, its blending with natural gas increases the mixture reactivity allowing to operate at leaner conditions with an increased stability.

Several studies have been already published on this subject both with experimental and numerical approaches. In most cases hydrogen-enrichment is performed in a premixed mode, i.e., adding hydrogen to the fuel before injection. However it can be more efficient to use a separate hydrogen injection as was done experimentally in [Oztarlik et al., 2020] and studied numerically with ARC by [Laera et al., 2020]. Direct Numerical Simulations (DNS) with detailed chemistry have been performed on canonical configurations to assess the benefits of hydrogen enrichment in terms of flame speed and increased reactivity [Di Sarli and Di Benedetto, 2007][Bougrine et al., 2011]. It has also been demonstrated experimentally by [Schefer, 2003] [Boushaki et al., 2012] that hydrogen-enrichment of a swirled methane/air flame improves its stability in lean conditions. Besides this beneficial effect, hydrogen enrichment modifies the flame behaviour. Depending on the hydrogen content, it may modify the flame shape, as observed in [Chterev and Boxx, 2021, Guiberti et al., 2015b]. This effect was retrieved with numerical simulation [Mercier et al., 2016] and will be the subject of Chapter 9. Hydrogen-enrichment was also shown to affect thermo-acoustic instabilities, increasing their frequency range and having a variable effect on the positive feedback depending on pressure conditions [Chterev and Boxx, 2021].

This part of the manuscript focuses on the reduction of an ARC relevant for the combustion of a methane/hydrogen blend with air in Chapter 7 and its application to the Large Eddy Simulation (LES), which fundamentals will be recalled in Chapter 8, of a swirled hydrogen-enriched premixed methane/air flame in Chapter 9.

Chapter 7

Chemical kinetics of methane/hydrogen blends

Contents

7.1 Introduction: selection of the chemical description model

Available detailed mechanisms are constructed in such a way that they can be used for any fuel. The CRECK mechanism [CRECK,] for example is proposed in reduced versions specific for a fuel, which are simple extractions from the same full scheme. As a consequence, any fuel or combinations of fuels, in this case methane and hydrogen, is accurately predicted with such full detailed mechanism. Therefore there is no need for specific development of detailed chemistry and we will use them as reference and starting point for our own chemistry models.

If the detailed mechanism cannot be used in the CFD simulations for obvious reasons, there is still a choice to be made between the various possibilities of reduced schemes, from global to ARC or even skeletal.

Global schemes for fuel blends may be simply written as:

$$(1-X_{H_2})CH_4+X_{H_2}H_2+\left(\frac{5-3X_{H_2}}{4}\right)O2 \longrightarrow (1-X_{H_2})CO_2+\left(\frac{1+(1-X_{H_2})}{2}\right)H_2O$$

where X_{H_2} is the mole fraction of hydrogen in the fuel. This considers the fact that the fuel blend $(1-X_{H_2})CH_4+X_{H_2}H_2$ is equivalent to a fuel of formula $C_{(1-X_{H_2})}H_{(4-2X_{H_2})}$.

As seen above, a supplementary parameter enters the scene when it comes to describe fuel blends. Additionally to the equivalence ratio of the mixture, the enrichment level is also a defining parameter. Still, with the view of an equivalent fuel as defined above, the equivalence ratio may be used solely to characterise the flame.

However, because H_2 has a much greater diffusivity than CH_4 the local composition may vary and lead to zones where initial mixture composition is no longer valid. In such case, flames will non only depend on the global equivalence ratio but will also change with the hydrogen content, which becomes an additional parameter. This has a direct consequence for tabulation methods (described in 3.2) which should add the enrichment level as a table parameter. Note also that the expression of the mixture fraction as expressed in Eq. 1.62 should be revised as it does not consider a varying H/C ratio. The coverage of the full range of equivalence ratio and hydrogen content, from 0 to 100% is therefore complex with pre-tabulation of laminar flame, hence the narrow range of table parameters used in the literature [Alaya et al., 2019][Hernández-Pérez et al., 2014].

A major advantage of ARC is to avoid such considerations as it behaves exactly like the detailed mechanism, i.e., it contains both hydrogen combustion and methane combustion and it is therefore able to handle any blend of the two fuels. This was confirmed for the LU19 scheme (introduced in Section 4.5.1) which allowed to obtain good results on premixed hydrogen flames, even though it was not explicitly designed by the authors for this fuel. As depicted in Fig. 7.1.1, the LU19 ARC mechanism perfectly predicts the combustion of hydrogen and methane/hydrogen blends for the range of operating conditions used for the scheme derivation for methane.

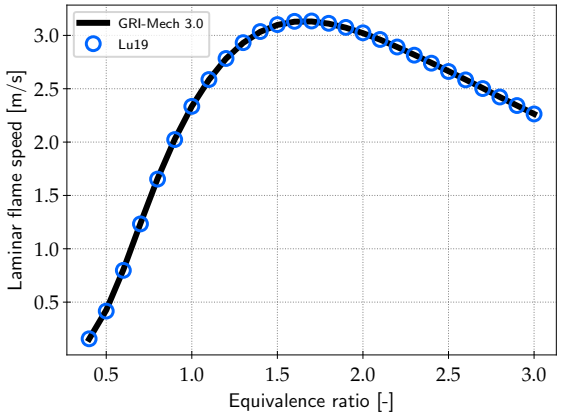

(a) Pure hydrogen-air premixed flame with varying equivalence ratio

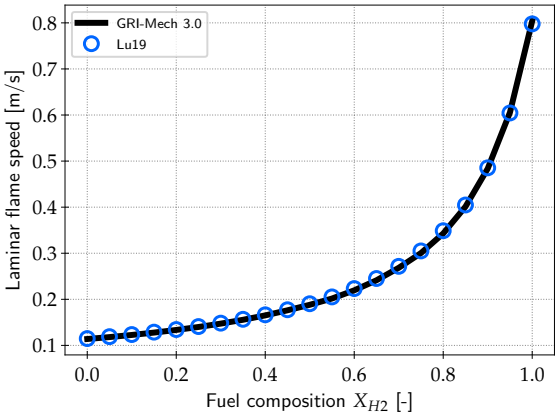

(b) Hydrogen/methane premixed flame with varying hydrogen content at $\phi = 0.6$

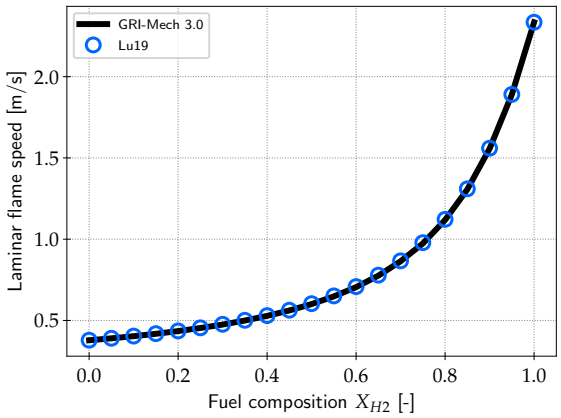

(c) Hydrogen/methane premixed flame with varying hydrogen content at $\phi = 1$

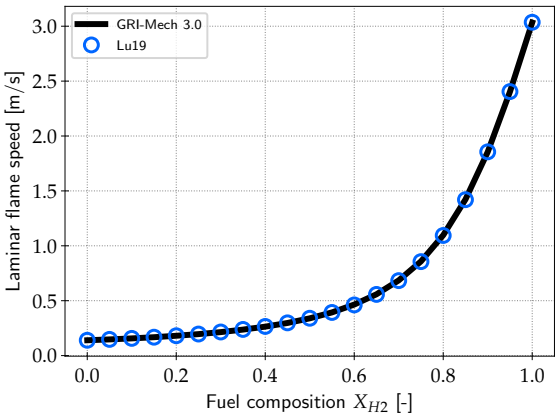

(d) Hydrogen/methane premixed flame with varying hydrogen content at $\phi = 1.4$

Figure 7.1.1: Laminar flame speed comparison between the GRI-Mech 3.0 (black lines) and LU19 ARC mechanism (blue circles) for (a) pure hydrogen and globally (b) lean, (c) stoichiometric and (d) rich methane/hydrogen blends. Inlet temperature of 300K at atmospheric pressure.

Thanks to this capability, a unique reduced ARC mechanism can be used to compute all operating points with different equivalence ratios and hydrogen enrichment levels. ARC schemes also ensure to correctly capture the particular behaviours induced by preferential diffusion. Such scheme has already been used by [Laera et al., 2020] to compute a non-premixed hydrogen enrichment of a methane-air flame where pure hydrogen is injected separately to play a similar role as a pilot flame.

A major drawback of hydrogen-enrichment is the increased NO_x emissions due to locally higher temperatures for a fixed equivalence ratio. It is therefore of primary importance to evaluate the impact of hydrogen-enrichment on NO_x emissions as it may counterbalance the gain in efficiency and in carbon emissions. For that reason, NO_x chemistry will subsequently be added to the target ARC mechanism.

7.2 NO_x emissions

NO_x is the generic denomination of nitric oxide (NO) and nitric dioxide (NO_2). The nitric dioxide is a harmful molecule formed from both natural phenomena (soil microbes, volcanoes, lightning) and combustion systems. It contributes to modified ozone concentrations [Romer et al., 2018], acid rains [Irwin and Williams, 1988] and respiratory issues [Int Panis et al., 2017].

The NO_x formation mechanisms are generally decomposed into several chemical pathways detailed in the following.

- **Thermal NO** described by [Zeldovich and Frank-Kamenetskii, 1962] is the formation of NO in the burnt gases where the temperature is sufficiently high. It is described by the Zeldovich mechanism representing the direct oxidation of nitrogen:

$$O + N_2 \leftrightarrow NO + N$$
$$N + O_2 \leftrightarrow NO + O$$
$$N + OH \leftrightarrow NO + H$$

  The first of these reactions features a high activation energy hence its activation only in hot gases. This process is typically slow compared to the others.

- The **prompt NO route**, initially suggested by [Fenimore, 1971], describes the rapid production occurring in the reaction zone from the interaction between N_2 and the radicals produced by the fuel oxidation. [Miller et al., 2005] suggested that the main reaction representing this pathway involves the NCN radical via the reaction:

$$N_2 + CH \leftrightarrow NCN + H$$

  The NO production through these pathway follows the evolution of laminar flame speed with equivalence ratio, i.e., peaks at slightly rich conditions where a large quantity of radicals is available.

- The **N_2O route** is the major contributor to NO emissions under lean premixed conditions [Drake et al., 1991] as N_2O is produced by a reaction between N_2 and O to finally produce NO via the following reactions:

$$N_2 + O + M \leftrightarrow N_2O + M$$
$$N_2O + O \leftrightarrow NO + NO$$
$$N_2O + H \leftrightarrow NO + NH$$

- For low flame temperatures, the **NNH pathway** [Purohit et al., 2021] becomes significant and is described by the reactions:

$$N_2 + H \leftrightarrow NNH$$
$$NNH + O \leftrightarrow NO + NH$$

- **Fuel NO** becomes relevant for fuels that contain nitrogen in their composition such as ammonia which is also actively studied as a candidate for decarbonated combustion [Kobayashi et al., 2019]. This pathway is therefore absent in hydrocarbon and hydrogen combustion.

NO_x detailed kinetics has been investigated for hydrogen flames by [Frassoldati et al., 2006] and updates stemming from experimental comparisons have been included inside the CRECK detailed mechanism that will be used in the following.

7.3 OH^* prediction

The species OH^* represents the electronically excited state of the OH radical. Photons are issued from the de-excitation of this molecule, leading to light emission and making the flame visible by human eyes. This phenomenon, known as OH-chemiluminescence, has been identified as a good marker of heat release as it takes place inside the reaction zone. This explains why it has become a common experimental combustion technique. However, the quantitative relationship between OH-chemiluminescence and the heat release is diffcult to establish. To allow quantitative comparison with simulation, a chemical kinetics mechanism for OH^* is included in the chemical scheme.

The kinetics mechanism of OH^* that was selected for this work is the one from [Kathrotia et al., 2010][Kathrotia et al., 2012] which was specifically validated for hydrogen combustion. [Zhao et al., 2018] confirmed that this mechanism (and more specifically the rate constant of the reaction $H + O + M \leftrightarrow OH^* + M$) is the only one in the literature able to capture emission peaks identified in experiments. The OH^* chemistry was extracted from the C1-C4 mechanism of [Kathrotia, 2011] as a sub-mechanism meaning that only the species and reactions relevant to the OH^* computation were kept.

The OH^* species is of particular interest in the context of hydrogen combustion as pure hydrogen flames are weakly visible with an emission spectrum between the ultra-violet and the visible blue [Zhao et al., 2018][Schefer et al., 2009].

Comparing the maximum values of OH^* and of the heat release rate in 1D premixed flames in Fig.7.3, the correlation between these two values seems straightforward for pure methane (Fig. 7.3.1a) but not so clear for pure hydrogen and blends of both fuels.

In Fig. 7.3.1c, 7.3.1d and 7.3.1e, it is observed that the OH^* mass fraction maximum value significantly increases with the hydrogen content until a peak value close to 90% enrichment, before rapidly decreasing in pure hydrogen. As seen in Fig. 7.3, the OH^* prediction becomes particularly interesting in that case because the simple correlation between the heat release rate and OH^* emission is no longer valid. The prediction of the OH^* species provides then a non-redundant information on the flame characteristics, and appears necessary to compare with OH-chemiluminescence images from experiments.

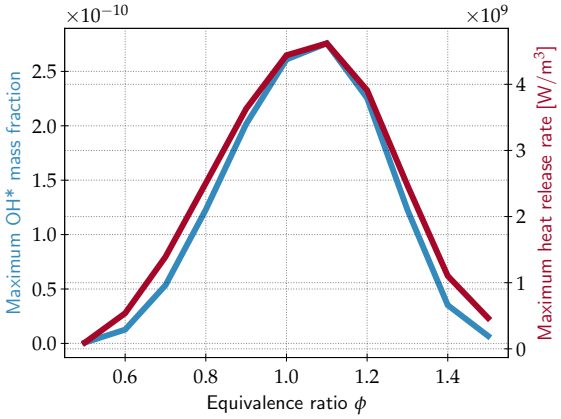

(a) Pure premixed methane-air flames with varying equivalence ratio

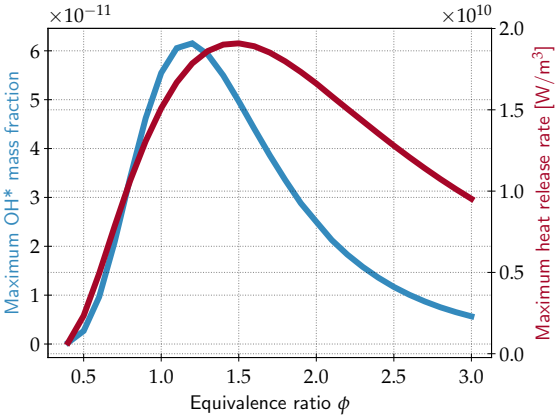

(b) Pure premixed hydrogen-air flames with varying equivalence ratio

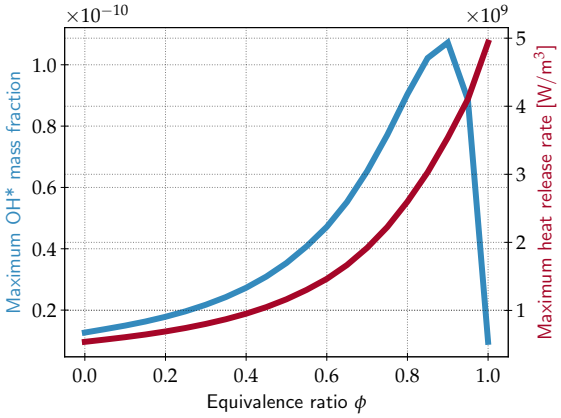

(c) Hydrogen/methane premixed flame with varying hydrogen content at $\phi = 0.6$

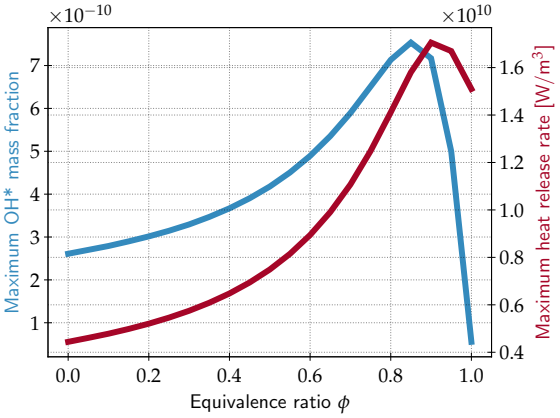

(d) Hydrogen/methane premixed flame with varying hydrogen content at $\phi = 1$

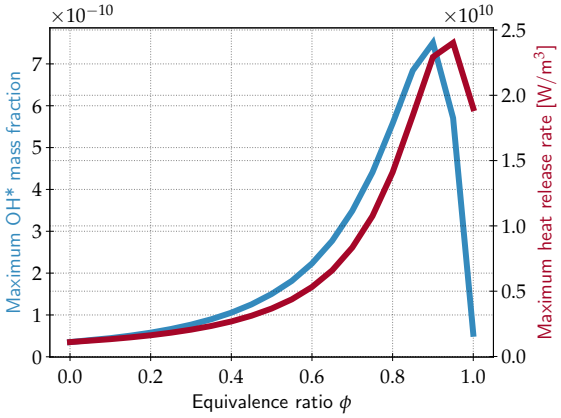

(e) Varying hydrogen mole fraction in the fuel at $\phi = 1.4$

Figure 7.3.1: Maximum value of the OH* mass fraction (left and blue) and the heat release rate (right and red) for (a) pure methane, (b) pure hydrogen and globally (c) lean, (d) stoichiometric and (e) rich methane/hydrogen blends. Inlet temperature of 300K at atmospheric pressure.

7.4 Reduction of the combustion kinetics of methane/hydrogen blends including NO_x and OH^* prediction

To be able to capture all the phenomena previously described, the reduction targets altogether the methane/air combustion, the NO_x emissions and the OH^* profiles. Indeed, as seen in Section 7.1 with the LU19 ARC scheme, it has been demonstrated that a scheme which is derived on methane-air combustion correctly predicts the effect of hydrogen addition.

Starting from the trimmed CRECK_2003_TOT_HT detailed mechanism used earlier in Section 4.5.3, further trimmed to 3 carbon-atoms molecules, the OH^* sub-mechanism described in 7.3 is added, giving a resulting mechanism of 154 species and 2363 reversible reactions. This detailed mechanism is called POLIMI_C1C3_NOx_Chemlum in the following. The canonical cases database is constituted from 2 stoichiometric isochoric reactors for ignition delay time assessment at initial temperatures of 1000 and 2000 K, and 3 freely propagating premixed flames at lean, stoichiometric and rich conditions with atmospheric fresh gases. Both for exercise and proof, the fuel for all the canonical cases is chosen to be methane. No hydrogen-enriched or pure hydrogen flame is present in the database in order to confirm the ARC capability of keeping the relevant pathways for hydrogen combustion. For the 0D cases, an error threshold of 10% was imposed on the ignition delay time and 1% on the maximum temperature reached after ignition. For the 1D cases, a 5% error threshold was set on the laminar flame speed and 1% on the maximum temperature. As we are interested in the NO_x emissions and more particularly the NO which is more abundant than NO_2, a 5% error was prescribed on its integrated value. The same threshold was also set on OH^*. The canonical cases and their associated error thresholds are summarised in Table 7.4.1.

The final mechanisms that was obtained using ARCANE comprises 27 species, 855 irreversible reactions and 25 QSS species, and will be referred in the following as Cazères27. This reduction corresponds to dividing the number of transported species by 5.7 and reactions by 5.5 giving an important reduction allowing to compute the chemistry in LES at a reasonable cost. Its validity is assessed with both a variation of the equivalence ratio and a variation of the hydrogen content in the fuel in Fig. 7.4.1 and Fig. 7.4.2.

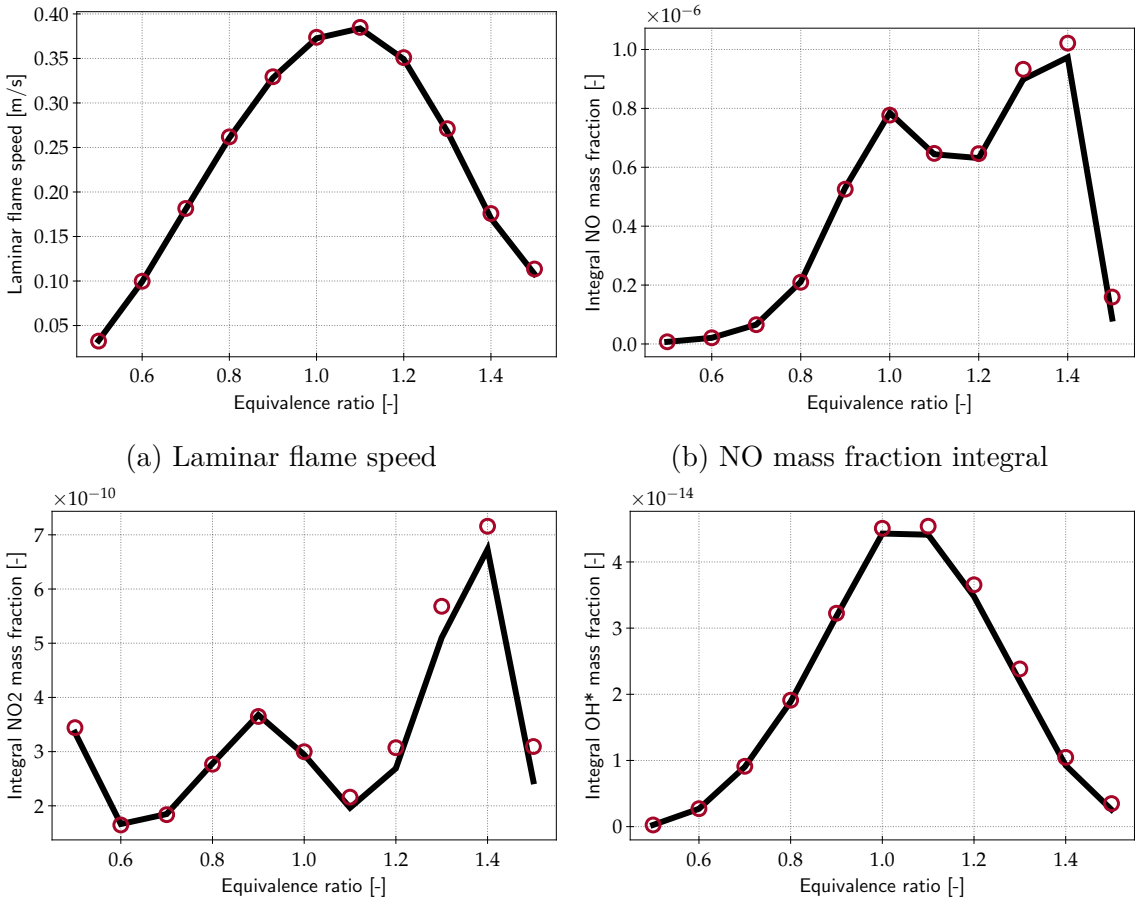

(a) Laminar flame speed

(b) NO mass fraction integral

(c) NO_2 mass fraction integral

(d) OH^* mass fraction integral

Figure 7.4.1: Validation of the reduced ARC mechanism for a range of equivalence ratio on pure methane-air laminar premixed flames with T_{inlet} = 300 K and P=1 bar. The black solid line stands for the detailed mechanism (POLIMI_C1C3_NOx_Chemlum) and red circles stand for the reduced mechanism (Cazères27)

Reactor type	0D Isochoric reactor	1D premixed flame
Temperature [K]	1000, 2000	300
Pressure [bar]	1	1
Equivalence ratio	1	0.6, 1, 1.4
Error threshold on Auto-ignition delay time	5 %	/
Error threshold on Laminar flame speed	/	5%
Error threshold on Maximum temperature	1%	1%
Error threshold on NO mass fraction integral	/	5%
Error threshold on OH^* mass fraction integral	/	5%

Table 7.4.1: Definition of the considered canonical cases and associated error thresholds applied to various quantities for methane-air reduction with NO_x and OH^* prediction.

Fig. 7.4.1 shows an excellent agreement between the detailed mechanism and the ARC (Cazères27) which is not surprising given that the mechanism was reduced specifically on cases in the same equivalence ratio range.

On pure hydrogen cases, the performances of the reduced mechanism in reproducing the detailed chemistry are even better because of the simplicity of hydrogen combustion as can be seen on Fig. 7.4.2

As was already seen with the simpler reduced mechanism LU19, the agreement is also really good for blends of methane and hydrogen, shown in Fig. 7.4.3 for a globally stoichiometric mixture with a maximum error of less than 2% (maximum for NO mass fraction integral for 90% hydrogen enrichment). Validation for lean and rich global equivalence ratios can be found in Appendix C.

The presently derived ARC will be used in the following to study the effect of hydrogen-enrichment on the flame shape in a Large Eddy Simulation (LES) of a confined swirled methane premixed flame inside an academic combustor. This effect on NO_x emissions as well as the relevance of the OH^* chemistry will also be

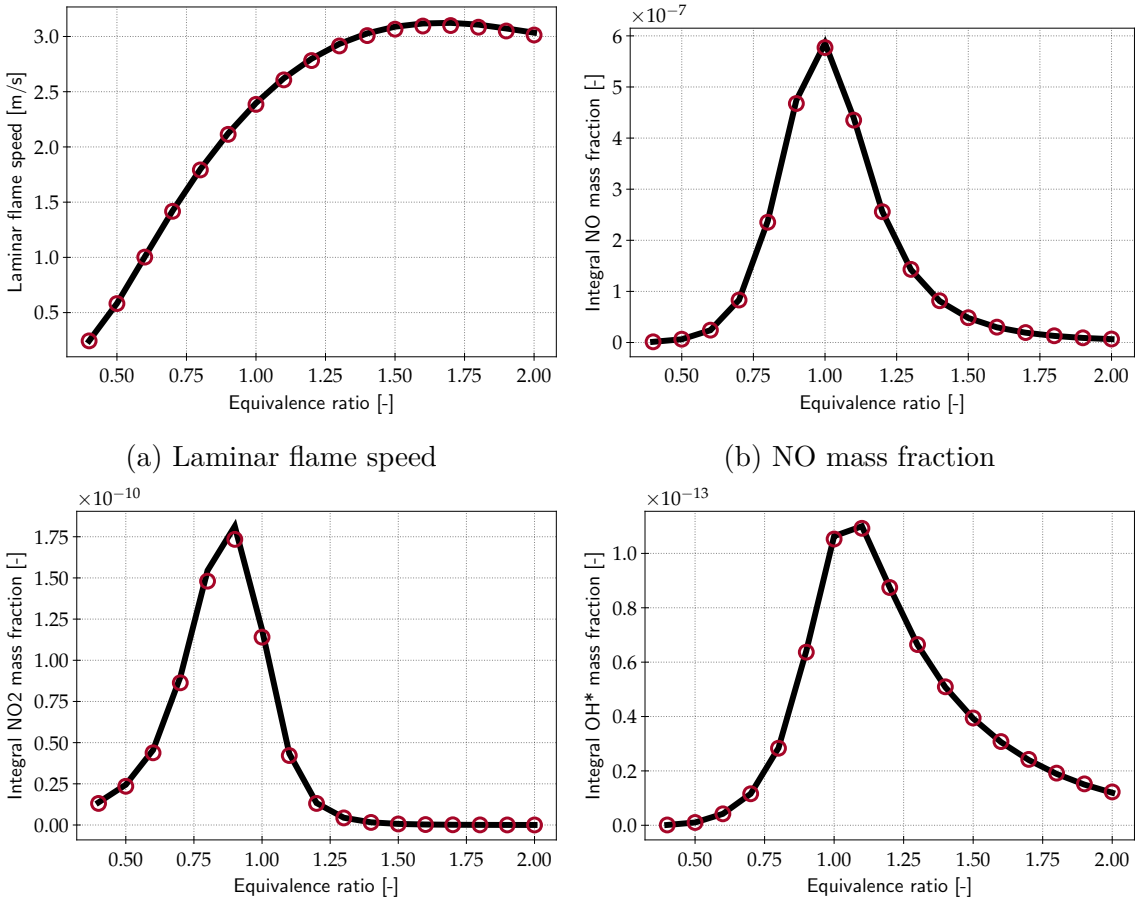

(a) Laminar flame speed

(b) NO mass fraction

(c) NO_2 mass fraction

(d) OH^* mass fraction

Figure 7.4.2: Validation of the reduced ARC mechanism for a range of equivalence ratio on pure hydrogen-air laminar premixed flames with T_{inlet} = 300 K and P=1 bar. The black solid line stands for the detailed mechanism (POLIMI_C1C3_NOx_Chemlum) and red circles stand for the reduced mechanism (Cazères27)

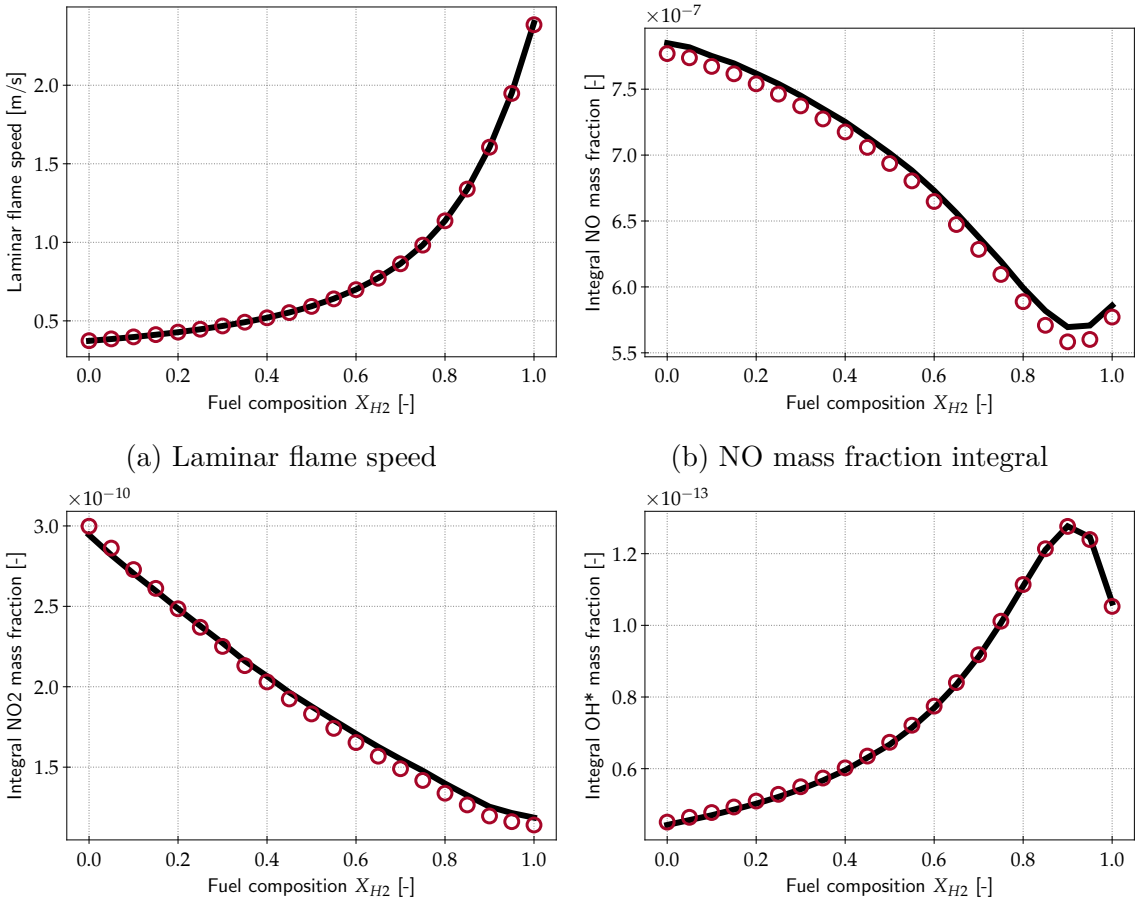

(a) Laminar flame speed

(b) NO mass fraction integral

(c) NO_2 mass fraction integral

(d) OH^* mass fraction integral

Figure 7.4.3: Validation of the reduced mechanism for a range of hydrogen-enrichment of methane-air laminar premixed flames with T_{inlet} = 300 K and P=1 bar at ϕ = 1. The black solid line stands for the detailed mechanism (POLIMI_C1C3_NOx_Chemlum) and red circles stand for the reduced mechanism (Cazères27)

investigated. The fundamentals of LES as well as the modelling approaches used for this work are described in Chapter 8 before describing the study in itself in Chapter 9.

Chapter 8

Fundamentals of Large Eddy Simulation of reacting turbulent flows

Contents

Because of operating conditions and size, most flows encountered in practical configurations are turbulent. In the case of combustion, turbulence is even necessary to reach sufficient both mixing and combustion efficiency. It is therefore essential to accurately predict not only the turbulent flow, but also the flame-turbulence interaction which strongly impacts the heat release rate.

Turbulence in industrial flows results from the competition between inertial and viscous forces and is therefore quantified by the Reynolds number defined as:

$$Re = \frac{UL}{\nu} \tag{8.1}$$

where U is the flow velocity, L a length characterising the system and ν the kinematic viscosity of the fluid.

When the Reynolds number exceeds the empirically peer-agreed value of 4000, a laminar flow becomes turbulent and vortices, or eddies, of several sizes l appear. From a mathematical point of view, it can be expressed as random fluctuations of the flow quantities around a statistical average value. According to the *energy cascade* theory introduced by [Richardson, 1922], the largest eddies, the ones seen by the naked eye, correspond to the integral length scale l_T and transfer their energy to the smallest size eddies which finally dissipate under the action of viscosity. In the dissipation regime, the inertial and viscous forces balance out so that the Reynolds number is of the order of unity. From Kolmogorov hypothesis [Kolmogorov, 1941], statistics of the smallest eddies follow a universal law and the associated length η_K, time τ_K and velocity u_K scales (called the Kolmogorov scale) have been determined by [Pope, 2000] as functions of the kinematic viscosity η and the dissipation rate ϵ only:

$$\eta_K = (\nu^3/\epsilon)^{\frac{1}{4}} \tag{8.2}$$

$$\tau_K = (\nu/\epsilon)^{\frac{1}{2}} \tag{8.3}$$

$$u_K = (\nu\epsilon)^{\frac{1}{4}} \tag{8.4}$$

In between the integral and the dissipation zones, the inertial zone is characterised by the dissipation rate and the turbulent energy density $E(k)$ decreases linearly in a log-log scale with the eddies wave number $k = 1/l$ and a slope of $-5/3$ in the academic case of Homogeneous Isotropic Turbulence.

The vast world of CFD is often decomposed according to which one of these different zones is resolved or modelled as depicted in Fig. 8.0.1. Direct Numerical Simulation (DNS) can be considered as the most accurate as all length scales are resolved. Considering the turbulent Reynolds number $Re_T = \frac{u_T l_T}{\nu}$ where u_T is the

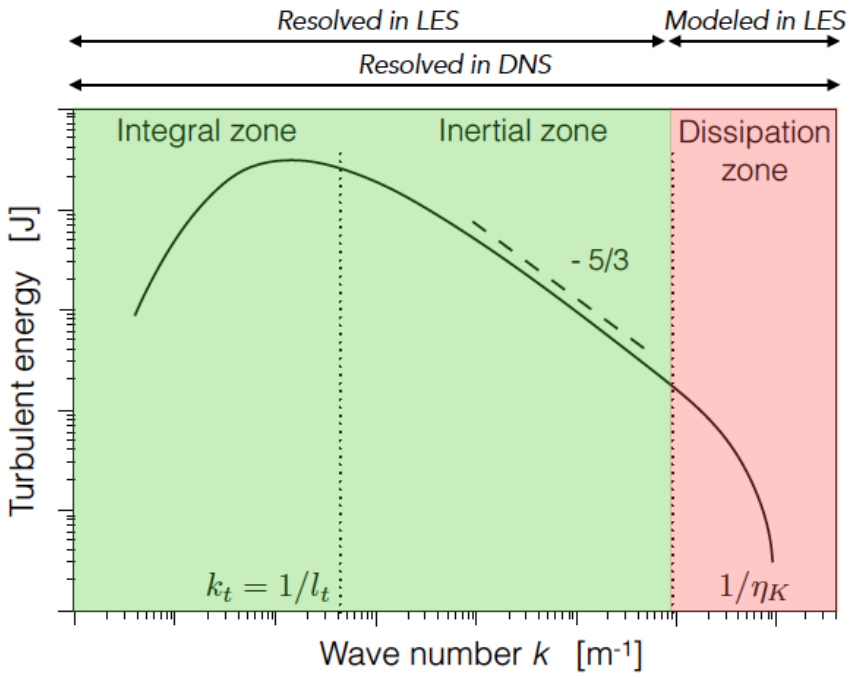

Figure 8.0.1: Sketch of the energy density spectrum $E(k)$ in homogeneous isotropic turbulence, showing the integral, inertial and dissipation zones. Adapted from [Felden, 2017].

velocity fluctuation, it can be found that $Re_T^{\frac{3}{4}} = \frac{l_T}{\eta_K}$, which prescribes the number of mesh points required by the DNS, taking n points in the Kolmogorov length scale, as $(nRe_T^{\frac{3}{4}})^3$. A rapid calculation indicates that this number becomes completely out of reach for practical 3D cases even at moderate Reynolds numbers and without chemical reactions. On the contrary, the Reynolds-Averaged approach (RANS) is very fast but by definition only resolves for the moments of the statistics and does not describe the true turbulent field.

The Large Eddy Simulation (LES) approach is intermediate in computational cost. By assuming a separation of scales, it filters out the smallest scales and only resolves the largest eddies contained in the integral and inertial zones. The dissipation zone indicated in Fig. 8.0.1 needs therefore to be modelled, but the more universal behaviour of the flow at these scales makes the modelling more simple than in RANS.

In this work, the simulations all use the LES approach, which is described in detail in the next section.

8.1 Governing equations of LES

In LES the separation of scales is obtained through a spatial filter applied to all flow variables. Although LES concepts and principle are derived with explicit filters [Sagaut, 1998] in practice the spatial filter is simply the grid. The smallest size flow structures are therefore the structures smaller than the grid resolution and are called *sub-grid scale* (sgs). Filtering the conservation equations of Section 1.6 leads to the equations described below with their sgs closure.

8.1.1 Filtered conservation equations

Details about the following formalism can be found in [Poinsot and Veynante, 2012].

For variable density problems a mass-weighted Favre filter is introduced as:

$$\tilde{f} = \frac{\overline{\rho f}}{\overline{\rho}} \tag{8.5}$$

where $\bar{\cdot}$ represents the spatial filter. This filtering leads to a decomposition of any quantity f in a filtered component $\tilde{f}$ and a sgs component noted f^{sgs} or f^T, respectively for sub-grid scale or turbulent, such as $f = \overline{f} + f^{sgs}$.

When applying this filtering to the mulit-species conservation equations of Section 1.6, the following system is obtained:

$$\frac{\partial \overline{\rho}}{\partial t} + \frac{\partial}{\partial x_i}(\overline{\rho}\tilde{u}_i) = 0 \tag{8.6}$$

$$\frac{\partial \overline{\rho}\tilde{u}_i}{\partial t} + \frac{\partial}{\partial x_i}(\overline{\rho}\tilde{u}_i\tilde{u}_j) = -\frac{\partial}{\partial x_i}(\tilde{P} - \overline{\tau_{ij}} - \overline{\tau_{ij}}^{sgs}) \tag{8.7}$$

$$\frac{\partial \overline{\rho}\tilde{Y_k}}{\partial t} + \frac{\partial \overline{\rho}(\tilde{u_i}\tilde{Y_k})}{\partial x_i} = -\frac{\partial}{\partial x_i}(\overline{J_{k,i}} + \overline{J_{k,i}}^{sgs}) + \overline{\dot{\omega}_k} \qquad i,j = 1, N_{dim}, k = 1, N_s \tag{8.8}$$

where $J_{i,k}$ is the species diffusive flux expressed with the Hirschfelder and Curtis approximation from Section 1.7.2 as $J_{k,i} = -\rho Y_k V_{k,i} = -\rho\left(\frac{W_k}{W} D_k \frac{\partial X_k}{\partial x_i} - Y_k V_i^c\right)$

$$\frac{\partial \overline{\rho}\tilde{E}}{\partial t} + \frac{\partial}{\partial x_i}\left(\overline{\rho}\tilde{E}u_i\right) = -\frac{\partial}{\partial x_i}\left(\overline{u_j\sigma_{ij}} + \overline{q_i} + \overline{q_i}^{sgs}\right) + \overline{\dot{Q}} \qquad i,j = 1, N_{dim}, k = 1, N_s \tag{8.9}$$

Filtered fluxes

The filtered fluxes appearing in the previous equations are approximated by calculating them from the filtered variables as follows:

$$\overline{\tau_{ij}} \approx -\frac{2}{3}\overline{\mu}\frac{\partial \tilde{u}_i}{\partial x_i}\delta_{ij} + \overline{\mu}\left(\frac{\partial \tilde{u}_i}{\partial x_j} + \frac{\partial \tilde{u}_j}{\partial x_i}\right) \tag{8.10}$$

with $\overline{\mu} \approx \mu(\tilde{T})$

$$\overline{J_{k,i}} = -\overline{\rho}\tilde{Y_k}\tilde{V_{k,i}} = -\overline{\rho}\left(\frac{W_k}{W}\overline{D_k}\frac{\partial \tilde{X_k}}{\partial x_i} - \tilde{Y_k}\tilde{V_i^c}\right) \tag{8.11}$$

with $\tilde{V_i^c} \approx \sum_{k=1}^{N_s} \frac{W_k}{W}\overline{D_k}\frac{\partial \tilde{X_k}}{\partial x_i}$

and $\overline{D_k} \approx \frac{\overline{\mu}}{\overline{\rho} Sc_k}$ in the context of simplified transport described in Section 1.7.3.

$$\overline{q_i} \approx -\overline{\lambda}\frac{\partial \tilde{T}}{\partial x_i} + \sum_{k=1}^{N_s} \overline{J_{k,i}}\tilde{h_{s,k}} \tag{8.12}$$

with $\overline{\lambda} \approx \frac{\overline{\mu}\overline{C_p}(\tilde{T})}{Pr}$ in the context of simplified transport described in Section 1.7.3.

Sub-grid scale fluxes

The sgs fluxes are unknown and require closure models describing their impact on the resolved scales.

The sgs momentum flux is modeled following the Bousinesq approxiation, i.e., introducing a sgs viscosity:

$$\overline{\tau_{ij}}^{sgs} = -\frac{2}{3}\overline{\rho}\nu^{sgs}\frac{\partial \tilde{u_i}}{\partial x_i}\delta_{ij} + \overline{\rho}\nu^{sgs}\left(\frac{\partial \tilde{u_i}}{\partial x_j} + \frac{\partial \tilde{u_j}}{\partial x_i}\right) \tag{8.13}$$

The expression of the sgs kinematic viscosity ν^{sgs} (also called turbulent viscosity) will be detailed in Section 8.1.2.

The sgs species fluxes follow the same approximation, introducing a turbulent Schmidt number:

$$\overline{J_{k,i}}^{sgs} = -\overline{\rho}\left(\frac{W_k}{W}\overline{D_k}^{sgs}\frac{\partial \tilde{X_k}}{\partial x_i} - \tilde{Y_k}V_i^{\tilde{c},sgs}\right) \tag{8.14}$$

where $V_i^{\tilde{c},sgs} = \sum_{k=1}^{N_s} \frac{W_k}{W} \overline{D_k}^{sgs} \frac{\partial \tilde{X}_k}{\partial x_i}$

and $\overline{D_k}^{sgs} = \frac{\nu^{sgs}}{Sc_k^{sgs}}$

The value of Sc_k^{sgs} is taken the same for all species k, equal to 0.6 in this work. It must be however noted that this value depends, in principle, on the turbulent flow and may vary even locally in the flow.

Finally the sgs energy flux is similarly modelled with a turbulent Prandtl number :

$$\overline{q_i}^{sgs} \approx -\lambda^{sgs} \frac{\partial \tilde{T}}{\partial x_i} + \sum_{k=1}^{N_s} \overline{J_{k,i}}^{sgs} \tilde{h_{s,k}} \tag{8.15}$$

where $\lambda^{sgs} = \frac{\bar{\rho} \nu^{sgs} \overline{C_p}(\tilde{T})}{Pr^s gs}$

Again Pr^{sgs} is taken constant equal to 0.6, which is an approximation of the same order as for the turbulent Schmidt numbers.

8.1.2 Turbulent viscosity

The turbulent viscosity ν^{sgs} present in the sub-grid scale fluxes needs a proper modelling in order to account for the energy transfer from small sgs scales to the largest scales.

The main models used in the AVBP solver are detailed below:

- The Smagorinsky model proposed in 1963 [Smagorinsky, 1963], expresses the turbulent viscosity based on a mixing-length analogy as:

$$\nu^{sgs} = (C_s \Delta) \sqrt{2 \tilde{S}_{ij} \tilde{S}_{ij}} \tag{8.16}$$

  where C_s is the model constant estimated from Kolmogorov spectrum, typically equal to 0.17, Δ is the characteristic filter size (equal to the cube-root of the cell volume for implicit grid filtering) and $\tilde{S}_{ij} = \frac{1}{2} \left(\frac{\partial \tilde{u_i}}{\partial x_j} + \frac{\partial \tilde{u_j}}{\partial x_i} \right)$.

This model supplies the right amount of kinetic energy dissipation in homogeneous isotropic turbulent. It is deemed to be too dissipative and not suited for transitional flows by [Germano et al., 1991]. It was extended into the so-called dynamic Smagorinsky (or Germano) model by introducing a dynamic evaluation of the C_s value of the model to no longer rely on user-input constant value. The procedure used to select this value is described in [Lilly, 1992].

- The WALE model proposed by [Nicoud and Ducros, 1999] writes the turbulent viscosity as:

$$\nu^{sgs} = (C_W \Delta)^2 \frac{(\mathcal{S}^d_{ij}\mathcal{S}^d_{ij})^{\frac{3}{2}}}{(\tilde{S}_{ij}\tilde{S}_{ij})^{\frac{5}{2}} + (\mathcal{S}^d_{ij}\mathcal{S}^d_{ij})^{\frac{5}{4}}} \tag{8.17}$$

with $\mathcal{S}^d_{ij} = \frac{1}{2}\left(\frac{\partial \tilde{u_i}}{\partial x_k}\frac{\partial \tilde{u_k}}{\partial x_j} + \frac{\partial \tilde{u_j}}{\partial x_k}\frac{\partial \tilde{u_k}}{\partial x_i}\right)$

where $C_W = 0.4929$ is the model constant. It was developed in order to recover the correct scaling laws in near-wall regions, which implies a decay with the distance to the solid boundary at the third power.

- The σ model, developed by [Nicoud et al., 2011], is based on the velocity gradient tensor $(\frac{\partial u_i}{\partial x_j})$ singular values $\sigma_1 \geq \sigma_2 \geq \sigma_3 \geq 0$. σ values are the square root of the eigenvalues of the matrix $\frac{\partial u_k}{\partial x_i}\frac{\partial u_k}{\partial x_j}$. For that model, the turbulent viscosity writes:

$$\nu^{sgs} = (C_\sigma \Delta)^2 \frac{\sigma_3 (\sigma_1 - \sigma_2)(\sigma_2 - \sigma_3)}{\sigma_1^2} \tag{8.18}$$

where $C_\sigma = 1.5$ the model constant. The objective of this model is to vanish in laminar flow conditions with non-zero velocity gradients, namely pure shear, solid rotation, and axisymmetric or isotropic expansions. It also displays the correct asymptotic behaviour in near-wall regions.

The characteristics of the models are summarised in Table 8.1.1. In this work, the σ model is employed as swirling flows tend to exhibit rotational structures making the Smagorinsky and WALE models possibly too dissipative.

	Smagorinsky	WALE	SIGMA
(Wall distance)^3 decay	No	Yes	Yes
Zero for solid rotation	Yes	No	Yes
Zero for pure shear	No	Yes	Yes
Zero for axisymmetric expansion	No	No	Yes
Zero for isotropic expansion	No	Yes	Yes

Table 8.1.1: Summary of the different turbulent viscosity models properties. Adapted from [Nicoud et al., 2011]

8.2 Turbulence-chemistry interaction

Similarly to laminar combustion introduced in Section 2.2, turbulent combustion regimes are different in premixed and non-premixed conditions. The interaction with turbulence is very different for these two types of flames and thus, different models are used for the filtered chemical mass and thermal source terms, $\overline{\dot{\omega}}_k$ and $\overline{\dot{Q}}$ respectively, appearing in Eqs. 8.8 and 8.9.

8.2.1 Turbulent premixed flames

The characteristic timescale τ_c of a premixed flame can be seen as the time required for the flame to propagate over its own diffusive thickness δ at its velocity s_l with:

$$\tau_c = \frac{\delta}{s_l} \tag{8.19}$$

When propagating in a turbulent flow, the flame interacts with the turbulent structures and the degree of interaction can be characterised with the ratio of characteristic timescales. As turbulence introduces a range of timescales, from the integral scale $\tau_T = \frac{l_T}{u_T}$ to the Kolmogorov scale $\tau_K = \frac{\eta_K}{u_K}$, two extreme timescale ratios may be written which are the Damköhler number Da and the Karlovitz number Ka :

$$Da = \frac{\tau_T}{\tau_c} = \frac{l_T s_l}{u_T \delta} \tag{8.20}$$

$$Ka = \frac{\tau_c}{\tau_K} = \frac{\eta_K s_l}{u_K \delta} \tag{8.21}$$

By making the assumption of unity Prandtl number (equal momentum and thermal diffusivity), giving $\delta s_l \approx \nu$, and using Eq. 8.2, the Karlovitz number can be expressed as:

$$Ka = \left(\frac{u_T}{s_l}\right)^{\frac{3}{2}} \left(\frac{l_T}{\delta}\right)^{\frac{-1}{2}} \tag{8.22}$$

Note that he turbulent Reynolds number can also be expressed as:

$$Re_T = \frac{u_T l_T}{s_l \delta} \tag{8.23}$$

From a qualitative analysis of the Damköhler and Karlovitz numbers, several flame regimes can be identified [Poinsot and Veynante, 2012]:

- When $Ka < 1$ (and subsequently $Da > 1$ as $\tau_T > \tau_K$), the flame thickness is smaller than the smallest turbulent structure. In this regime, called *thin flame* or *flamelet* regime, the flame front has a thin structure comparable to a laminar flame and is wrinkled by the turbulence. Depending on the ratio between the characteristic turbulent velocity u_T and the laminar flame speed s_l, two regions can be identified in this regime; if $u_T > s_l$ the flame is strongly wrinkled with local detachment of pockets of fresh or burnt gases, this regime is called *corrugated flame* regime. On the contrary, if $u_T < s_l$, the weaker flame front wrinkling does not alter the flame structure and the regime is called *wrinkled flame* regime.

- When $Ka > 1$ and $Da > 1$ ($\tau_K < \tau_c < \tau_T$), the small eddies penetrate into the preheat and reaction zones of the flame which is thickened under their action. This regime is referred to as the *thickened flame* regime.

- When $Da < 1$, the turbulence has an overall characteristic timescale smaller than the chemistry. The largest eddies induce a fast mixing and the flame locally behaves as a perfectly stirred reactor ($Da << 1$ limit)

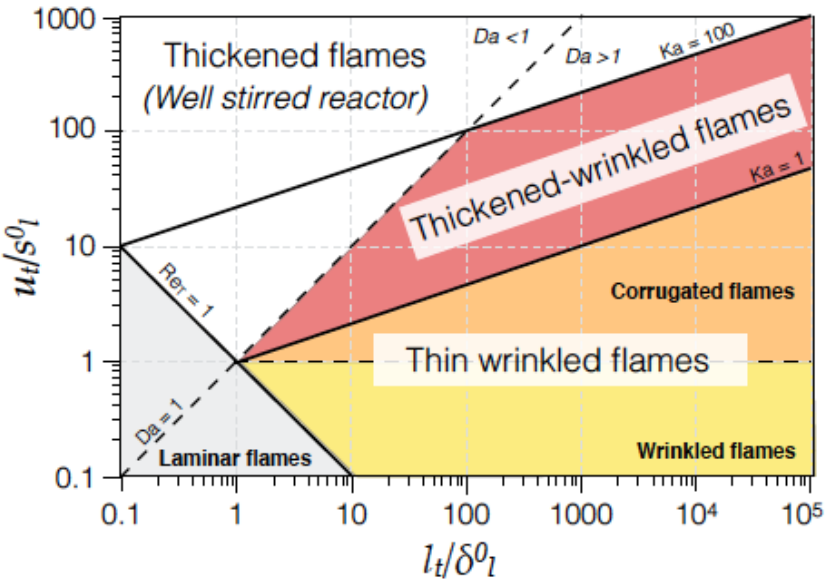

Figure 8.2.1: Turbulent combustion regimes in terms of length and velocity scales, [Felden, 2018] adapted from [Borghi, 1988] [Peters, 1999]

The aforementioned regimes are displayed on the Borghi diagram [Borghi, 1988] constructed with $\frac{l_T}{\delta}$ and $\frac{u_T}{s_l}$ as coordinates and shown in Fig. 8.2.1.

8.2.2 Turbulent diffusion flames

Diffusion flames being very sensitive to the local flow conditions, and more precisely to the local strain rate, the Damköhler number Da_{fl} uses the inverse of the strain rate as the flow timescale:

$$Da_{fl} = \frac{\tau_f}{\tau_c} \tag{8.24}$$

with $\tau_f = \frac{1}{\chi_{st}}$ where χ_{st} is the scalar dissipation rate of a passive scalar calculated at stoichiometry. Note that in the case of non-unity Lewis number, and/or different species Schmidt numbers, the mixture fraction can not be directly used as a passive scalar and other definitions must be used [Cuenot and Poinsot, 1994].

[Cuenot and Poinsot, 1994] identified this Damköhler number as an indicator of the flamelet regime, which is obtained for fast chemistry and/or small scalar dissipation rate. As such, several regimes separated by several transitional values of the Damköhler number were identified:

- In the high-Damköhler flamelet regime characterized by $Da^{fl} > Da^{LFA}$ with LFA standing for Laminar Flamelet Assumption, the flame is very thin and fast compared to the flow scales and is not perturbed by the turbulence, which only wrinkles the flame front.
- When the Damköhler number decreases, the flame becomes less resistant to strain and quenching finally occurs at the limit value Da^{ext}.
- Finally, in between the two above regimes, the flame inner structure is modified by the strain but keeps burning.

These regimes can be represented in a diagram similar to the one for turbulent premixed combustion using this time the Damköhler and turbulent Reynolds numbers as coordinates and shown in Fig. 8.2.2.

8.2.3 Turbulent combustion models

From the categorisation of premixed and non-premixed turbulent regimes, many models have been derived considering a sufficiently high Damköhler number in order to fall under the flamelet assumption which is believed to be the case for most combustion applications. An extensive review of the turbulent combustion modelling has been done by [Veynante and Vervisch, 2002b].

models such as the Eddy Dissipation Model (EDM) of [Magnussen and Hjertager, 1977] postulates that the local state of the turbulence will induce a rate limiting phenomenon through molecular mixing. Despite being valid for both premixed and non-premixed conditions, its use in the LES community stays limited. Another type of models is the level-set methods stemming from the G-equation proposed by [Spellman and Spellman, 2020] reformulated for LES by [Pitsch and De Lageneste, 2002]. The G-equation describes the motion of an iso-scalar surface separating fresh and burnt gases. This formulation improved by [Moureau et al., 2009] is valid over

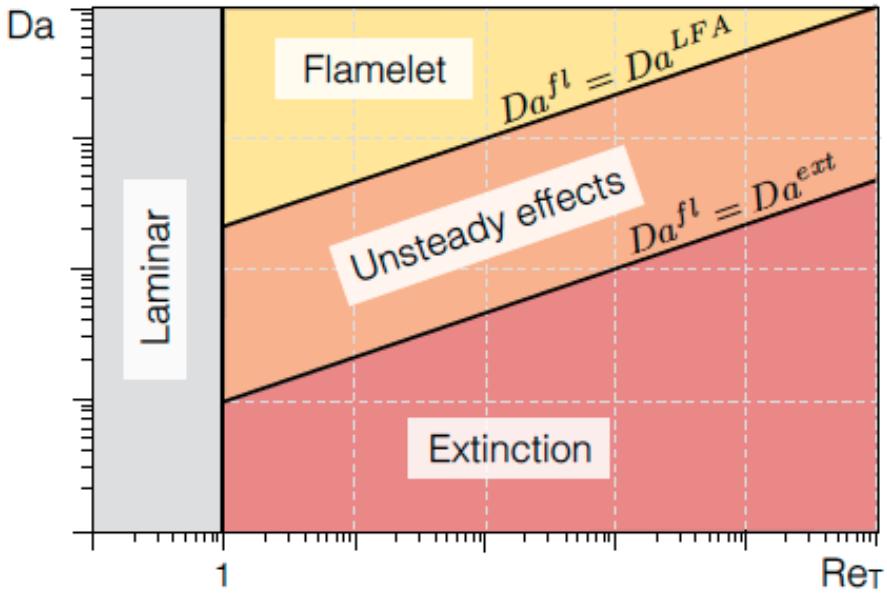

Figure 8.2.2: Turbulent combustion regimes in terms of Damköhler and turbulent Reynolds numbers, [Felden, 2018] adapted from [Cuenot and Poinsot, 1994] [Veynante and Vervisch, 2002a]

thin wrinkled flames and thickened-wrinkled flames regimes. However, probably due to a complex formulation requiring to solve simultaneously for the flame structure, it stays marginally used in LES.

The flame-turbulence interaction may be described with a statistical approach, introducing a Probability Density Function (PDF) to describe the variable statistics. A review of the use of PDF methods and the determination of probability density functions can be found in [Haworth, 2010]. In the context of LES, PDFs are used similarly to describe the sgs statistics.

The methodology retained in this work is based on the approach proposed by [Butler and O'Rourke, 1977] which is to consider a flame thicker than the actual one so that enough grid points discretise the flame front while keeping the correct laminar flame speed. This method is supposedly valid over the whole premixed combustion regime diagram. The sgs turbulence-chemistry interaction is modeled by estimating the sub-grid wrinkling and by correcting the filtered quantities $\overline{\dot{\omega}}_k$ and $\overline{\dot{Q}}$ accordingly.

This PhD thesis will use the Dynamically Thickened Flame model for LES (DTFLES) formulated by [Colin et al., 2000] [Legier et al., 2000a] for modelling turbulent premixed combustion. With the sensor developed by [Rochette et al., 2020], the model is able to deactivate when the combustion is identified as non-premixed. Indeed it is suggested in [Cuenot and Riber, 2017] that non-premixed flames adapt to the local mesh size and therefore do not need additional artificial thickening. However, the under-resolution of the flame thermal thickness leads to an over-estimation of the flame consumption speed and the sgs contribution is omitted. Work is currently ongoing on this topic and it will be checked in the solutions that non-premixed combustion is not a significant part of the flame. This approach has been successfully employed for partially premixed configurations over the last decades and in recent works [Jaravel, 2016][Felden, 2017][Collin, 2019b]. Details about its implementation into the LES solver AVBP are provided hereafter.

The Thickened Flame model for LES (TFLES)

The objective of this method is to broaden the flame front to allow a sufficient resolution on an LES mesh (typically 10 grid points in the flame front for ARCs). To yield the correct behaviour, the thickened flame must keep the same laminar flame speed as the original one.

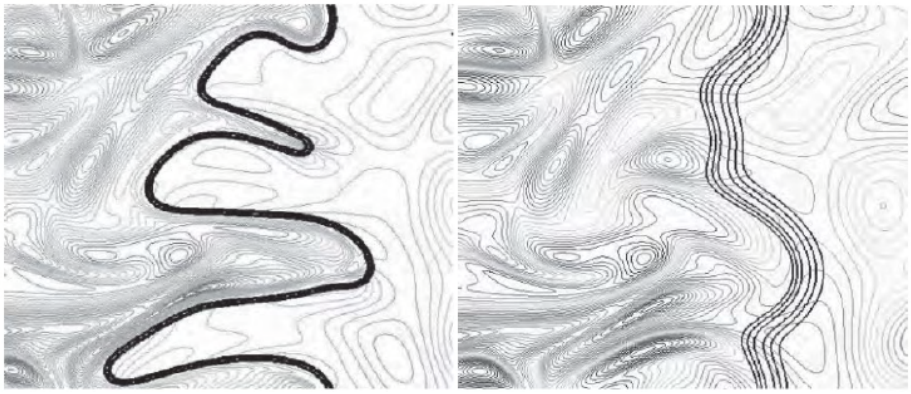

Figure 8.2.3: DNS of flame/vortex interactions. Left: non-thickened flame, right: thickened flame. From [Angelberger et al., 1998][Colin et al., 2000]

The reaction zone is thickened by applying a thickening factor $\mathcal{F}$ to the net production rates of the species as:

$$\dot{\omega}_k \rightarrow \frac{\dot{\omega}_k}{\mathcal{F}} \tag{8.25}$$

From asymptotic analysis [Poinsot and Veynante, 2012], the laminar flame speed s_l can be expressed as:

$$s_l \propto \frac{D_{th}}{\delta} \tag{8.26}$$

To ensure that the thickened flame laminar flame speed remains intact, the thermal and species diffusivities must be multiplied by the same thickening factor $\mathcal{F}$:

$$D_k \rightarrow \mathcal{F} D_k \quad D_{th} \rightarrow \mathcal{F} D_{th} \tag{8.27}$$

With these transformations, the gradients across the flame are decreased and broadened species profiles can be safely computed on a coarse grid. Note that the maximum values of the source terms are lowered but the integrals across the flame remain unchanged, hence the unchanged flame speed.

The efficiency function

From Fig. 8.2.3, it is clear that part of the flame surface area is lost by two effects : the thickened flame front is less wrinkled by the resolved flow structures than the thin flame, and the unresolved subgrid-scale flame wrinkling is missing. To recover the correct flame surface area, an efficiency function ϵ is applied so that:

$$s_l \rightarrow \epsilon s_l \tag{8.28}$$

In the code, this model is implemented as:

$$\dot{\omega}_k \rightarrow \frac{\dot{\omega}_k \epsilon}{\mathcal{F}} \tag{8.29}$$

and

$$D_k \rightarrow \mathcal{F}\epsilon D_k \quad D_{th} \rightarrow \mathcal{F}\epsilon D_{th} \tag{8.30}$$

The efficiency function ϵ is defined as the ratio between the unthickened flame thermal thickness δ and the thickened flame thermal thickness $\mathcal{F}\delta$ as:

$$\epsilon = \frac{\Xi(\delta)}{\Xi(\mathcal{F}\delta)} \tag{8.31}$$

From [Colin et al., 2000], the efficiency function relies on the assumption of equilibrium between the turbulence and the sub-grid flame surface and the evolution of the velocity fluctuations at the filter scale u'_Δ, determined with a similarity assumption removing the dilatational part of the velocity field.

The model for efficiency employed in this work, is the one from [Charlette et al., 2002] (referred as the Charlette model in the following) giving a power-law wrinkling law extending the one from [Colin et al., 2000].

The wrinkling factor Ξ writes:

$$\Xi(\delta_l) = \left(1 + min\left[\frac{\Delta_e}{\delta_l}\Gamma\left(\frac{\Delta_e}{\delta_l}, \frac{u'_{\Delta_e}}{S_l}, Re_{\Delta_e}\right)\right]\right)^{\beta} \tag{8.32}$$

where Γ is a function taking into account the sub-grid scale strain rate of all length scales smaller than Δ and $\beta = 0.5$ is a model constant parameter. This value β can also be retrieve dynamically with the Power-Law Dynamic Model from [Charlette et al., 2002].

The Dynamically Thickened Flame model for LES (DTFLES)

The thickened flame model was initially developed in the context of perfectly premixed flames which allows to apply the thickening factor on the entire domain. However, in most practical configurations reactants are not premixed prior injection and the modified species and thermal diffusivities may alter the mixing process in non-reactive zones. To cope with this problem, [Legier et al., 2000b] developed a dynamic version of the thickened flame model called Dynamically Thickened Flame model for LES (DTFLES) which applies thickening only at the flame location using a flame sensor.

The local thickening factor is defined as:

$$\mathcal{F}(x) = 1 + (\mathcal{F}_{max} - 1)S(x) \tag{8.33}$$

where $\mathcal{F}_{max}$ is the maximum thickening factor applied to the flame, estimated as a function of the cell size Δ as:

$$\mathcal{F}_{max} = \frac{N_c\Delta}{\delta} \tag{8.34}$$

with N_c the number of points in the thermal thickness, prescribed by the user.

$S(x)$ is the flame sensor based on the reaction rate expressed as:

$$S = tanh\left(C_1\frac{\Omega}{\Omega_0}e^{(1-C_2)\frac{E_a}{RT}}\right) \tag{8.35}$$

where C_1 and C_2 are model constants, Ω the modified reaction rate of a characteristic reaction and Ω_0 its maximum value computed from reference laminar premixed flames.

The above formulation of the sensor is difficult to adapt to ARC mechanisms where no single characteristic reaction can be identified. The methodology has been adapted in the PhD of [Jaravel et al., 2017b] where the sensor is based on the fuel consumption rate instead of a specific reaction and is expressed as:

$$S = max\left[min\left(2\mathcal{F}_{max}\frac{|\dot{\omega}_F|}{|\dot{\omega}_{F,0}|}, 0\right)\right] \tag{8.36}$$

Despite being adapted to ARC, this formulation still requires an estimation from a laminar flame canonical computation of $\dot{\omega}_{F,0}$. Determining a representative canonical flame may prove difficult in a context of strong mixing inhomogeneities which may appear for example in spray flames, or when dealing with preferential evaporation or preferential diffusion of multi-component fuels which are specifically the subject of the current work.

Generic flame sensor

A recent formulation called the Generic flame sensor was developed by [Rochette et al., 2020] with the objective of freeing the flame sensor from the need of user input parameters difficult to determine. The flame is detected by a geometrical shape analysis of any function f describing the chemical activity, taken here as the heat release rate, making the procedure independent of both the flame conditions and chemical kinetics modelling.

The algorithm uses the eigenvalues of the Hessian matrix of the chosen function f, defined as $H_{ij} = \frac{\partial^2 f}{\partial x_i \partial x_j}$, to identify local extrema in the f field. A geometrical flame front is then detected as sketched in Fig. 8.2.4.

With this formulation, the only input parameter is the number of grid points required in the thermal thickness N_c which, based on previous works is here fixed to a value of 6. Further details regarding the implementation of the method in the LES solver AVBP can be found in [Rochette et al., 2020].

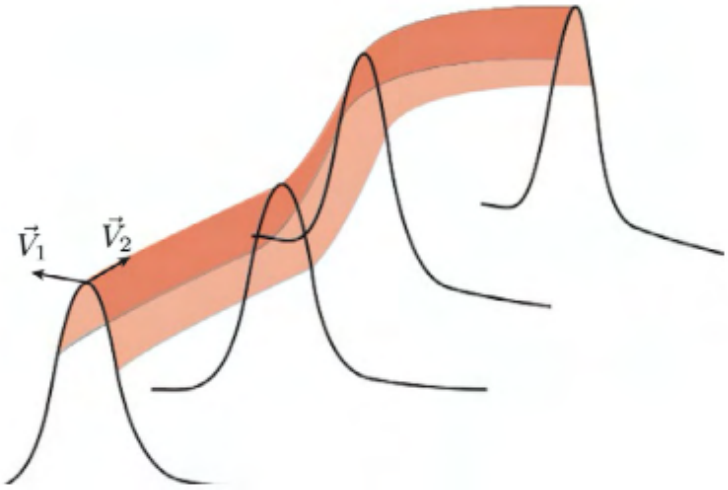

Figure 8.2.4: Sketch representing the detection of the chosen function local maximum. From [Rochette et al., 2020]

8.3 The AVBP solver

The development of the LES solver AVBP has been initiated more than twenty years ago by [Schønfeld and Rudgyard, 1999]. This code was developed to be efficient on unstructured grids in order to handle complex geometries and has grown to become massively parallel, solving the fully compressible Navier-Stokes equations. The main numerical features of AVBP have been presented in detail in the PhD thesis of [Lamarque, 2007]. The boundary conditions are based on the NSCBC formalism [Poinsot and Lele, 1992]. The numerical scheme for diffusive fluxes used in this work is a 2^{nd} order scheme in space and two schemes are used for the space and time discretization of the convective fluxes:

- The Lax-Wendroff (LW) scheme adapted from [Lax and Wendroff, 1960] to the cell-vertex method. It consists in a 2^{nd} order finite-volume centered scheme both in time and space using an explicit time integration with a single Runge-Kutta step.
- The Two-step Taylor Galerkin (TTGC) scheme developed by [Colin and Rudgyard, 2000]. It is a finite-element scheme with an explicit integration in time, 3^{rd} order accurate in space and time and specifically built for LES.

The stability of the centred numerical schemes is ensured by an artificial viscosity operator.

8.4 Integration of stiff chemistry

As previously emphasised, the reduced combustion chemistry stays stiff with small chemical timescales even after the quasi-steady state assumption. The flow timescale dictated by the CFL number for a typical LES computation with explicit time integraion (even when considering the acoustic CFL number based on the sound celerity) does not go below $dt = 1e^{-8}$ seconds. The explicit integration of chemistry leads to a species mass variation of $\dot{\omega}_k * dt$, which may be much larger than the available amount of the species k and result in negative mass fractions. To avoid this, dt must be decreased until no over-consumption is observed, which considerably increases the computational cost.

In order to run a reactive flow simulation at the CFL timestep, [Blanchard et al., 2021] developed a semi-implicit integration method called exponential method. It is similar to the semi-implicit approach of ODEPIM **??** introducing a more accurate estimation of the species mass fraction prediction.

The chemical source term $\dot{c}_k = \frac{\dot{\omega}_k}{W_k}$ can be written from Eqs. 1.19 and 1.20 as:

$$\dot{c}_k = \frac{Destruction_k}{c_k} c_k + Creation_k \tag{8.37}$$

This equation is rewritten with $\frac{Destruction_k}{c_k} = A_k$ and $Creation_k = B_k$ as:

$$\dot{c}_k = A_k c_k + B_k \tag{8.38}$$

At iteration n, A_k and B_k depend on the local thermodynamic state and some species j different from species k. It is assumed that the species k is of the order 1 in all reactions where it is consumed. This is indeed the case for most elementary reactions of an ARC scheme.

Integrating Eq. 8.38 is then easily found to give at iteration $n + 1$:

$$c_k^{n+1} = \left(c_k^n + \frac{B_k^n}{A_k^n} \right) e^{A_k^n dt} - \frac{B_k^n}{A_k^n} \tag{8.39}$$

From there:

$$\dot{c}_k = \frac{c_k^{n+1} - c_k^n}{dt} \tag{8.40}$$

This formulation ensures the positivity of the species mass fractions for any value of the source terms and for any time step. However it does not ensure the atom conservation which must be enforced by a correction step. The atomic excess (or deficit) is quantified as $dn_e = \sum_k^{N_s} (c_k^{n+1} - c_k) n_{e,k}$ for each element and is dispatched over the most prominent species containing these atoms.

Advantages of using this method have been demonstrated on laminar and turbulent diffusion flames for methane/oxygen combustion in rocket engine conditions [Blanchard et al., 2021]. It must be noted that despite increasing drastically the robustness of the chemical integration, the correct evaluation of the chemical source term stays dependent of the time step used for the computation. For transient processes where the stiff timescales of the chemistry play an important role, the increase of the time step should be considered with care.

Chapter 9

Application to the VALOGAZ test rig

Contents

As stressed in the previous sections, the prediction of the impact of hydrogen enrichment on hydrocarbon/air flames is critical for further development of this tech-

nology. In this work, the VALOGAZ test rig built and measured at EM2C laboratory has been selected as a test case for the assessment of the current ARC performances.

9.1 Experimental setup and results

9.1.1 Experimental setup

The VALOGAZ test rig studied at EM2C laboratory has been the subject of several publications in the past few years [Guiberti et al., 2015a][Mercier et al., 2016]. This burner consists of a rectangular combustion chamber with quartz windows on each face and metal rods on each corner. This injection system takes a premixed mixture of any blend of methane and hydrogen with air that flows inside a changeable swirler. The premixed reactants exiting the swirler go into a tube inside which a metal rod can be found that ends 2 mm after the combustion chambers starts. The experimental apparatus is represented in Fig. 9.1.1.

The operating points of interest in this study are the ones described in [Mercier et al., 2016] which are related to two levels of enrichment: 40% methane / 60% hydrogen corresponding to a moderate enrichment case and referred to in the following as **60% case**, and 10% methane / 90% hydrogen corresponding to a heavy enrichment case and referred to in the following as **90% case**. Both fuel blends are mixed with air to obtain a premixed mixture at an equivalence ratio of 0.7.

Cold flow measurements were performed by replacing the premixed gases by only air and the velocities were obtained via Particle Imagery Velocity (PIV) measurements.

In all three cases, (Cold flow; 60% case and 90% case) the inlet mass flow rate was prescribed to ensure the same bulk velocity at the exit of the injection tube of $U\_bulk = 14m.s^{-1}$.

For the 60% case, temperature measurements were performed at the locations indicated on Fig. 9.1.2. The vertical steel bars temperature on the corners of the combustion chamber (red in Fig. 9.1.2) were measured between z = 16 mm and z = 56 mm and feature a linear increase with the distance to the dump plate from T = 593 K to T = 637 K. These temperatures were measured by thermocouples. From

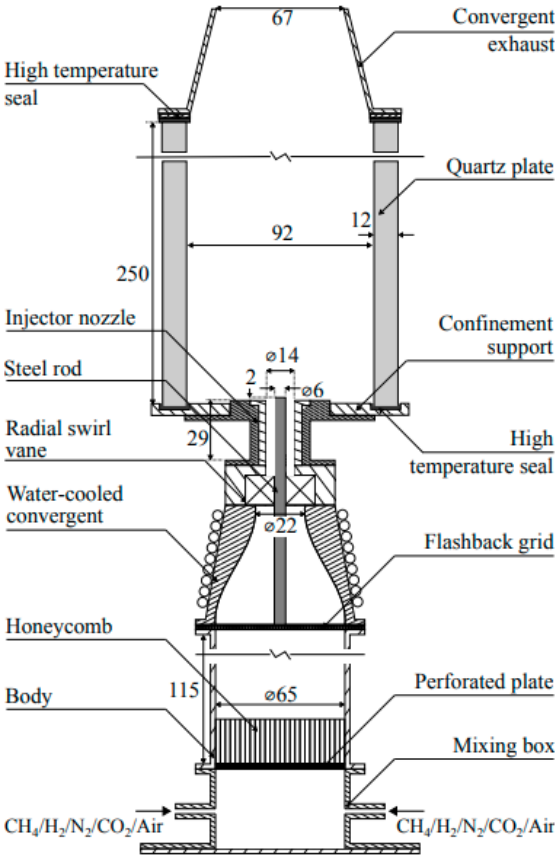

Figure 9.1.1: Schematic of the experimental VALOGAZ burner. From [Guiberti et al., 2015b]

Laser Induced Phosphorescence (LIP) measurements (blue in Fig. 9.1.2), the central rod has been found to have a constant temperature of 500 K. The temperature of the disk around the injector increases linearly with the radius from T = 435 K at r = 7 mm to T = 516 K at z = 25 mm. Finally, the temperature measurements on the quartz window are presented in Fig. 9.1.3.

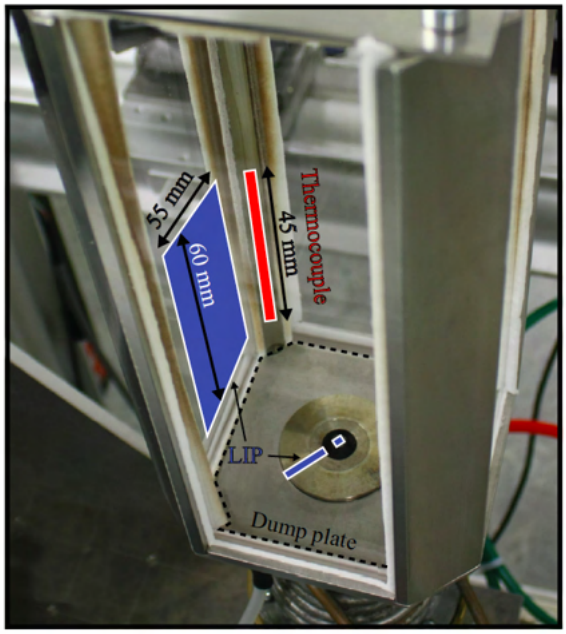

Figure 9.1.2: Photograph of the VALOGAZ combustion chamber showing the location of the temperature measurements. From [Mercier et al., 2016]

9.1.2 Experimental results

The main result emerging from this configuration, described in details in [Guiberti et al., 2015b] and [Mercier et al., 2016], is a transition from a V-shaped flame to an M-shaped flame when increasing the hydrogen enrichment. Figure 9.1.4 shows the normalised Abel deconvoluted OH^* chemiluminescence signal and the mean binarised OH-Planar Laser Induced Fluorescence (PLIF) extracted from measurements for both the 60% case and the 90% case.

At EM2C, a numerical study has been conducted within the PhD of R. Mercier [Mercier et al., 2014] with the low-Mach LES solver YALES2 developped at CORIA [Moureau et al., 2011] together with the F-TACLES model [Fiorina et al., 2010] for subgrid flame-turbulence interaction adapted to account for heat losses. It was found that the transition from a V-shaped flame to an M-flame shape is not retrieved when assuming adiabatic walls. Indeed in this case, an M-shaped flame is found whatever the hydrogen enrichment. Consequently, the V-shaped flame present in the 60% case is due to the extinction of the outer flame branch because of heat

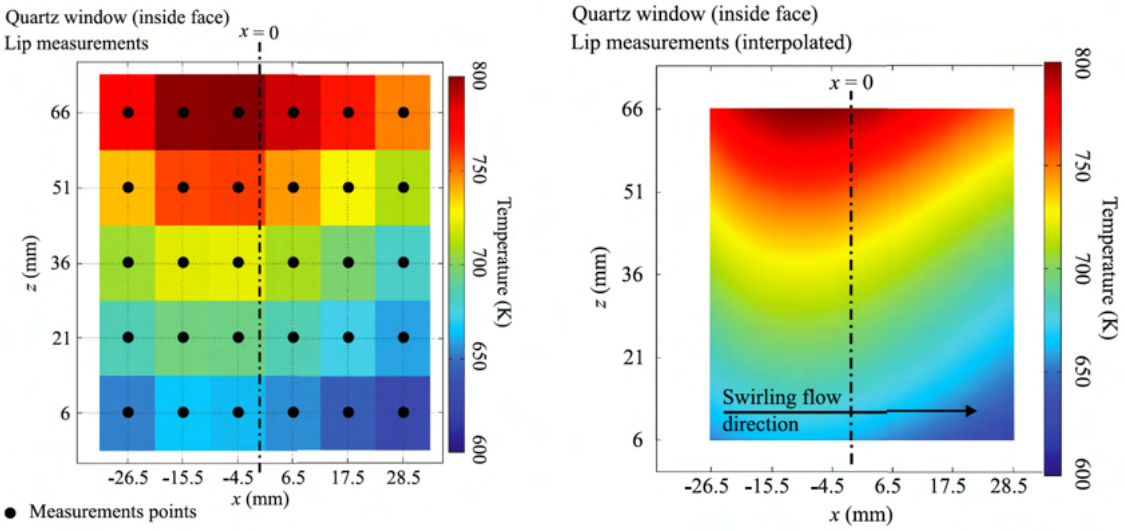

(a) LIP measurements (b) Linearly interpolated LIP measurements

Figure 9.1.3: Measured temperature at the inner surface of the quartz window for the 60% case. From [Mercier et al., 2016]

losses. Moreover from the experiments, it appears that the V-shape is also well defined with a zero probability of having an outer flame branch. However, this probability was not found to be zero in the numerical simulations performed using YALES2. The authors imputed this prediction error to the F-TACLES model that does not explicitly include the effect of local strain rate and the heat losses in the wrinkling modelling.

Because those two effects are intrinsically taken into account using ARC coupled to the DTFLES model, the present work aims to analyze more in details the effect of hydrogen enrichment on the flame shape transition.

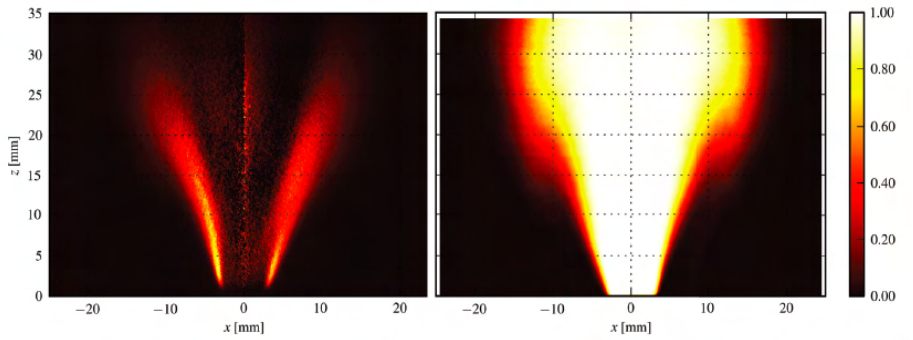

(a) 60% case

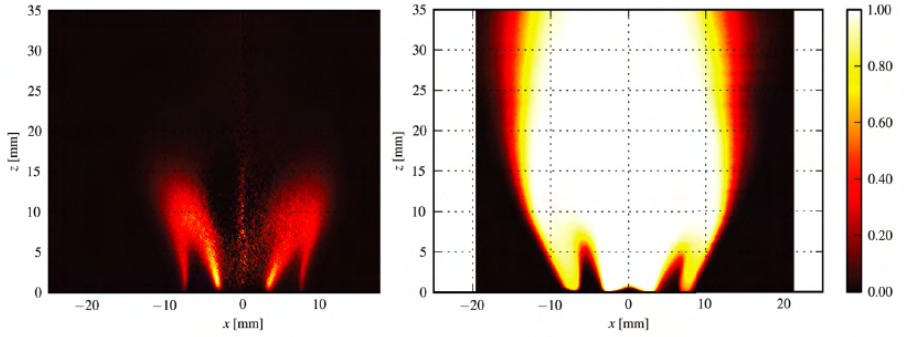

(b) 90% case

Figure 9.1.4: Left: normalised Abel deconvoluted OH* chemiluminescence signal. Right: mean binarised OH-PLIF. From [Mercier et al., 2016]

9.2 Numerical setup

9.2.1 Numerical models

The 60% case and the 90% cases previously described will be simulated using the LES solver AVBP using the Lax-Wendroff convection scheme (8.3) with the Cazères29 ARC mechanism derived in Section 7.4. Moreover, LES are performed with the exponential integration methodology (8.38) and the DTFLES using the Charlette efficiency function 8.2.3 based on the generic sensor (8.2.3). The sgs turbulence is modelled by the σ model (8.1.2) and the simplified transport model described in Section 1.7.3 is employed.

Laminar flame speed $[m.s^{-1}]$	Detailed mechanism	ARC	Error (%)
Without Soret effect	0.595	0.594	0.1
With Soret effect	0.576	0.576	0
Error (%)	3.2	3.0	

(a) 60% case

Laminar flame speed $[m.s^{-1}]$	Detailed mechanism	ARC	Error (%)
Without Soret effect	0.726	0.718	1.1
With Soret effect	0.661	0.659	0.3
Error (%)	9.8	8.2	

(b) 90% case

Table 9.2.1: Laminar flame speed values for (a) the 60% case and (b) the 90% case 1D premixed laminar flames depending on the Soret effect and varying the chemical scheme.

9.2.2 Transport model

The chemical scheme reduction has been performed using the mixture averaged assumption for the diffusion coefficients of the species described in Section 1.7. As discussed in Section 1.7, the Soret effect is by default deactivated. However, because of the high hydrogen content of the blend in the two operating cases studied, this effect is not negligible in the two cases studied here. As an illustration on the two laminar 1D premixed flames representative of the present study i.e. T = 300K, P = 1bar, $\phi = 0.7$, and $X_{H_2} = 0.6$ and 0.9, the over-prediction of the laminar flame speed due to the mixture averaged assumption is 3.2 and 9.8% respectively.

As expected, the reduced mechanism validity remains when changing the transport modelling with marginally better results when accouting for the Soret effect as illustrated in Tab. 9.2.1.

In order to keep an accurate description of the transport, the Schmidt numbers and the Prandtl number required for the simplified transport description used in AVBP are extracted from the 2 representative laminar premixed flames with the multi-component diffusion coefficients and the Soret effect enabled. The change in computed coefficients is displayed in Tab. 9.2.2. In order to account for the Soret effect, the thermal diffusivity, represented by the Prandtl number, is decreased while

	Without Soret effect	With Soret effect
Prandtl	0.654	0.691
Schmidt CH4	0.727	0.688
Schmidt H2	0.213	0.202
Schmidt N2	0.818	0.742
Schmidt O2	0.768	0.755
Schmidt O	0.492	0.507
Schmidt OH	0.497	0.516

Table 9.2.2: Schmidt and Prandtl numbers of the main species obtained with optimisation on the flames with the mixture-averaged transport model compared to the ones obtained with the multi-component transport model with the Soret effect.

Laminar flame speed error [%]	Without Soret effect	With Soret effect
60% case	3.0	1.7
90% case	5.4	0.3

Table 9.2.3: Error on laminar flame speed between the flames computed with the detailed mechanism and Soret effect enabled and the ones computed with ARC mechanism optimised without and with Soret effect enabled.

the main species diffusivity is increased resulting in a wider reaction zone. It can be noted that the diffusivity of the radical species O and OH is slightly decreased.

For these two representative cases, the optimisation of the Schmidt and Prandtl numbers on the cases with Soret effect enabled allows a reasonable error on the prediction of the laminar flame speeds when using a simplified transport.

9.2.3 Numerical domain

In order to save computational time, the swirler is not computed and an inlet velocity profile with injection of isotropic turbulence set with a 10% velocity fluctuation compared to the inlet axial velocity is prescribed similarly as in [Mercier et al., 2014]. The numerical domain is represented in red in Fig. 9.2.1

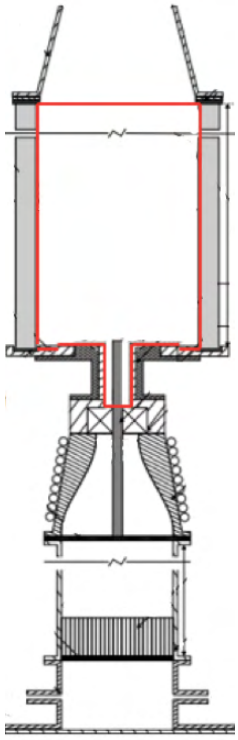

Figure 9.2.1: Schematic of the experimental setup with numerical domain represented in red.

The numerical domain is discretised with an unstructured mesh composed of 45.358.966 tetrahedrons and 7.815.406 nodes with an increasing cell size towards the outlet. The flame zone has been specifically refined to a characteristic mesh size of the order of 50 μm in order to sufficiently resolve the flame without requiring a strong thickening factor. From laminar premixed 1D cases, the thermal thicknesses of the 60% and 90% cases are respectively 442.8 and 348 μm. Thus, 9 and 7 points respectively are used to describe the thermal thickness. The grid size is displayed in Fig. 9.2.2.

9.2.4 Boundary conditions

The experimental volume flow rate imposed at the computational domain inlet is retrieved from the experimental profiles available at the location $z = 2mm$,. This

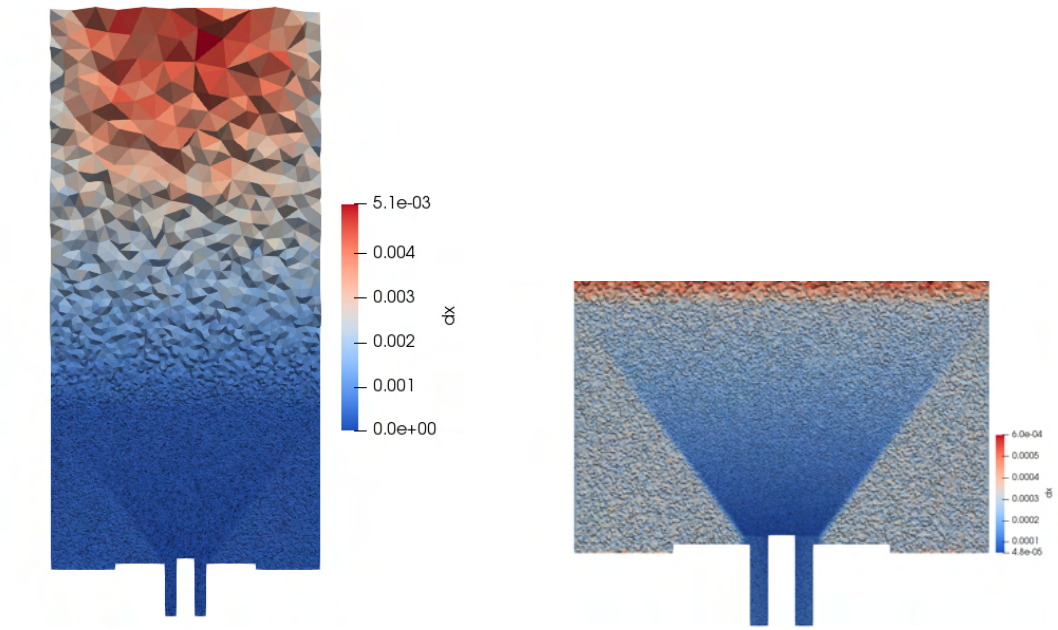

(a) Full domain (b) Zoom on the supposed flame location

Figure 9.2.2: Grid size δ_x on the central vertical slice of the domain

volume flow rate is $1.66e^{-3}m^3/s$. The radial and ortho-radial velocity profiles extracted from the experiment at $z = 2mm$ are moreover super-imposed at the inlet. Then, the bulk velocity at the computational domain inlet is computed and equal to $13.22m.s^{-1}$. Depending on the studied case, only the composition of the inlet flow is varied (pure air, 60% case conditions or 90% conditions) while keeping a constant volumetric flow rate and the same velocity profiles. At the outlet of the computational domain, atmospheric pressure is prescribed. Furthermore, the wall temperature measurements are imposed on the computational domain walls as isothermal boundary conditions. Because the measurements do not cover the entire chamber, the results are extrapolated to the unmeasured areas.

On the quartz wall, the interpolating function is extended sideways and towards the bottom while the maximum temperature on top is extended to the outlet to avoid absurd values from interpolation. The linear evolution of the corner steel bars is applied along its whole length. The temperature profiles from the inside of the chamber can be visualised in Fig. 9.2.3a. On the bottom of the chamber, the linear evolution of the temperature is simply extended to the unmeasured regions and can

be seen on Fig. 9.2.3b.

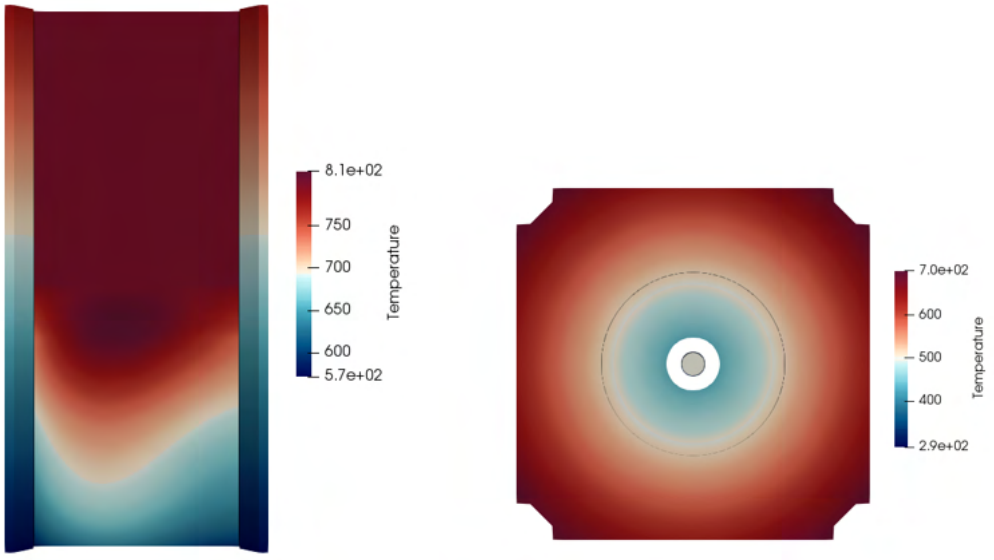

(a) Chamber side (b) Chamber bottom

Figure 9.2.3: Thermal boundary condition on (a) one of the quartz wall and the 2 adjacent vertical steel bars as seen from the inside of the combustion chamber and (b) the bottom of the combustion chamber as seen from the inside.

Finally, to avoid a too high gradient from the transition from 293 K to 500 K between the central rod side and its tip, a linear transition between these values is applied near the tip small enough to avoid preheating the inlet mixture.

The prescribed isothermal boundary conditions correspond to the 60% case as none were available for the 90% case, and will be applied on both reactive cases. The adiabatic temperature of the 90% enrichment mixture being higher than the 60% enrichment mixture (respectively 1890K and 1963K), one can expect higher temperatures on the boundary conditions and this approximation must be kept in mind while analysing the results in the 90% case.

9.3 Cold flow validation

The non-reactive flow with air only injected is first compared to the experimental PIV measurements.

The swirl number, representing the ratio between the axial and the ortho-radial momentum fluxes, is computed with the formula given by [Gupta et al., 1984] which read:

$$S = \frac{\int_{r_{min}}^{r_{max}} uvr^2 dr}{r_{max} \int_{r_{min}}^{r_{max}} u^2 r dr} \tag{9.1}$$

where r is the radius, u the axial velocity, v the ortho-radial velocity and r_{min} and r_{max} are the integration bounds. In the VALOGAZ test rig, the injection tube is a hollow cylinder thus r_{min} is taken as the inner radius $3e^{-3}$m and r_{max} as the outer radius $7e^{-3}$m.

The experimentalists give a swirl number based on geometrical considerations of 0.33. When computing the swirl number with the previous formula on the experimental velocity profiles provided at 2mm from the dump plane, a swirl number of 0.31 was found. The same swirl number of 0.31 was also found when performing the same computation on the profiles given by the LES.

Comparing the time-averaged axial velocity fields taken on the central plane of the domain, the experimental and the numerical results are in reasonable agreement. The Inner Recirculation Zone (IRZ) located at the tip of the bluff body is correctly predicted both in size and intensity. Above this zone, the simulation features a high velocity zone that is not visible in the experimental data, also the swirled flow aperture is slightly lower in the numerical simulation and is linked to the lowest decrease in the axial velocity downstream.

Despite those slight deviations, the agreement between the measurements and the LES is good enough for the cold flow to analyse the velocity profiles along the chamber in Fig. 9.3.2. The radial velocity features an over prediction of the velocities towards the centre suggesting an interaction of the flow in the central axis. Also, this velocity is shown to be decreasing less quickly in the simulation that it does in the experiment when going downstream of the chamber. In the axial velocity profiles,

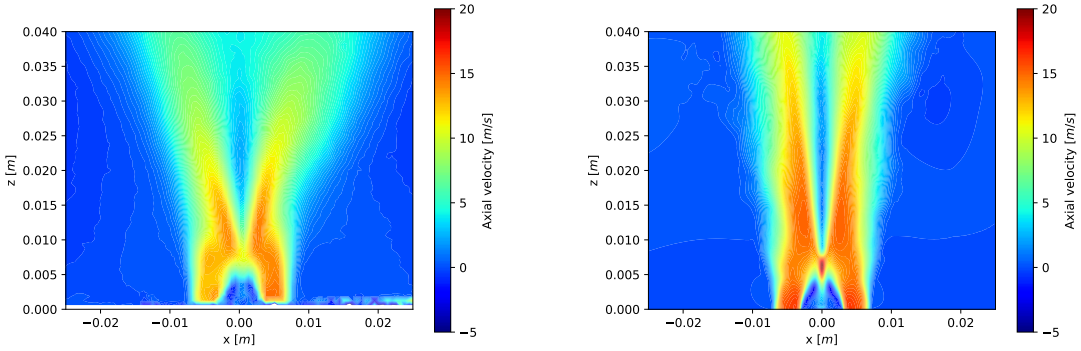

(a) Experimental data

(b) Simulation data

Figure 9.3.1: Axial velocity field in the y-plane close to the injector.

the same over prediction as the centre can be observed at z = 4 and 6 mm as well as a resulting under prediction at z = 10 mm.

This effect at the centre is linked to the lower aperture that was seen in the velocity fields.

Overall, there is a good agreement with the experimental data and these discrepancies are similar to the one observed in [Mercier et al., 2016] using the YALES2 solver.

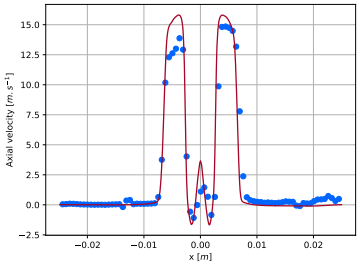

(a) Axial velocity at z = 2mm

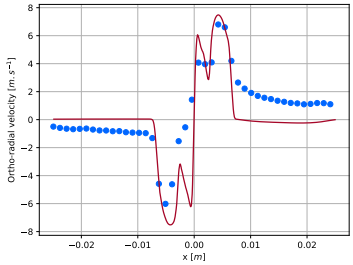

(b) Ortho-radial velocity at z = 2mm

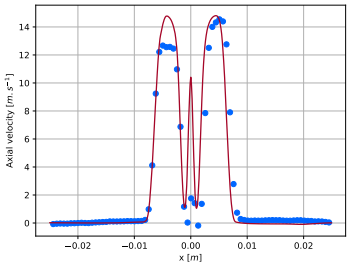

(c) Axial velocity at z = 4mm

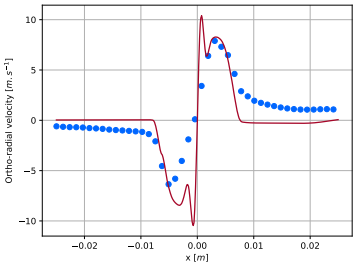

(d) Ortho-radial z = 4mm

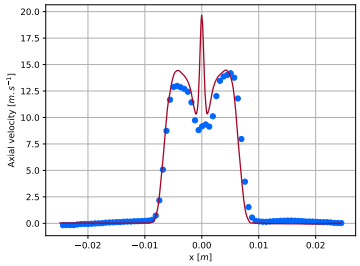

(e) Axial velocity at z = 6mm

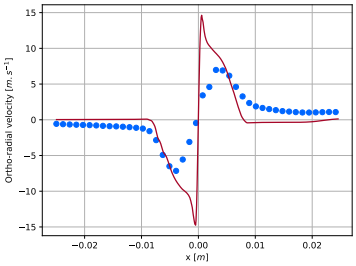

(f) Ortho-radial z = 6mm

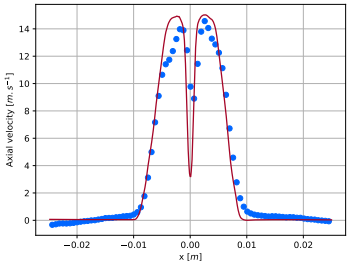

(g) Axial velocity at z = 10mm

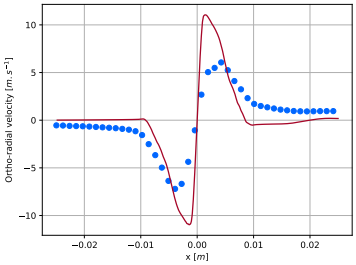

(h) Ortho-radial z = 10mm

Figure 9.3.2: (Left) Axial and (Right) ortho-radial velocity profiles at several downstream locations. Blue circles stand for the experimental data whereas red solid lines represent the numerical results.

9.4 Flame structure

The flames for the 60% case and the 90% case have been initialised by filling the top half of the combustor with their corresponding equilibrium mixtures (burnt gases at $\phi = 0.7, T = T^{ad} and X = X^{eq}$ as described in 1.5.1). The computation timestep for both simulations was based on the CFL number and gave $dt = 7e^{-8}$ s. The convective time of the flow is estimated to 1.3 ms, however the recirculation zones take longer to be filled and the simulation were run to reach a physical time of 40 ms. After that time, the results were averaged over 1 ms with a sampling frequency of 1μs. The time-averaged heat release rate fields are presented on Fig. 9.4.1 for the 60% case and the 90% case.

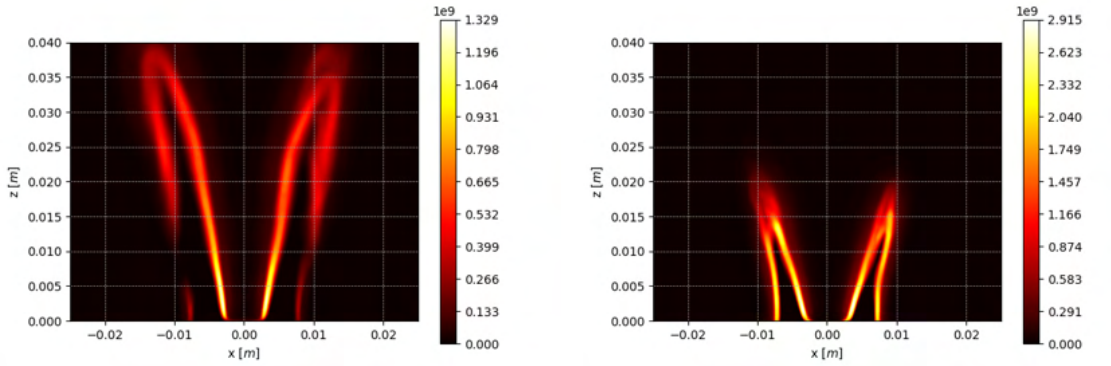

(a) 60% case (b) 90% case

Figure 9.4.1: Time-averaged heat release rate fields for (a) the 60% case and (b) the 90% case.

Heat release rate is classically analysed in numerical simulations to identify the flame shape. In Fig. 9.4.1, the shape transition experimentally observed between the 60% case and the 90% case is retrieved: when increasing the hydrogen enrichment, the flame shortens and the outer branch of the flame intensifies to reach an intensity equivalent to the inner branch.

From Fig. 9.4.2, the increase in heat release when enriching the flame is evidenced with a difference of 54% of the maximum heat release rate. The proper comparison of the flames can then only be done by a normalisation of each case in order to identify the flame structures.

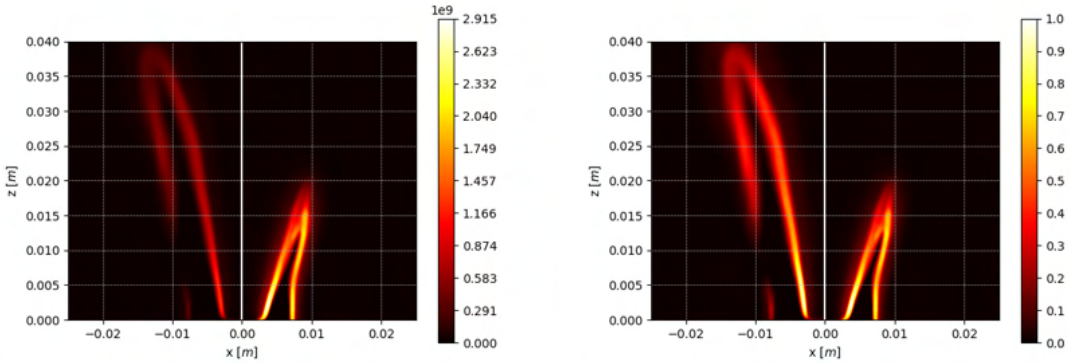

(a) Time-averaged heat release rate fields (b) Normalised heat release rate field

Figure 9.4.2: Comparison of the time-averaged heat release rate fields with the 60% on the left half of the figure and the 90% case on the right half. The heat release rate is represented with (a) the values from the simulation and (b) normalised by the maximum of each case.

If compared to the flame structures observed experimentally in Fig. 9.1.4, the present simulation exhibits slightly longer flames in both cases. Moreover for the 60% case, the outer flame branch should be extinguished while in the present simulation there are still traces of heat release all the way down to the injector.

From what was discussed in Section 7.3, the correlation between the heat release rate and the emission of OH* radical is not direct and may lead to a biased interpretation of the simulation result. For that reason, the time-averaged mass fraction fields of OH* computed in the simulation are displayed in Fig. 9.4.3.

While the 90% case stays qualitatively very similar when focusing either on heat release rate or OH^* mass fraction, the flame structure identified from the 60% case bears some differences depending on the quantity considered. The outer branch depicted by OH* is weaker and seems also shorter compared to what is observed when considering the heat release rate.

An other interesting property of OH* is that for both cases, the mass fraction values are similar in the flame (with a difference of maximum value of 19%) and a direct comparison without normalisation can be done as depicted in Fig. 9.4.4; Fig. 9.4.4b does not bring new information compared to Fig. 9.4.4a.

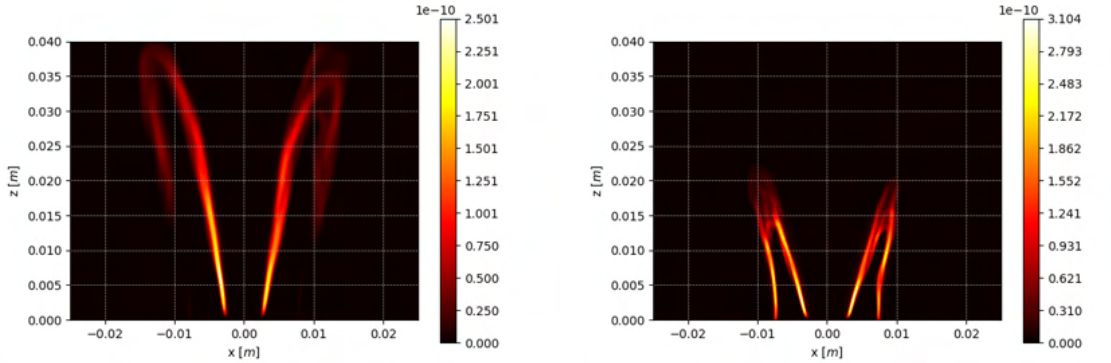

(a) 60% case (b) 90% case

Figure 9.4.3: Time-averaged OH* mass fraction fields for (a) the 60% case and (b) the 90% case.

The difference between these two fields can be directly seen on Fig. 9.4.5.

Using the heat release rate as an indicator of the flame, an outer branch is clearly visible for the 60 % case. However, this branch does not appear so clearly when using the OH* field. For direct comparison with experiment that uses OH* chemiluminescence, the latter is more adequate to identify the flame structure.

When plotting iso-lines of mass fraction on that field, as depicted in Fig 9.4.6, the outer branch is only partially engulfed inside the iso-line representing 10% of the maximum value. From that observation, it feels safe to assume that the V-shaped flame observed in the experiments corresponds well with the present numerical simulation. In that case, the numerical simulation shows weak flame structures that seem hardly accessible to experimental measurements.

When applying iso-lines to the heat release rate field, as displayed in Fig. 9.4.7, it appears clearly the previous conclusion could not be drawn from that field as the outer branch contains zones with heat release above 30% of the fields maximum and with also small structures at 20% of the maximum value at the outer exit of the injector.

Figure 9.4.8 finally displays time-averaged fields of temperature. The thermal boundary condition has an important effect on the temperature of the ORZ in the

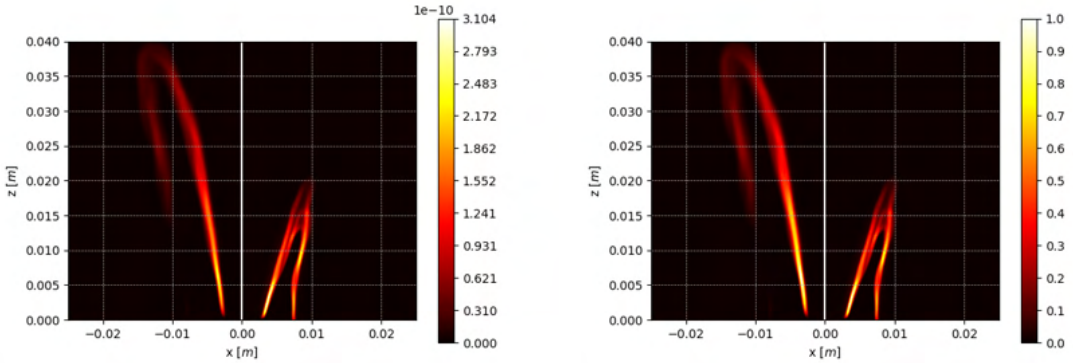

(a) Time-averaged OH* fields (b) Normalised OH* field

Figure 9.4.4: Comparison of time-averaged OH* mass fraction fields with the 60% case on the left half of the figure and the 90% case on the right half. The OH* mass fraction is represented with (a) the values from the simulation and (b) normalised by the maximum of each case.

60% case while the strong heat release of the 90% case compensates the heat losses on the dump plate in the 90% case. It is interesting to observe that the maximum temperature exceeds the theoretical adiabatic flame temperature for the inlet conditions that is 1890 K and 1960 K respectively. This increase in the burnt gas temperature can actually be explained by preferential diffusion effects, as analysed hereafter.

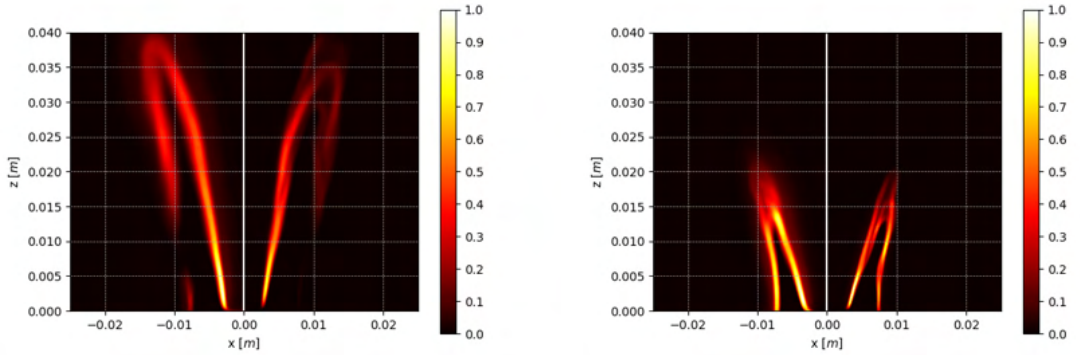

(a) 60% case (b) 90% case

Figure 9.4.5: Mirrored fields (positive abscissa value is actually the symmetric of the left half) of heat release rate and OH* mass fraction for (a) the 60% case and (b) the 90% case.

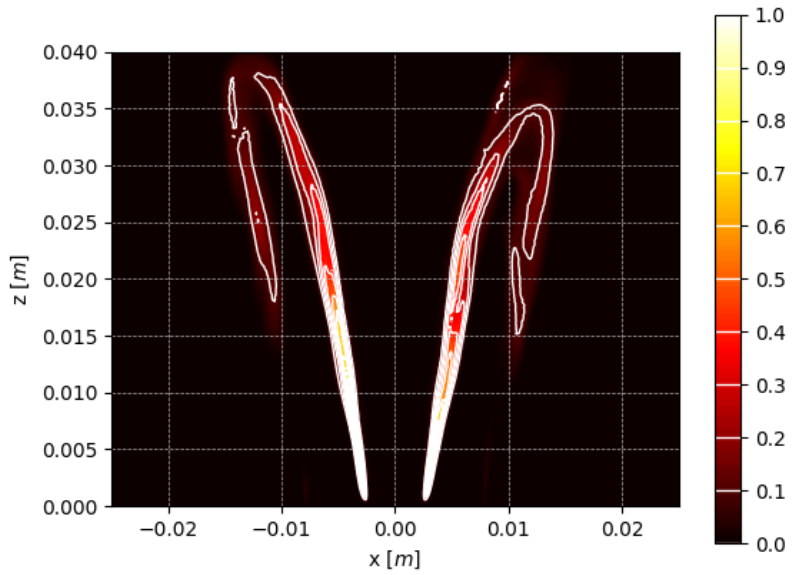

Figure 9.4.6: OH* mass fraction field for the 60% case normalised by its maximum value with iso-lines every 10% of this maximum value.

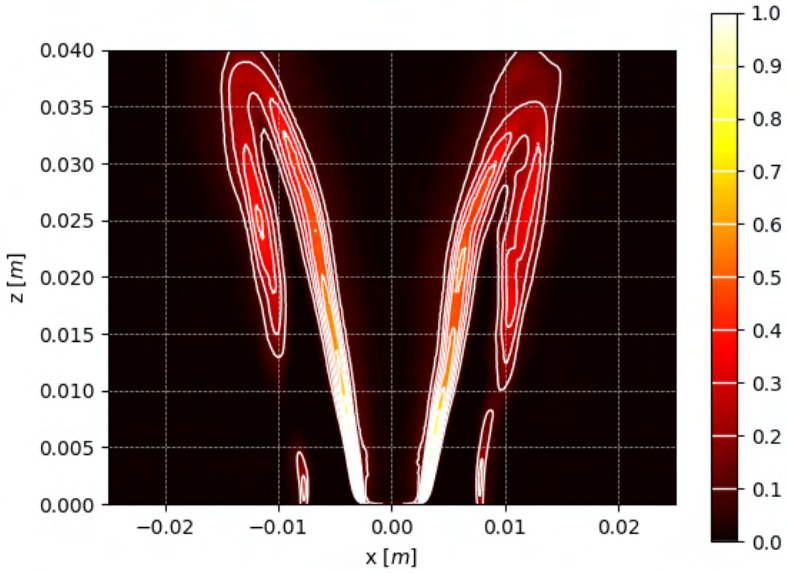

Figure 9.4.7: Heat release rate field for the 60% case normalised by its maximum value with iso-lines every 10% of this maximum value.

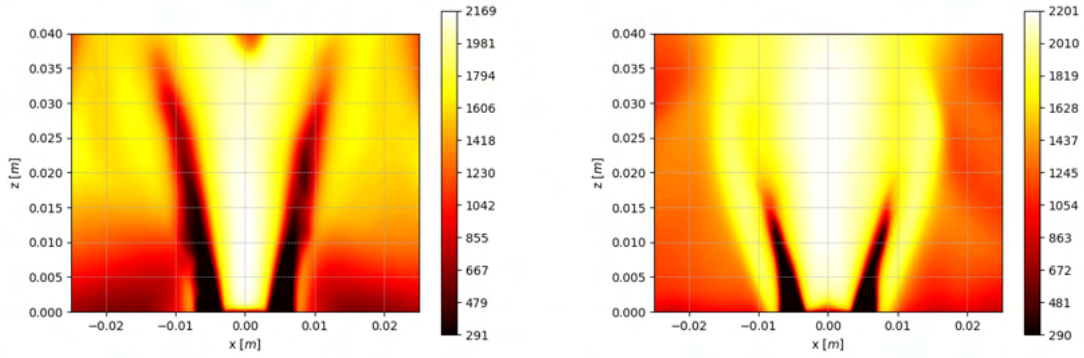

(a) 60% case (b) 90% case

Figure 9.4.8: Average temperature fields for (a) the 60% case and (b) the 90% case.

9.5 Preferential diffusion effects

An other interesting aspect of this configuration is the effect of preferential diffusion. It is well known that because hydrogen is a small molecule, it diffuses more inside the mixture compared to other species such as O2 or N2.

This differential diffusion can be first observed looking at the equivalence ratio inside the combustor that is supposed to be 0.7 as prescribed at the fully-premixed inlet.

From atomic budget, it is possible to both retrieve the local equivalence ratio ϕ, using Eq. 1.71, and the local hydrogen enrichment level noted $\tilde{X}_{H_2}$. Because of diffusion, the actual enrichment level will vary locally around the prescribed values of 60% and 90% and this quantity gives an information on what was the hydrogen enrichment of the mixture that burned at this location.

The equivalent enrichment ratio $\tilde{X}_{H_2}$ is written as:

$$\tilde{X}_{H_2} = \frac{1 - 4\alpha}{1 - 2\alpha} \tag{9.2}$$

where α is the local ratio of carbon atoms and hydrogen atoms as $\alpha = \frac{n_C}{n_H}$.

Both quantities are displayed in Fig. 9.5.1 for the 60% case and in Fig. 9.5.2 for case 90%.

For both the 60% case and the 90% case, the hydrogen from the premixed mixture diffuses towards the burnt gases leading to overall rich conditions with a higher enrichment ratio in the IRZ and along the flame. Towards the flame tip and its wake, the decrease of the hydrogen enrichment leads to a lower equivalence ratio explaining especially the decrease in heat release rate that is observed at the tip of the 90% flame (Fig. 9.4.1b). This behaviour is confirmed when looking at the instantaneous fields presented in Fig. 9.5.4.

For the 60% case, while the field of equivalence ratio (Fig. 9.5.1a) bears the same characteristics, the enrichment ratio is more perturbed and shows alternate zones of lower and higher enrichment ratios. From the instantaneous field in Fig. 9.5.3b, important segregation of higher and lower enrichment zones is observed due

to turbulence and suggests that burnt gases from both zones are mixing back into the IRZ to reach the base enrichment level but with an overall richer mixture. Because of the lower amount of hydrogen in the premixed mixture, its diffusion is less important and interacts with turbulence leading to complex structures that are richer than the fully premixed mixture prescribed at inlet but a similar enrichment ratio.

It needs to be noted that because of the equivalence ratio expression, its deviation tends not to be symmetric around the base value (0.7 in that case, corresponding to white in the following figures). On the contrary, the enrichment ratio deviation is symmetric in instantaneous fields by construction. Undershoot such as the drop in Fig. 9.5.4b can be explained by 3D effects.

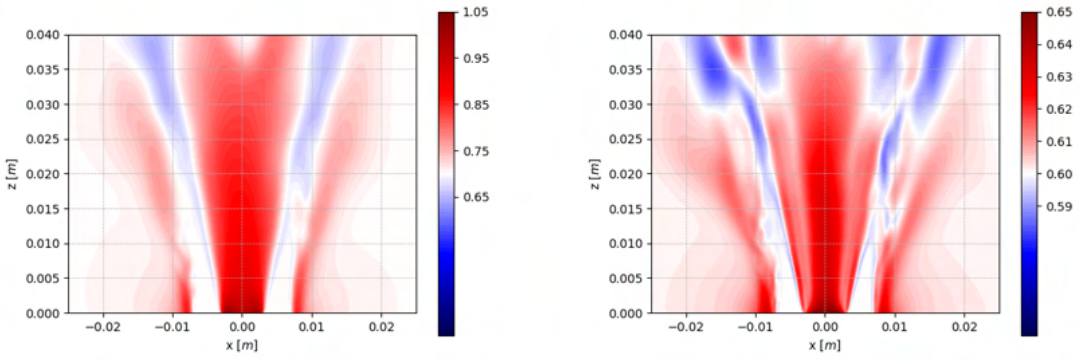

(a) Equivalence ratio field ϕ (b) Equivalent enrichment ratio field $\tilde{X}_{H_2}$

Figure 9.5.1: Local (a) equivalence ratio ϕ and (b) equivalent enrichment ratio $\tilde{X}_{H_2}$ for an averaged solution of the 60% case.

The increase in equivalence ratio is responsible for the high temperatures in the IRZ. As seen in Fig. 9.5.5, an equivalence ratio around stoiechiometry results in a higher adiabatic temperature for both enrichment level. However, due to heat losses in the system, the maximum temperature of 2170 and 2200 K for the 60% and 90% cases respectively, does not correspond to the theoretical values of these new conditions (2270 and 2335 K respectively) as represented by solid lines in the figure.

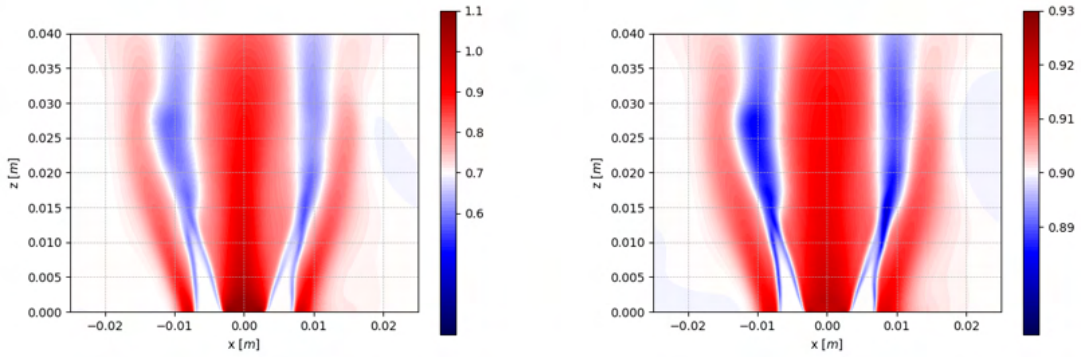

(a) Equivalence ratio field ϕ (b) Equivalent enrichment ratio field $\tilde{X}_{H_2}$

Figure 9.5.2: Local (a) equivalence ratio ϕ and (b) equivalent enrichment ratio $\tilde{X}_{H_2}$ for the averaged solution of the 90% case.

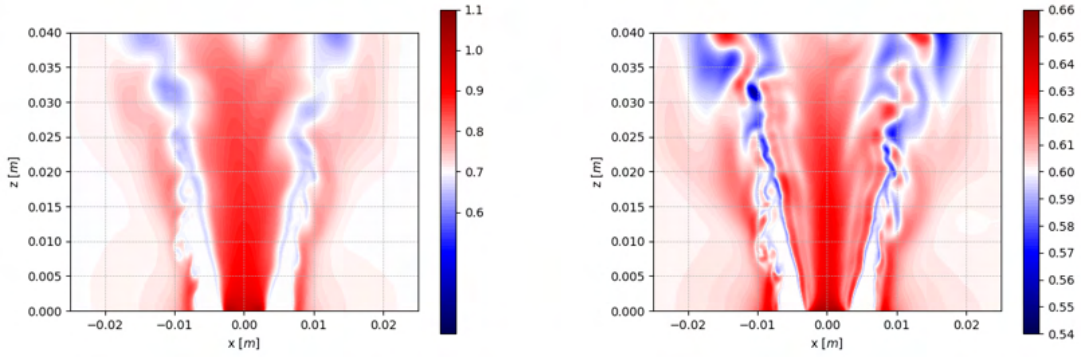

(a) Equivalence ratio field ϕ (b) Equivalent enrichment ratio field $\tilde{X}_{H_2}$

Figure 9.5.3: Local (a) equivalence ratio ϕ and (b) equivalent enrichment ratio $\tilde{X}_{H_2}$ for an instantaneous solution of the 60% case.

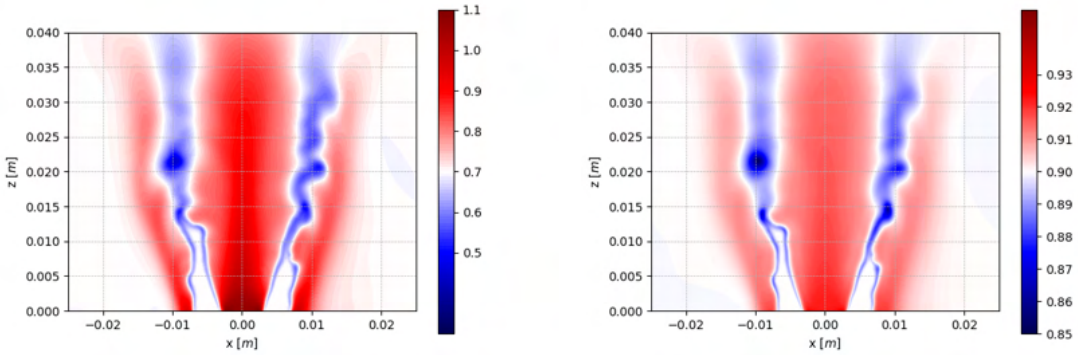

(a) Equivalence ratio field ϕ (b) Equivalent enrichment ratio field $\tilde{X}_{H_2}$

Figure 9.5.4: Local (a) equivalence ratio ϕ and (b) equivalent hydrogen fuel mole fraction $\tilde{X}_{H_2}$ for the instantaneous solution of the 90% case.

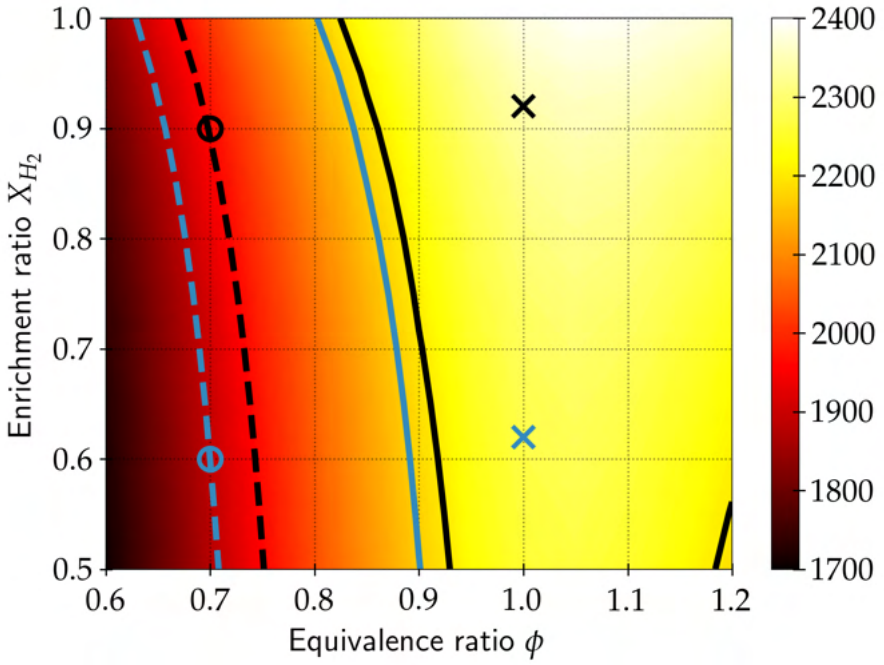

Figure 9.5.5: Adiabatic flame temperature as a function of equivalence ratio and enrichment ratio. Theoretical adiabatic temperatures are represented with iso-lines. Blue lines correspond to the 60% case whereas black lines correspond to the 90% case. Dashed lines are the temperatures at the initial conditions and solid lines correspond to the maximum temperatures reached in the domain. Symbols indicate the conditions of equivalence ratio and enrichment in the fresh gases (circles) and the IRZ (crosses).

9.6 Effect of enrichment on NO_x chemistry

Despite not being measured in the experimental campaigns, the NO_x emissions were studied in the present work. The objective is to determine the effect of enrichment on NO_x emissions and to assess the predictive capabilities of the current methodology.

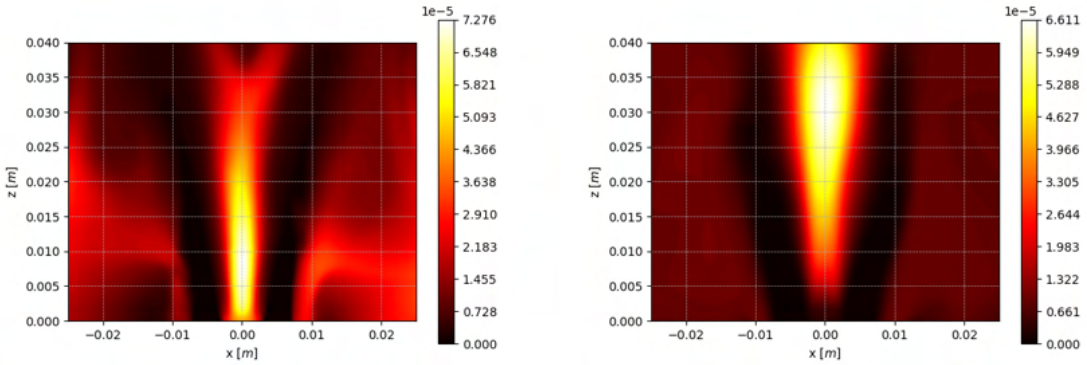

(a) 60% case (b) 90% case

Figure 9.6.1: Time-averaged NO mass fraction fields for (a) the 60% case and (b) the 90% case.

From the time-averaged fields of NO mass fraction, it appears clearly that a larger amount of NO mass fraction is present in the IRZ corresponding to higher temperature in the domain for both enrichment levels (Fig. 9.4.8), suggesting a production of NO via the thermal route.

While the maximum mass fraction level of both cases is similar ($6.6e^{-5}$ for 60% and $7.3e^{-5}$ for 90%), it is interesting to see that this value is higher for the 60% case despite its maximum temperature being lower. This suggests that an additional production pathway is present in that case increasing the NO mass fraction.

Observing the fields of the NO creation term (positive part of the mass net production rate) in Fig. 9.6.3, an important source term is present at the flame root with an order of magnitude higher than in the thermal zone.

Because of the higher content in carbonated species, this specific route might correspond to the prompt one promoted by NCN. This species has been set in a quasi-steady state in the ARC scheme and cannot be specifically identified in the

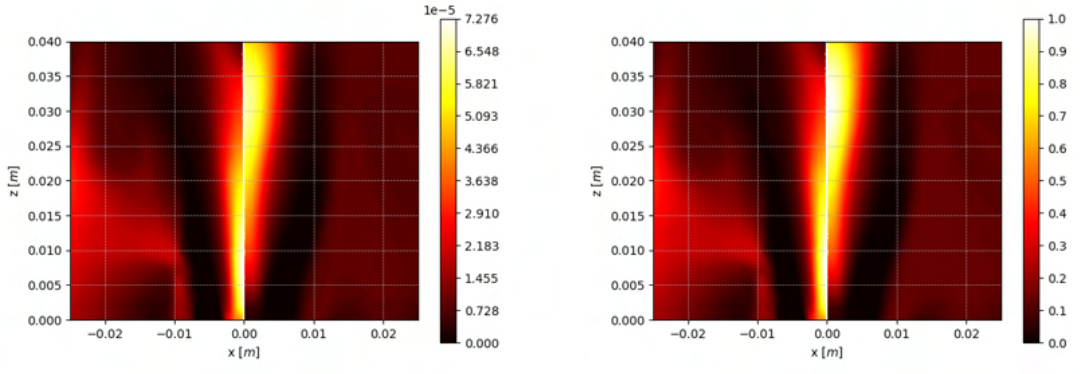

(a) Time-averaged NO mass fraction fields (b) Normalised NO mass fraction fields

Figure 9.6.2: Comparison of the time-averaged NO mass fraction fields with the 60% on the left half of the figure and the 90% case on the right half. The NO mass fraction is represented with (a) the values from the simulation and (b) normalised by the maximum of each case.

time-averaged fields, as well as CH that is the reactant of the characteristic reaction. Although not being significant for this route, HCN being a transported species is a good indicator of the presence of carbonated radicals leading to prompt NO formation.

An import concentration of HCN is observed along the reaction zone in Fig. 9.6.5 especially at the flame root where the high production zone was observed earlier supporting the theory of an enhanced prompt route. This species despite being present in the 90%, is marginal in that case compared to the 60% case as seen in Fig. 9.6.6b.

Because of its lower temperature in the ORZ, the 60% case also exhibits high amounts of NO_2 as displayed in Fig. 9.6.7 and 9.6.8. This NO2 production is to be correlated with the NO source terms that can be observed in the 60% case inside the ORZ in the temperature gradient. Of course the presence of NO_2 must be added to the NO in order to have an overall count of the NO_x emissions.

The present study suggests that a moderate amount of hydrogen enrichment leads to a more important amount of NO_x because of the activation of a NO_2 pathway and a stronger prompt pathway compared to an enrichment of 90%. Because the results

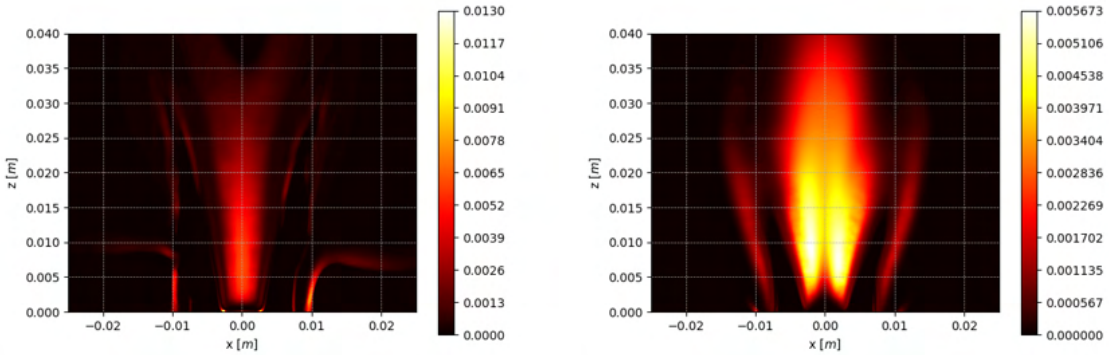

(a) 60% case (b) 90% case

Figure 9.6.3: Time-averaged NO mass source term for (a) the 60% case and (b) the 90% case.

were produced late in the PhD, the combustion chamber could not be completely filled and no precise quantification of the NO_x could be done before the end of the PhD. However, the summation of the NO and NO_2 concentrations on an axial cut of the domain suggests that the total amount of NO_x is 2 times more important in the 60% case than in the 90% case with 5 times more NO_2 because of the low temperature in the recirculation zones.

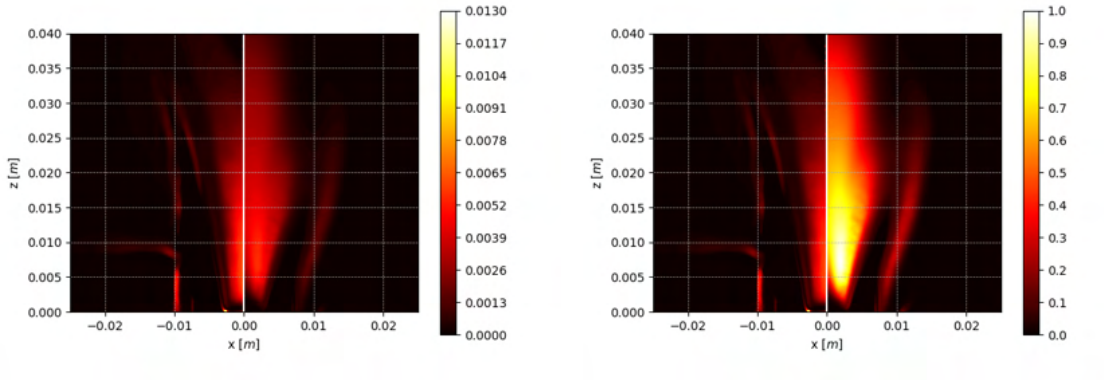

(a) Time-averaged NO mass source term fields (b) Normalised NO mass source term field

Figure 9.6.4: Comparison of the time-averaged NO mass source term fields with the 60% on the left half of the figure and the 90% case on the right half. NO mass source term is represented with (a) the values from the simulation and (b) normalised by the maximum of each case.

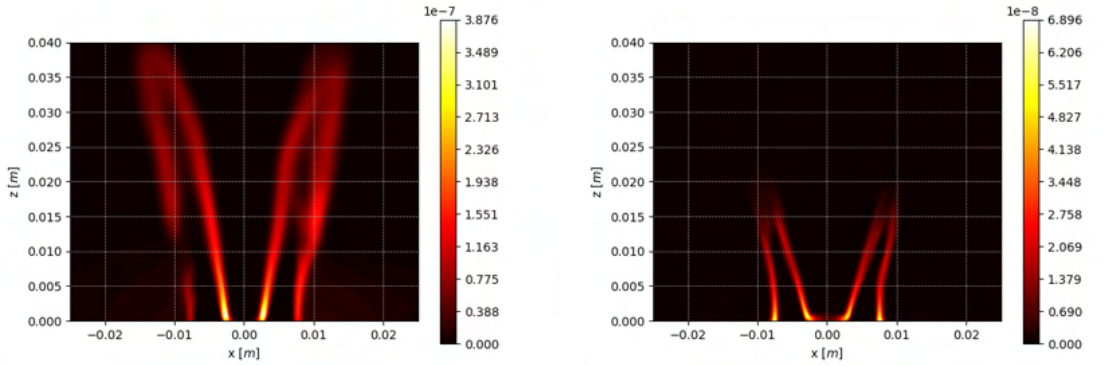

(a) 60% case (b) 90% case

Figure 9.6.5: Time-averaged HCN mass fraction fields for (a) the 60% case and (b) the 90% case.

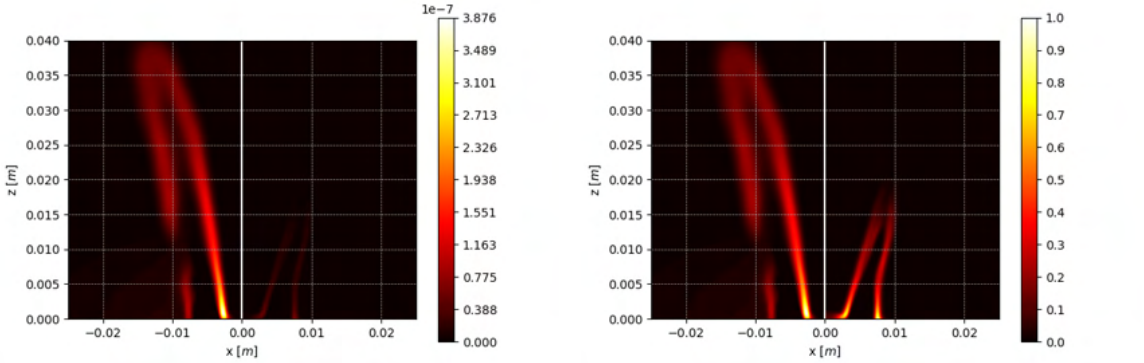

(a) Time-averaged NO mass fraction fields (b) Normalised HCN mass fraction fields

Figure 9.6.6: Comparison of the time-averaged HCN mass fraction fields with the 60% on the left half of the figure and the 90% case on the right half. The HCN mass fraction is represented with (a) the values from the simulation and (b) normalised by the maximum of each case.

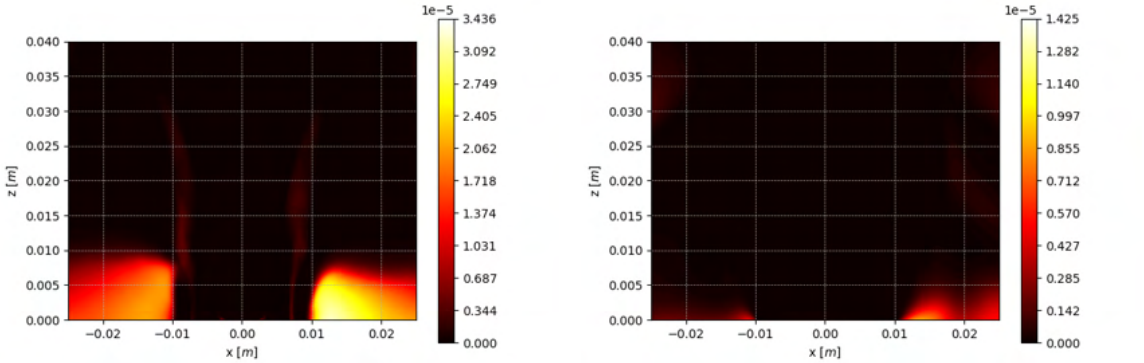

(a) 60% case (b) 90% case

Figure 9.6.7: Time-averaged NO_2 mass fraction fields for (a) the 60% case and (b) the 90% case.

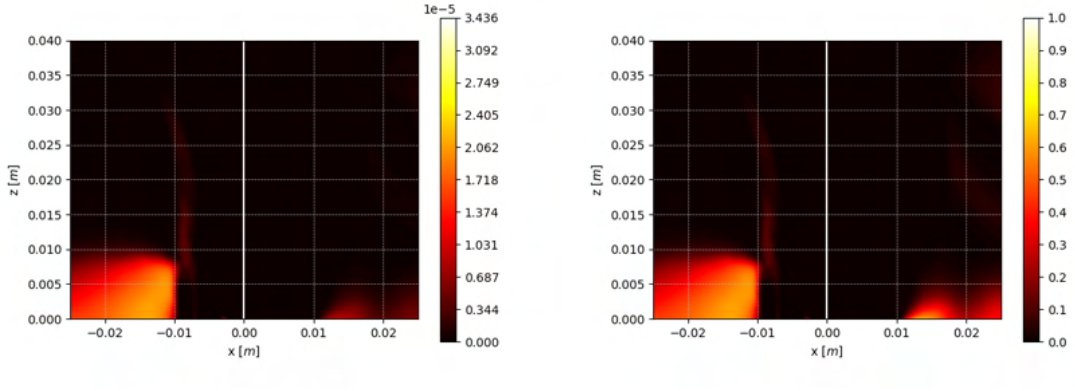

(a) Time-averaged NO_2 mass fraction fields (b) Normalised NO_2 mass fraction fields

Figure 9.6.8: Comparison of the time-averaged NO_2 mass fraction fields with the 60% on the left half of the figure and the 90% case on the right half. The NO_2 mass fraction is represented with (a) the values from the simulation and (b) normalised by the maximum of each case.

9.7 Conclusions

The methodology based on ARC coupled to TFLES has shown to be able to predict the effect of hydrogen enrichment in methane/air turbulent flames, with a good accuracy and also to provide important information about the underlying mechanisms of such flames.

The inadequacy between heat release rate and the OH chemiluminescence as been brought to light and further work is needed in order to improve the link between experiments and numerical simulation. As their diagnostics both increase in precision, they must be correlated accurately in order to agree on the quantities of interest and how they can help to better compare and understand complex flames structures.

The well known diffusive behaviour of hydrogen inside a premixed mixture has also been enhanced and is thought to be an important aspect of the anchoring mechanisms on the burner tip with a local variation of the actual hydrogen enrichment. For moderate enrichment of 60%, the amount of hydrogen being lower, its diffusion enters in competition with the turbulence leading to very inhomogeneous enrichment ratios inside the flame.

Finally, the computation with ARC was used in order to identify the effects of the enrichment on the NO_x emissions. While a higher enrichment leads to a higher burnt gases temperature and a higher efficiency of the NO thermal route, the lower temperature in the recirculation zones of the 60% case seems to promote other routes leading to an overall higher amount of NO_x. In the absence of experimental measurements and giving the long computation times needed to achieve a correct prediction of NO_x, these conclusions need to be further validated. However, this study constitutes a proof of the ability of the methodology to reproduce complex behaviours in such flames and is a step further toward the goal of the CFD which is to be fully predictive.

Part III

Combustion of multi-component jet fuels droplets

Chapter 10

Introduction

Contents

10.1 The JETSCREEN project

The JETSCREEN project [1] is a project funded by the European Union's Horizon 2020 research and innovation programme that started in June 2017 and ended officially in December 2020. Its goal was to develop a screening and optimisation platform for alternative aviation fuels. From screening tools developed by the several partners the platform aimed at:

- Streamlining the alternative aviation fuel approval process
- Assessing the compatibility of fuel composition/properties with respect to the fuel system and the combustion system
- Quantifying the added value of alternative fuels

[1] Project web site: https://www.jetscreen-h2020.eu/

- Optimising fuel formulation in order to attain the full environmental potential of synthetic and conventional fuels

In this context, the numerical simulations performed at CERFACS stand as macroscopic assessments of the fuel composition effects on several combustion features which are flame structure, Lean Blow-Out (LBO), ignition and thermo-acoustic instabilities.

This work comes in the overall project at the end of several subprocesses, namely: the production of the fuels from manufacturers, the fuel characterisation (done by IFPEN [Hajiw-Riberaud and Alves-Fortunato, 2020]), the kinetics modelling for high temperature combustion (done by POLIMI [Mehl and Pelucchi, 2020]) and finally, the reduction of these kinetics for application to canonical cases and 3D Large Eddy Simulations.

10.2 Spray combustion

As aviation fuels are liquid at ambient temperature and pressure, the study of their combustion into an aeronautical engine requires knowledge about the liquid phase as well as the gaseous phase. Through various designs of injectors and combustion chambers designs, many combustion regimes can be observed. Several parameters determine those regimes additionally to the mass flow rates and cold flow dynamics that can already be found for gaseous flames.

First, liquid injection leads to a spray which results from a complex atomization process. The spatial distribution of the droplets as well as their velocity and size statistics greatly affect the actual feeding of the flame. It was found by [Burgoyne and Cohen, 1954] that for the case of a single droplet at rest, smaller droplets evaporate fast enough to lead to a gaseous-like flame, while larger droplets burn individually with their surrounding environment. In a real spray, droplets of different sizes coexist and the resulting spray flame has a structure in between these two extreme cases. Secondly, liquid properties play an important role in both injection, via density, and evaporation via volatility. In case of multi-component fuels, the actual composition greatly impacts these properties and must be taken into account. Several studies investigated these different effects on the flame structure over the years both from an experimental [Khalil and Whitelaw, 1977][de Oliveira and Mastorakos, 2019] and

numerical point of view [Jones et al., 2012][Felden et al., 2018a].

In addition, and as said in the previous section, specific operating conditions which are critical for design must be considered, introducing other types of combustion regimes. Lean Blow-Out (LBO) corresponds to flame extinction due to the depleting of the fuel mass flow rate, and is a design parameter subjected to certification. Ignition, and more particularly high-altitude relight [Giusti et al., 2018] is most critical for obvious reasons. This subject is a rich yet not completely mastered research field. The study of sparked ignition has introduced the concept of Minimum Ignition Energy (MIE) [Bane et al., 2013, Ballal and Lefebvre, 1975a, Ballal and Lefebvre, 1975b], which ensures the formation of a flame kernel. However under the effect of turbulence, ignition is a stochastic process, described with ignition probability maps [Neophytou et al., 2012, Eyssartier et al., 2013, Esclapez et al., 2021]. New ignition systems based on lasers [Moesl et al., 2009, Gebel et al., 2015] or short plasma discharges [Shiraishi et al., 2009, Lefkowitz et al., 2015] are currently being investigated. Fuel sprays make ignition even more complex as they lead to a very heterogeneous fuel field. An extensive review on forced ignition of turbulent spray flames may be found in [Mastorakos, 2017].

The modelling of the kerosene is also in question and will be further discussed in 11. The multi-component surrogate modelling of kerosene was not kept in [Felden, 2017] because the reduction of the detailed kinetic mechanism from [Narayanaswamy et al., 2016b] with YARC did not give a sufficiently reduced mechanism with a skeletal mechanism composed of 139 species and 1148 reactions, which is indeed far too much for use in LES. In this work, ARCANE was able to provide sufficiently reduced mechanisms allowing spray flames computations with a multi-component representation of the liquid fuel.

In this part the derivation of a surrogate model for the considered fuels will be first reviewed (Chapter 11). Chemistry reduction with ARCANE will follow in Chapter 12 . Finally the ARC mechanisms will be used to study the effect of the fuel composition on a spray flame propagation in Chapter 14.

Chapter 11

Modelling of complex fuels

Contents

11.1 Physical properties and real fuel composition

In the previous part, natural gas was represented with methane only. Despite not being 100% accurate, it is a reasonable approximation as the other constituents are mainly impurities whic do not impact combustion. Such simple mono-component description is not valid for real fuels such as kerosene which is actually a blend of a multitude of hydrocarbons with various masses and molecular properties. These hydrocarbons can be categorised in different families according to their chemical structure:

- **Alkanes** (also called paraffins) are species of general composition C_nH_{2n+2} and are the most known hydrocarbons with n from 1 to typically 20. This family contains methane ($n = 1$), butane ($n = 4$) and dodecane ($n = 12$) to only mention a few . Their structure is composed of carbon atoms with only single

carbon-carbon bonds. Alkanes are saturated hydrocarbons and exhibit many interesting properties such as a low freezing point, a low density and a high energy density [Lefebvre and Ballal, 2010].

Starting from butane, this family splits into 2 sub-families: the normal alkanes, denoted with a suffix *n-* before the molecule name, and the iso-alkanes, denoted with the suffix *i-* before the molecule name.

The **normal alkanes** have a linear carbon chain meaning that each carbon atom is bonded to only two other carbon atoms (or only one if it is at an extremity).

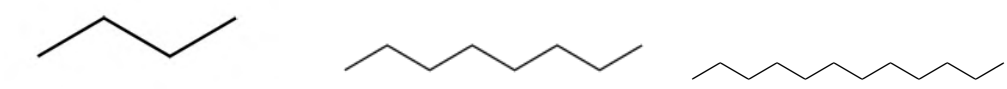

(a) n-butane (C_4H_{10}) (b) n-octane (C_8H_{18}) (c) n-dodecane ($C_{12}H_{26}$)

Figure 11.1.1: n-alkanes

The **iso-alkanes** are branched molecules meaning that some carbon atoms bear more than 2 bonds with other carbon atoms. From a purely chemical aspect, the term *iso* (standing for isomer) should only be used for the isomers with only one methyl group (CH_3). However in the combustion community it is used to refer to the most common isomer of the corresponding n-alkane.

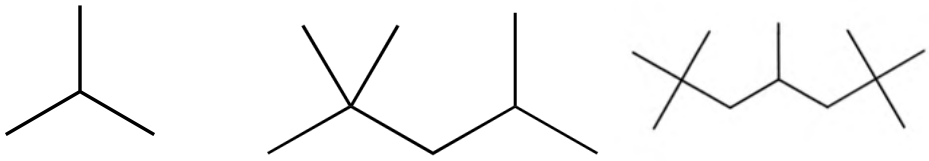

(a) i-butane or 2-methylpropane (b) i-octane or 2,2,4-trimethylpentane (c) i-dodecane or 2,2,4,6,6-pentamethylheptane

Figure 11.1.2: i-alkanes

This specific branching of the iso-alkanes result in a higher reactivity compared to its normal version for high temperature regime and much lower reactivity in low temperature region.

- **Cyclo-alkanes** are species of general formula C_nH_{2n} and can be viewed as an n-alkane looping on itself. They are named according to their n-alkane

constituent. In this family also falls alkanes with a ring and linear chains attached to them. It also includes species with more than one ring (called naphtenes, not to be confused with naphtalene) having the general formula $C_nH_{2(n+1-r)}$ where r is the number of rings. They exhibit the same level of energy density and low soot production as paraffins.

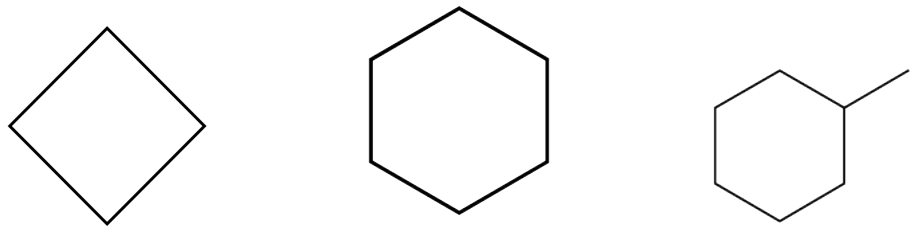

(a) cyclobutane (C_4H_8) (b) cyclohexane (C_6H_{12}) (c) methylcyclohexane (C_7H_{14})

Figure 11.1.3: Cycloalkanes

- The last family contains the **aromatic compounds**. Aromatic compounds are defined by a ring similar to the cycloalkanes but with delocalised electrons. This delocalisation is either represented with a ring having a double carbon-carbon bond alternating with a single carbon-carbon bond or with carbons having 1.5 bond orders with electrons floating around the ring. The most basic aromatic compound is benzene that has the general formula C_6H_6. This family contains all species which exhibit this benzene ring. When more than two benzene rings are present in the structure, the species are defined as **di-aromatics** and **polyaromatics**, the simplest di-aromatic being called naphtalene. Because they are unsaturated molecules, they contain less hydrogen and as a result, their specific energy is lower than alkanes and cyclo-alkanes.

The composition of Jet A1 (in mass), which is the reference fuel in aeronautics, has been measured as follows in the context of the JETSCREEN project:

- 19.2 % of n-alkanes
- 30.7 % of i-alkanes
- 32.9 % of cycloalkanes

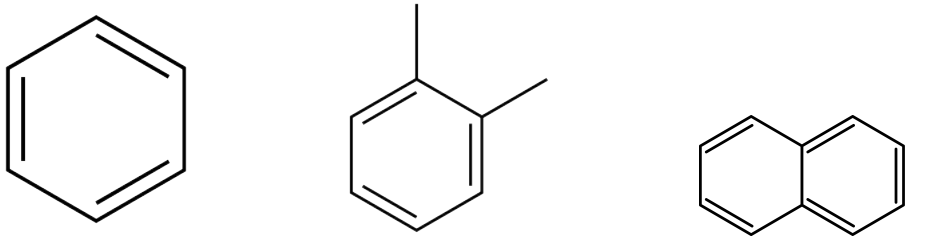

(a) benzene (C_6H_6) (b) ortho-xylene (C_8H_{10}) (c) naphtalene (C_10H_8)

Figure 11.1.4: Aromatics

- 15.5 % of aromatics
- 1.7 % of di-aromatics

Inside each family, the mass is not evenly distributed among all the possible species and the detailed composition is generally represented as in Fig. 11.1.5 which represents the mass distribution in each family depending on the species number of carbon atoms [1].

From everything discussed in this section, it is clear that including the real fuel composition in a CFD computation is not feasible. Even the reduction of kinetics will prove to be difficult as the number of species in the fuel will greatly limit the reduction process. Moreover the detailed composition is usually unknown as only global properties are given by oil companies.

From the above data, the fuel can be first approximated by its mean chemical formula. In the case of Jet A1, this formula is $C_{10.52}H_{17.78}$ and an existing molecule with a similar formula can be used as an approximate fuel model. This molecule is usually selected from similar liquid fuel thermodynamic and mechanical properties. In the case of Jet A1, a possible equivalent molecule is 1,2,3,4-tetramethylcyclohexane [Hajiw-Riberaud and Alves-Fortunato, 2020]. However this molecule is not guaranteed to correctly represent the reactivity of the fuel.

It is therefore necessary to develop other modelling strategies for the fuel composition able to correctly predict its atomization, evaporation and combustion.

[1] The detailed composition was obtain by comprehensive two-dimensional gas chromatography (GCxGC) as part of the JETSCREEN project. The author would like to thank Maira Alves-Fortunato at IFPEN for providing the data.

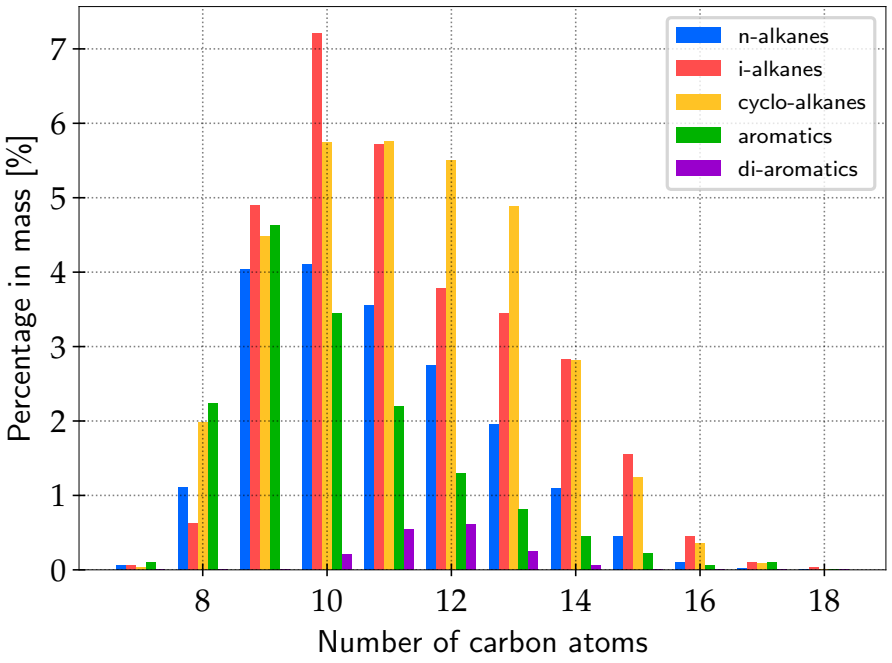

Figure 11.1.5: Mass distribution (in percentage of the total mass) according to the number of carbon atoms in the species and its family (n-alkanes in blue, iso-alkanes in red, cyclo-alkanes in yellow, aromatics in green and di-aromatics in purple) for Jet A1.

11.2 Mono-component surrogate

The simplest methodology to model a fuel is to represent it as a single species. Kerosenes are often modeled with n-decane ($C_{10}H_{22}$) or n-dodecane ($C_{12}H_{26}$) as this species represents the most abundant family (alkanes) and is close to the average chemical formula of the fuel. Looking back at the composition of Jet A1, this choice may be surprising as the highest percentage corresponds to iso-alkanes and cycloalkanes while n-alkanes come third. It is explained by the species reactivity, too high for iso-alkanes and too low for cyclo-alkanes, while n-alkanes are intermediate. These simple surrogates have been largely used in the literature [Dagaut and Gail, 2007] with a skeletal kinetic mechanism [Luche, 2003]. In order to perform faster computations, [Franzelli et al., 2010a] proposed a two-step global scheme able to capture the main combustion features, i.e., the adiabatic flame temperature, the laminar flame speed and the auto-ignition delay time. This mechanism was constructed

from the 3-components surrogate of [Dagaut and Gail, 2007] (74 % n-decane, 15% n-propylbenzene and 11% n-propylcyclohexane in mole), reduced to a single species with the formula $C_{10}H_{20}$ derived with thermodynamic properties computed as a linear combination of the constituent properties. To better describe the flame structure at a still reasonable cost, kinetic reduction with the ARC methodology was performed and used in [Jaravel, 2016][Franzelli et al., 2017]. Both the two-step and ARC schemes are currently used in industry.

By not conserving a correct H/C ratio and being too simplistic, these single component surrogates do not exhibit the correct pyrolysis behaviour which is a key aspect of hydrocarbon combustion. This was partly overcome by the HyChem methodology, discussed in Section 4.2.2, which builds a correct pyrolysis scheme for a mono-component surrogate fuel, with kinetic parameters fitted on experimental data. This methodology has been successfully used in LES of industrial combustion chamber by [Felden et al., 2018a] and showed good results in terms of accuracy and computational cost. However, this approach does not allow to describe phenomena such as preferential evaporation arising from the multi-component nature of the liquid fuel, or soot formation which is very sensitive to the fuel formula. Therefore a multi-component approach will be kept in this work.

11.3 Multi-component surrogate

From the detailed composition of the fuels, specific representative components are chosen to represent accurately the fuel. The accuracy of the multi-component surrogate depends on the number of species chosen as representatives and varies according to the fuel considered. For kerosene, several surrogates have been proposed in the literature [Edwards and Maurice, 2001][Humer et al., 2007][Dagaut et al., 2006][Westbrook et al., 2009]. The multi-component approach allows to account for more kinetic pathways which can be useful for soot production for example, or for preferential evaporation effects that have been shown to play a key role in auto-ignition [Stagni et al., 2017] as well as spray flame propagation [Shastry et al., 2020b]. It also allows to study fuel effects, as is the objective here in the context of the JETSCREEN project. Indeed, as the studied fuels are relatively close to each other, a mono-component surrogate approach would lead to the same surrogate, most likely n-dodecane. In addition, the pyrolysis mechanism with Hychem is not available for all fuels and aside from the Jet-A1, they are not assured to correspond to the exact fuels studied here.

The multi-component surrogate modelling of kerosene was not kept in [Felden, 2017] because the reduction of the detailed kinetic mechanism from [Narayanaswamy et al., 2016b] with YARC did not give a sufficiently reduced mechanism with a skeletal mechanism composed of 139 species and 1148 reactions, which is indeed far too much for use in LES.

Fortunately, as shown in Section 4.5.2, ARCANE was able to correctly reduce the detailed mechanism from POLIMI without introducing a large error and without particular difficulty. The reduction was also performed on the Narayanaswamy mechanism for a slightly different surrogate in [Shastry et al., 2020b] without any problems.

Chapter 12

Reduction of multi-component fuels

Contents

12.1 JETSCREEN fuels

In the context of the JETSCREEN project, 3 fuels referenced as A1, B1 and C1 are considered and described below. The fuels have been chosen for their differences with A1 being the reference fuel, already used in all commercial aircraft engines, B1 being a sustainable synthetic fuel and C1 being an example of a "bad" replacement for kerosene.

From a palette of candidate components displayed in Fig. 12.1.1 [1], the 3-components composition was selected through an optimisation process to match the experimental data available within the project by the CRECK modelling Team from Politechnico Di Milano partly based on the previous work of [Narayanaswamy and Pepiot, 2018].

The optimisation targets were in that case, the Derived Cetane Number (DCN), the H/C ratio, the distribution of mass within the different component families, the average molecular weight, the threshold sooting index, the liquid density, the liquid viscosity and distillation curves (displayed in Fig. 12.1.2).

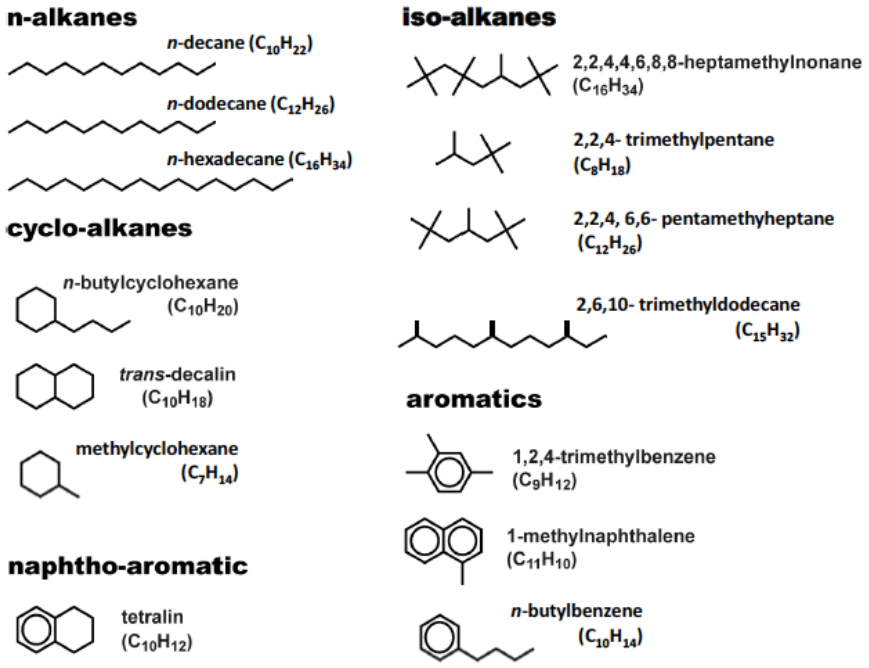

Figure 12.1.1: Palette of candidate components for the surrogate formulation. From internal project reports by Marco Mehl and Matteo Pelucchi [Mehl and Pelucchi, 2020]

[1] The palette represented here lacks the xylene species which is an aromatic of formula C_8H_{10} with two methyl groups. Xylene possesses 3 isomers; ortho-, meta- and para-xylene that are respectively the 1,2-dimethylbenzene, 1,3–dimethylbenzene and 1,4-dimethylbenzene. The xylene species used in the following is a lumped species representing these three isomers.

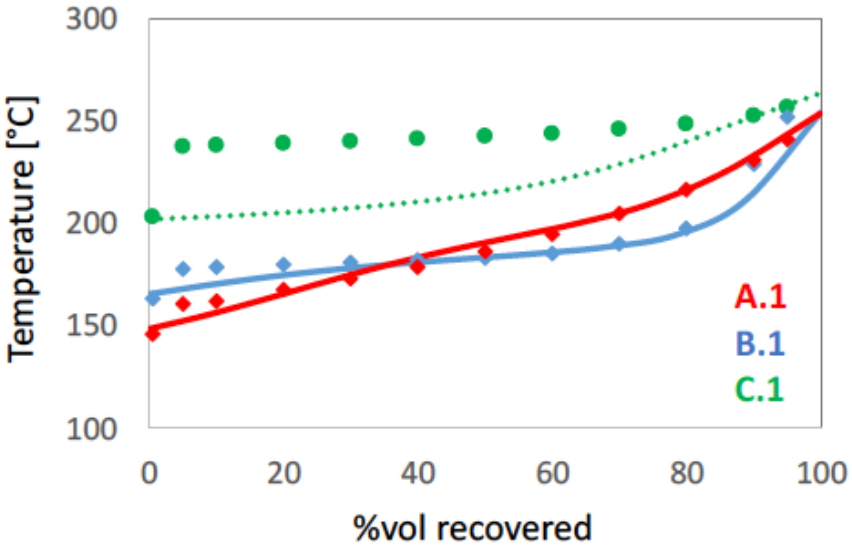

Figure 12.1.2: Measured distillation curves of the three fuels considered in the model (symbols) and calculated equilibrium distillation curves of their surrogates. From internal project reports by Marco Mehl and Matteo Pelucchi [Mehl and Pelucchi, 2020]

12.1.1 Standard aviation fuel: Jet A1 (A1)

The A1 fuel corresponds to a standard aviation fuel, the Jet A1, defined by the Aviation Fuel Quality Requirements for Jointly Operated Systems (AFQRJOS). This fuel is the most used type of kerosene in civil aviation and as such, the reference fuel for the study of alternative fuels in the JETSCREEN project and more largely in aviation fuel studies.

The surrogate that was chosen is the one from [Humer et al., 2011] already used in 4.5.2 consisting (in mole fraction) of 60% of n-dodecane 20% of methyl-cyclohexane and 20% of xylene. The three components are chosen to actually represent the predominant hydrocarbon classes that are present in the real fuel composition (discussed in Section 11.1) and they were already used in different proportions in [Narayanaswamy and Pepiot, 2018]. N-dodecane is the representative of the straight alkanes (C_nH_{2n+2}) and as discussed in Section 11.2 is often chosen as single component surrogate of kerosene. Methyl-cyclohexane is a representative of the

cyclo-alkanes here with a methyl complex attached to it. Finally, xylene represents the aromatic components, here with 2 methyl complexes, which carry double bond carbon liaisons and have been identified as playing a major role in soot formation. The xylene in this mechanism is a lumped species representative of the three xylene isomers; ortho-, meta- and para-xylene.

From the detailed analysis of the real fuel properties done by IFPEN as part of the project [Hajiw-Riberaud and Alves-Fortunato, 2020], the A1 fuel exhibits an H/C ratio of 1.94 and a liquid density at ambient conditions of 789.7 $kg.m^{-3}$. Using the surrogate formulation and simple mixing law, we obtained a H/C ratio of 2 and a liquid density at ambient conditions of 775 $kg.m^{-3}$.

12.1.2 Alcohol to Jet Synthetic Paraffinic Kerosene: ATJ-SPK (B1)

This fuel is produced via the ATJ-SPK process standing for Alcohol to Jet Synthetic Paraffinic Kerosene. This process is a biotechnological process to produce bio-kerosene derived from biomass. Iso-butanol created by fermentation of biomass is dehydrated to form the corresponding olefin which is hydrotreated to finally form the iso-alkanes constituting this fuel [Geleynse et al., 2018]. This fuel has been certified since 2016 for a 30% blending in volume with classical jet fuels. The particularity of B1 fuels is that it only contains iso-alkanes, so that the selection of the representative families in the palette 12.1.1 is straightforward. From the GCxGC data in Fig. 12.1.3, it is clear that iso-dodecane is the major component of the fuel. The surrogate was selected as 8% of iso-octane (C_8H_{18}), 84% of iso-dodecane ($C_{12}H_{26}$) and 8% of iso-cetane ($C_{16}H_{34}$).

From real fuel analysis, B1 exhibits an H/C ratio of 2.16 and a liquid density at ambient conditions of 758.5 $kg.m^{-3}$. The surrogate formulation being the real composition, the H/C ratio is the same. However because of the simple mixing law used, the liquid density is slightly different with a value of 749 $kg.m^{-3}$.

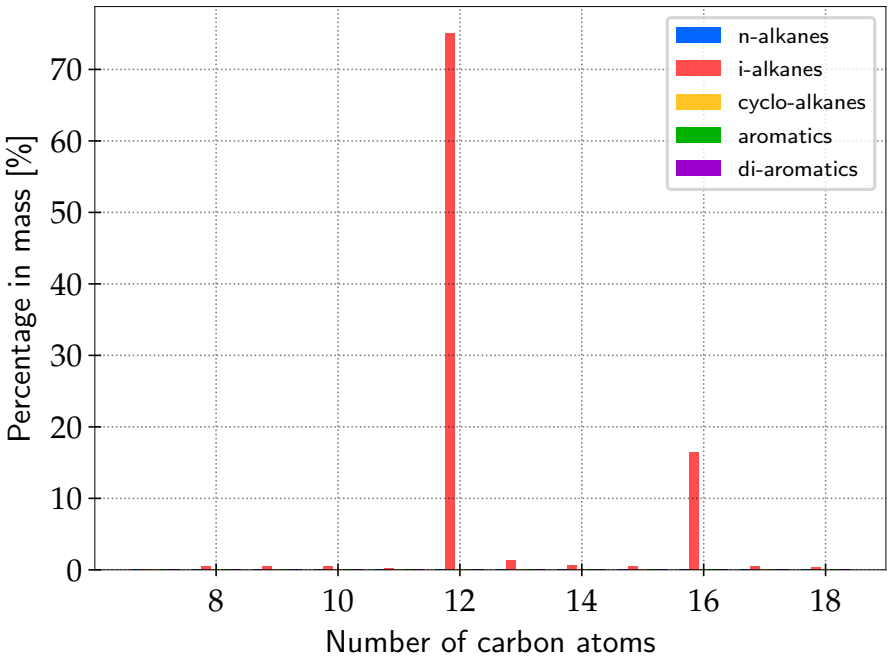

Figure 12.1.3: Mass distribution (in percentage of the total mass) according to the number of carbon atoms in the species and their family (n-alkanes in blue, iso-alkanes in red, cyclo-alkanes in yellow, aromatics in green and di-aromatics in purple) for the B1 fuel.

12.1.3 High-aromatic content Jet A1 (C1)

The last fuel of interest for this work is a high-aromatic content Jet A1. Compared to the classical Jet A1 fuel, it contains 55% of cyclo-alkanes and 20% of aromatics (2% mono-aromatics and 18% di-aromatics), to be compared to respectively 33% and 17% in A1. From Fig. 12.1.4, cyclo-alakanes and aromatics are clearly dominant and a shift towards higher carbon numbers can also be observed. It should be noted that within the project, a 10-components surrogate was originally proposed for this fuel to maintain a level of accuracy similar to the others and a larger error was then allowed on the surrogate properties in order to lower the number of components to 3. A 10-components surrogate was not conceivable to obtain a kinetic mechanism suitable for LES simulations (i.e., with a number of transported species less than 40). The 3-components surrogate for C1 is composed of 60% of decalin, 20% of methylnaphthalene and 20% of i-dodecane.

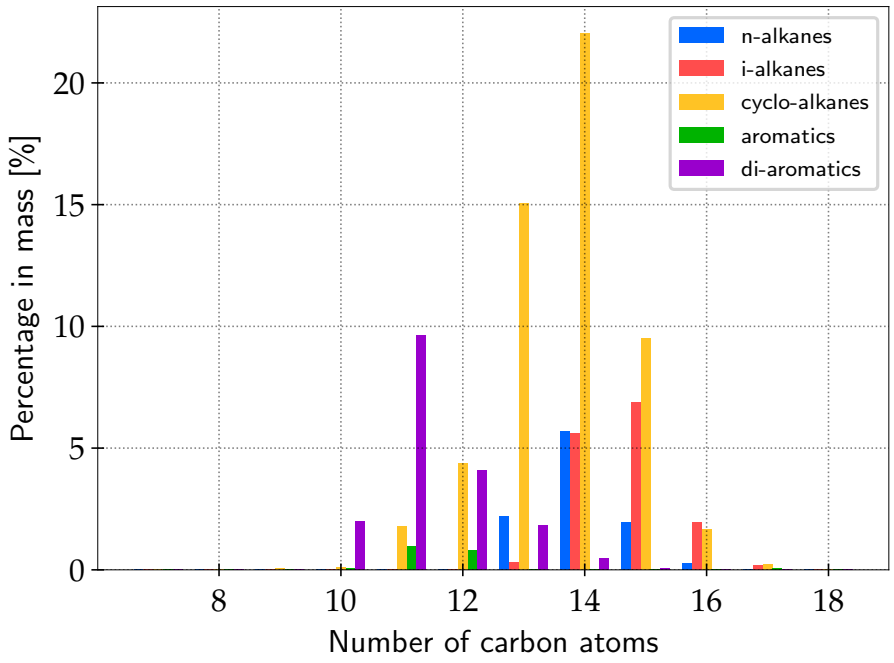

Figure 12.1.4: Mass distribution (in percentage of the total mass) according to the number of carbon atoms in the species and their family (n-alkanes in blue, iso-alkanes in red, cyclo-alkanes in yellow, aromatics in green and di-aromatics in purple) for the C1 fuel.

From real fuel analysis, C1 exhibits an H/C ratio of 1.73 and a liquid density at ambient conditions of 860.2 $kg.m^{-3}$. From the surrogate formulation, we obtained a H/C ratio of 1.70 and a liquid density at ambient conditions of 888 $kg.m^{-3}$ using simple mixing law. Note that the density is higher compared to the two other fuels.

In the context of alternative fuels for clean combustion, C1 can right away be considered as a bad choice. Indeed [Olson et al., 1985] already found that a higher amount of aromatics induces more soot formation. In addition, the liquid density of this fuel is too high to be certified as a viable jet fuel. C1 is therefore included in the study for comparison purposes only.

It should also be noted that while formulating the surrogate for the C1 fuel, deviations between the experimental and modelled distillation curves were observed because of a lack of components in the palette able to both reproduce the H/C ratio and the distillation curve. Priority was given to the H/C ratio because of its

critical role in combustion. However, the low volatility of this fuel is still qualitatively recovered by the surrogate.

12.2 Reduction of chemical kinetics of surrogates

The previously presented 3-components surrogates of kerosene and alternative kerosene can all be computed with the CRECK_1909_TOT_HT mechanism [2] that includes the palette used for their generation.

Using ARCANE, the 3 surrogates, summarised in Tab. 12.2.1, were reduced with the same targets and thresholds.

Using the CRECK_1909_TOT_HT mechanism [3] as the detailed mechanism, reduced mechanisms have been obtained based on the following cases: 2 isochoric reactors at 1 bar, stoechiometry and initial temperature of 1500 and 2000K and 3 laminar premixed flames at 1 bar, fresh gases temperature of 400K and three equivalence ratios of 0.6, 1 and 1.4. These conditions were chosen in accordance with the target applications. In particular only high temperature combustion was of interest. The error thresholds were imposed as 15% error on the ignition delay time for the reactors and 5% error on the laminar flame speed and 1% error on the final temperature for the premixed flames. The cases and their associated errors are summarised in Tab. 12.2.2.

On these cases, the targets were chosen as the fuel species, the heat release rate, CO and CO_2. Even though targeting the heat release rate might have been sufficient to estimate the reduction coefficients (DRGEP and LOI), the 3 fuel species, the intermediate species CO and the burnt product CO_2 were added to further constrain the reduction and ensure good results.

At the skeletal step of the reduction, whereas the A1 and B1 reach respectively 52 and 54 species, the C1 does not go below 80 species which would require a large amount of species to be approximated as quasi-steady state species to go below 40 species in the final reduced mechanism. The iso-dodecane being also in the B1 surrogate, it seems that the two double ringed species (methylnaphthalene and decalin)

[2] September 2019 version
[3] September 2019 version

Fuel	component name	component class	raw formula	X	Y
	n-dodecane	n-alkane	$C_{12}H_{26}$	0.6	0.578
A1	methyl-cyclohexane	cyclo-alkane	C_7H_{14}	0.2	0.198
	xylene	aromatic	C_8H_{11}	0.2	0.224
	iso-octane	iso-alkane	C_8H_{18}	0.08	0.0536
B1	iso-dodecane	iso-alkane	$C_{12}H_{26}$	0.84	0.84
	iso-cetane	iso-alkane	$C_{16}H_{34}$	0.08	0.1064
	decalin	cyclo-alkane (two rings)	$C_{10}H_{18}$	0.6	0.570
C1	iso-dodecane	iso-alkane	$C_{12}H_{26}$	0.2	0.234
	methyl-naphthalene	di-aromatic	$C_{11}H_{10}$	0.2	0.196

Table 12.2.1: Composition of the fuels surrogates with their mole (X) and mass fractions (Y) in the fuel.

Reactor type	0D Isochoric reactor	1D premixed flame
Temperature [K]	1500, 2000	400
Pressure [bar]	1	1
Equivalence ratio	1	0.6, 1, 1.4
Error threshold on Auto-ignition delay time	15 %	/
Error threshold on Laminar flame speed	/	5% *
Error threshold on Maximum temperature	/	1% *

Table 12.2.2: Definition of the reference canonical cases and their associated error thresholds applied to various quantities for the 3-components surrogates reductions. * Error thresholds multiplied by 2 in the case of C1 fuel reduction.

exhibit a more complex pyrolysis process requiring many more species. For that reason, the thresholds on the errors for the laminar flames where multiplied by 2 to obtain a sufficiently reduced mechanism for C1.

After applying this modification to the C1 and performing the QSS step of the reduction, the mechanisms summarised in Tab. 12.2.3 were obtained.

	transported species	irreversible reactions	QSS species
A1	36	543	16
B1	31	394	24
C1	35	420	33

Table 12.2.3: Reduced mechanism size for each surrogate.

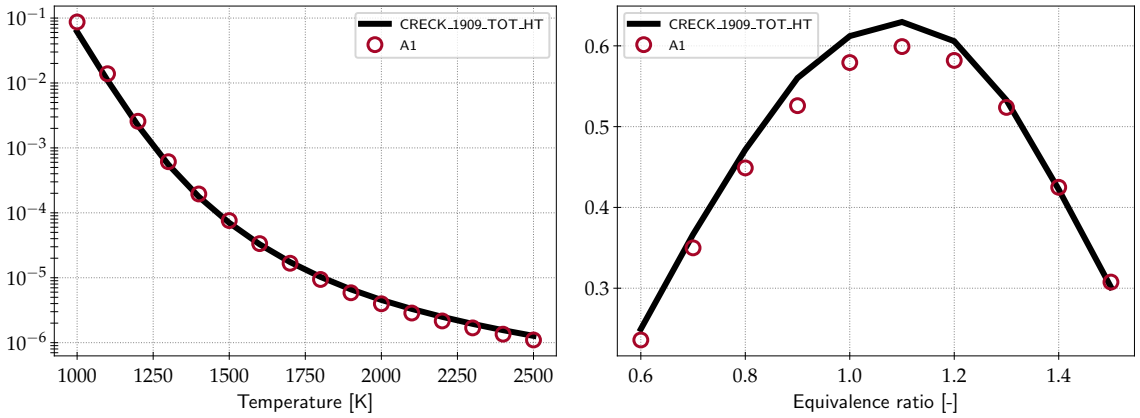

(a) Ignition delay time

(b) Laminar flame speed

Figure 12.2.1: Validation of the reduced mechanism for A1 fuel for (a) ignition delay time at stoichiometry and 1 bar for a range of temperature and (b) laminar flames speeds for a fresh gas temperature of 400K and 1 bar for a range of equivalence ratio. The black solid line stands for the detailed mechanism (CRECK_1909_TOT_HT) and red circles stand for the reduced mechanism (A1).

The ARC mechanisms that will be referenced for generality as A1, B1 and C1 are then validated on a broader range of temperatures and equivalence ratios as displayed in Fig. 12.2.1, 12.2.2 and 12.2.3.

For A1 and B1, the agreement outside of the reduction cases is good with an error staying below a reasonable value of 20% for the ignition delay time, 6% for the laminar flame speed and 1.5% for the maximum temperature.

For C1 fuel, while a good agreement is found for the laminar flame speed, for the final temperature and for the ignition delay time above 1500 K, the mechanism behaves poorly for lower temperatures with an error higher by 2 orders of magnitude

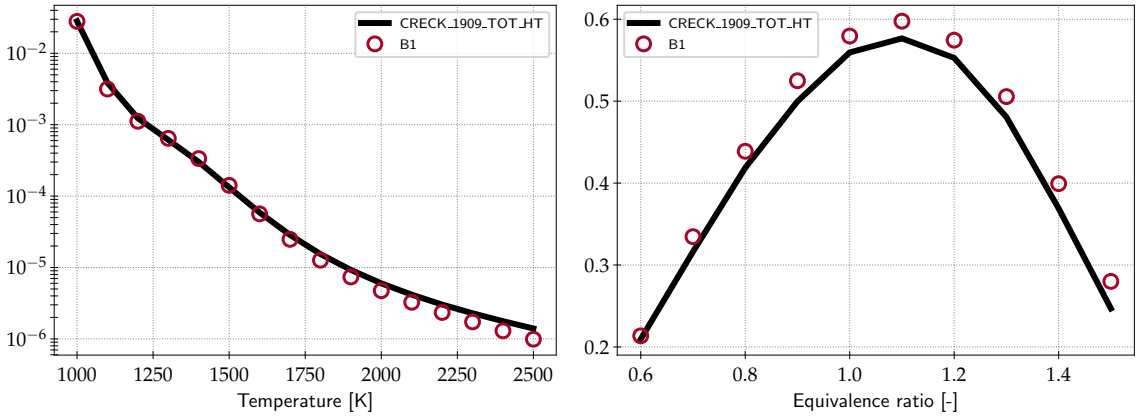

(a) Ignition delay time (b) Laminar flame speed

Figure 12.2.2: Validation of the reduced mechanism for B1 fuel for (a) ignition delay time at stoichiometry and 1 bar for a range of temperature and (b) laminar flames speeds for a fresh gas temperature of 400K and 1 bar for a range of equivalence ratio. The black solid line stand for the detailed mechanism (CRECK_1909_TOT_HT) and red circles stand for the reduced mechanism (B1).

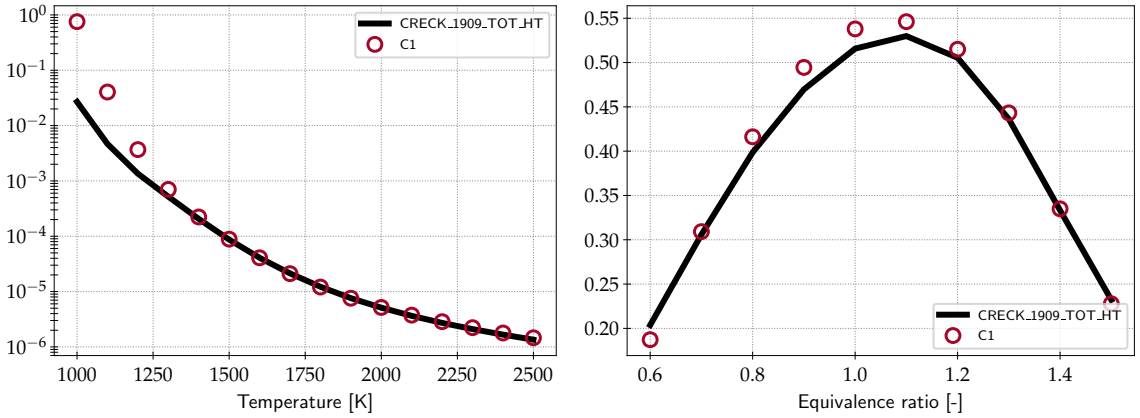

(a) Ignition delay time (b) Laminar flame speed

Figure 12.2.3: Validation of the reduced mechanism for C1 fuel for (a) ignition delay time at stoichiometry and 1 bar for a range of temperature and (b) laminar flames speeds for a fresh gas temperature of 400K and 1 bar for a range of equivalence ratio. The black solid line stand for the detailed mechanism (CRECK_1909_TOT_HT) and red circles stand for the reduced mechanism (C1).

at 1000 K. In the systems studied within the JETSCREEN project, focusing on stabilised flames where only few cold pockets of fresh gases are likely to auto-ignite and ignition processes majorly occur with a thermal runaway happening above 1500 K, the poor agreement at these lower temperatures should not be an issue. However this result denotes the particularity of the mechanism for C1 which appears more sensitive to the operating conditions than the for the two other fuels. The increase of the error tolerances, even though they were not to the reactor cases, may have played a role in that behaviour by discarding important pathways affecting the reactor chemical evolution at moderate temperatures.

12.3 Comparison of the fuel burning properties

Figure 12.3.1 compares the ignition delay and laminar flame speed of the three fuels, as obtained with detailed chemistry. A clear trend can be seen where A1 is the most reactive fuel, followed by B1 and finally C1.

An interesting result is that whereas the ignition delay time comparison is similar in the detailed and ARC mechanisms, the laminar flame speed difference observed between A1 and B1 with the detailed mechanism is almost absent with ARC, especially around stoichiometry.

Looking closely to the reaction zone of the three reference laminar premixed flames obtained with the ARCs mechanisms on Fig. 12.3.3, the hierarchy of the laminar flame speeds is retrieved with the A1 fuel having a higher maximum heat release rate than B1, which itself has a higher maximum heat release rate than C1. However these differences tend to disappear at stoichiometry. A particular behaviour of the B1 can be identified in the rich case, also visible but less strong in the stoiciometric case, is an inflexion of the heat release rate profile in the early reaction zone. This inflexion is due to the fast pyrolysis of the branched alkanes composing the fuel through endothermic reactions as seen in Fig. 12.3.4 showing the endothermic and exothermic parts of the net heat release rate.

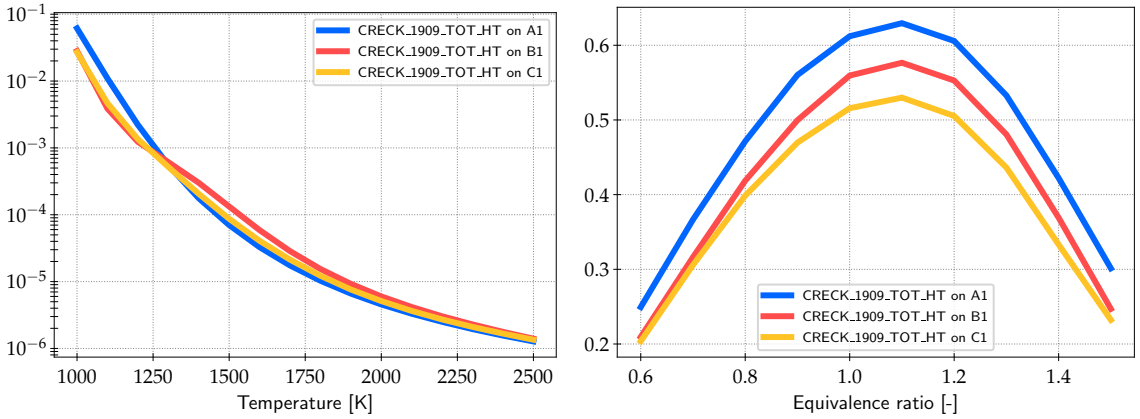

(a) Ignition delay time (b) Laminar flame speed

Figure 12.3.1: Comparison between the 3 surrogates computed with the detailed mechanism on (a) ignition delay time at stoichiometry and 1 bar for a range of temperature and (b) laminar flames speeds for a fresh gas temperature of 400K and 1 bar for a range of equivalence ratio. Blue corresponds to A1, red to B1 and yellow to C1.

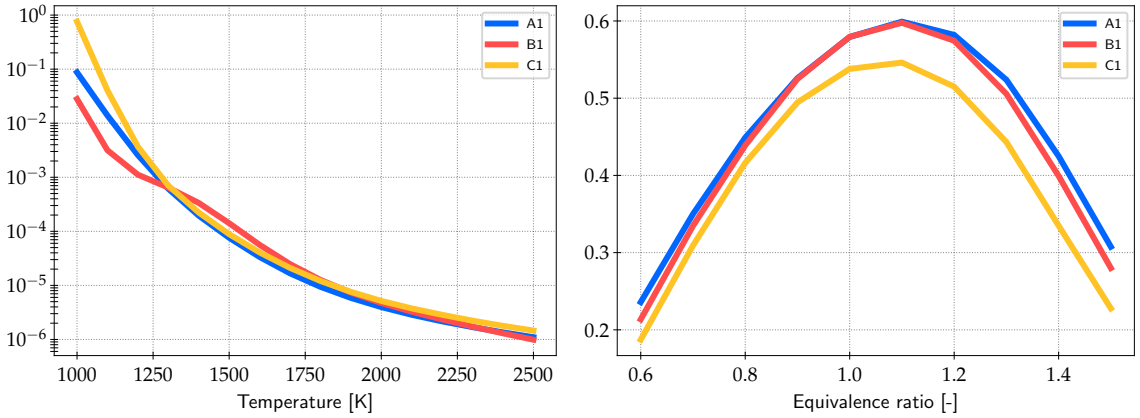

(a) Ignition delay time (b) Laminar flame speed

Figure 12.3.2: Comparison between the 3 surrogates computed with their respective reduced mechanism on (a) ignition delay time at stoichiometry and 1 bar for a range of temperature and (b) laminar flames speeds for a fresh gas temperature of 400K and 1 bar for a range of equivalence ratio. Blue corresponds to A1, red to B1 and yellow to C1.

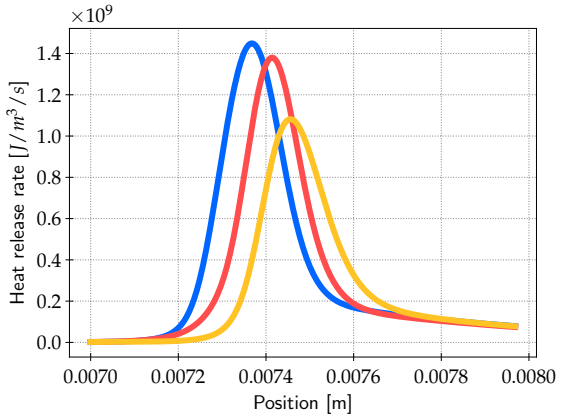

(a) $\phi = 0.6$

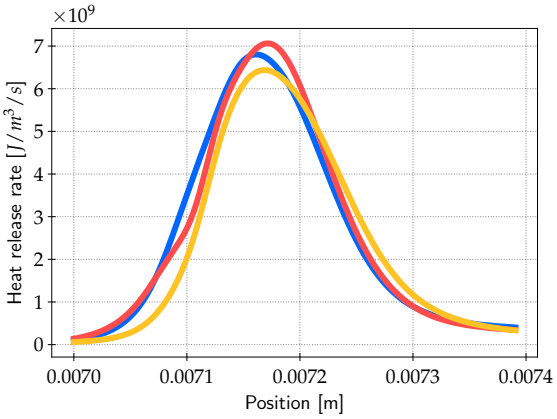

(b) $\phi = 1$

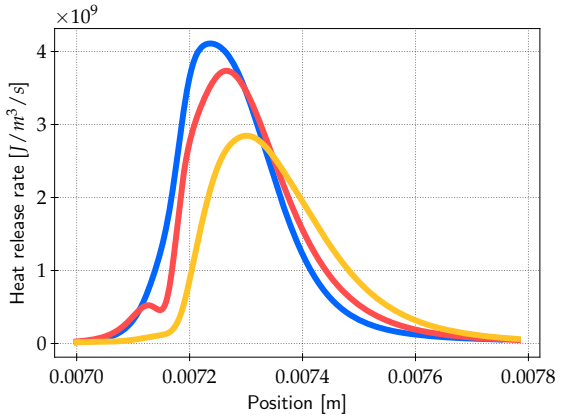

(c) $\phi = 1.4$

Figure 12.3.3: Comparison of the heat release rate in the reaction zone of the 3 surrogates computed with their respective ARC mechanism at (a) lean conditions, (b) stoichiometry and (c) rich conditions. Blue corresponds to A1, red to B1 and yellow to C1.

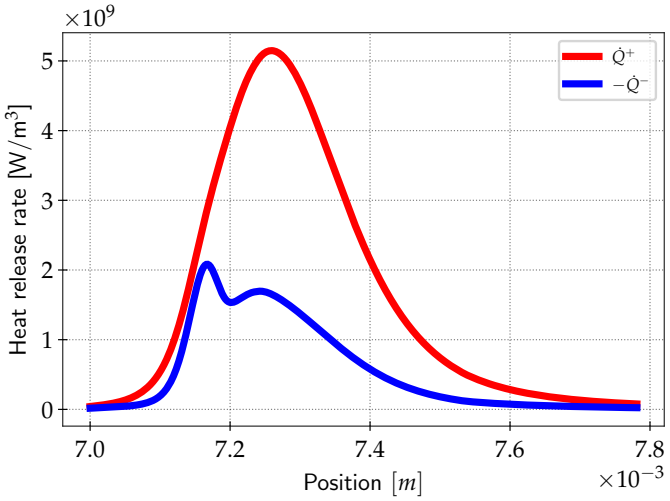

Figure 12.3.4: Comparison of the endothermic, $-\dot{Q}^-$, (in blue) and exothermic $\dot{Q}^+$, (in red) components of the heat release rates in the reaction zone of B1 surrogate in rich conditions.

12.4 Conclusion

The detailed mechanism for the 3 fuel surrogates has been successfully reduced into an ARC scheme for each fuel surrogate. The agreement between the ARCs and the detailed mechanism are good and their reduction was efficient enough to obtain affordable mechanisms for CFD. However, because of its complexity, the C1 mechanism, that was already deviating from the experimental data with the detailed chemistry, required to increase the error thresholds in order to obtain a sufficiently reduced mechanism.

The successful reduction of mechanism for these 3 fuels starting from a large detailed mechanism constitutes an achievement compared to the previous work of [Felden, 2017]. Further improvement in ARCANE regarding the methodology has been done since, and future works might expect better agreement with slightly more reduced mechanisms.

The fundamental differences between the 3 fuels in terms of burning are also highlighted and will give hints about their behaviour in more complex flames.

The reductions were performed during the development of ARCANE and are a

posteriori not considered optimum (compared for example to the mechanism presented in Section 4.5.2 even though it has 3 more transported species). However, they present a fairly good agreement with the detailed mechanism and show the capabilities of obtaining affordable ARCs for 3-component surrogates.

These mechanisms will be used in the following for spray flames.

Chapter 13

Fundamentals of two-phase combustion

Contents

13.1 Euler-Lagrange formalism

For aeronautical engines where the liquid fuel is atomised into a spray before entering the combustion chamber, there are two ways to account for the presence of this liquid phase in LES equations:

- The Euleurian formalism, in which the liquid phase is considered continuous and resolved on the same grid than the gaseous phase.

- The Lagrangian formalism, in which the spray is considered as a collection of discrete droplets tracked individually.

The Eulerian formalism in AVBP does not allow for the consideration of poly-dispersed sprays where several particles of different size can coexist inside a cell. Sectional methods allowing to recover the spray poly-dispersion imply the resolution of additional liquid phase equations and therefore lead to an important numerical cost [Laurent and Massot, 2001]. For this reason, the Lagrangian formalism implemented in the AVBP code is retained [Senoner, 2010][Sierra Sànchez, 2012][Paulhiac, 2015].

13.2 Dispersed phase

In this work, a dispersed phase is assumed and several assumptions are made:

- The droplets are considered stable with high surface tension meaning that they are considered spherical with no possibility to break-up.
- The only force applied on the droplets is drag (gravity is neglected).
- The spray is not dense enough for the droplets to interact with each other and are considered to be independent from one another.
- The droplets have an infinite conductivity meaning that the temperature is uniform in the droplets.

The liquid-gas interaction is two-way with exchange of mass, momentum and energy between the two phases.

The point source approach is adopted, where the droplets are described as points following point mechanics laws.

The droplet (or particle) is characterised by its position $x_{p,i}$, its mass $m_{p,i}$, its velocity $u_{p,i}$, its temperature T_p.The subscript p refers to the droplet (particle) and liq to liquid properties. Each droplet follows the evolution equations written as:

$$\frac{dx_{p,i}}{dt} = u_{p,i} \tag{13.1}$$

$$\frac{d(m_p u_{p,i})}{dt} = F_{p,i}^{ext} \tag{13.2}$$

$$\frac{dm_p}{dt} = \dot{m}_p \tag{13.3}$$

$$\frac{d(m_p h_{s,p})}{dt} = \dot{\Phi}_p \tag{13.4}$$

where $h_{s,p}$ is the latent heat of vaporisation at the droplet temperature.

$F_{p,i}^{ext}$, $\dot{m}_p$ and $\dot{\Phi}_p$ are the phase exchange source terms corresponding respectively to momentum, mass and energy.

The expression of these source terms is explained hereafter.

13.3 Exchange terms

13.3.1 Drag force

As explained in the modelling assumptions, the only external force the particle is subjected to is the drag force which is expressed in its general form as:

$$F_{p,i}^{ext} = \frac{1}{2}\rho_{liq}\mathcal{C}_D\mathcal{A}(u_i - u_{p,i})^2 \tag{13.5}$$

where $\mathcal{A} = \pi r_p^2$ is the projected area of the droplet and $\mathcal{C}_D$ the drag coefficient.

The drag coefficient has been found to be very dependent on the relative velocity between the gas and the droplet and can be expressed as a function of the particle Reynolds number Re_p defined as:

$$Re_p = \frac{u_{relative} d_p}{\nu_{liq}} \tag{13.6}$$

with $u_{relative} = \sqrt{\sum_i^{N_{dim}} (u_i - u_{p,i})^2}$ the second norm of the relative velocity between the gas and the particle.

An empirical drag correlation as a function of the particle Reynolds number for $Re_p < 800$ has been proposed by [Schiller and Naumann, 1935] extending the one from [Oseen, 1927] and writes:

$$\mathcal{C}_D = \frac{24}{Re_p}(1 + 0.15 Re_p^{0.687}) \tag{13.7}$$

13.3.2 Evaporation model

Single component evaporation

The evaporation model is responsible for the estimation of the mass and energy exchange term, $\dot{m}_p$ and $\dot{\mathcal{Q}}_p$. In this work, the analytical Spalding model for the evaporation of isolated spherical droplets [Spalding, 1953] is used. In this model, the droplet is assumed to be at thermal equilibrium with the surrounding gas. Under these conditions the classical d^2 law found by [Godsave, 1953] which states that the squared diameter of the droplet varies linearly is retrieved. The gaseous field is then considered in a quasi-steady state meaning that the evolution equations are independent of time. The hypothesis upon which the droplet is homogeneous and isotropic is recalled. From these assumptions, the mass and thermal evolution of the droplet can be written in a spherical referential as a function of only the distance between the droplet surface (with the subscript ζ) and the far-field (with the subscript ∞) as:

$$\rho u_{p,i} r_p^2 = (u_{p,i} r_p^2)_\zeta = \frac{\dot{m}_\mathcal{K}}{4\pi} \tag{13.8}$$

$$\rho u_{p,i} r_p^2 \frac{dY_{\mathcal{K}}}{dr} = \frac{d}{dr}\left(\rho D_{\mathcal{K}} r^2 \frac{dY_{\mathcal{K}}}{dr}\right) \tag{13.9}$$

$$\rho u_{p,i} r_p^2 \frac{dC_p T}{dr} = \frac{d}{dr}\left(\frac{\lambda}{C_p} r^2 \frac{dC_p T}{dr}\right) \tag{13.10}$$

where the subscript $\mathcal{K}$ denotes the liquid species. where the subscript $\mathcal{K}$ denotes a species initially present in the liquid phase. At some point, the species $\mathcal{K}$ will be both in liquid and gaseous state.

Under the quasi-steady state assumption, the gaseous mass source term is directly related to the particle mass evolution $\dot{m}_p$ as:

$$\dot{m}_{\mathcal{K}} = -\dot{m}_p \tag{13.11}$$

A schematic of the evaporation process is represented in Fig. 13.3.1.

Far-field properties are evaluated at the nodes of the cell containing the droplet, while gaseous properties are interpolated at the droplet location and are noted $T_{@p}$ and $Y_{\mathcal{K}@p}$. Because the particle temperature is uniform, the surface temperature T_ζ corresponds to the particle temperature T_p.

The evaporated species mass fraction at the surface of the droplet $Y_{\mathcal{K},\zeta}$ is evaluated from the saturation vapour pressure $P_{sat,\mathcal{K}}$ as:

$$Y_{\mathcal{K},\zeta} = X_{\mathcal{K},\zeta} \frac{W_{\mathcal{K}}}{\overline{W}_\zeta} \tag{13.12}$$

where $X_{\mathcal{K},\zeta}$ the evaporated species surface mole fraction is computed with the Clausius-Clapeyron relation considering thermodynamic equilibrium as:

$$X_{\mathcal{K},\zeta} = \frac{P_{sat,\mathcal{K}}}{P_{@p}} \tag{13.13}$$

and $\overline{W}_\zeta$ is the mean molecular weight at the droplet surface written as:

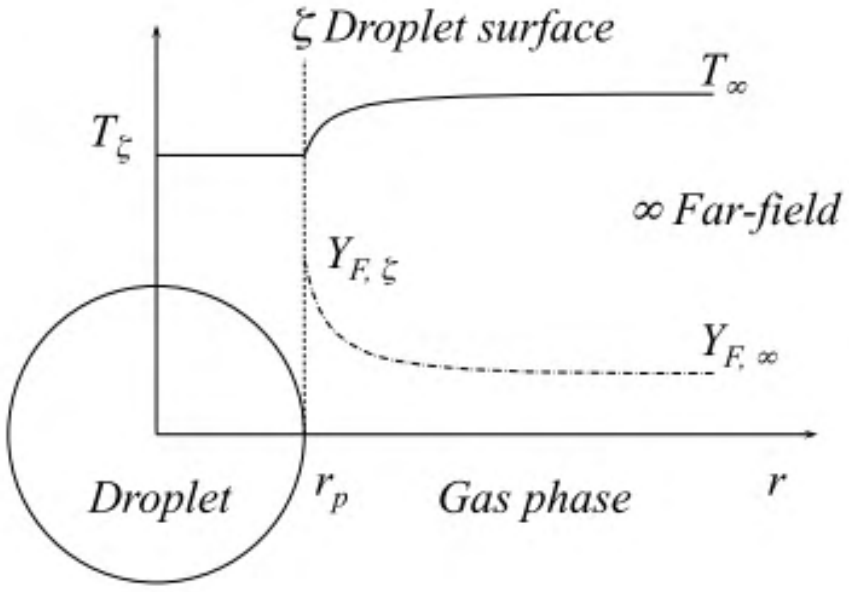

Figure 13.3.1: Evolution of the temperature and liquid species mass fraction (noted F here) along the radial distance from a spherical droplet surface, adapted from [Potier, 2018]

$$\overline{W} = X_{\mathcal{K},\zeta} W_{\mathcal{K}} + (1 - X_{\mathcal{K},\zeta}) W_{mixture@p} \tag{13.14}$$

As reviewed by [Miller et al., 1998], because the model assumes that the vapour and surrounding gas properties are constant in space, one must define an average state representing the real spatial variations. The reference temperature and the reference vapour mass fractions are written with the "1/3 rule" as:

$$T_{ref} = T_{\zeta} + \frac{1}{3}(T_{@p} - T_{\zeta}) \tag{13.15}$$

$$Y_{\mathcal{K},ref} = Y_{\mathcal{K},\zeta} + \frac{1}{3}(Y_{\mathcal{K}@p} - Y_{\mathcal{K},\zeta}) \tag{13.16}$$

The terms $\rho D_{\mathcal{K}}$ and $\frac{\lambda}{C_p}$ respectively from Eqs. 13.9 and 13.10 are determined from an evaporation Schmidt number $Sc_{\mathcal{K},evap}$ and an evaporation Prandtl number Pr_{evap} retrieved from the gaseous species, and the viscosity computed from the Wilkes equation (Eq. 1.44) as :

$$\rho D_{\mathcal{K}} = \frac{\mu(T_{ref})}{Sc_{\mathcal{K},evap}} \tag{13.17}$$

$$\frac{\lambda}{C_p} = \frac{\mu(T_{ref})}{Pr_{evap}} \tag{13.18}$$

The integration of Eq. 13.9 between the droplet surface and the surrounding gas leads to:

$$\dot{m}_p = -2\pi d_p \rho D_{\mathcal{K}} \ln(B_M + 1) \tag{13.19}$$

where B_M is the mass Spalding transfer number given by:

$$B_M = \frac{Y_{\mathcal{K},\zeta} - Y_{\mathcal{K}@p}}{1 - Y_{\mathcal{K},\zeta}} \tag{13.20}$$

The integration of Eq. 13.10 gives

$$\frac{dC_{p,liq}T_p}{dt} = \frac{1}{m_p}\left(2\pi d_p \frac{\lambda}{C_P}\left(C_P\left(T_{@p}\right)T_{@p} - C_P\left(T_p\right)\right)T_p\right)\frac{\ln\left(B_T+1\right)}{B_T} + \dot{m}_p L_{v,\mathcal{K}}\left(T_p\right)\Bigg) \tag{13.21}$$

where $L_{v,\mathcal{K}}(T_p)$ is the latent heat of vaporisation of the liquid species $\mathcal{K}$ and B_T is the temperature Spalding transfer number given by:

$$B_T = \left(1 + B_M\right)^{\frac{Pr_{evap}}{Sc_{\mathcal{K},evap}}} - 1 \tag{13.22}$$

Abramzon & Sirignano correction

The hypothesis upon which the gas and the droplet are at rest is not always true in practical applications and an important relative velocity between the gas and the droplet (of the order of $Re_p \approx 500$) leads to an enhanced evaporation process. [Ranz, 1952] introduced a Sherwood and Nusselt number, Sh and Nu respectively in order to model this effect:

$$Sh = 2 + 0.55 Re_p^{\frac{1}{2}} Sc_{\mathcal{K},evap}^{\frac{1}{3}} \tag{13.23}$$

$$Nu = 2 + 0.55 Re_p^{\frac{1}{2}} Pr_{evap}^{\frac{1}{3}} \tag{13.24}$$

These numbers were later modified by [Abramzon and Sirignano, 1989] to account for the vapour film around the droplet allowing a more accurate estimation of the fluxes as:

$$Sh^* = 2 + \frac{(Sh-2)}{F_M} \tag{13.25}$$

$$Nu^* == 2 + \frac{(Nu-2)}{F_T} \tag{13.26}$$

where

$$F_M = (1 + B_M)^{0.7} \frac{\ln(1 + B_M)}{B_M} \tag{13.27}$$

$$F_T = (1 + B_T)^{0.7} \frac{\ln(1 + B_T)}{B_T} \tag{13.28}$$

Eqs. 13.19 and 13.21 are then modified to account for this effect as:

$$\dot{m}_p = -Sh^* \pi d_p \frac{\mu(T_{ref})}{Sc_{\mathcal{K},evap}} \ln(B_M + 1) \tag{13.29}$$

$$\frac{dC_{p,liq}T_p}{dt} = \frac{1}{m_p} \left(Nu^* \pi d_p \frac{\mu(T_{ref})}{Pr_{evap}} C_P(T_{ref})(T_{@p} - T_p) \frac{\ln(B_T + 1)}{B_T} + \dot{m}_p L_{v,\mathcal{K}}(T_p) \right) \tag{13.30}$$

Multi-component evaporation model

As described in Section 11.1, the composition of a real fuel is complex and involves a large number of species. In order to be consistent with the multi-components surrogates chosen for the gaseous phase, the liquid phase should also consider a multi-components formulation.

The two major families of multi-component models are the continuous and discrete models. In the first family, the experimental composition of the liquid fuel involving many species is modelled through a probability distribution function (PDF) used to track the mass distribution of a family of chemical components (n-alkanes, aromatics, etc.) [Hallett, 2000]. This method allows a very accurate representation of the physical properties of the droplets however this model requires a lot of data that are in practice not compatible with the ARC methodology for the gas phase as it would produce too many vapour species for the gas phase kinetics, and possibly introduce too complex chemistry for some species.

For that reason, the second family of methods will be used in this work and has been integrated in AVBP. In the discrete multi-components model [Ra and Reitz, 2009], both the liquid and gaseous fuel surrogates are the same and the evaporation of each species is tracked individually while the droplet characteristics correspond to mixing values. The model is based on the equations previously presented where $\mathcal{K}$ represents now not only one species but any species present in the surrogate model. The liquid molar and mass fractions are introduced as $X_{liq,\mathcal{K}}$ and $Y_{liq,\mathcal{K}}$ respectively with $\sum_k^{N_{liq}} X_{liq,\mathcal{K}} = \sum_k^{N_{liq}} Y_{liq,\mathcal{K}} = 1$ with N_{liq} the number of liquid species in the droplet. Note that because of preferential evaporation, the number of liquid species may decrease in time if one or several species completely evaporates before the others.

The liquid density ρ_{liq} is found through a simple molar averaging as:

$$\rho_{liq} = \sum_k^{N_{liq}} \rho_{liq,\mathcal{K}} X_{liq,\mathcal{K}} \tag{13.31}$$

The liquid heat capacity $C_{p,liq}$ is found through a mass averaging:

$$C_{p,liq} = \sum_k^{N_{liq}} C_{p,liq,\mathcal{K}} Y_{liq,\mathcal{K}} \tag{13.32}$$

The Clausius-Clapeyron relation giving the surface mole fraction now accounts for the different liquid species as:

$$X_{\mathcal{K},\zeta} = X_{\mathcal{K},liq} \frac{P_{sat,\mathcal{K}}}{P_{@p}} \tag{13.33}$$

and the mean molecular weight at the droplet surface $\overline{W}_\zeta$ now writes:

$$\overline{W}_\zeta = \sum_{\mathcal{K}}^{N_{liq}} X_{\mathcal{K},\zeta} W_{\mathcal{K}} + (1 - X_{\mathcal{K},\zeta}) W_{mixture@p} \tag{13.34}$$

Eq. 13.29 no longer gives the global mass variation of the particle but the mass variation of the species $\mathcal{K}$ and writes:

$$\dot{m}_{\mathcal{K},p} = -Sh^* \pi d_p \rho D_{\mathcal{K}} \ln(B_M + 1) \tag{13.35}$$

with $\sum_{\mathcal{K}}^{N_{liq}} \dot{m}_{\mathcal{K},p} = \dot{m}_p$

Eq. 13.29 also changes to:

$$\frac{dC_{p,liq}T_p}{dt} = \frac{1}{m_p}\left(Nu^* \pi d_p \lambda(T_{ref})(T_{@p} - T_p)\frac{\ln(B_T+1)}{B_T} + \sum_{\mathcal{K}}^{N_{liq}} \dot{m}_{\mathcal{K},p} L_{v,\mathcal{K}}(T_p)\right) \tag{13.36}$$

Note that the approximations introduced in Eqs. 13.17 and 13.18 for $D_{\mathcal{K}}$, λ and μ are no longer used and more precise estimations using temperature polynomials from [Yaws, 2009][Yaws, 2015] are preferred.

13.4 Gaseous phase coupling

The coupling between the liquid and gaseous phase is done by simply transferring conservatively $\dot{m}_p$, $F^{ext}_{p,i}$ and $\dot{\Phi}_p$ for all droplets to the gaseous phase.

- Source term of mass added to the RHS of Eq. 8.6:

$$S_m^{l\to g} = \frac{1}{\Delta V}\sum_p^{N_p} \Psi_p \dot{m}_p \tag{13.37}$$

- Source term of evaporating species added to the RHS of Eq. 8.7:

$$S_{m_k}^{l\to g} = \frac{1}{\Delta V}\sum_p^{N_p} \Psi_p \dot{m}_{\mathcal{K},p}\delta_{k,\mathcal{K}} \tag{13.38}$$

- Source term of momentum added to the RHS of Eq. 8.8:

$$S_{mu,i}^{l\to g} = \frac{1}{\Delta V}\sum_p^{N_p} \Psi_p(-m_p F^{ext}_{p,i} + \dot{m}_p u_{p,i}) \tag{13.39}$$

- Source term of energy added to the RHS of Eq. 8.9:

$$S_{m_\mathcal{K}}^{l\to g} = \frac{1}{\Delta V}\sum_{p}^{N_p}\Psi_p\left(-m_p\underline{F_p^{ext}}.\underline{u_p} + \frac{1}{2}\dot{m}_p||\underline{u_p}||^2 - \dot{\Phi}_p\right) \tag{13.40}$$

ΔV is the local control volume where the particle is located and N_p the number of particles in that volume. Ψ_p is the inverse distance interpolation function between the particle position and the grid nodes.

Chapter 14

One-dimensional premixed flames fed by Lagrangian droplets

Contents

The effect of the fuel with a multi-component description on the spray flame stabilised inside a combustor can be apprehended with a canonical one-dimensional steady flame with droplet injection.

14.1 Previous work on multi-component spray flame propagation

Propagation of a spray flame in a canonical one-dimensional configuration was already studied by [Rochette et al., 2019]. In this study Lagrangian n-heptane droplets were injected with different relative velocities compared to the air just in front of the flame as depicted in Fig. 14.1.1. By avoiding pre-evaporation, this method allows to control the composition of the reactant mixture seen by the flame. In this work combustion was described with a 2-step chemical mechanism.

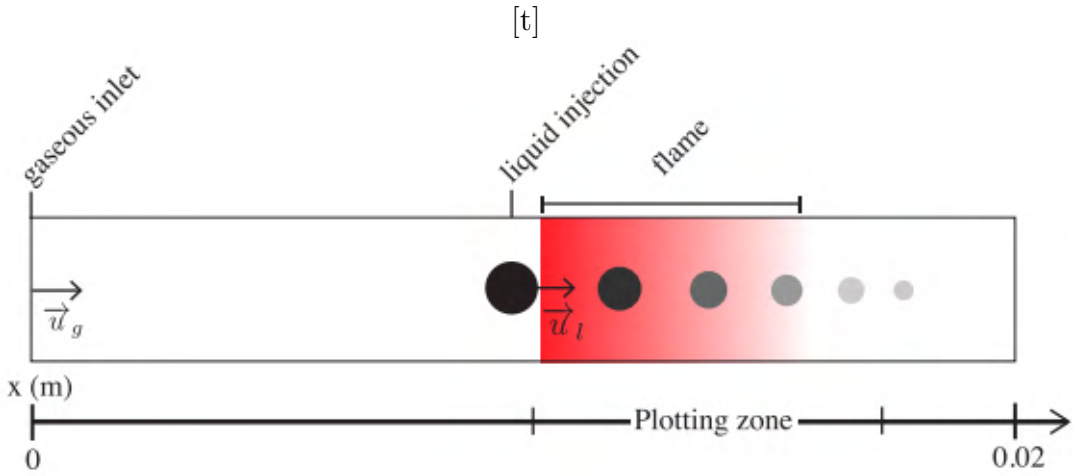

Figure 14.1.1: One-dimensional two-phase flame from [Rochette et al., 2019]

A similar study was later conducted by [Shastry et al., 2020b] for a Jet-A1 3-components surrogate using an ARC mechanism, with an emphasis on the effects of the multi-components description. The surrogate was made of n-dodecane, methylcyclohexane and xylene in different proportions than previously stated in Section 12. This work used a surrogate composed of 30.3% of n-dodecane, 48.5% of methylcyclohexane and 21% of xylene in volume from [Narayanaswamy et al., 2016a]. The differences between the two surrogates arise from the optimisation method that was used to produce them and the parameters weighting of the selected parameters. This surrogate was more focused on retrieving the H/C ratio, the cetane number and the threshold sooting index while the surrogate from Section 12 has a better overall agreement especially on molecular weight. The ARC mechanism was derived from the

detailed mechanism of [Narayanaswamy et al., 2016a]. As in [Rochette et al., 2019], the two-phase flame speed and flame structure were studied for different relative velocities between the droplet and the fresh gases as well as for different equivalence ratio and liquid loading of the unburned mixture. The full paper is available in Appendix D and only a short summary is reported here.

The droplet evaporation model described in Section 13.3.2 was first validated against experiment and showed a good agreement concerning the evolution of the Normalised Diameter (ND) and the temperature (see Figure 14.1.2). The different volatilities of the components lead to the variation in time of the composition of the evaporation flux, as shown in Fig. 14.1.2. The most volatile species methylcyclohexane evaporates first, followed by xylene and finally n-dodecane.

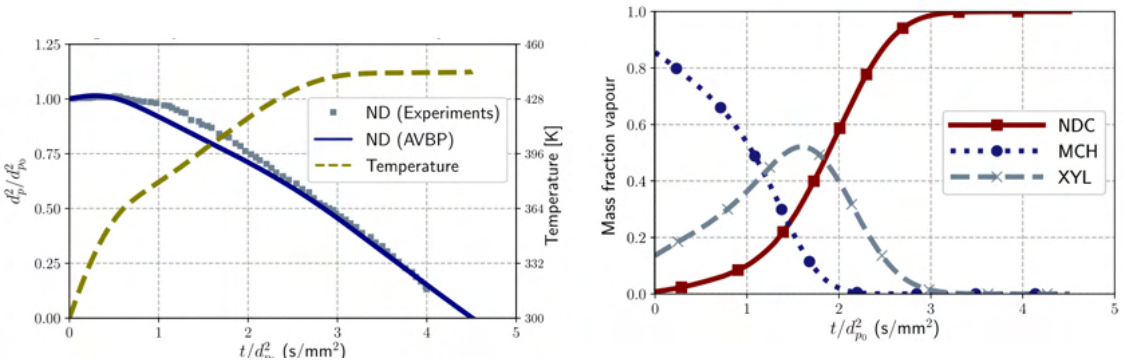

(a) Evolution of ND and temperature (b) Composition of the evaporating flux

Figure 14.1.2: Single droplet of Jet-A1 evaporation. $d_{p_0} = 1000$ μm at 300 K in quiescent air at 773 K. From [Shastry et al., 2020b]

Flames were then obtained with a mixture of fuel and air injected at 400K and 1 bar. Three cases were computed. In Case A the gaseous equivalence ratio ϕ_g was 0.8 (lean) and the liquid injection was set to a liquid equivalence ratio ϕ_l of 0.1, giving a total equivalence ratio $\phi_{tot} = \phi_l + \phi_g = 0.9$. Case B also features a gaseous equivalence ratio ϕ_g of 0.8 and has a liquid equivalence ratio of 0.5, reaching a rich total equivalence ratio of 1.3. Finally, for Case C, the total equivalence ratio comes entirely from the liquid part with $\phi_g = 0$ and $\phi_{tot} = \phi_l = 0.9$. The simulated operating conditions are summarised in Fig. 14.1.3.

Depending on the droplet size and velocity, two limiting cases were found in Cases A and B. Firstly, for small or slow droplets, evaporation is fast enough to make the effective equivalence ratio ϕ_{eff}, which is defined as the equivalence ratio of

Conditions of simulated cases.

Case name	ϕ_{tot}	$\phi_{gas,liq}$	u^*	d_{p_0} (μm)
A	0.9	$\phi_{gas} = 0.8$ $\phi_{liq} = 0.1$	1, 30	5–80
B	1.3	$\phi_{gas} = 0.8$ $\phi_{liq} = 0.5$	1, 30	5–80
C	0.9	$\phi_{gas} = 0.0$ $\phi_{liq} = 0.9$	1, 30	5–80

Figure 14.1.3: Operating conditions studied in [Shastry et al., 2020b]

the equivalent gaseous flame, is equal to the total equivalence ratio ϕ_{tot}. The second limiting case corresponds to larger or faster droplets, which do not evaporate fast enough to feed the flame resulting in $\phi_{eff} = \phi_g$.

In Case B a small secondary reaction zone is observed due to the high amount of available fuel vapour, which reacts with the remaining oxygen from the lean primary reaction zone. Moreover, because in this case $\phi_{tot} = 1.3$ and the effective equivalence ratio ϕ_{eff} can reach stoichiometry, it is possible to find values of droplet size and velocity giving a laminar flame speed higher than the purely gaseous laminar flame speed at ϕ_{tot}.

From these observations, a correlation for the effective equivalence ratio ϕ_{eff} was obtained:

$$\phi_{eff} = \sum_{\mathcal{K}} \left(\frac{\delta_L^0}{max(\delta_L^0, \delta_{ev}^{\mathcal{K}})} \right)^{\frac{2}{3}} \left(\frac{s_{\mathcal{K}}}{s_{Jet-A1}} \right) \phi_l + \phi_g \tag{14.1}$$

where δ_L^0 is the laminar flame thickness, $\delta_{ev}^{\mathcal{K}}$ the evaporation thickness of component $\mathcal{K}$, $s_{\mathcal{K}}$ the molar stoichiometric ratio of the component $\mathcal{K}$ and s_{Jet-A1} the molar stoichiometric ratio of the blend. The validity of the correlation was demonstrated with a comparison with simulation results, presented in Fig. 14.1.4.

Case C, that was only piloted by evaporation, was found more complex and found to fall out of the aforementioned correlation.

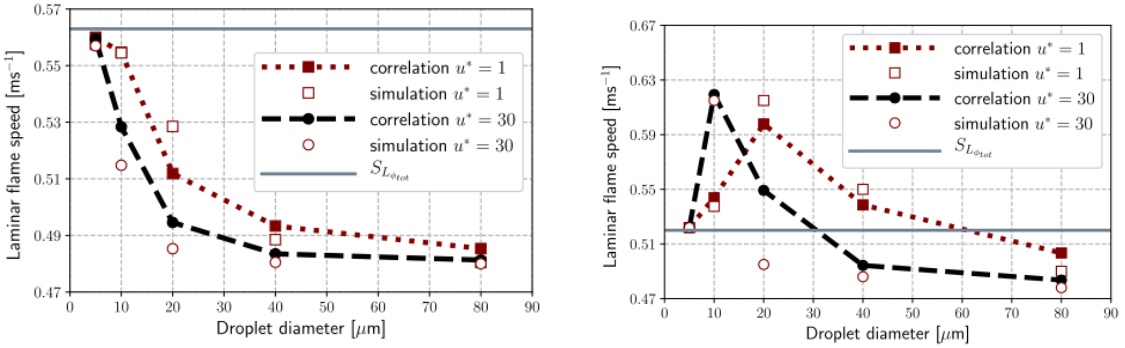

(a) Two-phase flame speed of Jet-A1 vs initial droplet diameter. Comparison between simulations and correlations for Case A.

(b) Two-phase flame speed of Jet-A1 vs initial droplet diameter. Comparison between simulations and correlations for Case B.

Figure 14.1.4: Single droplet of Jet-A1 evaporation. $d_{p_0} = 1000$ μm at 300K in quiescent air at 773 K. From [Shastry et al., 2020b]

14.2 Numerical setup for two-phase flames with the JETSCREEN fuels

The computational domain consists in a 0.02 m long one-dimensional uniform cartesian grid containing 2000 elements. The cell size of $\Delta x = 10$ μm enables to sufficiently resolve the flame front without thickening it. Indeed, as for all the studied flames the gaseous laminar flame thickness is around 300 μm and because of the liquid phase, the flames are always thicker. This ensures a minimum of 10 points in the thermal flame thickness. The actual thickness of the flames will be later assessed.

For each of the fuels A1, B1 and C1, 2 droplet sizes will be considered : 20 μm and 60 μm and no fuel vapor is injected ($\phi_g = 0$).

The droplets are injected with air at the same temperature of 300 K, ahead of the flame at x=0.005 m. Downstream this point, the domain is initialised with air at 2500 K to establish a flame. This initialisation ensures that a flame is created once enough liquid fuel has evaporated. The inlet velocity is adapted jointly with the droplet injection velocity $u_g = u_{droplet}$ in order to keep a null relative velocity between the two phases. The total equivalence ratio is $\phi_{tot} = \phi_l = 1$.

With the general formula of $n_{e,phase}$ denoting the number of moles of the element

e in the specific phase (gas or liquid) written as :

$$n_{e,phase} = \sum_{k}^{N_s} \frac{n_{e,k} m_{k,phase}}{W_k} = m_{phase} \sum_{k}^{N_s} \frac{Y_{k,phase}}{W_k} \tag{14.2}$$

where $n_{e,k}$ is the number of element e in species k and $m_{k,phase}$ is the mass of species k in the considered phase, one obtains :

$$\phi_g = \frac{2n_{C,gas} + 0.5n_{H,gas}}{n_{O,gas}} \tag{14.3}$$

$$\phi_l = \frac{2n_{C,liquid} + 0.5n_{H,liquid}}{n_{O,gas}} \tag{14.4}$$

Because the liquid equivalence ratio ϕ_l depends on the gaseous density, values higher than the targeted equivalence ratio can arise when droplets are present in a zone where the gaseous density is lower than the fresh gas density. For that reason, a normalised liquid equivalence ratio is preferred and is written as:

$$\phi_l^* = \phi_l \frac{\rho_g}{\rho_{g,0}} \tag{14.5}$$

where ρ_g is the gas density and $\rho_{g,0}$ its inlet value.

The total equivalence ratio ϕ_{tot} can be retrieved by:

$$\phi_{tot} = \phi_g + \phi_l = \frac{2(n_{C,gas} + n_{C,liquid}) + 0.5(n_{H,gas} + n_{H,liquid})}{n_{O,gas}} \tag{14.6}$$

The normalisation applied on ϕ_l is also applied on ϕ_{tot} with $\phi_{tot}^* = \phi_g + \phi_l^*$. For the sake of simplicity, ϕ_l^* and ϕ_{tot}^* will be referenced as ϕ_l and ϕ_{tot} in the following.

For a stoichiometric mixture, the expected component mass fractions are reported in the following table.

Fuel	component name	stoichiometric mass fraction
	n-dodecane	$45.54e^{-3}$
A1	methyl-cyclohexane	$8.75e^{-3}$
	xylene	$9.46e^{-3}$
	iso-octane	$3.37e^{-3}$
B1	iso-dodecane	$52.70e^{-3}$
	iso-cetane	$6.08e^{-3}$
	decalin	$37.38e^{-3}$
C1	iso-dodecane	$12.81e^{-3}$
	methyl-naphthalene	$15.35e^{-3}$

Table 14.2.1: Mass fractions of the fuel components for blends mixed at stoichiometric conditions with air.

14.3 Flame structure

The flames in the above conditions were found more difficult to stabilise than flames with $\phi_g \neq 0$, for which the laminar flame speed varies only slightly around the value expected at ϕ_g. When $\phi_g = 0$ evaporation may significantly modify the flame speed.

Note that because of the discretisation and the frequency of injection of the particles, the profiles shown hereafter are not perfectly smooth.

14.3.1 A1 flame

For clarity the fuel species which are n-dodecane, methyl-cyclohexane and xylene, are abbreviated as *nc*12, *mcyc* and *xyl* respectively in the following figures, and are represented by the same colours used in Chap. 12 for the different components classes with n-dodecane in blue, methyl-cyclohexane in yellow and xylene in green.

Case of 20 μm droplets

The spatial evolution of the gaseous and liquid equivalence ratio in Fig. 14.3.1 gives a first indication on the droplet evaporation process. The droplets are first evaporating slowly between their injection point at 5 mm and approximately 7.4 mm, before rapidly reaching full evaporation at 9 mm. Note that the total equivalence ratio does not stay constant at 1, and slightly decrease in the flame zone. This is due to transport effects: because of droplet inertia, it does not accelerate as the gas through the flame but with some delay. In addition, preferential diffusion effects may also lead to variations of the equivalence ratio. These effects disappear in the burnt gas where the equivalence ratio comes back to 1.

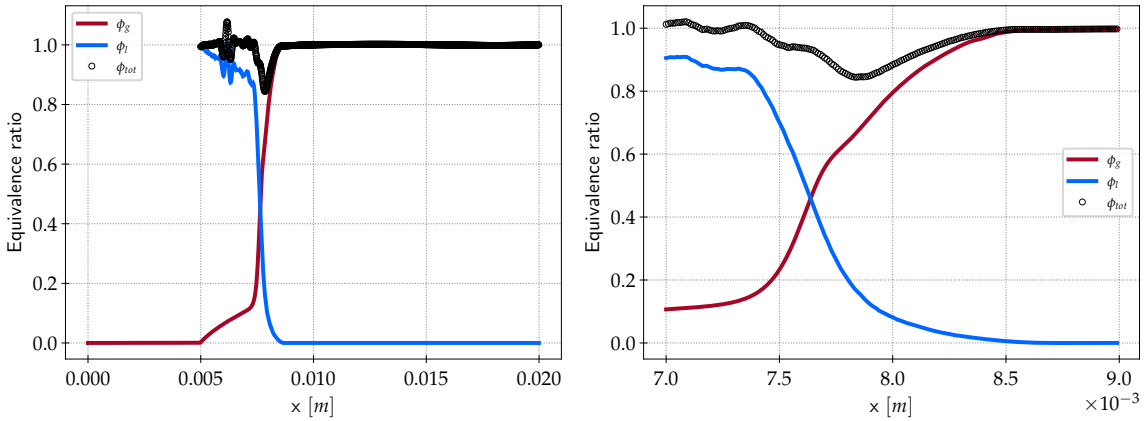

(a) Full domain (b) Zone of interest

Figure 14.3.1: Spatial profile of the gaseous equivalence ratio ϕ_g (solid red line), the liquid equivalence ratio ϕ_l (solid blue line) and the total equivalence ratio ϕ_{tot} (black circles) on (a) the full domain and (b) the zone of interest.

The first phase of evaporation corresponds to the cold reactant mixture feeding the flame, where the low temperature leads to a very slow evaporation of the most volatile species which are methyl-cyclohexane and xylene as seen in Fig. 14.3.2. In this zone the combustion source terms are zero.

Figure 14.3.3 represents the liquid mass of each components in the domain. Before the flame front, only a small amount of n-dodecane has evaporated whereas nearly half of the initial methyl-cyclohexane mass has evaporated. However, this zone has a negligible impact on the reaction zone as it only elevates the gaseous equivalence

ratio to 0.1 which is not sufficient to allow sustainable combustion.

The reaction zone is shown in Fig. 14.3.4 with the species consumption rates and the heat release rate. The methyl-cyclohexane which evaporates first, also burns first, followed by xylene and finally n-dodecane, which stretches the reaction zone toward the burnt gas side, under the effect of flow acceleration.

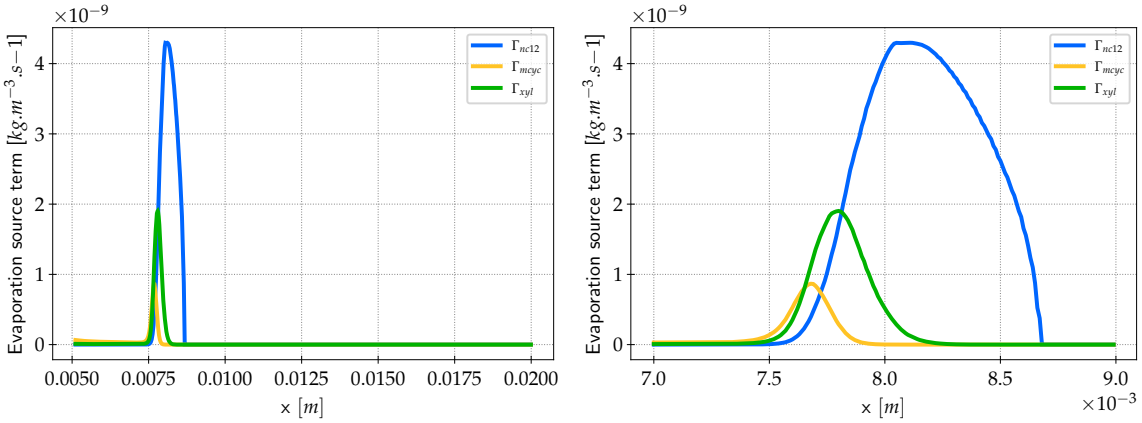

(a) Full domain (b) Zone of interest

Figure 14.3.2: Spatial profile of the evaporation mass flow rate for each fuel species n-dodecane, methyl-cyclohexane and xylene (respectively in blue, yellow and green) on (a) the full domain and (b) the zone of interest for A1 with 20 μm droplets.

Figures 14.3.6 to 14.3.8 compare the normalised evaporation and consumption rates for each species. For the most volatile species which are methyl-cyclohexane and xylene, it exists a zone on the fresh mixture side where only evaporation occurs and the fuel vapour is not consumed. This explains their peak mass fractions just in front of the flame. Then in the flame and in the burnt gas, the vapour of the two species is consumed as soon as it is produced and therefore keeps a negligible mass fraction. On the contrary, n-dodecane vapour is produced slowly and is quickly consumed. While being the major component of the fuel, n-dodecane mass fraction in the gas stays therefore very small in comparison to the other two components. N-dodecane is also the species feeding the trailing heat release zone located between 8 and 9 mm. Because if this slow evaporation, n-dodecane is not fully contributing to the flame propagation.

Finally, the delay in the peaks between methyl-cyclohexane consumption rate and heat release rate, represented by the vertical grey line in Fig. 14.3.7 is due

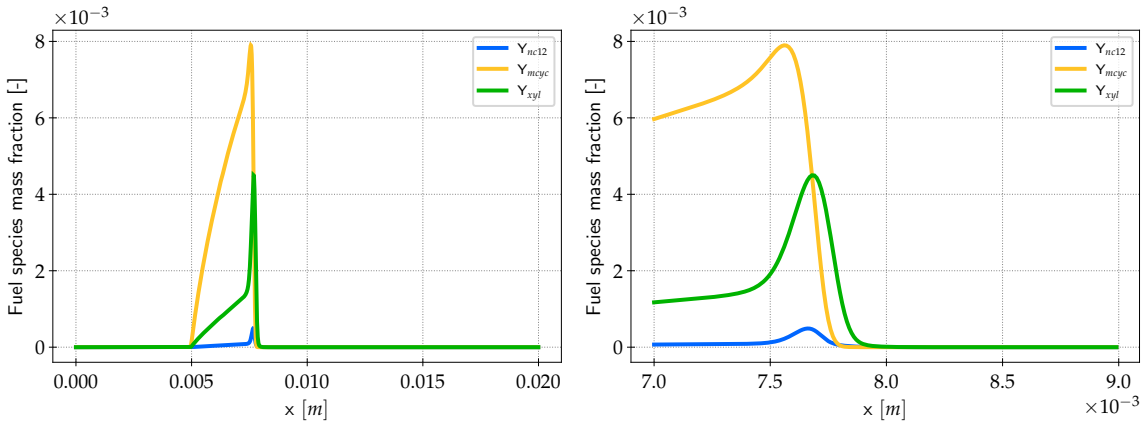

(a) Full domain (b) Zone of interest

Figure 14.3.3: Spatial profile of the fuel species mass fractions n-dodecane, methyl-cyclohexane and xylene (respectively in blue, yellow and green) on (a) the full domain and (b) the zone of interest for A1 with 20 μm droplets.

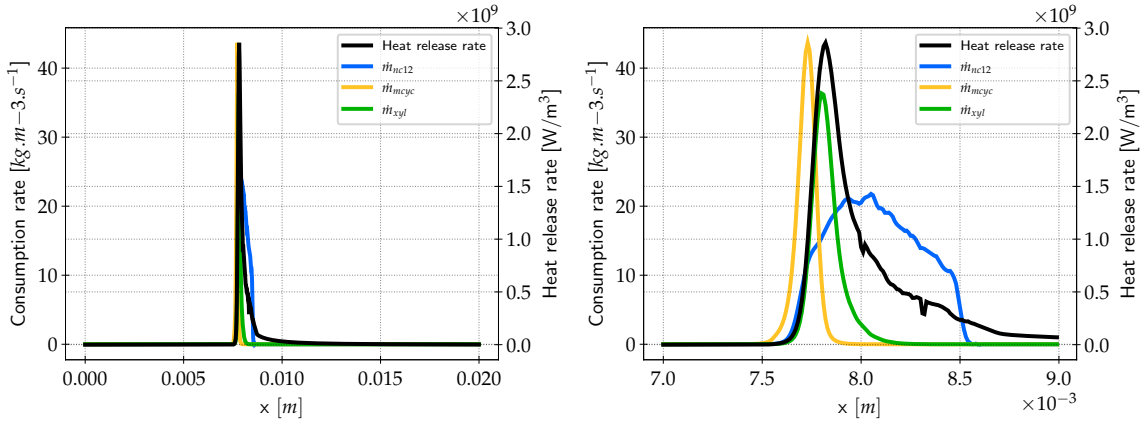

(a) Full domain (b) Zone of interest

Figure 14.3.4: Spatial profile of the fuel species consumption rates n-dodecane, methyl-cyclohexane and xylene (respectively in blue, yellow and green) and the heat release rate (black) on (a) the fuel domain and (b) the zone of interest for A1 with 20 μm droplets.

to the endothermic pyrolysis phase of the fuel component which occurs before the exothermic oxidation phase.

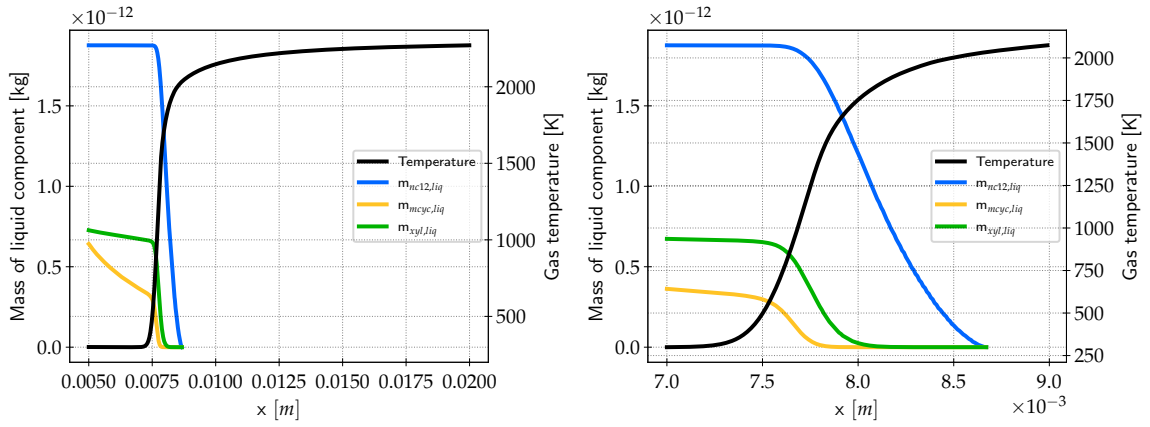

(a) Full domain (b) Zone of interest

Figure 14.3.5: Gaseous temperature (black) and mass of the liquid components; n-dodecane, methyl-cyclohexane and xylene (respectively in blue, yellow and green) on (a) the fuel domain and (b) the zone of interest for A1 with 20 μm droplets.

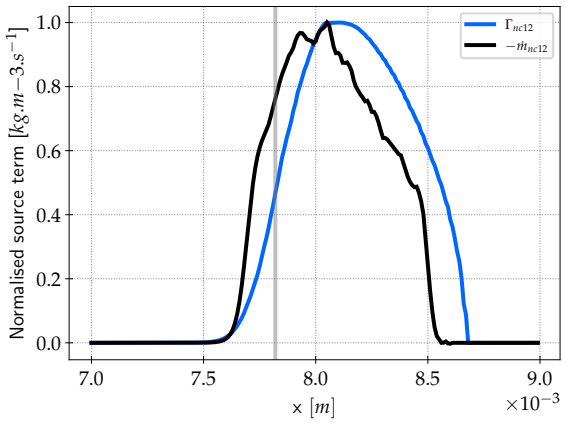

Figure 14.3.6: Spatial profile of the normalised evaporation source term (blue) and the normalised consumption rate (black) of n-dodecane on the zone of interest for A1 with 20 μm droplets. The vertical grey line represents the position of the peak heat release rate.

60 μm droplet

Overall, and according to Fig. 14.3.9, the 60 μm droplet flame appears as a widened version of the previous flame, with an extended slow evaporation zone followed by

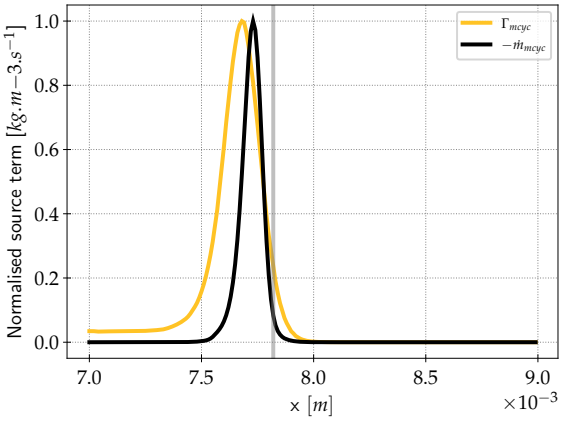

Figure 14.3.7: Spatial profile of the normalised evaporation source term (yellow) and the normalised consumption rate (black) of methyl-cyclohexane on the zone of interest for A1 with 20 μm droplets. The vertical grey line represents the position of the peak heat release rate.

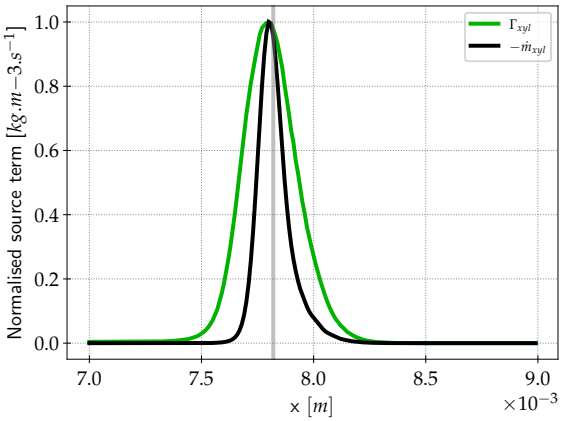

Figure 14.3.8: Spatial profile of the normalised evaporation source term (green) and the normalised consumption rate (black) of xylene on the zone of interest for A1 with 20 μm droplets. The vertical grey line represents the position of the peak heat release rate.

an also extended high evaporation and reactive zone between. The longer slow evaporation zone is due to the difficulty of stabilising the flame at the exact same location as the previous one. Nevertheless, the same gaseous equivalence ratio of approximately 0.1 is reached at the end of this zone which makes the comparison of

the downstream region valid.

The larger droplets lead to a slower evaporation and a longer evaporation zone. Estimating this length by considering the position between 10% (to avoid considering the slow evaporation zone) and 100% of the total mass evaporation, we obtain an evaporation thickness of 1.73 mm for the 20 μm droplets and 4.62 μm for the 60 μm droplets, which gives a ratio of 2.67 between the two cases.

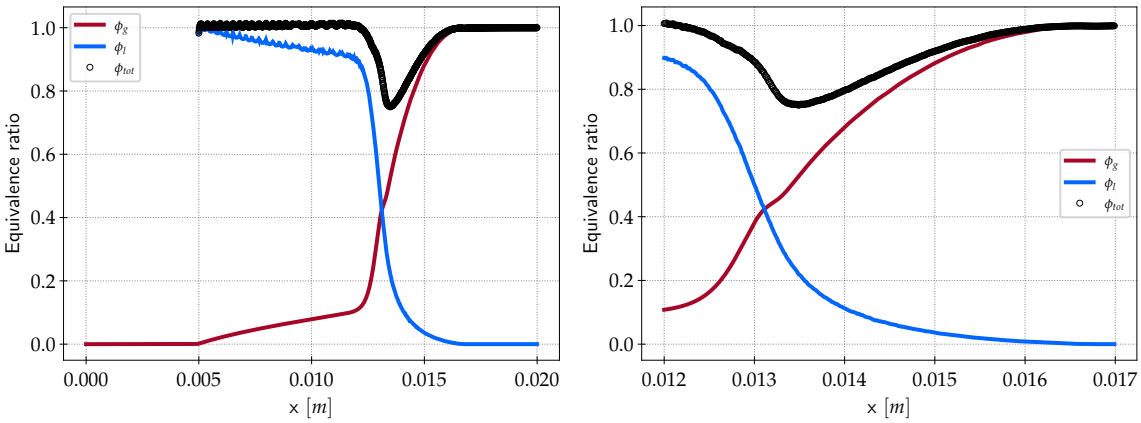

(a) Full domain (b) Zone of interest

Figure 14.3.9: Spatial profile of the gaseous equivalence ratio ϕ_g (solid red line), the liquid equivalence ratio ϕ_l (solid blue line) and the total equivalence ratio ϕ_{tot} (black circles) on (a) the full domain and (b) the zone of interest for A1 with 60 μm droplets.

From Fig. 14.3.10, the staged evaporation seems slightly more pronounced but keeps the same hierarchy than in the previous case, with methyl-cyclohexane and xylene being responsible for the peak of heat release rate. The trailing heat release zone is also longer due to the larger droplet size and slower evaporation of the n-dodecane, also visible in Fig. 14.3.13. In terms of consumption rate, the methyl-cyclohexane, in Fig. 14.3.15 behaves similarly to the 20 μm droplets case with only a slight shift of the evaporation peak toward the burnt gas side, due to slower evaporation. Xylene and n-dodecane differ more strongly.Xylene, represented in 14.3.16 starts to be consumed sooner compared to its evaporation rate and subsists further downstream of the flame front as the droplets survive longer beyond the flame front.

That is also the case for n-dodecane, but here, the consumption rate represented

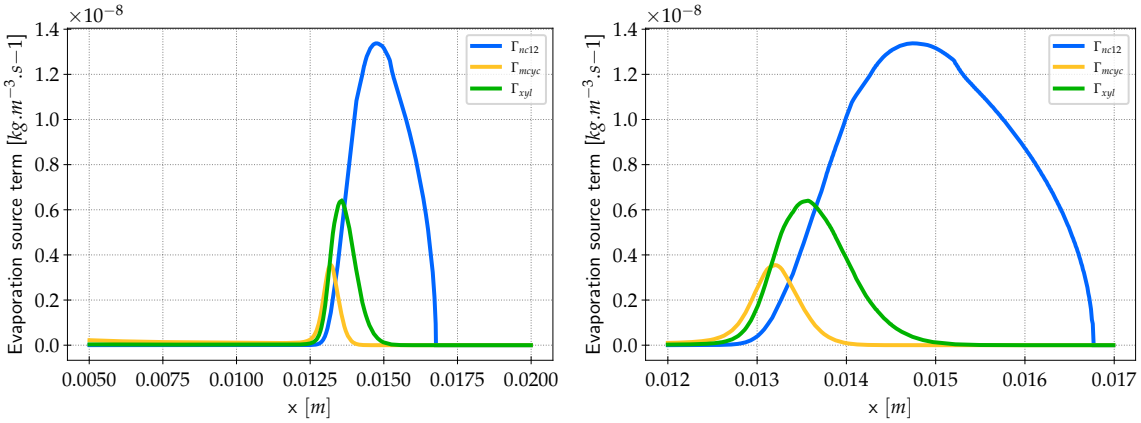

(a) Full domain (b) Zone of interest

Figure 14.3.10: Spatial profile of the evaporation mass flow rate for each fuel species n-dodecane, methyl-cyclohexane and xylene (respectively in blue, yellow and green) on (a) the full domain and (b) the zone of interest for A1 with 60 μm droplets..

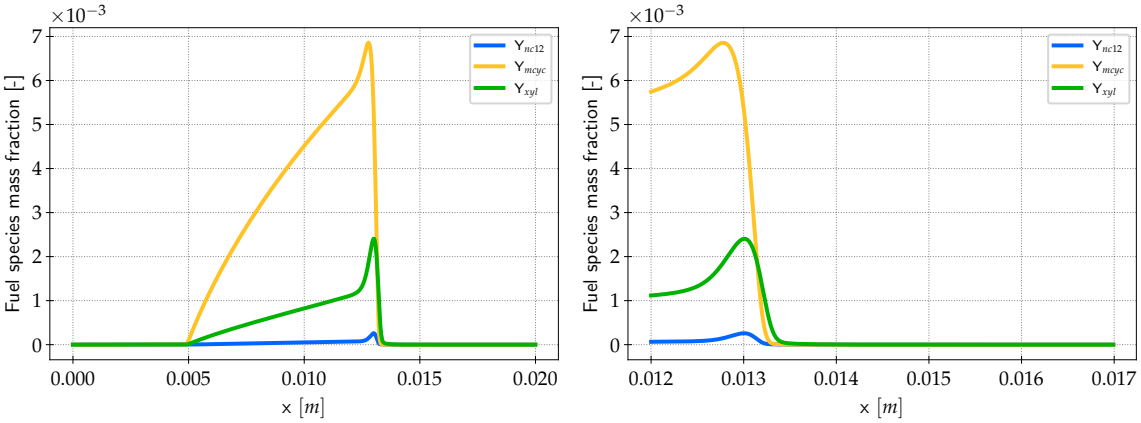

(a) Full domain (b) Zone of interest

Figure 14.3.11: Spatial profile of the fuel species mass fractions n-dodecane, methyl-cyclohexane and xylene (respectively in blue, yellow and green) on (a) the full domain and (b) the zone of interest for A1 with 60 μm droplets.

in Fig. 14.3.14 becomes locally stiff with important oscillations meaning that the evaporated n-dodecane is consumed within one timestep via pyrolysis.

To summarize, similar conclusions can be drawn for both droplet sizes, larger

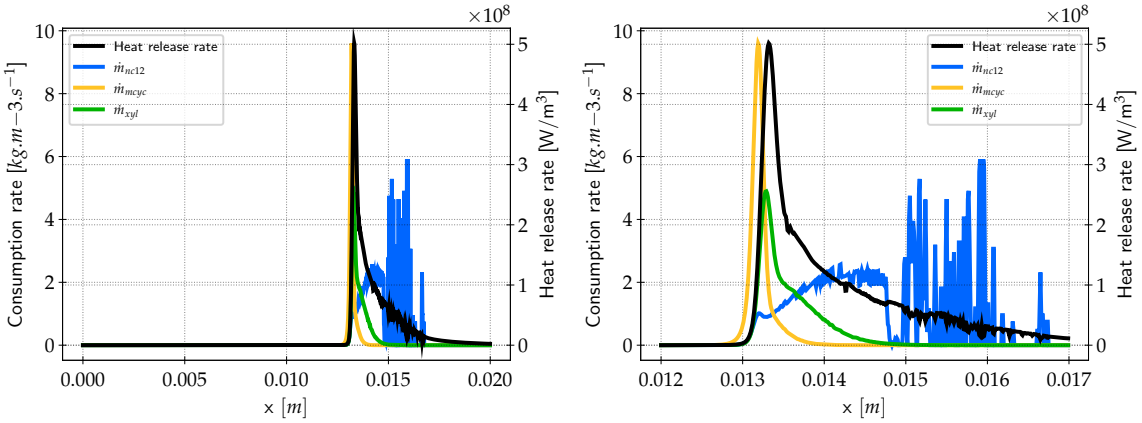

(a) Full domain (b) Zone of interest

Figure 14.3.12: Spatial profile of the fuel species consumption rates n-dodecane, methyl-cyclohexane and xylene (respectively in blue, yellow and green) and the heat release rate (black) on (a) the full domain and (b) the zone of interest for A1 with 60 μm droplets.

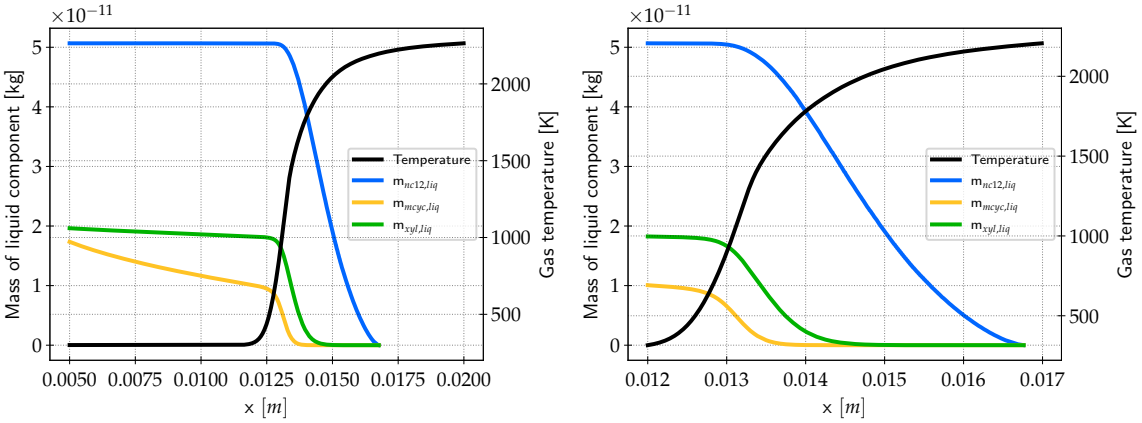

(a) Whole droplet life (b) Zone of interest

Figure 14.3.13: Gaseous temperature (black) and mass of the liquid components; n-dodecane, methyl-cyclohexane and xylene (respectively in blue, yellow and green) on (a) the fuel domain and (b) the zone of interest for A1 with 60 μm droplets.

droplets only accentuating the effects of multi-component evaporation without modifying the qualitative behaviour of the flame. For that reason, only the 20 μm droplets cases will be commented for the two other alternative fuels B1 and C1. The 60 μm

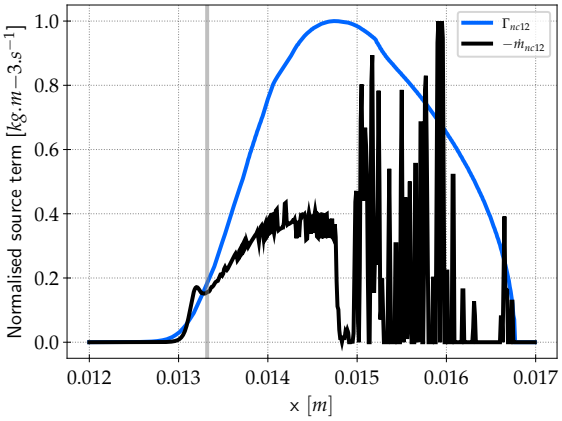

Figure 14.3.14: Spatial profile of the normalised evaporation source term (blue) and the normalised consumption rate (black) of n-dodecane on the zone of interest for A1 with 60 μm droplets. The vertical grey line represents the position of the peak heat release rate.

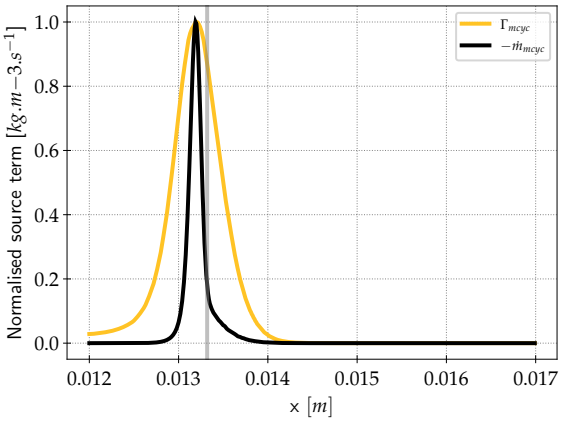

Figure 14.3.15: Spatial profile of the normalised evaporation source term (yellow) and the normalised consumption rate (black) of methyl-cyclohexane on the zone of interest for A1 with 60 μm droplets. The vertical grey line represents the position of the peak heat release rate.

droplets cases with B1 and C1 are displayed in Appendix E.

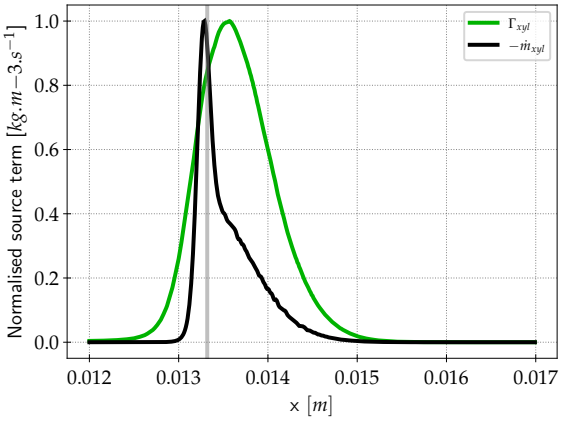

Figure 14.3.16: Spatial profile of the normalised evaporation source term (green) and the normalised consumption rate (black) of xylene on the zone of interest for A1 with 60 μm droplets. The vertical grey line represents the position of the peak heat release rate.

14.3.2 B1 flame

As for the previous section, the fuel species which are iso-octane, iso-dodecane and iso-cetane, are abbreviated $ic8$, $ic12$ and $ic16$ respectively in the following figures. As these species all belong to the same chemical class, iso-dodecane is represented by the colour used in Chap. 12 for the iso-alkanes class i.e. red while iso-octane will be in pink and iso-cetane in brown.

All components being iso-alkanes, the hierarchy of volatility in B1 is straightforward : the lighter the component, the more volatile. Iso-octane is then the first component to evaporate but given that it only constitutes 5.36 % of the total fuel mass, it features a low evaporation source term as represented in Fig. 14.3.17. Its only presence does not seem to be enough to start combustion as its consumption rate, represented on Fig. 14.3.19, peaks at the same location as the one of iso-dodecane. Iso-dodecane being by far the major component of B1, it is obviously the element driving the flame propagation with a consumption rate peaking right after the peak evaporation as seen in Fig. 14.3.22.

Finally, iso-cetane evolution is quite different with a delayed evaporation. Because of this late evaporation occurring in a hot zone as seen in Fig. 14.3.20, the evaporation rate, represented in 14.3.23 has an exponential-like evolution compared

to the classical parabolic-like evolution with a consumption rate following the same trend.

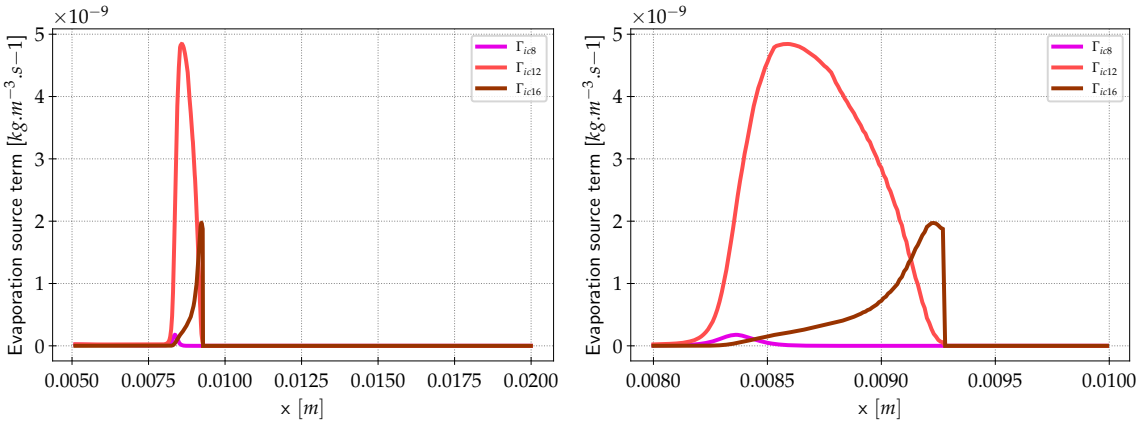

(a) Full domain (b) Zone of interest

Figure 14.3.17: Spatial profiles of the evaporation mass flow rate for each fuel species iso-octane, iso-dodecane and iso-cetane (respectively in pink, red and maroon) on (a) the full domain and (b) the zone of interest for B1 with 20 μm droplets.

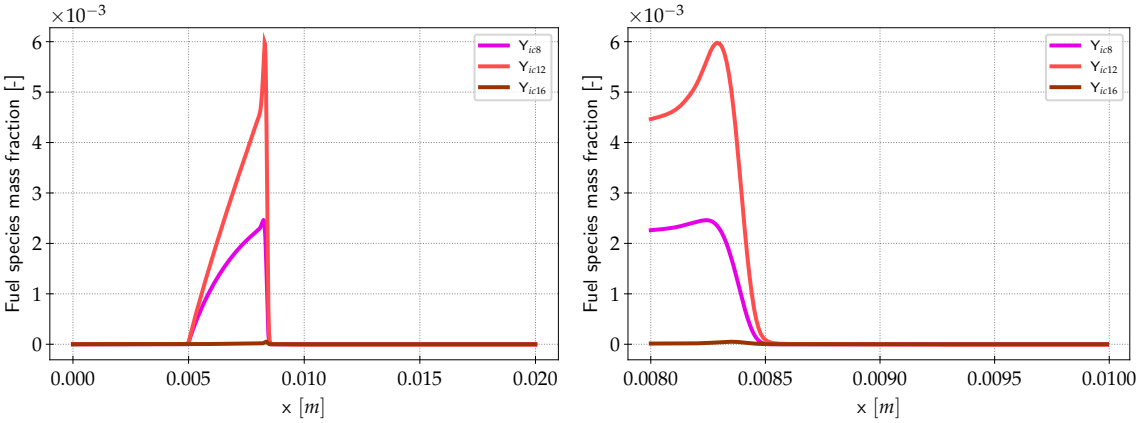

(a) Full domain (b) Zone of interest

Figure 14.3.18: Spatial profiles of the fuel species mass fractions iso-octane, iso-dodecane and iso-cetane (respectively in pink, red and maroon) on (a) the full domain and (b) the zone of interest for B1 with 20 μm droplets.

An evaporation thickness of 1.39 mm is obtained by using the same estimation as for A1. This flame is the shortest and this can be explained by the flame being

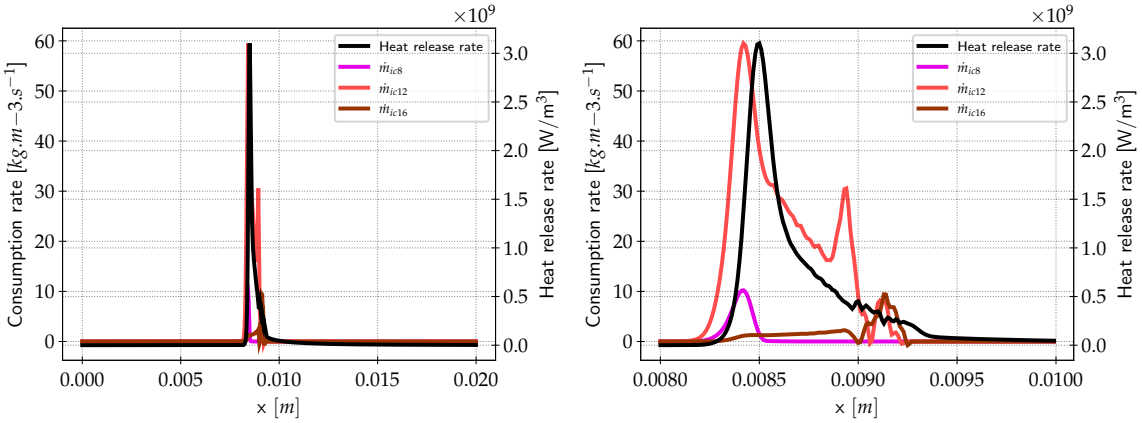

(a) Full domain (b) Zone of interest

Figure 14.3.19: Spatial profiles of the fuel species consumption rates iso-octane, iso-dodecane and iso-cetane (respectively in pink, red and maroon) and the heat release rate (black) on (a) the full domain and (b) the zone of interest for B1 with 20 μm droplets.

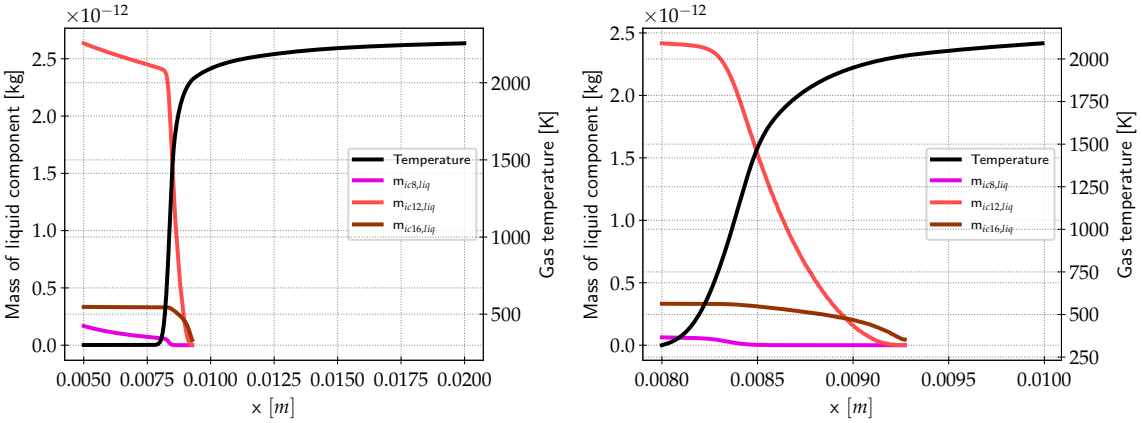

(a) Whole droplet life (b) Zone of interest

Figure 14.3.20: Gaseous temperature (black) and mass of the liquid components; iso-octane, iso-dodecane and iso-cetane (respectively in pink, red and maroon) on (a) the whole droplet lifespan and (b) the zone of interest for B1 with 20 μm droplets.

close to a mono-component surrogate considering the high amount of iso-dodecane. Iso-cetane in particular, despite not being volatile, evaporates rapidly because of the heat generated by the iso-dodecane combustion. Iso-octane, given its low content in

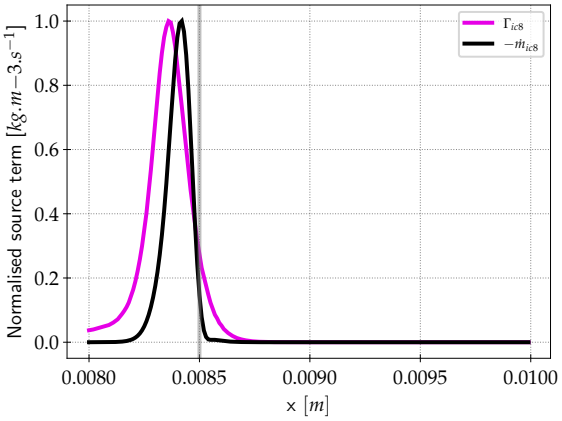

Figure 14.3.21: Spatial profiles of the normalised evaporation source term (pink) and the normalised consumption rate (black) of iso-octane on the zone of interest for B1 with 20 μm droplets. The vertical grey line represents the position of the peak heat release rate.

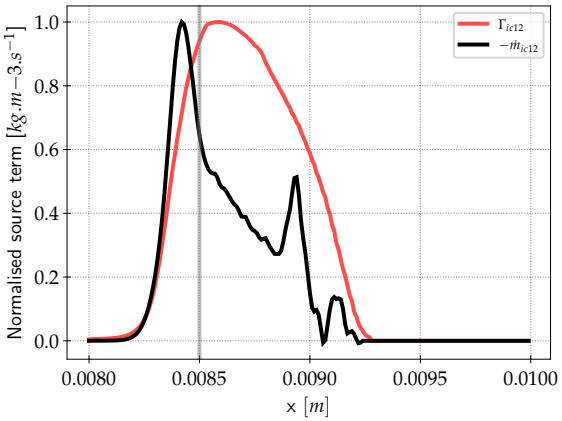

Figure 14.3.22: Spatial profile of the normalised evaporation source term (red) and the normalised consumption rate (black) of iso-dodecane on the zone of interest for B1 with 20 μm droplets. The vertical grey line represents the position of the peak heat release rate.

the fuel, seems to have an overall small impact on the flame.

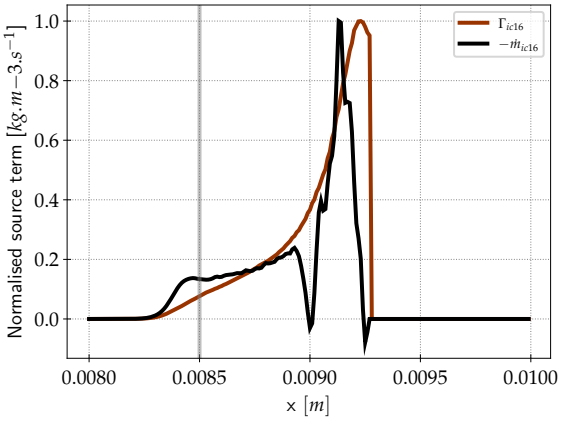

Figure 14.3.23: Spatial profile of the normalised evaporation source term (maroon) and the normalised consumption rate (black) of iso-cetane on the zone of interest for B1 with 20 μm droplets. The vertical grey line represents the position of the peak heat release rate.

14.3.3 C1 flame

Here, the fuel species which are decalin, iso-dodecane and methyl-naphthalene, are abbreviated *deca*, *ic*12 and *mnap* respectively in the following figures. The species are represented by the colour used in Chap. 12 with decalin in yellow, iso-dodecane in red and methyl-naphthalene in purple.

The important peak that can be observed on methyl-naphthalene around 12 mm in Fig. 14.3.24 is actually the droplet reaching its boiling conditions leading to an instantaneous evaporation of the remaining liquid. Again, a staged evaporation is observed with iso-dodecane evaporating the earliest before the flame front, followed by decalin and methyl-naphthalene after the primary reactive zone.

From Fig. 14.3.26, the decalin and iso-dodecane follow the same behaviour with the differences between the two coming from their different mass content in the liquid phase.

Before boiling, methyl-naphthalene behaves similarly to iso-cetane in B1 with an exponential-like evolution of the evaporation source term due to its presence in hot gases.

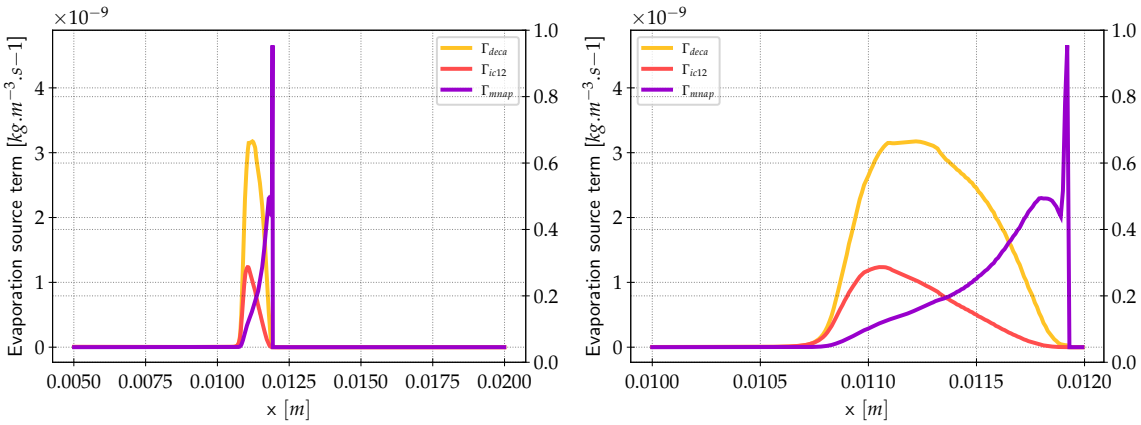

(a) Full domain (b) Zone of interest

Figure 14.3.24: Spatial profiles of the evaporation mass flow rate for each fuel species decalin, iso-dodecane and methyl-naphthalene (respectively in yellow, red and purple) and the heat release rate (black) on (a) the full domain and (b) the zone of interest for C1 with 20 μm droplets.

In this case, methyl-naphthalene is in high enough amount to induce a secondary reaction zone around 15 mm differing from the previously observed trailing heat release zone.

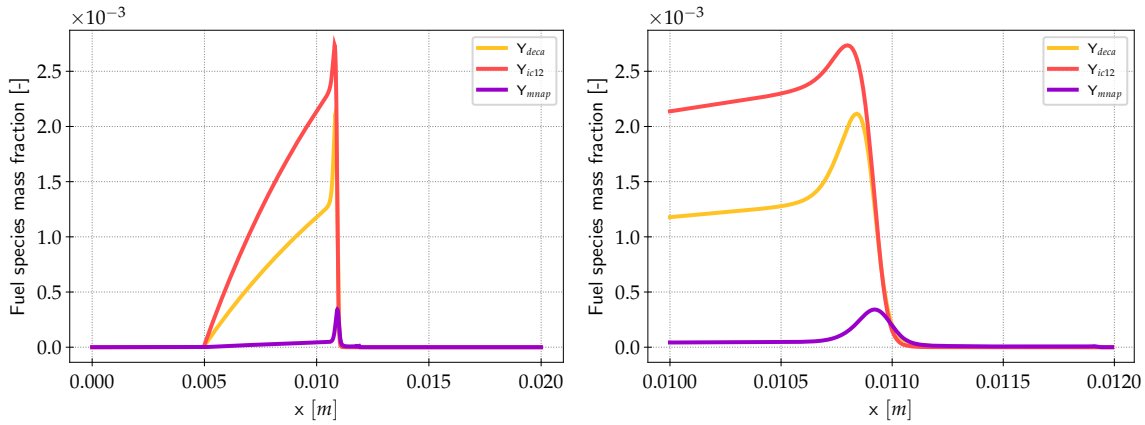

(a) Full domain (b) Zone of interest

Figure 14.3.25: Spatial profiles of the fuel species mass fractions decalin, iso-dodecane and methyl-naphthalene (respectively in yellow, red and purple) on (a) the full domain and (b) the zone of interest for C1 with 20 μm droplets.

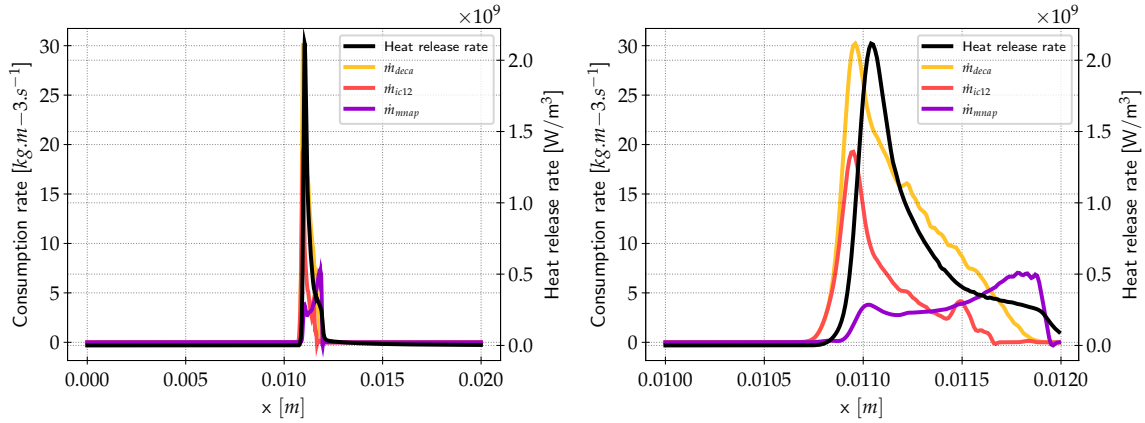

(a) Full domain (b) Zone of interest

Figure 14.3.26: Spatial profiles of the fuel species consumption rates decalin, iso-dodecane and methyl-naphthalene (respectively in yellow, red and purple) and the heat release rate (black) on (a) the full domain and (b) the zone of interest for C1 with 20 μm droplets.

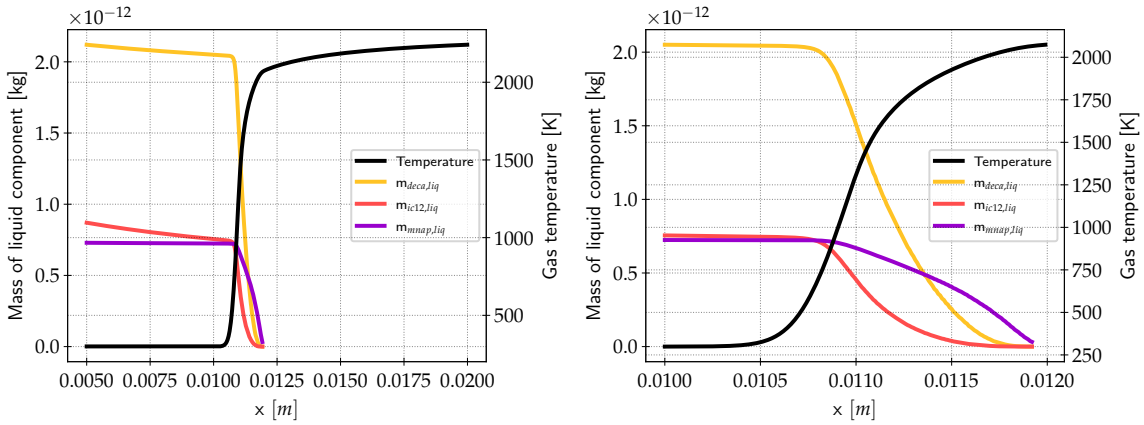

(a) Whole droplet life

(b) Zone of interest

Figure 14.3.27: Gaseous temperature (black) and mass of the liquid components; decalin, iso-dodecane and methyl-naphthalene (respectively in yellow, red and purple) on (a) the whole droplet lifespan and (b) the zone of interest for C1 with 20 μm droplets.

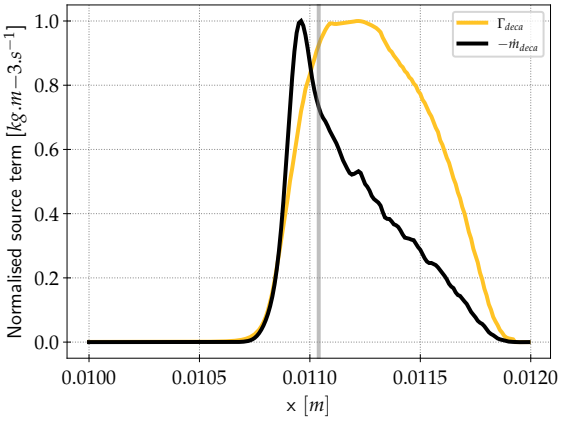

Figure 14.3.28: Spatial profiles of the normalised evaporation source term (yellow) and the normalised consumption rate (black) of decalin on the zone of interest for C1 with 20 μm droplets. The vertical grey line represents the position of the peak heat release rate.

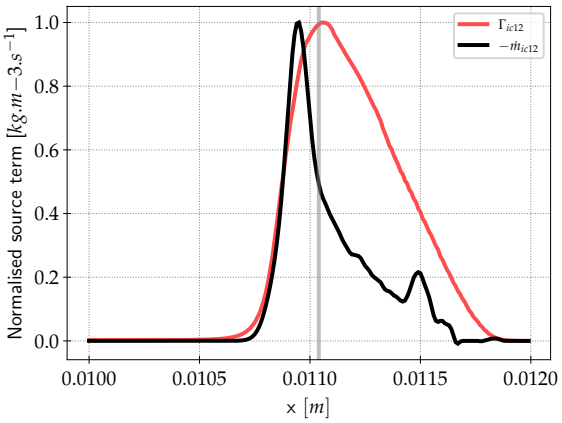

Figure 14.3.29: Spatial profiles of the normalised evaporation source term (red) and the normalised consumption rate (black) of iso-dodecane on the zone of interest for C1 with 20 μm droplets. The vertical grey line represents the position of the peak heat release rate.

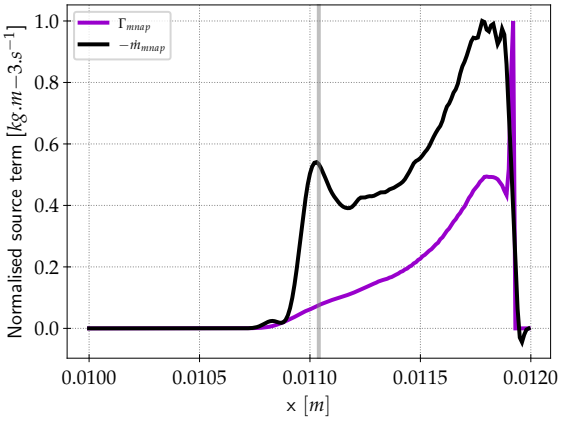

Figure 14.3.30: Spatial profiles of the normalised evaporation source term (purple) and the normalised consumption rate (black) of methyl-naphthalene on the zone of interest for C1 with 20 μm droplets. The vertical grey line represents the position of the peak heat release rate.

14.4 Summary of the fuel effect on flames

For all cases, the evaporation process is fast enough to reach a stoichiometric equivalence ratio by the end of the domain. However, it is seen that because of their composition, the fuels do not exhibit the same flame structure, especially considering the consumption of each component.

An important advantage of ARC compared to global schemes is the presence of a pyrolysis zone for all fuels that can be observed for example in Fig. 14.3.7, 14.3.21 and 14.3.28. The consumption peak happens before the heat release rate peak (grey vertical line) meaning that these species are not directly responsible for the heat release. Because this phenomenon is endothermic, it can lead to a negative heat release rate in cases were more staging between pyrolysis and oxidation is present.

Computations are stabilised with inlet velocities, corresponding here to the actual flame speed, as reported in Tab. 14.4.1.

From these values of flame speed, the same hierarchy as for the gaseous flames (Section 12 Fig. 12.3.2) is found, with A1 and B1 being very similar and C1 having a lower reactivity.

To compare with, the values of laminar flame speed for fresh gases at 300K, 1 bar and stoichiometry are 0.366, 0.365 and 0.344 $m.s^{-1}$ for the A1, B1 and C1 respectively. Of course, these values are purely indicative as these fuels are not gaseous at these conditions but they can serve as a good indicator of the differences between the fuels.

The impact of droplet size differs between the fuels. More precisely, A1 and B1 two-phase flame speed stay similar for both droplet sizes, with a 58% decrease from

	$20\mu m$	$60\mu m$
A1	0.31	0.13
B1	0.31	0.13
C1	0.28	0.10

Table 14.4.1: Inlet velocity (in $m.s^{-1}$) required to achieve a stabilised flame, giving the actual flame speed for each fuel with either a 20 μm or 60 μm droplet.

	$20\mu m$	$60\mu m$
A1	0.653	0.470
B1	0.650	0.460
C1	0.628	0.477

Table 14.4.2: Gaseous equivalence ratio at the peak value of heat release rate.

20 to 60 μm droplets, whereas the two-phase flame speed of C1 decreases more, by 64% for the same droplet sizes. For purely gaseous flames, the difference between A1 and C1 flame speeds is 6%; it increases to 9.7 % for 20 μm droplets and finally to 23 % in the 60 μm droplets case.

An important quantity for two-phase flames, which explains the difference in flame speeds between gas or liquid fuel, is the "effective" equivalence ratio seen by the flame, i.e., the true reactant mixture composition at the flame location [Rochette et al., 2018]. Interestingly, the values of the gaseous equivalence ratio ϕ_g at the peak value of heat release rate reported in Tab. 14.4.2 are consistent with the flame speed difference between gas and liquid fuels. For the 20 μm droplets for example, C1 is observed to burn at a lower equivalence ratio than A1 and B1 with a value of 0.628, i.e., further away from stoichiometry, meaning a larger difference with the stoichiometric gaseous flame speed. This effect is increased at 60 μm droplet size, with an even lower value of ϕ_g at the flame. The same happens to A1 and B1 flames, which however experience similar decreases of ϕ_g and therefore similar flame speeds in all cases. Note however that at 60 μm droplet size, ϕ_g for C1 has less decreased than for A1 and B1 while its flame speed has decreased more. This qualitative difference shows that the actual composition at the flame location plays an important role. The B1 fuel being constituted of only iso-alkanes which are very reactive, it keeps burning fast at low equivalence ratio. The situation is more complex for A1 and C1 combustion, driven by a competition between species with different levels of volatility and reactivity. For example C1 is composed of decalin which is not very reactive but volatile and iso-dodecane which is less volatile but more reactive. For A1, this competition stands between methyl-cyclohexane and xylene on one side and n-dodecane on the other side. This competition does not evolve the same for A1 and C1 when increasing the droplet size leading to different evolutions of the flame speed with the equivalence ratio at the flame front.

In terms of pollutant emissions, while again A1 and B1 present a similar behaviour

concerning the CO and CO_2 production, C1 exhibits a different trend.

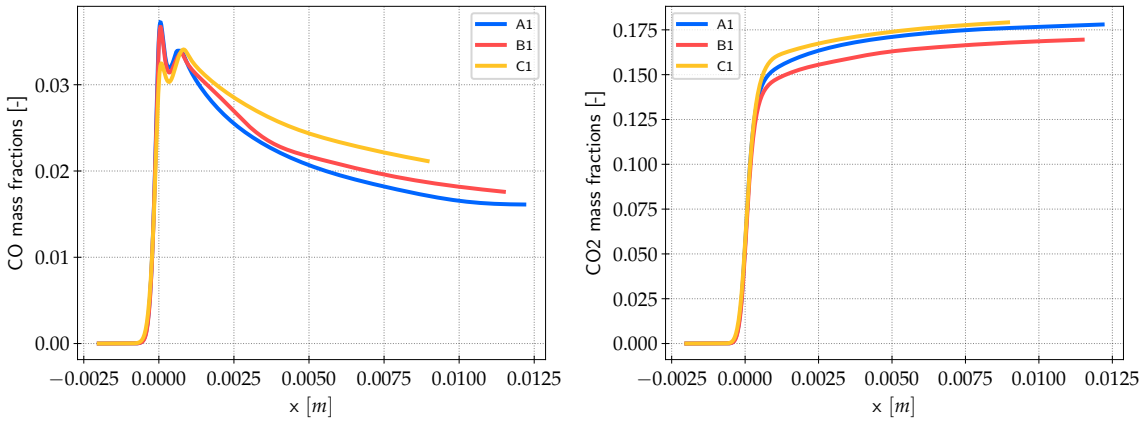

(a) CO (b) CO_2

Figure 14.4.1: Mass fraction profiles of (a) CO and (b) CO_2 for A1 (blue), B1 (red) and C1 (yellow) two-phase flames with 20 μm droplets. The x-coordinate has been shifted for an easier comparison.

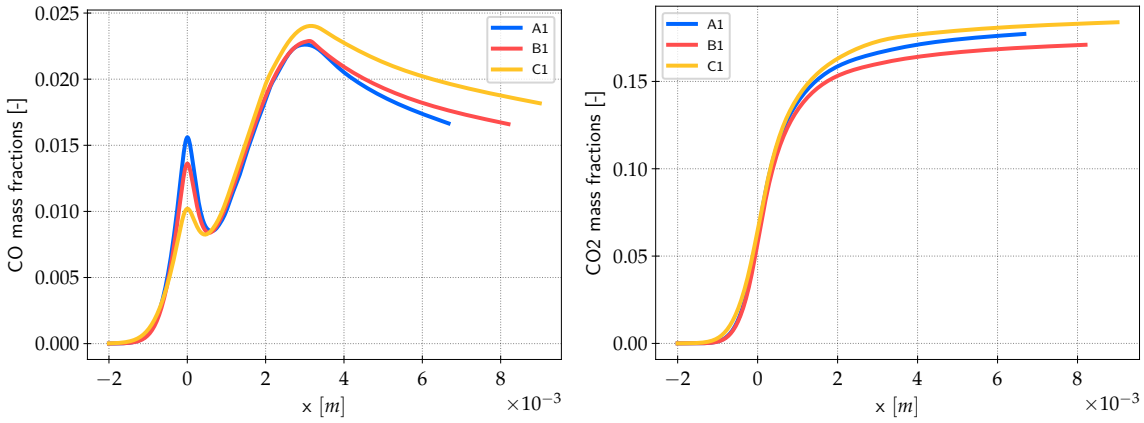

(a) CO (b) CO_2

Figure 14.4.2: Mass fraction profiles of (a) CO and (b) CO_2 for A1 (blue), B1 (red) and C1 (yellow) two-phase flames with 60 μm droplets. The x-coordinate has been shifted for an easier comparison.

Fig. 14.4.1 and 14.4.2 present the evolution of CO and CO_2 for the 20 and 60 μm droplets respectively, and for the three fuels. The profiles are spatially shifted to locate the peak heat release rate locations at the zero abscissa.

The CO_2 profiles increase right after the flame front and tend towards a plateau with a monotonous evolution. This increase is slower with larger droplets which tend to thicken the reaction zone.

The CO profiles exhibit a more interesting shape with two distinct peaks. The first peak, which is also observed in gaseous flames, happens at the flame front location and corresponds to the production of this species by fast oxidation reactions. Further downstream, a second peak appears for both droplet sizes before a decrease towards equilibrium. For the 20 μm droplets, this second peak is about the magnitude of the first one and close to the flame front. For all fuels in this case, similar peak values are reached and differences appear in the post-flame near-equilibrium values. In the 60 μm droplets case differences are more pronounced with opposite hierarchies in the two peaks: the first peak value for A1 is higher than for B1, itself higher than for C1, with A1 and B1 being again closer, while the second peak value is highest for C1. Differently from the 20 μm droplets, the second peak reaches higher values than the first peak. From the reaction rates profiles in E, this production peaks result from the H-abstraction from HCO happening downstream of the flame front.

Overall, the C1 fuel is expected to produce more CO and CO_2 than the two other fuels. While A1 is producing more CO_2 than B1, the latter produces more CO. This highlights the importance of fuel composition for pollutant emissions which may differ event for two fuels having similar flame behaviours.

Concerning the sooting behaviour of the flames, a first evaluation is made here with acetylene (C_2H_2) which is a major soot precursor. Although not used as a target for the chemistry reduction, acetylene is present in all mechanisms and can be analysed to give a first glance at the soot emissions of these fuels.

Figure 14.4.3 shows that acetylene is produced in the pyrolysis zone of the flame ahead of the flame front and is still produced behind in lower quantities. Larger levels are obtained for the 20 μm droplet cases compared to the 60 μm droplet cases. In the first case, all fuels lead to similar profiles with only a difference with C1 in the trailing, slightly higher in acethlene concentration. In the cases of 60 μm droplets, the mass fraction profiles differ more in the peak values: the A1 peak is higher than the C1 peak, and both are higher than the B1 peak, which has a relatively low value. In the burnt gases, acetylene stabilises at the same level for all fuels.

Integrating the mass fractions profiles over the spatial domain gives the values reported in 14.4.3.

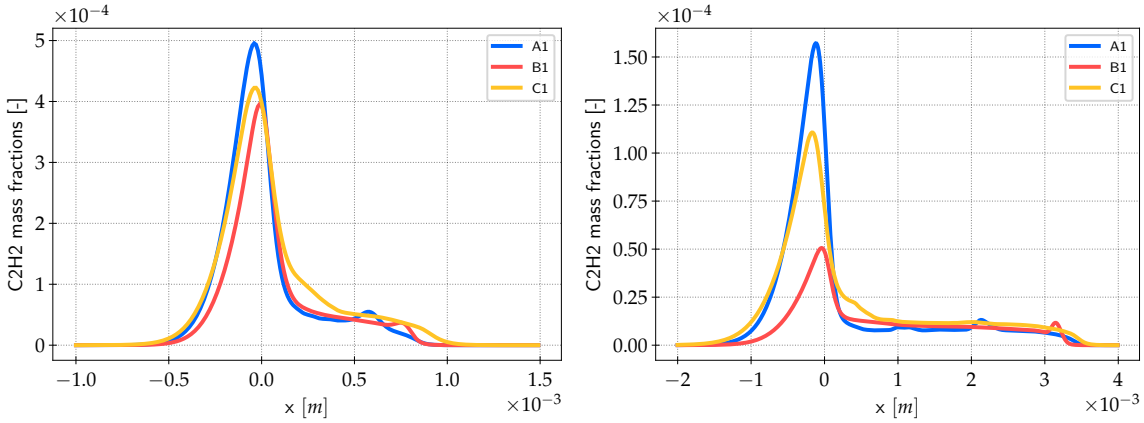

(a) 20 μm droplets (b) 60 μm droplets

Figure 14.4.3: Mass fraction profiles of C_2H_2 for A1 (blue), B1 (red) and C1 (yellow) two-phase flames with 20 μm (left) and 60 μm (right) droplets. The x-coordinate has been shifted for an easier comparison.

	$20\mu m$	$60\mu m$
A1	$1.591e-07$	$1.119e-07$
B1	$1.298e-07$	$0.584e-07$
C1	$1.735e-07$	$1.126e-07$

Table 14.4.3: Total mass fraction of acetylene (spatial integral of (C_2H_2) profiles)

For both droplet sizes, the acetylene integral of B1 is significantly lower than the ones of A1 and C1, with this difference increasing with the droplet size (from 18% to 48% difference with A1).

C1 acetylene integral is higher than A1 despite the higher A1 peak value. However, the difference between the two values decreases with the droplet size (9% to 0.6%), contrary to what was obtained for B1.

The present surrogate formulations transcribe well the literature correlation between the soot precursors and the aromatic content of the fuels. Indeed B1 which does not contain any aromatic species produces the lowest amount of acetylene. Conversely C1 producing a larger amount of soot precursors is an expected behaviour from its high aromatic content. The soot emissions and the correct prediction of

their behaviour was not targeted for the present chemistry reduction. This led several species known as soot precursors (products from the fuel pyrolysis) to be considered in Quasi-Steady State, disabling the possibility to study their evolution. In future work, the reduction should take into account all major soot precursors, possibly including Poly-Aromatic Hydrocarbons (PAH), to allow a detailed study of soot production.

14.5 Conclusion and Perspectives

The multi-component approach chosen in this work enables to capture the different behaviours in terms of evaporation and subsequently flame structure resulting from the composition disparities in the fuels.

While having very similar overall features, the A1 and B1 fuels exhibit differences in the staging of their combustion. While their major components n-dodecane and iso-dodecane are chemically different in terms of reactivity with iso-dodecane being more reactive, the early evaporation of methyl-cyclohexane and xylene leads to reactions happening earlier thus compensating this lack of reactivity.

Similarities are also found between B1 and C1 regarding their less volatile component, iso-cetane and methyl-naphtalene respectively, with a specific evaporation regime due to their presence in the liquid phase far inside the burnt gases.

This work paves the way for future studies regarding the specificities of fuels in terms of pollutant emissions. Although straightforward conclusions can already be drawn, such as the higher soot production by C1 combustion due to its high aromatic content, the accurate prediction of he fuel effect on pollutant emissions require an adequate chemistry description. Specific ARCs must then be constructed with these specific targets.

The outcome of the study presented in this chapter has allowed to initiate further work on the stability of spray flames, carried out in 3D configurations in the PhD projects of Jonathan Wirtz and Varun Shastry at CERFACS. [Komaraek et al., 2020, Ruoff et al., 2020, Voivenel et al., 2020].

Chapter 15

Conclusions and Perspectives

The main objective of this PhD thesis was to improve the generation methodology of Analytically Reduced Chemistry (ARC). This was done with the creation of the reduction code ARCANE tailored to minimise the required user expertise in chemical kinetics and their reduction and to ensure a virtually unlimited range of applications. This code has become a generic tool at CERFACS where more and more Large Eddy Simulations (LES) use detailed chemistries with very specific conditions. Industry has growing interest in more precise chemical kinetics description that suit their needs and ARCANE has been able to help in several projects and collaborations. It was used in published work for the reduction of methane/oxygen combustion in cryogenic conditions [Blanchard et al., 2021], n-heptane spray flames [Wirtz et al., 2020], diluted methane/air flames [Jiang et al., 2021], premixed methane/air flames with separated hydrogen injection [Laera et al., 2020] and also in unpublished work for various liquid fuels with either NO_x emissions, soot precursors predictions or ammonia combustion. The code also integrates several chemical analysis tools, from chemical time scales to more thorough analyses of the reactions at each position/time of canonical cases.

To demonstrate the added value of such semi-detailed description of combustion chemistry, the reduction methodology was applied to two cases where it is of particular interest. The first case is the 3D LES of a confined swirled premixed combustion chamber burning hydrogen-enriched methane with air. The reduction performed for that case proved the robustness and strength of the ARC methodology, which allowed to reduce to a single mechanism the combustion chemistry of both methane and hy-

drogen, and of their blends while targeting methane combustion only. This was shown to be valid for the basic combustion features, the NO_x emissions and the OH^* emissions. The LES results showed a good agreement with experiment, retrieving the transition from a V-shaped flame to an M-Shaped flame when raising the hydrogen content from 60% to 90% in volume. Comparing the fields of heat release rate and OH^*, questions are raised about the adequacy between OH-chemiluminescence images and numerical quantities available from the simulations. Indeed, the correlation with the numerical heat release rate is not clear and the OH^* field seems more appropriate. Predictions of NO_x emissions have also been performed showing that for a 60% content, NO is produce by three mechanisms (thermal, prompt and NO_2) while only the thermal route remains with a higher enrichment level. Proper quantification of this NO production should be performed in order to accurately identify the benefits of the enrichment in that case in terms of NO_x.

The methodology was then applied on 3 aviation fuels represented by 3-component surrogates. These fuels were the standard Jet-A1 labelled A1, a Sustainable Aviation Fuel (SAF), the ATJ-SPK, labelled B1 and a high aromatic content fuel labelled C1. For each fuel, an ARC has been derived with a sufficient reduction allowing a reasonable cost in the CFD code. Such reduction was not previously accessible with previous reduction codes. The 3 ARCs were successfully integrated within the code AVBP and their differences were assessed on one-dimensional spray flames. For all fuels, the flame structure was found to be driven by the most volatile species showing the importance of differential evaporation in the behaviour of spray flames. The A1 and B1 fuels were shown to be very similar both in gaseous and spray flames despite their differences in composition. The C1 is shown to be less reactive than the other two while producing more CO and CO_2 as pollutants. A first look at soot precursors suggest that B1 is less likely to produce soot than A1 itself less likely than C1. However, a reduction targeting the relevant soot production pathways should be done in order to properly compare the sooting potential of each fuel and go one step further in their characterisation.

Future work will use these mechanisms in ignition conditions to identify differences in their ignition capabilities in 0D canonical configurations as well as 3D LES.

ARCANE and its framework have been written in an objective of easily incorporating more and more methods to make it a powerful tool for the study and generation of chemical kinetics mechanisms.

The pyrolysis lumping from [Heberle and Pepiot, 2020b] is currently being inte-

grated within ARCANE in order to be able to reduce heavy fuels kinetics in a similar way of HyChem but using numerical data and the capabilities of the codes. This methodology will be particularly interesting to further reduce the numerical cost of such kinetic mechanisms and assess the limits of the underlying hypothesis.

The 1D spray flames will also be of particular interest as reference reduction cases. Coupled with a solver reproducing these simple spray flames with detailed chemistry, ARCANE will be able to use these flames as reference and produce a reduced mechanism tailored for spray flames. Such reduction could show if a reduction on gaseous flames only is accurate enough to capture spray flames complexity.

For industrial consideration, ARC is still expensive and a automatic generation methodology of global mechanisms has also been included in the code. The global mechanisms are optimised to fit the detailed mechanism data with the same versatility as the ARC reduction.

The present work will hopefully increase the use of ARC for the studies to come taking away the struggle of properly reducing a mechanism that is both computer efficient and accurate. The study of complex fuels with more than one components being set to be more and more common, this work highlights several of their specificities and may serve as a stepping stone for future works.

Bibliography

[Abou-Taouk et al., 2016] Abou-Taouk, A., Farcy, B., Domingo, P., Vervisch, L., Sadasivuni, S., and Eriksson, L.-E. (2016). Optimized Reduced Chemistry and Molecular Transport for Large Eddy Simulation of Partially Premixed Combustion in a Gas Turbine. *Combustion Science and Technology*, 188(1):21–39. 67

[Abramzon and Sirignano, 1989] Abramzon, B. and Sirignano, W. A. (1989). Droplet vaporization model for spray combustion calculations. *International Journal of Heat and Mass Transfer*, 32(9):1605–1618. 208

[Ahima, 2020] Ahima, R. S. (2020). Global warming threatens human thermoregulation and survival. 1

[Alaya et al., 2019] Alaya, M., Ennetta, R., and Said, R. (2019). Investigation of hydrogen blending effects on turbulent methane flame properties using PDF-Monte Carlo method and FGM chemistry tabulation approach. *Fuel*, 254(April):115645. 104

[Angelberger et al., 1998] Angelberger, C., Veynante, D., Egolfopoulos, F. N., and Poinsot, T. (1998). Large eddy simulations of combustion instabilities in premixed flames. In *Proceedings of the Summer Program*, pages 61–82. Center for Turbulence Research, NASA Ames/Stanford Univ. 131

[Bahlouli et al., 2014] Bahlouli, K., Atikol, U., Khoshbakhti Saray, R., and Mohammadi, V. (2014). A reduced mechanism for predicting the ignition timing of a fuel blend of natural-gas and n-heptane in HCCI engine. *Energy Conversion and Management*, 79:85–96. 76

[Ballal and Lefebvre, 1975a] Ballal, D. R. and Lefebvre, A. H. (1975a). The influence of flow parameters on minimum ignition energy and quenching distance. *Symposium (International) on Combustion*, 15(1):1473–1481. 175

[Ballal and Lefebvre, 1975b] Ballal, D. R. and Lefebvre, A. H. (1975b). The influence of spark discharge characteristics on minimum ignition energy in flowing gases. *Combustion and Flame*, 24(C):99–108. 175

[Ballal and Lefebvre, 1981] Ballal, D. R. and Lefebvre, A. H. (1981). A general model of spark ignition for gaseous and liquid fuel-air mixtures. In Institute, T. C., editor, *Symposium (International) on Combustion*, volume 18, pages 1737–1746. 290

[Bane et al., 2013] Bane, S. P., Ziegler, J. L., Boettcher, P. A., Coronel, S. A., and Shepherd, J. E. (2013). Experimental investigation of spark ignition energy in kerosene, hexane, and hydrogen. *Journal of Loss Prevention in the Process Industries*, 26(2):290–294. 175

[Battin-Leclerc et al., 2011] Battin-Leclerc, F., Blurock, E., Bounaceur, R., Fournet, R., Glaude, P.-A., Herbinet, O., Sirjean, B., and Warth, V. (2011). Towards cleaner combustion engines through groundbreaking detailed chemical kinetic models. *Chem. Soc. Rev.*, 40(9):4762. 46

[Bellemans et al., 2020] Bellemans, A., Kincaid, N., Deak, N., Pepiot, P., and Bisetti, F. (2020). P-DRGEP: a novel methodology for the reduction of kinetics mechanisms for plasma-assisted combustion applications. *Proceedings of the Combustion Institute*, page S1540748920304569. 93

[Bilger et al., 1991] Bilger, R., Esler, M., and Starner, S. (1991). On reduced mechanisms for methane-air combustion. In Smooke, M. D., editor, *Reduced Kinetic Mechanisms and Asymptotic Approximations for Methane-Air Flames*, volume 384, pages 86–110. Springer-Verlag, Berlin/Heidelberg. Series Title: Lecture Notes in Physics. 34

[Blanchard et al., 2021] Blanchard, S., Cazères, Q., and Cuenot, B. (2021). Chemical modelling for methane oxy-combustion in liquid rocket engines. *Unpublished*. 93, 96, 136, 137, 245

[Bodenstein, 1913] Bodenstein, M. (1913). Ëine Theorie der photochemischen Beaktionsgeschwindigkeiten. *Zeitschrift für Physikalische Chemie*, page 69. 61

[Borghi, 1988] Borghi, R. (1988). Turbulent combustion modelling. *Progress in Energy and Combustion Science*, 14(4):245–292. 127

[Bougrine et al., 2011] Bougrine, S., Richard, S., Nicolle, A., and Veynante, D. (2011). Numerical study of laminar flame properties of diluted methane-hydrogen-air flames at high pressure and temperature using detailed chemistry. *International Journal of Hydrogen Energy*, 36(18):12035–12047. 101

[Boushaki et al., 2012] Boushaki, T., Dhué, Y., Selle, L., Ferret, B., and Poinsot, T. (2012). Effects of hydrogen and steam addition on laminar burning velocity of methane-air premixed flame: Experimental and numerical analysis. *International Journal of Hydrogen Energy*, 37(11):9412–9422. 101

[Buekers et al., 2014] Buekers, J., Van Holderbeke, M., Bierkens, J., and Int Panis, L. (2014). Health and environmental benefits related to electric vehicle introduction in EU countries. *Transportation Research Part D: Transport and Environment*, 33:26–38. 3

[Bulat et al., 2014] Bulat, G., Jones, W. P., and Marquis, A. J. (2014). NO and CO formation in an industrial gas-turbine combustion chamber using LES with the Eulerian sub-grid PDF method. *Combustion and Flame*, 161(7):1804–1825. 5

[Burgoyne and Cohen, 1954] Burgoyne, J. and Cohen, L. (1954). The effect of drop size on flame propagation in liquid aerosols. *Proceedings of the Royal Society of London. Series A. Mathematical and Physical Sciences*, 225(1162):375–392. 174

[Butler and O'Rourke, 1977] Butler, T. D. and O'Rourke, P. J. (1977). A numerical method for two dimensional unsteady reacting flows. *Symposium (International) on Combustion*, 16(1):1503–1515. 130

[Cailler, 2020] Cailler, M. (2020). Development of a virtual optimized chemistry method. Application to hydrocarbon/air combustion. *Combustion and Flame*, page 22. 49

[Cailler et al., 2017] Cailler, M., Darabiha, N., Veynante, D., and Fiorina, B. (2017). Building-up virtual optimized mechanism for flame modeling. *Proceedings of the Combustion Institute*, 36(1):1251–1258. 49, 67

[Campet, 2019] Campet, R. (2019). Simulation and optimization of steam-cracking processes. *These de doctorat de l'Universite de Toulouse*. 87

[Cazères et al., 2021] Cazères, Q., Pepiot, P., and Riber, E. (2021). A fully automatic procedure for the analytical reduction of chemical kinetics mechanisms for Computational Fluid Dynamics applications. 303(December 2020). 66

[Charlette et al., 2002] Charlette, F., Meneveau, C., and Veynante, D. (2002). A power-law flame wrinkling model for LES of premixed turbulent combustion Part II: Dynamic formulation. *Combustion and Flame*, 131(1-2):181–197. 132, 133

[Chen, 1997] Chen, J. (1997). Development of reduced mechanisms for numerical modelling of turbulent combustion. In *Workshop on Numerical Aspects of Reduction in Chemical Kinetics*. CERMICS-ENPC Cite Descartes Champus sur Marne, France. 76

[Chterev and Boxx, 2021] Chterev, I. and Boxx, I. (2021). Effect of hydrogen enrichment on the dynamics of a lean technically premixed elevated pressure flame. *Combustion and Flame*, 225:149–159. 101

[Colin et al., 2000] Colin, O., Ducros, F., Veynante, D., and Poinsot, T. (2000). A thickened flame model for large eddy simulations of turbulent premixed combustion. *Physics of Fluids*, 12(7):1843–1863. 130, 131, 132

[Colin and Rudgyard, 2000] Colin, O. and Rudgyard, M. (2000). Development of high-order Taylor-Galerkin schemes for unsteady calculations. *Journal of Computational Physics*, 162(2):338–371. 135

[Collin, 2019a] Collin, F. (2019a). *Modeling and Numerical Simulation of Two-Phase Ignition in Gas Turbine*. PhD thesis. 5

[Collin, 2019b] Collin, F. (2019b). *Modeling and Numerical Simulation of Two-Phase Ignition in Gas Turbine*. PhD thesis, Université de Toulouse. 130

[Collin-Bastiani et al., 2020] Collin-Bastiani, F., Riber, E., and Cuenot, B. (2020). Study of inter-sector spray flame propagation in a linear arrangement of swirled burners. *Proceedings of the Combustion Institute*, page S1540748920300985. 93

[CRECK,] CRECK. Polimi mechanisms website. http://creckmodeling.chem.polimi.it/menu-kinetics/menu-kinetics-detailed-mechanisms. 81, 103

[Cuenot and Poinsot, 1994] Cuenot, B. and Poinsot, T. (1994). Effects of curvature and unsteadiness in diffusion flames. Implications for turbulent diffusion combustion. *Symposium (International) on Combustion*, 25(1):1383–1390. 127, 128, 129

[Cuenot and Riber, 2017] Cuenot, B. and Riber, E. (2017). *Simulation des Grandes Echelles de flammes de spray et modélisation de la combustion non-prémélangée*. PhD thesis. 130

[Curran, 2019] Curran, H. J. (2019). Developing detailed chemical kinetic mechanisms for fuel combustion. *Proceedings of the Combustion Institute*, 37(1):57–81. 4, 12

[Dagaut et al., 2006] Dagaut, P., El Bakali, A., and Ristori, A. (2006). The combustion of kerosene: Experimental results and kinetic modelling using 1- to 3-component surrogate model fuels. *Fuel*, 85(7-8):944–956. 182

[Dagaut and Gail, 2007] Dagaut, P. and Gail, S. (2007). Kinetics of gas turbine liquid fuels combustion: Jet-a1 and bio-kerosene. *Proceedings of the ASME Turbo Expo*, 2:93–101. 181, 182

[de Oliveira and Mastorakos, 2019] de Oliveira, P. M. and Mastorakos, E. (2019). Mechanisms of flame propagation in jet fuel sprays as revealed by OH/fuel planar laser-induced fluorescence and OH* chemiluminescence. *Combustion and Flame*, 206:308–321. 174

[Di Sarli and Di Benedetto, 2007] Di Sarli, V. and Di Benedetto, A. (2007). Laminar burning velocity of hydrogen-methane/air premixed flames. *International Journal of Hydrogen Energy*, 32(5):637–646. 101

[Drake et al., 1991] Drake, M. C., Ratcliffe, J. W., Blint, R. J., Carter, C. D., and Laurendeau, N. M. (1991). Measurements and modeling of flamefront no formation and superequilibrium radical concentrations in laminar high-pressure premixed flames. *Symposium (International) on Combustion*, 23(1):387–395. 107

[Eckel et al., 2019] Eckel, G., Grohmann, J., Cantu, L., Slavinskaya, N., Kathrotia, T., Rachner, M., Le Clercq, P., Meier, W., and Aigner, M. (2019). LES of a swirl-stabilized kerosene spray flame with a multi-component vaporization model and detailed chemistry. *Combustion and Flame*, 207:134–152. 290

[Edwards and Maurice, 2001] Edwards, T. and Maurice, L. Q. (2001). Surrogate mixtures to represent complex aviation and rocket fuels. *Journal of Propulsion and Power*, 17(2):461–466. 182

[Esclapez et al., 2021] Esclapez, L., Collin-Bastiani, F., Riber, E., and Cuenot, B. (2021). A statistical model to predict ignition probability. *Combustion and Flame*, 225:180–195. 175

[Eyssartier et al., 2013] Eyssartier, A., Cuenot, B., Gicquel, L. Y., and Poinsot, T. (2013). Using LES to predict ignition sequences and ignition probability of turbulent two-phase flames. *Combustion and Flame*, 160(7):1191–1207. 175

[Faramawy et al., 2016] Faramawy, S., Zaki, T., and Sakr, A. A. (2016). Natural gas origin, composition, and processing: A review. *Journal of Natural Gas Science and Engineering*, 34:34–54. 3

[Felden, 2017] Felden, A. (2017). Development of Analytically Reduced Chemistries (ARC) and applications. *These de doctorat de l'Universite de Toulouse*, page 213. 5, 6, 41, 58, 119, 130, 175, 183, 198

[Felden, 2018] Felden, A. (2018). Development of Analytically Reduced Chemistries (ARC) and applications. *These de doctorat de l'Universite de Toulouse*, page 213. 127, 129

[Felden et al., 2018a] Felden, A., Esclapez, L., Riber, E., Cuenot, B., and Wang, H. (2018a). Including real fuel chemistry in LES of turbulent spray combustion. *Combustion and Flame*, 193:397–416. 175, 182

[Felden et al., 2018b] Felden, A., Esclapez, L., Riber, E., Cuenot, B., and Wang, H. (2018b). Including real fuel chemistry in LES of turbulent spray combustion. *Combustion and Flame*, 193:397–416. 289, 292

[Fenimore, 1971] Fenimore, C. P. (1971). Formation of nitric oxide in premixed hydrocarbon flames. *Symposium (International) on Combustion*, 13(1):373–380. 107

[Fiorina et al., 2015a] Fiorina, B., Mercier, R., Kuenne, G., Ketelheun, A., Avdić, A., Janicka, J., Geyer, D., Dreizler, A., Alenius, E., Duwig, C., Trisjono, P., Kleinheinz, K., Kang, S., Pitsch, H., Proch, F., Cavallo Marincola, F., and Kempf, A. (2015a). Challenging modeling strategies for LES of non-adiabatic turbulent stratified combustion. *Combustion and Flame*, 162(11):4264–4282. 47

[Fiorina et al., 2015b] Fiorina, B., Veynante, D., and Candel, S. (2015b). Modeling Combustion Chemistry in Large Eddy Simulation of Turbulent Flames. *Flow Turbulence Combust*, 94(1):3–42. 47

[Fiorina et al., 2010] Fiorina, B., Vicquelin, R., Auzillon, P., Darabiha, N., Gicquel, O., and Veynante, D. (2010). A filtered tabulated chemistry model for LES of premixed combustion. *Combustion and Flame*, 157(3):465–475. 47, 67, 142

[Fournet et al., 2000] Fournet, R., Warth, V., Glaude, P. A., Battin-Leclerc, F., Scacchi, G., and Me, G. M. C. (2000). Automatic reduction of detailed mechanisms of combustion of alkanes by chemical lumping. *International Journal of Chemical Kinetics*, page 16. 56

[Franzelli et al., 2012a] Franzelli, B., Riber, E., Gicquel, L. Y., and Poinsot, T. (2012a). Large Eddy Simulation of combustion instabilities in a lean partially premixed swirled flame. *Combustion and Flame*, 159(2):621–637. 5

[Franzelli et al., 2012b] Franzelli, B., Riber, E., Gicquel, L. Y., and Poinsot, T. (2012b). Large Eddy Simulation of combustion instabilities in a lean partially premixed swirled flame. *Combustion and Flame*, 159(2):621–637. 49

[Franzelli et al., 2010a] Franzelli, B., Riber, E., Sanjosé, M., and Poinsot, T. (2010a). A two-step chemical scheme for kerosene-air premixed flames. *Combustion and Flame*, 157(7):1364–1373. 181

[Franzelli et al., 2010b] Franzelli, B., Riber, E., Sanjosé, M., and Poinsot, T. (2010b). A two-step chemical scheme for kerosene–air premixed flames. *Combustion and Flame*, 157(7):1364–1373. 49

[Franzelli et al., 2017] Franzelli, B., Vié, A., Boileau, M., Fiorina, B., and Darabiha, N. (2017). Large Eddy Simulation of Swirled Spray Flame Using Detailed and

Tabulated Chemical Descriptions. *Flow, Turbulence and Combustion*, 98(2):633–661. 182

[Frassoldati et al., 2010] Frassoldati, A., Cuoci, A., Faravelli, T., Niemann, U., Ranzi, E., Seiser, R., and Seshadri, K. (2010). An experimental and kinetic modeling study of n-propanol and iso-propanol combustion. *Combustion and Flame*, 157(1):2–16. 46

[Frassoldati et al., 2006] Frassoldati, A., Faravelli, T., and Ranzi, E. (2006). A wide range modeling study of NOx formation and nitrogen chemistry in hydrogen combustion. *International Journal of Hydrogen Energy*, 31(15):2310–2328. 107

[Frouzakis and Boulouchos, 2000] Frouzakis, C. E. and Boulouchos, K. (2000). Analysis and Reduction of the CH $_4$ -Air Mechanism at Lean Conditions. *Combustion Science and Technology*, 159(1):281–303. 53

[Gallen et al., 2019] Gallen, L., Felden, A., Riber, E., and Cuenot, B. (2019). Lagrangian tracking of soot particles in les of gas turbines. *Proceedings of the Combustion Institute*, 37(4):5429–5436. 5

[García-Robledo et al., 2016] García-Robledo, C., Kuprewicz, E. K., Staines, C. L., Erwin, T. L., and Kress, W. J. (2016). Limited tolerance by insects to high temperatures across tropical elevational gradients and the implications of global warming for extinction. *Proceedings of the National Academy of Sciences of the United States of America*, 113(3):680–685. 2

[García-Ybarra et al., 1984] García-Ybarra, P., Nicoli, C., and Clavin, P. (1984). Soret and Dilution Effects on Premixed Flames. *Combustion Science and Technology*, 42(1-2):87–109. 25

[Gardiner, 2012] Gardiner, W. J. (2012). *Gas-phase combustion chemistry*. Springer Science & Business Media. 12

[Gebel et al., 2015] Gebel, G. C., Mosbach, T., Meier, W., and Aigner, M. (2015). Optical and spectroscopic diagnostics of laser-induced air breakdown and kerosene spray ignition. *Combustion and Flame*, 162(4):1599–1613. 175

[Geleynse et al., 2018] Geleynse, S., Brandt, K., Garcia-Perez, M., Wolcott, M., and Zhang, X. (2018). The Alcohol-to-Jet Conversion Pathway for Drop-In Biofuels: Techno-Economic Evaluation. *ChemSusChem*, 11(21):3728–3741. 188

[Germano et al., 1991] Germano, M., Piomelli, U., Moin, P., and Cabot, W. H. (1991). A dynamic subgrid-scale eddy viscosity model. *Physics of Fluids A: Fluid Dynamics*, 3(7):1760–1765. 124

[Gicquel and Darabiha, 2000] Gicquel, O. and Darabiha, N. (2000). Laminar premixed hydrogen/air counterflow flmae simulation using flame prolongation of idlm with differential diffusion. *Proceedings of the Combustion Institute*. 47

[Gilbert et al., 1983] Gilbert, R. G., Luther, K., and Troe, J. (1983). Theory of Thermal Unimolecular Reactions in the Fall-off Range. II. Weak Collision Rate Constants. *Berichte der Bunsengesellschaft für physikalische Chemie*, 87(2):169–177. 20

[Gimeno-Escobedo et al., 2019] Gimeno-Escobedo, E., Cubero, A., Ochoa, J. S., and Fueyo, N. (2019). A reduced mechanism for the prediction of methane-hydrogen flames in cooktop burners. *International Journal of Hydrogen Energy*, 44(49):27123–27140. 76

[Giovangigli, 2015] Giovangigli, V. (2015). Multicomponent transport in laminar flames. *Proceedings of the Combustion Institute*, page 13. 28

[Giusti and Mastorakos, 2017] Giusti, A. and Mastorakos, E. (2017). Detailed chemistry LES/CMC simulation of a swirling ethanol spray flame approaching blow-off. *Proceedings of the Combustion Institute*, 36(2):2625–2632. 289

[Giusti et al., 2018] Giusti, A., Sitte, M. P., Borghesi, G., and Mastorakos, E. (2018). Numerical investigation of kerosene single droplet ignition at high-altitude relight conditions. *Fuel*, 225(December 2017):663–670. 175

[Godsave, 1953] Godsave, G. A. (1953). Studies of the combustion of drops in a fuel spray-the burning of single drops of fuel. *Symposium (International) on Combustion*, 4(1):818–830. 204

[Goodwin et al., 2017] Goodwin, D. G., Moffat, H. K., and Speth, R. L. (2017). Cantera: An object-oriented software toolkit for chemical kinetics, thermodynamics, and transport processes. `http://www.cantera.org`. Version 2.3.0. 28, 38, 67, 74

[Goussis and Lam, 1992] Goussis, D. A. and Lam, S. H. (1992). A study of homogeneous methanol oxidation kinetics using CSP. *Symposium (International) on Combustion*, 24(1):113–120. 63

[Govindaraju et al., 2019] Govindaraju, P. B., Jaravel, T., and Ihme, M. (2019). Coupling of turbulence on the ignition of multicomponent sprays. *Proceedings of the Combustion Institute*, 37(3):3295–3302. 289

[Guiberti et al., 2015a] Guiberti, T., Durox, D., Scouflaire, P., and Schuller, T. (2015a). Impact of heat loss and hydrogen enrichment on the shape of confined swirling flames. *Proceedings of the Combustion Institute*, 35(2):1385–1392. 140

[Guiberti et al., 2015b] Guiberti, T. F., Durox, D., Scouflaire, P., and Schuller, T. (2015b). Impact of heat loss and hydrogen enrichment on the shape of confined swirling flames. *Proceedings of the Combustion Institute*, 35(2):1385–1392. 101, 141, 142

[Gupta et al., 1984] Gupta, A. K., Lilley, D. G., and Syred, N. (1984). *Swirl flows*. Abacus Press. 150

[Hajiw-Riberaud and Alves-Fortunato, 2020] Hajiw-Riberaud, M. and Alves-Fortunato, M. (2020). Jetscreen - d2.1 – report about the detailed chemical composition of the fuels and pseudo-components formula. *JETSCREEN project deliverable*. 174, 180, 188

[Hallett, 2000] Hallett, W. L. (2000). A simple model for the vaporization of droplets with large numbers of components. *Combustion and Flame*, 121(1-2):334–344. 209

[Hauer et al., 2020] Hauer, M. E., Fussell, E., Mueller, V., Burkett, M., Call, M., Abel, K., McLeman, R., and Wrathall, D. (2020). Sea-level rise and human migration. *Nature Reviews Earth & Environment*, 1(1):28–39. 2

[Haworth, 2010] Haworth, D. C. (2010). Progress in probability density function methods for turbulent reacting flows. *Progress in Energy and Combustion Science*, 36(2):168–259. 130

[Hayashi et al., 1977] Hayashi, S., Kumagai, S., and Sakai, T. (1977). Propagation velocity and structure of flames in droplet-vapor-air mixtures. *Combustion Science and Technology*, 15(5-6):169–177. 290

[Heberle and Pepiot, 2020a] Heberle, L. and Pepiot, P. (2020a). Automatic identification and lumping of high-temperature fuel decomposition pathways for chemical kinetics mechanism reduction. *Proceedings of the Combustion Institute*, page S1540748920304211. 59

[Heberle and Pepiot, 2020b] Heberle, L. and Pepiot, P. (2020b). Automatic identification and lumping of high-temperature fuel decomposition pathways for chemical kinetics mechanism reduction. *Proceedings of the Combustion Institute*, 000:1–9. 246

[Herbinet et al., 2010] Herbinet, O., Pitz, W. J., and Westbrook, C. K. (2010). Detailed chemical kinetic mechanism for the oxidation of biodiesel fuels blend surrogate. *Combustion and Flame*, 157(5):893–908. 46

[Hernández-Pérez et al., 2014] Hernández-Pérez, F. E., Groth, C. P., and Gülder, L. (2014). Large-eddy simulation of lean hydrogen-methane turbulent premixed flames in the methane-dominated regime. *International Journal of Hydrogen Energy*, 39(13):7147–7157. 104

[Herzler and Naumann, 2009] Herzler, J. and Naumann, C. (2009). Shock-tube study of the ignition of methane/ethane/hydrogen mixtures with hydrogen contents from 0% to 100% at different pressures. *Proceedings of the Combustion Institute*, 32(1):213–220. 38

[Hirshfelder and Curtiss, 1954] Hirshfelder, J. O. and Curtiss, C. F.and Bird, . R. B. (1954). *Molecular theory of gases and liquids*. Materials Sciences. 27

[Huang et al., 2005] Huang, H., Fairweather, M., Griffiths, J., Tomlin, A., and Brad, R. (2005). A systematic lumping approach for the reduction of comprehensive kinetic models. *Proceedings of the Combustion Institute*, 30(1):1309–1316. 57

[Humer et al., 2007] Humer, S., Frassoldati, A., Granata, S., Faravelli, T., Ranzi, E., Seiser, R., and Seshadri, K. (2007). Experimental and kinetic modeling study of combustion of JP-8, its surrogates and reference components in laminar non-premixed flows. *Proceedings of the Combustion Institute*, 31 I(1):393–400. 182

[Humer et al., 2011] Humer, S., Seiser, R., and Seshadri, K. (2011). Experimental Investigation of Combustion of Jet Fuels and Surrogates in Nonpremixed Flows. *Journal of Propulsion and Power*, 27(4):847–855. 80, 187

[Ihme and Pitsch, 0008] Ihme, M. and Pitsch, H. (20008). Modeling of radiation and nitric oxide formation in turbulent nonpremixed flames using a flamelet/progress variable formulation. *Phys. Fluids*, page 21. 48

[Int Panis et al., 2017] Int Panis, L., Provost, E. B., Cox, B., Louwies, T., Laeremans, M., Standaert, A., Dons, E., Holmstock, L., Nawrot, T., and De Boever, P. (2017). Short-term air pollution exposure decreases lung function: a repeated measures study in healthy adults. *Environmental health : a global access science source*, 16(1):60. 106

[Irwin and Williams, 1988] Irwin, J. G. and Williams, M. L. (1988). Acid rain: Chemistry and transport. *Environmental Pollution*, 50(1-2):29–59. 106

[Jaravel, 2016] Jaravel, T. (2016). Prediction of pollutants in gas turbines using Large Eddy Simulation. *These de doctorat de l'Universite de Toulouse*. 6, 130, 182

[Jaravel et al., 2017a] Jaravel, T., Riber, E., Cuenot, B., and Bulat, G. (2017a). Large Eddy Simulation of an industrial gas turbine combustor using reduced chemistry with accurate pollutant prediction. *Proceedings of the Combustion Institute*, 36(3):3817–3825. 5

[Jaravel et al., 2017b] Jaravel, T., Riber, E., Cuenot, B., and Bulat, G. (2017b). Large Eddy Simulation of an industrial gas turbine combustor using reduced chemistry with accurate pollutant prediction. *Proceedings of the Combustion Institute*, 36(3):3817–3825. 134

[Jaravel et al., 2018] Jaravel, T., Riber, E., Cuenot, B., and Pepiot, P. (2018). Prediction of flame structure and pollutant formation of Sandia flame D using Large Eddy Simulation with direct integration of chemical kinetics. *Combustion and Flame*, 188:180–198. 76, 78

[Jaravel et al., 2019] Jaravel, T., Wu, H., and Ihme, M. (2019). Error-controlled kinetics reduction based on non-linear optimization and sensitivity analysis. *Combustion and Flame*, 200:192–206. 51

[Javed et al., 2013] Javed, I., Baek, S. W., Waheed, K., Ali, G., and Cho, S. O. (2013). Evaporation characteristics of kerosene droplets with dilute concentrations of ligand-protected aluminum nanoparticles at elevated temperatures. *Combustion and flame*, 160(12):2955–2963. 293

[Jiang et al., 2021] Jiang, B., Brouzet, D., Talei, M., Gordon, R. L., Cazères, Q., and Cuenot, B. (2021). Turbulent flame-wall interactions for flames diluted by hot combustion products. *Under review*. 93, 245

[Jones et al., 2012] Jones, W. P., Lyra, S., and Navarro-Martinez, S. (2012). Numerical investigation of swirling kerosene spray flames using Large Eddy Simulation. *Combustion and Flame*, 159(4):1539–1561. 175

[Jorgenson and Jorgenson, 2021] Jorgenson, M. T. and Jorgenson, J. C. (2021). Arctic Connections to Global Warming and Health. *Climate Change and Global Public Health*, pages 91–110. 2

[Kathrotia, 2011] Kathrotia, T. (2011). *Reaction Kinetics Modeling of OH*, CH*, and C_1tn2* Chemiluminescence*. 108

[Kathrotia et al., 2010] Kathrotia, T., Fikri, M., Bozkurt, M., Hartmann, M., Riedel, U., and Schulz, C. (2010). Study of the H+O+M reaction forming OH*: Kinetics of OH* chemiluminescence in hydrogen combustion systems. *Combustion and Flame*, 157(7):1261–1273. 108

[Kathrotia et al., 2012] Kathrotia, T., Riedel, U., Seipel, A., Moshammer, K., and Brockhinke, A. (2012). Experimental and numerical study of chemiluminescent species in low-pressure flames. *Applied Physics B: Lasers and Optics*, 107(3):571–584. 108

[Khalil and Whitelaw, 1977] Khalil, E. E. and Whitelaw, J. H. (1977). Aerodynamic and thermodynamic characteristics of kerosene-spray flames. *Symposium (International) on Combustion*, 16(1):569–576. 174

[Kobayashi et al., 2019] Kobayashi, H., Hayakawa, A., Somarathne, K. D. A., and Okafor, E. C. (2019). Science and technology of ammonia combustion. *Proceedings of the Combustion Institute*, 37(1):109–133. 107

[Kolmogorov, 1941] Kolmogorov, A. N. (1941). The local structure of turbulence in incompressible viscous fluid for very large reynolds numbers. *Proceedings of the USSR Academy of Sciences*, 30:299—-303. 118

[Komaraek et al., 2020] Komaraek, T., Ruoff, S., and Wirtz, J. (2020). Jetscreen - d6.4 – simulations of the sbb burner with respect to flame position. *JETSCREEN project deliverable*. 243

[Konnov et al., 2018] Konnov, A. A., Mohammad, A., Kishore, V. R., Kim, N. I., Prathap, C., and Kumar, S. (2018). A comprehensive review of measurements and data analysis of laminar burning velocities for various fuel+air mixtures. *Progress in Energy and Combustion Science*, 68:197–267. 46

[Koumentakos, 2019] Koumentakos, A. G. (2019). Developments in electric and green marine ships. *Applied System Innovation*, 2(4):1–21. 3

[Kubisch et al., 2015] Kubisch, E. L., Corbalán, V., Ibargüengoytía, N. R., and Sinervo, B. (2015). Local extinction risk of three species of lizard from Patagonia as a result of global warming. *Canadian Journal of Zoology*, 94(1):49–59. 2

[Kumar et al., 2020] Kumar, A., Yadav, J., and Mohan, R. (2020). Global warming leading to alarming recession of the Arctic sea-ice cover: Insights from remote sensing observations and model reanalysis. *Heliyon*, 6(7):e04355. 2

[Laera et al., 2020] Laera, D., Agostinelli, P. W., Selle, L., Cazères, Q., Oztarlik, G., Schuller, T., Gicquel, L., and Poinsot, T. (2020). Stabilization mechanisms of CH4 premixed swirled flame enriched with a non-premixed hydrogen injection. *Proceedings of the Combustion Institute*, 000:1–9. 93, 101, 106, 245

[Laidler, 1984] Laidler, K. J. (1984). The development of the Arrhenius equation. *J. Chem. Educ.*, 61(6):494. 17

[Lam and Goussis, 1994] Lam, S. H. and Goussis, D. A. (1994). The CSP method for simplifying kinetics. *Int. J. Chem. Kinet.*, 26(4):461–486. 63

[Lamarque, 2007] Lamarque, N. (2007). *Schémas numériques et conditions limites pour la simulation aux grandes échelles de la combustion diphasique dans les foyers d'hélicoptère*. PhD thesis, Université de Toulouse. 135

[Laurent and Massot, 2001] Laurent, F. and Massot, M. (2001). Multi-fluid modelling of laminar polydisperse spray flames: Origin, assumptions and comparison of sectional and sampling methods. *Combustion Theory and Modelling*, 5(4):537–572. 202

[Lax and Wendroff, 1960] Lax, P. D. and Wendroff, B. (1960). Systems of conservation laws. *Communications on Pure and Applied Mathematics*, 13:217–237. 135

[Lefebvre and Ballal, 2010] Lefebvre, A. H. and Ballal, D. R. (2010). *Gas turbine combustion: alternative fuels and emissions*. CRC press. 178

[Lefkowitz et al., 2015] Lefkowitz, J. K., Guo, P., Ombrello, T., Won, S. H., Stevens, C. A., Hoke, J. L., Schauer, F., and Ju, Y. (2015). Schlieren imaging and pulsed detonation engine testing of ignition by a nanosecond repetitively pulsed discharge. *Combustion and Flame*, 162(6):2496–2507. 175

[Legier et al., 2000a] Legier, J. P., Poinsot, T., and Veynante, D. (2000a). Dynamically thickened flame LES model for premixed and non-premixed turbulent combustion. *Proceedings of the Summer Program, Centre for Turbulence Research*, pages 157–168. 130

[Legier et al., 2000b] Legier, J. P., Poinsot, T., and Veynante, D. (2000b). Dynamically thickened flame LES model for premixed and non-premixed turbulent combustion. In *Proceedings of the Summer Program, Centre for Turbulence Research*, pages 157–168. Center for Turbulence Research, NASA Ames/Stanford Univ. 133

[Lilly, 1992] Lilly, D. K. (1992). A proposed modification of the Germano subgrid-scale closure method. *Physics of Fluids A: Fluid Dynamics*, 4(3):633–635. 124

[Løvås et al., 2002] Løvås, T., Mauss, F., Hasse, C., and Peters, N. (2002). Development of adaptive kinetics for application in combustion systems. *Proceedings of the Combustion Institute*, 29(1):1403–1410. 64, 70

[Lu et al., 2001] Lu, T., Ju, Y., and Law, C. K. (2001). Complex CSP for chemistry reduction and analysis. *Combustion and Flame*, 126(1-2):1445–1455. 63

[Lu and Law, 2005] Lu, T. and Law, C. K. (2005). A directed relation graph method for mechanism reduction. *Proceedings of the Combustion Institute*, 30(1):1333–1341. 53

[Lu and Law, 2006] Lu, T. and Law, C. K. (2006). Systematic Approach To Obtain Analytic Solutions of Quasi Steady State Species in Reduced Mechanisms. *J. Phys. Chem. A*, 110(49):13202–13208. 61, 62, 67

[Lu and Law, 2008] Lu, T. and Law, C. K. (2008). A criterion based on computational singular perturbation for the identification of quasi steady state species: A reduced mechanism for methane oxidation with NO chemistry. *Combustion and Flame*, 154(4):761–774. 76

[Lu and Law, 2009] Lu, T. and Law, C. K. (2009). Toward accommodating realistic fuel chemistry in large-scale computations. *Progress in Energy and Combustion Science*, 35(2):192–215. 67

[Luche, 2003] Luche, J. (2003). Obtention de modèles cinétiques réduits de combustion Application à un mécanisme du kérosène. 181

[Luche et al., 2004] Luche, J., Reuillon, M., Boettner, J.-C., and Cathonnet, M. (2004). Reduction of large detailed kinetics mechanisms: Applications to kerosene/air combustion. *Combustion Science and Technology*, 176(11):1935–1963. 53

[Løvs et al., 2000] Løvs, T., Nilsson, D., and Mauss, F. (2000). Automatic reduction procedure for chemical mechanisms applied to premixed methane/air flames. *Proceedings of the Combustion Institute*, 28(2):1809–1815. 64

[Magnussen and Hjertager, 1977] Magnussen, B. F. and Hjertager, B. H. (1977). On mathematical modeling of turbulent combustion with special emphasis on soot formation and combustion. In *Symposium (International) on Combustion*, volume 16, pages 719–729. The Combustion Institute, Pittsburgh. 128

[Massias et al., 1999] Massias, A., Diamantis, D., Mastorakos, E., and Goussis, D. A. (1999). An algorithm for the construction of global reduced mechanisms with CSP data. *Combustion and Flame*, 117(4):685–708. 63

[Masson-Delmotte et al.,] Masson-Delmotte, V., Zhai, P., Pörtner, H.-O., Roberts, D., Skea, J., Shukla, P. R., Pirani, A., Moufouma-Okia, W., Péan, C., Pidcock, R., Connors, S., Matthews, J. B. R., Chen, Y., Zhou, X., Gomis, M. I., Lonnoy, E., Maycock, T., Tignor, M., and Waterfield, T. Global warming of 1.5°C An IPCC Special Report on the impacts of global warming of 1.5°C above pre-industrial levels and related global greenhouse gas emission pathways, in the context of strengthening the global response to the threat of climate change,. Technical report, International Panel on Climate Change. 2

[Mastorakos, 2017] Mastorakos, E. (2017). Forced ignition of turbulent spray flames. *Proceedings of the Combustion Institute*, 36(2):2367–2383. 175

[Mathur and Saxena, 1967] Mathur, S. and Saxena, S. C. (1967). Methods of calculating thermal conductivity of binary mixtures involving polyatomic gases. *Appl. sci. Res.*, 17(2):155–168. 28

[Mehl and Pelucchi, 2020] Mehl, M. and Pelucchi, M. (2020). Jetscreen - d2.5 – report about the high temperature regime regarding auto-ignition, combustion and soot. *JETSCREEN project deliverable*. 174, 186, 187

[Mehl et al., 2011] Mehl, M., Pitz, W. J., Westbrook, C. K., and Curran, H. J. (2011). Kinetic modeling of gasoline surrogate components and mixtures under engine conditions. *Proceedings of the Combustion Institute*, 33(1):193–200. 46

[Mercier et al., 2014] Mercier, R., Auzillon, P., Moureau, V., Darabiha, N., Gicquel, O., Veynante, D., and Fiorina, B. (2014). LES modeling of the impact of heat losses and differential diffusion on turbulent stratified flame propagation: Application to the TU Darmstadt stratified flame. *Flow, Turbulence and Combustion*, 93(2):349–381. 142, 146

[Mercier et al., 2016] Mercier, R., Guiberti, T. F., Chatelier, A., Durox, D., Gicquel, O., Darabiha, N., Schuller, T., and Fiorina, B. (2016). Experimental and numerical investigation of the influence of thermal boundary conditions on premixed swirling flame stabilization. *Combustion and Flame*, 171:42–58. 101, 140, 142, 143, 144, 151

[Miller et al., 2005] Miller, J. A., Pilling, M. J., and Troe, J. (2005). Unravelling combustion mechanisms through a quantitative understanding of elementary reactions. *Proceedings of the Combustion Institute*, 30(1):43–88. 107

[Miller et al., 1998] Miller, R. S., Harstad, K., and Bellan, J. (1998). Evaluation of equilibrium and non-equilibrium evaporation models for many-droplet gas-liquid flow simulations. *International Journal of Multiphase Flow*, 24(6):1025–1055. 207

[Moesl et al., 2009] Moesl, K. G., Vollmer, K. G., Sattelmayer, T., Eckstein, J., and Kopecek, H. (2009). Experimental study on laser-induced ignition of swirl-stabilized kerosene flames. *Journal of Engineering for Gas Turbines and Power*, 131(2):1–8. 175

[Moureau et al., 2011] Moureau, V., Domingo, P., and Vervisch, L. (2011). From Large-Eddy Simulation to Direct Numerical Simulation of a lean premixed swirl flame: Filtered laminar flame-PDF modeling. *Combustion and Flame*, 158(7):1340–1357. 142

[Moureau et al., 2009] Moureau, V., Fiorina, B., and Pitsch, H. (2009). A level set formulation for premixed combustion LES considering the turbulent flame structure. *Combustion and Flame*, 156(4):801–812. 128

[Nadakkal-Appukuttan et al., 2020] Nadakkal-Appukuttan, S., Riber, E., Cuenot, B., and Gilles, T. (2020). Large eddy simulation of reactive flow on the fire side of a steam cracking furnace. In *INFUB-12*, Porto (Portugal). 93

[Narayanaswamy and Pepiot, 2018] Narayanaswamy, K. and Pepiot, P. (2018). Simulation-driven formulation of transportation fuel surrogates. *Combustion Theory and Modelling*, 22(5):883–897. 186, 187

[Narayanaswamy et al., 2016a] Narayanaswamy, K., Pitsch, H., and Pepiot, P. (2016a). A component library framework for deriving kinetic mechanisms for multi-component fuel surrogates: Application for jet fuel surrogates. *Combustion and Flame*, 165:288–309. 214, 215, 291

[Narayanaswamy et al., 2016b] Narayanaswamy, K., Pitsch, H., and Pepiot, P. (2016b). A component library framework for deriving kinetic mechanisms for multi-component fuel surrogates: Application for jet fuel surrogates. *Combustion and Flame*, 165:288–309. 175, 183

[Neophytou and Mastorakos, 2009] Neophytou, A. and Mastorakos, E. (2009). Simulations of laminar flame propagation in droplet mists. *Combustion and Flame*, 156(8):1627–1640. 290

[Neophytou et al., 2012] Neophytou, A., Richardson, E. S., and Mastorakos, E. (2012). Spark ignition of turbulent recirculating non-premixed gas and spray flames: A model for predicting ignition probability. *Combustion and Flame*, 159(4):1503–1522. 175

[Nicoud and Ducros, 1999] Nicoud, F. and Ducros, F. (1999). Subgrid-scale stress modelling based on the square of the velocity gradient tensor. *Flow, Turbulence and Combustion*, page 18. 124

[Nicoud et al., 2011] Nicoud, F., Toda, H. B., Cabrit, O., Bose, S., and Lee, J. (2011). Using singular values to build a subgrid-scale model for large eddy simulations. *Physics of Fluids*, 23(8):085106. 124, 125

[Niemeyer et al., 2010] Niemeyer, K. E., Sung, C.-J., and Raju, M. P. (2010). Skeletal mechanism generation for surrogate fuels using directed relation graph with error propagation and sensitivity analysis. *Combustion and Flame*, 157(9):1760–1770. 95

[Noh et al., 2018] Noh, D., Gallot-Lavallée, S., Jones, W. P., and Navarro-Martinez, S. (2018). Comparison of droplet evaporation models for a turbulent, non-swirling jet flame with a polydisperse droplet distribution. *Combustion and Flame*, 194:135–151. 289

[O'hayre et al., 2016] O'hayre, R., Cha, S.-W., Colella, W., and Prinz, F. B. (2016). *Fuel cell fundamentals*. John Wiley & Sons. 100

[Olson et al., 1985] Olson, D. B., Pickens, J. C., and Gill, R. J. (1985). The effects of molecular structure on soot formation II. Diffusion flames. *Combustion and Flame*, 62(1):43–60. 190

[Oseen, 1927] Oseen, C. W. (1927). *Hydrodynamik*. Leipzig. 204

[Oztarlik et al., 2020] Oztarlik, G., Selle, L., Poinsot, T., and Schuller, T. (2020). Suppression of instabilities of swirled premixed flames with minimal secondary hydrogen injection. *Combustion and Flame*, 214:266–276. 101

[Pantea et al., 2014] Pantea, C., Gupta, A., Rawlings, J. B., and Craciun, G. (2014). The QSSA in Chemical Kinetics: As Taught and as Practiced. In Jonoska, N. and Saito, M., editors, *Discrete and Topological Models in Molecular Biology*, pages 419–442. Springer Berlin Heidelberg, Berlin, Heidelberg. Series Title: Natural Computing Series. 62

[Paulhiac, 2015] Paulhiac, D. (2015). *Modélisation de la combustion d'un spray dans un brûleur aéronautique*. PhD thesis, Institut National Politechnique de Toulouse. 202

[Pejpichestakul et al., 2019] Pejpichestakul, W., Ranzi, E., Pelucchi, M., Frassoldati, A., Cuoci, A., Parente, A., and Faravelli, T. (2019). Examination of a soot model in premixed laminar flames at fuel-rich conditions. *Proceedings of the Combustion Institute*, 37(1):1013–1021. 17

[Pepiot, 2008] Pepiot, P. (2008). Automatic strategies to model transportation fuel surrogates. *Stanford University PhD thesis*. 56, 63, 72, 76, 291

[Pepiot-Desjardins and Pitsch, 2008a] Pepiot-Desjardins, P. and Pitsch, H. (2008a). An automatic chemical lumping method for the reduction of large chemical kinetic mechanisms. *Combustion Theory and Modelling*, 12(6):1089–1108. 57, 67

[Pepiot-Desjardins and Pitsch, 2008b] Pepiot-Desjardins, P. and Pitsch, H. (2008b). An efficient error-propagation-based reduction method for large chemical kinetic mechanisms. *Combustion and Flame*, 154(1-2):67–81. 54, 55, 67, 68

[Perkins-Kirkpatrick and Lewis, 2020] Perkins-Kirkpatrick, S. E. and Lewis, S. C. (2020). Increasing trends in regional heatwaves. *Nature Communications*, 11(1):1–8. 1

[Peters, 1984] Peters, N. (1984). Laminar diffusion flamelet models in non-premixed turbulent combustion. *Progress in Energy and Combustion Science*, 10(3):319–339. 46

[Peters, 1992] Peters, N. (1992). Fifteen Lectures on Laminar and Turbulent Combustion. 19

[Peters, 1999] Peters, N. (1999). The turbulent burning velocity for large-scale and small-scale turbulence. *Journal of Fluid Mechanics*, 384:107–132. 127

[Pitsch and De Lageneste, 2002] Pitsch, H. and De Lageneste, L. D. (2002). Large-eddy simulation of premixed turbulent combustion using a level-set approach. *Proceedings of the Combustion Institute*, 29(2):2001–2008. 128

[Poinsot and Lele, 1992] Poinsot, T. and Lele, S. (1992). Boundary conditions for direct simulations of compressible viscous flows. *Journal of Computational Physics*, 101(1):104–129. 135

[Poinsot and Veynante, 2012] Poinsot, T. and Veynante, D. (2012). *Theoretical and Numerical Combustion*. 3. ed. edition. 24, 33, 120, 126, 131

[Pope, 2000] Pope, S. B. (2000). *Turbulent Flows*. Cambridge University Press. 118

[Potier, 2018] Potier, L. (2018). *Large Eddy Simulation of the combustion and heat transfer in sub-critical rocket engines*. PhD thesis. 206

[Proch and Kempf, 2015] Proch, F. and Kempf, A. (2015). Modeling heat loss effects in the large eddy simulation of a model gas turbine combustor with premixed flamelet generated manifolds. *Proceedings of the Combustion Institute*, 35(3):3337–3345. 48

[Purohit et al., 2021] Purohit, A. L., Nalbandyan, A., Malte, P. C., and Novosselov, I. V. (2021). NNH mechanism in low-NOx hydrogen combustion: Experimental and numerical analysis of formation pathways. *Fuel*, 292:120186. 107

[Ra and Reitz, 2009] Ra, Y. and Reitz, R. D. (2009). A vaporization model for discrete multi-component fuel sprays. *International Journal of Multiphase Flow*, 35(2):101–117. 210

[Ranz, 1952] Ranz, W. (1952). Evaporation from drops 1. *Chem. Eng. Prog*, 48(3):141–146. 208

[Ranzi et al., 2015] Ranzi, E., Cavallotti, C., Cuoci, A., Frassoldati, A., Pelucchi, M., and Faravelli, T. (2015). New reaction classes in the kinetic modeling of low temperature oxidation of n-alkanes. *Combustion and Flame*, 162(5):1679–1691. 17, 46

[Ranzi et al., 2001] Ranzi, E., Dente, M., Goldaniga, A., Bozzano, G., and Faravelli, T. (2001). Lumping procedures in detailed kinetic modeling of gasification, pyrolysis, partial oxidation and combustion of hydrocarbon mixtures. *Progress in Energy and Combustion Science*, 27(1):99–139. 56

[Ranzi et al., 2012a] Ranzi, E., Frassoldati, A., Grana, R., Cuoci, A., Faravelli, T., Kelley, A., and Law, C. (2012a). Hierarchical and comparative kinetic modeling of laminar flame speeds of hydrocarbon and oxygenated fuels. *Progress in Energy and Combustion Science*, 38(4):468–501. 46

[Ranzi et al., 2012b] Ranzi, E., Frassoldati, A., Grana, R., Cuoci, A., Faravelli, T., Kelley, A. P., and Law, C. K. (2012b). Hierarchical and comparative kinetic modeling of laminar flame speeds of hydrocarbon and oxygenated fuels. *Progress in Energy and Combustion Science*, 38(4):468–501. 291

[Ranzi et al., 2014] Ranzi, E., Frassoldati, A., Stagni, A., Pelucchi, M., Cuoci, A., and Faravelli, T. (2014). Reduced Kinetic Schemes of Complex Reaction Systems: Fossil and Biomass-Derived Transportation Fuels. *Int. J. Chem. Kinet.*, 46(9):512–542. 17, 46, 81

[Rauch et al., 2012] Rauch, B., Calabria, R., Chiariello, F., Le Clercq, P., Massoli, P., and Rachner, M. (2012). Accurate analysis of multicomponent fuel spray evaporation in turbulent flow. *Experiments in fluids*, 52(4):935–948. 291

[Requia et al., 2018] Requia, W. J., Mohamed, M., Higgins, C. D., Arain, A., and Ferguson, M. (2018). How clean are electric vehicles? Evidence-based review of the effects of electric mobility on air pollutants, greenhouse gas emissions and human health. *Atmospheric Environment*, 185:64–77. 3

[Richardson, 1922] Richardson, L. F. (1922). Weather prediction by numerical process. *Cambridge, The University press*, pages 135–149. 118

[Risser and Wehner, 2017] Risser, M. D. and Wehner, M. F. (2017). Attributable Human-Induced Changes in the Likelihood and Magnitude of the Observed Extreme Precipitation during Hurricane Harvey. *Geophysical Research Letters*, 44(24):457–12. 1

[Rochette et al., 2018] Rochette, B., Collin-Bastiani, F., Gicquel, L., Vermorel, O., Veynante, D., and Poinsot, T. (2018). Influence of chemical schemes, numerical method and dynamic turbulent combustion modeling on LES of premixed turbulent flames. *Combustion and Flame*, 191:417–430. 239

[Rochette et al., 2019] Rochette, B., Riber, E., and Cuenot, B. (2019). Effect of non-zero relative velocity on the flame speed of two-phase laminar flames. *Proceedings of the Combustion Institute*, 37(3):3393–3400. 214, 215, 290, 292, 294, 296, 299, 300

[Rochette et al., 2020] Rochette, B., Riber, E., Cuenot, B., and Vermorel, O. (2020). A generic and self-adapting method for flame detection and thickening in the thickened flame model. *Combustion and Flame*, 212:448–458. 130, 134, 135

[Romer et al., 2018] Romer, P. S., Duffey, K. C., Wooldridge, P. J., Edgerton, E., Baumann, K., Feiner, P. A., Miller, D. O., Brune, W. H., Koss, A. R., De Gouw, J. A., Misztal, P. K., Goldstein, A. H., and Cohen, R. C. (2018). Effects of temperature-dependent NOx emissions on continental ozone production. *Atmospheric Chemistry and Physics*, 18(4):2601–2614. 106

[Root et al., 2003] Root, T. L., Price, J. T., Hall, K. R., Schneider, S. H., Rosenzweig, C., and Pounds, J. A. (2003). Fingerprints of global warming on wild animals and plants. *Nature*, 421(6918):57–60. 2

[Ruoff et al., 2020] Ruoff, S., Mosbach, T., Cantu, L., Eckel, G., Meier, W., Wirtz, J., Riber, E., and Cuenot, B. (2020). Jetscreen - d6.2 – impact of fuel on lbo (experimental and numerical work). *JETSCREEN project deliverable*. 243

[Sabia et al., 2013] Sabia, P., de Joannon, M., Picarelli, A., and Ragucci, R. (2013). Methane auto-ignition delay times and oxidation regimes in MILD combustion at atmospheric pressure. *Combustion and Flame*, page 9. 38

[Sagaut, 1998] Sagaut, P. (1998). *Introduction à la simulation des grandes échelles*. Springer, mathématiq edition. 120

[Sánchez et al., 2015] Sánchez, A. L., Urzay, J., and Liñán, A. (2015). The role of separation of scales in the description of spray combustion. *Proceedings of the Combustion Institute*, 35(2):1549–1577. 289

[Schaaf et al., 2014] Schaaf, T., Grünig, J., Schuster, M. R., Rothenfluh, T., and Orth, A. (2014). Methanation of CO2 - storage of renewable energy in a gas distribution system. *Energy, Sustainability and Society*, 4(1):1–14. 100

[Schefer, 2003] Schefer, R. W. (2003). Hydrogen enrichment for improved lean flame stability. *International Journal of Hydrogen Energy*, 28(10):1131–1141. 101

[Schefer et al., 2009] Schefer, R. W., Kulatilaka, W. D., Patterson, B. D., and Settersten, T. B. (2009). Visible emission of hydrogen flames. *Combustion and Flame*, 156(6):1234–1241. 108

[Schiller and Naumann, 1935] Schiller, L. and Naumann, Z. (1935). A drag coefficient correlation. *Z.Ver.Deutsch.Ing*, 77(13-14):318–320. 204

[Schønfeld and Rudgyard, 1999] Schønfeld, T. and Rudgyard, M. (1999). Steady and Unsteady Flows Simulations Using the Hybrid Flow Solver AVBP. *AIAA journal*, 37(11):1378–1385. 135

[Senoner, 2010] Senoner, J.-M. (2010). *thèse suivante Simulations aux grandes échelles de l'écoulement diphasique dans un brûleur aéronautique par une approche Euler-Lagrange*. PhD thesis, Institut National Politechnique de Toulouse. 202

[Shastry et al., 2020a] Shastry, V., Cazeres, Q., Rochette, B., Riber, E., and Cuenot, B. (2020a). Numerical study of multicomponent spray flame propagation. *Proceedings of the Combustion Institute*, page S154074892030540X. 93

[Shastry et al., 2020b] Shastry, V., Cazeres, Q., Rochette, B., Riber, E., and Cuenot, B. (2020b). Numerical study of multicomponent spray flame propagation. *Proceedings of the Combustion Institute*, 000:1–11. 182, 183, 214, 215, 216, 217

[Shiraishi et al., 2009] Shiraishi, T., Urushihara, T., and Gundersen, M. (2009). A trial of ignition innovation of gasoline engine by nanosecond pulsed low temperature plasma ignition. *Journal of Physics D: Applied Physics*, 42(13). 175

[Sierra Sànchez, 2012] Sierra Sànchez, P. (2012). *Modeling the dispersion and evaporation of sprays in aeronautical combustion chambers*. PhD thesis, Institut National Politechnique de Toulouse. 202

[Sirignano, 2010] Sirignano, W. A. (2010). *Fluid dynamics and transport of droplets and sprays*. Cambridge University press. 289, 292, 293, 299

[Smagorinsky, 1963] Smagorinsky, J. (1963). General circulation experiments with the primitive equations. *Monthly weather review*. 123

[Smith et al., 1999] Smith, G. P., Golden, D. M., Frenklach, M., Moriarty, N. W., Eiteneer, B., Goldenberg, M., Bowman, C. T., Hanson, R. K., Song, S., Gardiner Jr., W. C., Lissianski, V. V., and Qin, Z. (1999). GRI-Mech. *http://combustion.berkeley.edu/gri-mech/*. 76

[Spalding, 1953] Spalding, D. B. (1953). The combustion of liquid fuels. In *Symposium (International) on Combustion*, volume 4, pages 847–864. The Combustion Institute, Pittsburgh. 204

[Spellman and Spellman, 2020] Spellman, F. R. and Spellman, F. R. (2020). *Combustion Theory*. Benjamin Cummings, Menlo Park, CA. 128

[Stagni et al., 2014] Stagni, A., Cuoci, A., Frassoldati, A., Faravelli, T., and Ranzi, E. (2014). Lumping and Reduction of Detailed Kinetic Schemes: an Effective Coupling. *Ind. Eng. Chem. Res.*, 53(22):9004–9016. 56

[Stagni et al., 2017] Stagni, A., Esclapez, L., Govindaraju, P., Cuoci, A., Faravelli, T., and Ihme, M. (2017). The role of preferential evaporation on the ignition of multicomponent fuels in a homogeneous spray/air mixture. *Proceedings of the Combustion Institute*, 36(2):2483–2491. 182, 289

[Stagni et al., 2016] Stagni, A., Frassoldati, A., Cuoci, A., Faravelli, T., and Ranzi, E. (2016). Skeletal mechanism reduction through species-targeted sensitivity analysis. *Combustion and Flame*, 163:382–393. 51, 68

[Stewart et al., 1989] Stewart, P. H., Larson, C. W., and Golden, D. M. (1989). Pressure and Temperature Dependence of Reactions Proceeding Via A Bound Complex. 2. Application to 2CH3 ~ C2Hs + H. *Combustion and Flames*, page 7. 20

[Sun et al., 2010] Sun, W., Chen, Z., Gou, X., and Ju, Y. (2010). A path flux analysis method for the reduction of detailed chemical kinetic mechanisms. *Combustion and Flame*, 157(7):1298–1307. 53

[Sung et al., 2001] Sung, C., Law, C., and Chen, J.-Y. (2001). Augmented reduced mechanisms for NO emission in methane oxidation. *Combustion and Flame*, 125(1-2):906–919. 76

[Taherkhani et al., 2020] Taherkhani, M., Vitousek, S., Barnard, P. L., Frazer, N., Anderson, T. R., and Fletcher, C. H. (2020). Sea-level rise exponentially increases coastal flood frequency. *Scientific Reports*, 10(1):1–17. 2

[Tinoco and Jaworski, 2014] Tinoco, I. and Jaworski, A., editors (2014). *Physical chemistry: principles and applications in biological sciences*. Pearson advanced chemistry series. Pearson, Boston, Mass., 5. ed., internat. ed edition. OCLC: 829243499. 16

[Turanyi, 1990] Turanyi, T. (1990). Sensitivity analysis of complex kinetic systems. Tools and applications. *J Math Chem*, 5(3):203–248. 51

[Vajda et al., 1985] Vajda, S., Valko, P., and Turányi, T. (1985). Principal component analysis of kinetic models. *Int. J. Chem. Kinet.*, 17(1):55–81. 51

[van Oijen et al., 2001] van Oijen, J., Lammers, F., and de Goey, L. (2001). Modeling of complex premixed burner systems by using flamelet-generated manifolds. *Combustion and Flame*, 127(3):2124–2134. 47

[Van Rossum and Drake, 2009] Van Rossum, G. and Drake, F. L. (2009). *Python 3 Reference Manual*. CreateSpace, Scotts Valley, CA. 92

[Veynante and Vervisch, 2002a] Veynante, D. and Vervisch, L. (2002a). Turbulent combustion modeling. *Progress in Energy and Combustion Science*, 28(3):193–266. 129

[Veynante and Vervisch, 2002b] Veynante, D. and Vervisch, L. (2002b). Turbulent combustion modeling. *Progress in Energy and Combustion Science*, 28(3):193–266. 128

[Vogel et al., 2020] Vogel, M. M., Zscheischler, J., Fischer, E. M., and Seneviratne, S. I. (2020). Development of Future Heatwaves for Different Hazard Thresholds. *Journal of Geophysical Research: Atmospheres*, 125(9):e2019JD032070. 1

[Voivenel et al., 2020] Voivenel, L., May-Carles, J.-B., Puggelli, S., Bodoc, V., Garraud, J., Gajan, P., Bigot, F., Doublet, P., Sebbane, D., Shastry, V., Riber, E., and Cuenot, B. (2020). Jetscreen - impact of fuel on flame transfer function / combustion stability (experimental and numerical work). *JETSCREEN project deliverable*. 243

[Waage and Gulberg, 1986] Waage, P. and Gulberg, C. M. (1986). Studies concerning affinity. *J. Chem. Educ.*, 63(12):1044. 16

[Wang et al., 2018] Wang, H., Xu, R., Wang, K., Bowman, C. T., Hanson, R. K., Davidson, D. F., Brezinsky, K., and Egolfopoulos, F. N. (2018). A physics-based approach to modeling real-fuel combustion chemistry - I. Evidence from experiments, and thermodynamic, chemical kinetic and statistical considerations. *Combustion and Flame*, 193:502–519. 57, 59

[Westbrook and Dryer, 1981] Westbrook, C. K. and Dryer, F. L. (1981). Simplified Reaction Mechanisms for the Oxidation of Hydrocarbon Fuels in Flames. *Combustion Science and Technology*, 27(1-2):31–43. 48

[Westbrook et al., 2009] Westbrook, C. K., Pitz, W. J., Herbinet, O., Curran, H. J., and Silke, E. J. (2009). A comprehensive detailed chemical kinetic reaction mechanism for combustion of n-alkane hydrocarbons from n-octane to n-hexadecane. *Combustion and Flame*, 156(1):181–199. 182

[Wilke, 1950] Wilke, C. R. (1950). A Viscosity Equation for Gas Mixtures. *The Journal of Chemical Physics*, 18(4):517–519. 28

[Wirtz et al., 2020] Wirtz, J., Cuenot, B., and Riber, E. (2020). Numerical study of a polydisperse spray counterflow diffusion flame. *Proceedings of the Combustion Institute*, page S1540748920300900. 93, 245

[Wunderling et al., 2020] Wunderling, N., Willeit, M., Donges, J. F., and Winkelmann, R. (2020). Global warming due to loss of large ice masses and Arctic summer sea ice. *Nature Communications*, 11(1):1–8. 2

[Xu et al., 2018] Xu, R., Wang, K., Banerjee, S., Shao, J., Parise, T., Zhu, Y., Wang, S., Movaghar, A., Lee, D. J., Zhao, R., Han, X., Gao, Y., Lu, T., Brezinsky, K., Egolfopoulos, F. N., Davidson, D. F., Hanson, R. K., Bowman, C. T., and Wang, H. (2018). A physics-based approach to modeling real-fuel combustion chemistry – II. Reaction kinetic models of jet and rocket fuels. *Combustion and Flame*, 193:520–537. 57, 58

[Yadav et al., 2020] Yadav, J., Kumar, A., and Mohan, R. (2020). Dramatic decline of Arctic sea ice linked to global warming. *Natural Hazards*, 103(2):2617–2621. 2

[Yamashita et al., 1996] Yamashita, H., Shimada, M., and Takeno, T. (1996). A numerical study on flame stability at the transition point of jet diffusion flames. *Symposium (International) on Combustion*, 26(1):27–34. 41

[Yaws, 2009] Yaws, C. L. (2009). *Transport Properties of Chemicals and Hydrocarbons*. William Andrew. 211

[Yaws, 2015] Yaws, C. L. (2015). *The Yaws Handbook of Physical Properties for Hydrocarbons and Chemicals*. Gulf Professional Publishing. 211

[You and Xu, 2010] You, C. F. and Xu, X. C. (2010). Coal combustion and its pollution control in China. *Energy*, 35(11):4467–4472. 3

[Zeldovich and Frank-Kamenetskii, 1962] Zeldovich, Y. B. and Frank-Kamenetskii, D. A. (1962). *Selected works of Ya. B. Zeldovich, Chemical Physics and Hydrodynamics,*. Princeton University Press. 106

[Zhao et al., 2018] Zhao, M., Buttsworth, D., and Choudhury, R. (2018). Experimental and numerical study of OH* chemiluminescence in hydrogen diffusion flames. *Combustion and Flame*, 197:369–377. 108

[Zhu, 2015] Zhu, M. (2015). Simulation aux grandes échelles du craquage thermique dans l'industrie pétrochimique. *These de doctorat de l'Universite de Toulouse*, page 247. 87

Appendix A

ARCANE demo file basic/interface.py

```
# Import statements
import ARCANE.cases as cases
import ARCANE.mechanisms as mechanisms
import ARCANE.graphs as graphs

# ------------------------------- #
# User-defined variables
# ------------------------------- #

# cti file containing initial mechanism
cti = "cti/gri30.cti"

# Create ARCANE mechanism instance
# This object is an enhanced Cantera Solution object carrying useful information
current_mechanism = mechanisms.Mechanism(cti, name='GRI-Mech30')

# Initialize folders

# Where to store generated cti files (mechanism database)
# Creates the mechanisms directory(default is 'mechs')
# If the initialization is not written, default directory will be initialized
# mechanisms.init_mechanism_database(mechdir="mechs_demo")

# Where to store all simulation results (case database)
# Creates the cases directory(default is 'cases')
```

```
# If the initialization is not written, default directory will be initialized
# cases.init_case_database(casedir="cases_demo")

# Fuel composition
fuel = "X/CH4/1"

# Air composition
air = "X/O2/1/N2/3.76"

# ------------------------------- #

# Definition of cases

# List in which the different cases will be stored
cases_list = []

# Case selection: "0DIsochoric", "0DIsobaric", "1DPremixed", "1DCounterFlow",
# "1DFlamelet", "1DBurner", "Custom" or "all"
run_reactor = "all"

# Zero-dimensional isochoric reactor

if run_reactor in ["0DIsochoric", "all"]:

    # Thermodynamic ranges
    temperature_range = "1000/1600/100"  # = [1000, 1100, 1200, 1300, 1400, 1500, 1600]
    pressure_range = "1e5-2e5-5e5"       # = [1e5, 2e5, 5e5]
    phi_range = "1"                      # = [1]

    # Creation of the cases
    cases_list.extend(cases.create_case(reactor="0DIsochoric",            # Type of reactor
                                        mechanism=current_mechanism,      # Mechanism object
                                        fuel=fuel,                        # Fuel composition
                                        oxidizer=air,                     # Oxidizer composition
                                        pressure=pressure_range,          # Initial pressure
                                        temperature=temperature_range,    # Initial temperature
                                        phi=phi_range))                   # Equivalence ratio


# Zero-dimensional isobaric reactor

if run_reactor in ["0DIsobaric", "all"]:

    # Thermodynamic ranges
    temperature_range = 1000
    pressure_range = 1e5
```

```
    phi_range = 1

    # Here the composition is specified in mass due to the "Y" keyword at the beginning
    composition = "Y/CH4/0.5/O2/2/N2/6.58"

    # Creation of the cases
    cases_list.extend(cases.create_case(reactor="0DIsobaric",
                                        mechanism=current_mechanism,
                                        fuel=fuel,
                                        oxidizer=air,
                                        pressure=pressure_range,
                                        temperature=temperature_range,
                                        composition=composition))

# One-dimensional freely propagating premixed flame

if run_reactor in ["1DPremixed", "all"]:

    # Thermodynamic ranges
    temperature_range = 300
    pressure_range = "1e5-2e5-5e5"
    phi_range = 1

    cases_list.extend(cases.create_case(reactor="1DPremixed",
                                        mechanism=current_mechanism,
                                        fuel=fuel,
                                        oxidizer=air,
                                        pressure=pressure_range,
                                        temperature=temperature_range,
                                        phi=phi_range))

# One-dimensional counter-flow diffusion flame

if run_reactor in ["1DCounterFlow", "all"]:

    # Thermodynamic ranges
    fuel_temperature_range = 1000
    fuel_velocity_range = "50-100"
    oxidizer_temperature_range = 1000
    oxidizer_velocity_range = 50
    pressure_range = 10e5

    oxidizer = "X/O2/1"

    cases_list.extend(cases.create_case(reactor="1DCounterFlow",
                                        mechanism=current_mechanism,
```

```
                                        pressure=pressure_range,
                                        fuel=fuel,
                                        fuel_temperature=fuel_temperature_range,
                                        oxidizer=oxidizer,
                                        oxidizer_temperature=oxidizer_temperature_range,
                                        fuel_velocity=fuel_velocity_range,
                                        oxidizer_velocity=oxidizer_velocity_range,
                                        width=1))

# One-dimensional counter-flow diffusion flame in mixture fraction space (flamelet)

if run_reactor in ["1DFlamelet", "all"]:

    # Thermodynamic ranges
    fuel_temperature_range = 300
    oxidizer_temperature_range = 300
    pressure_range = 1e5
    scalar_dissipation_rate_range = "1-10-50"

    oxidizer = "X/O2/1"

    cases_list.extend(cases.create_case(reactor="1DFlamelet",
                                        mechanism=current_mechanism,
                                        fuel=fuel,
                                        oxidizer=oxidizer,
                                        pressure=pressure_range,
                                        fuel_temperature=fuel_temperature_range,
                                        oxidizer_temperature=oxidizer_temperature_range,
                                        scalar_dissipation_rate=scalar_dissipation_rate_range))

# One-dimensional burner flame

if run_reactor in ["1DBurner", "all"]:

    # Thermodynamic ranges
    temperature_range = 300
    pressure_range = 1.0125e5
    phi_range = 1
    velocity_range = "0.1-0.15"

    cases_list.extend(cases.create_case(reactor="1DBurner",
                                        mechanism=current_mechanism,
                                        fuel=fuel,
                                        oxidizer=air,
                                        phi=phi_range,
                                        pressure=pressure_range,
```

```
                                    temperature=temperature_range,
                                    velocity=velocity_range))  # or mass_flow_rate

# Case computed from an outside function

if run_reactor in ["Custom", "all"]:

    # Definition of your function
    # mechanism, temperature, pressure and composition are mandatory arguments
    def equilibrate(mechanism, temperature, composition, pressure, Tmax, step):

        import numpy as np

        ctmech = mechanism.ctmech
        Temps = list(range(int(temperature), Tmax, step))
        ctmech.TPX = temperature, pressure, composition

        x_store = np.zeros(len(Temps), 'd')
        T_store = np.zeros(len(Temps), 'd')
        P_store = np.zeros(len(Temps), 'd')
        Y_store = np.zeros([len(Temps), ctmech.n_species], 'd')

        for index, T in enumerate(Temps):
            ctmech.TP = T, pressure
            ctmech.equilibrate('TP')
            x_store[index] = index
            T_store[index] = T
            P_store[index] = pressure
            Y_store[index, :] = ctmech.Y

        ###########################################################
        # This is the data format you need to give to ARCANE #
        ###########################################################

        # Corresponding data
        ###################################
        # grid, T, P, Y are mandatory
        data = [x_store, T_store, P_store]
        for i in range(len(Y_store[0, :])):
            data.append(Y_store[:, i])
        ###################################
        # grid, T, P, Y are mandatory
        data_names = ['Grid', 'Temperature', 'Pressure']
        for spec_name in ctmech.species_names:
            data_names.append(spec_name)
        ###################################
```

```
        return data, data_names

        ########################################################

    # Here create your case with all the parameters you need,
    # Their names must match what you wrote in the function
    cases_list.extend(cases.create_case(reactor="Custom",
                                        mechanism=current_mechanism,
                                        # This is your actual function (mandatory)
                                        function=equilibrate,
                                        temperature=300,
                                        pressure="1e5-2e5",
                                        composition='X/CH4/50/O2/50',
                                        Tmax=3000,
                                        step=100))

# Run simulations
cases.run_cases(cases_list, current_mechanism, overwrite=True)
```

Appendix B

ARCANE demo file basic/error.py

```
# Import statements
import ARCANE.cases as cases
import ARCANE.mechanisms as mechanisms
import ARCANE.error as error

# ------------------------------- #
# User-defined variables
# ------------------------------- #

# cti file containing initial mechanism
cti_old = "cti/gri211.cti"

# cti file containing initial mechanism
cti_new = "cti/gri30.cti"

# Air composition
air = "X/O2/0.21/N2/0.79"

# ------------------------------- #

# Create ARCANE mechanism instance
old_mechanism = mechanisms.Mechanism(cti_old, name='GRI-Mech211')

# Fuel composition
fuel = "X/CH4/1"


def rho_final(case, mechanism):
```

```
    """

    :param case:
    :param mechanism:
    :return:
    """

    data = case.extract_profile(mechanism)
    names_dict = case.names_dictionary(mechanism)

    value = data[-1, names_dict['Density']]

    return value


def rho_min(case, mechanism):
    """

    :param case:
    :param mechanism:
    :return:
    """

    data = case.extract_profile(mechanism)
    names_dict = case.names_dictionary(mechanism)

    value = min(data[:, names_dict['Density']])

    return value


# Definition of cases
caselist = []
caselist.extend(cases.create_case(reactor="0DIsochoric",
                                  mechanism=old_mechanism,
                                  fuel=fuel,
                                  oxidizer=air,
                                  pressure="1e5",
                                  temperature="1000",
                                  phi="1",
                                  error_dict={'tig': 1,
                                              'hr max': 1}))

caselist.extend(cases.create_case(reactor="0DIsochoric",
                                  mechanism=old_mechanism,
                                  fuel=fuel,
```

```
                                    oxidizer=air,
                                    pressure="1e5",
                                    temperature="1600",
                                    phi="1",
                                    error_dict={'tig': 1,
                                                'HR max': 1,
                                                'NO end': 1}))

caselist.extend(cases.create_case(reactor="1DPremixed",
                                    mechanism=old_mechanism,
                                    fuel=fuel,
                                    oxidizer=air,
                                    pressure="1e5",
                                    temperature="300",
                                    phi="0.6-1-1.6",
                                    error_dict={'Sl': 1,
                                                'u end': 1,
                                                'temperature end': 1,
                                                'Thickness': 1,
                                                rho_final: 1,
                                                rho_min: 1}))

# Possibilities for the error are :
#
# Temperature
# Pressure
# Heat Release rate
# Thickness
# Velocity
# Species mass fractions
#
# with and associated method : init, end, min, max, mean, int (for integral)
# and dist (distance between the curves)
#
# Plus scalars quantities :
# Auto-ignition delay time
# Laminar flame speed
#
# You can also use a function as a key;
# This function must return a scalar value and take case and mechanism as arguments

# Run simulations
cases.run_cases(caselist, old_mechanism)

# Create reference custom mechanism instance
new_mechanism = mechanisms.Mechanism(cti_new, name='GRI-Mech30')
```

```
# Run simulations with custom kinetics
cases.run_cases(caselist, new_mechanism)

# display errors corresponding to error_dict
for case in caselist:
    error.case_error(case, old_mechanism, mechanism=new_mechanism)

# Computing a specific error
error_hr_int = error.compute_error('HR integral', caselist[2],
                                   old_mechanism, case=caselist[4])

print('\nRelative difference of integral heat release rate between lean and rich flame:')
print(error_hr_int[0], '(with values of the integral respectively',
                      error_hr_int[1], 'and', error_hr_int[2], ')')
```

Appendix C

Further validation of the Cazères27 mechanism

Validation of the Cazères27 reduced mechanism on a lean (0.6) (Fig.C.0.1) and rich (1.4) mixture (Fig. C.0.1).

The mechanism can also be validated on maximum values of the species of interest NO, NO_2 and OH^* as well as CO_2 and CO.

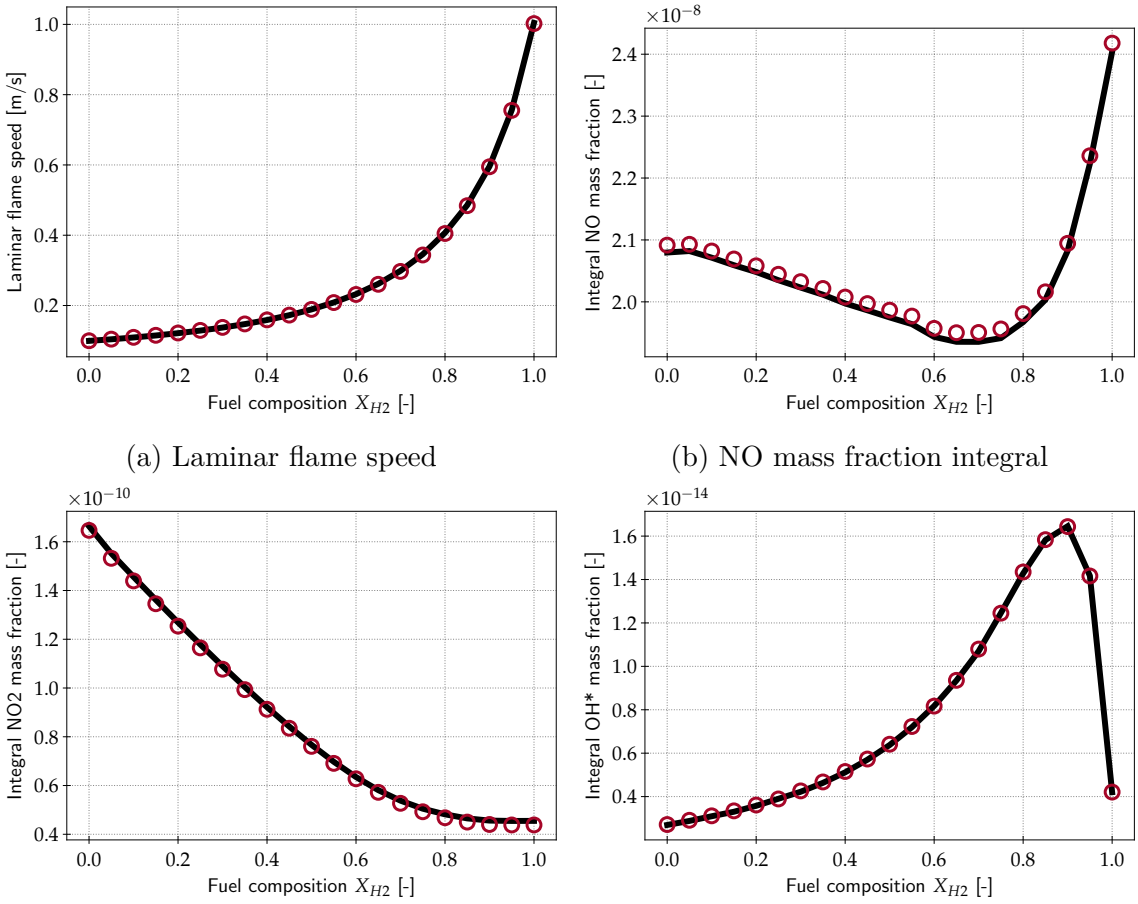

(a) Laminar flame speed

(b) NO mass fraction integral

(c) NO_2 mass fraction integral

(d) OH^* mass fraction integral

Figure C.0.1: Validation of the reduced mechanism for a range of hydrogen enrichment of methane laminar premixed flames with T_{inlet} = 300 K and 1 bar at ϕ = 0.6. The black solid line stand for the detailed mechanism (POLIMI_C1C3_NOx_Chemlum) and red circles stand for the reduced mechanism (Cazères27)

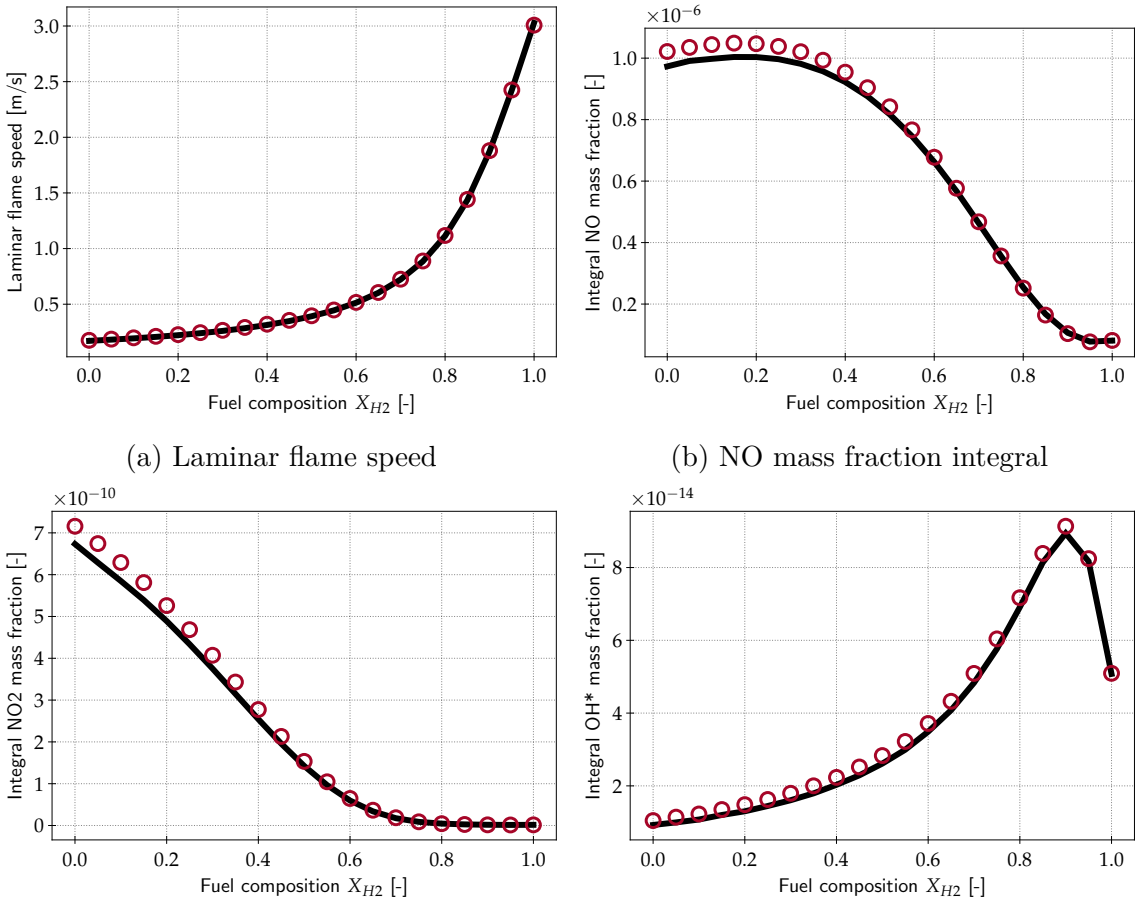

(a) Laminar flame speed

(b) NO mass fraction integral

(c) NO_2 mass fraction integral

(d) OH^* mass fraction integral

Figure C.0.2: Validation of the reduced mechanism for a range of hydrogen enrichment of methane laminar premixed flames with $T_{inlet} = 300$ K and 1 bar at $\phi = 1.4$. The black solid line stand for the detailed mechanism (POLIMI_C1C3_NOx_Chemlum) and red circles stand for the reduced mechanism (Cazères27)

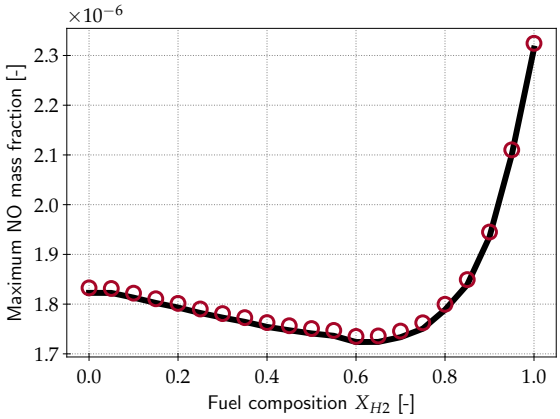

(a) Maximum NO mass fraction

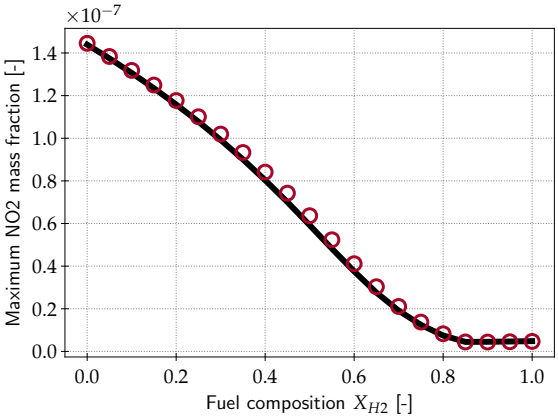

(b) Maximum NO_2 mass fraction

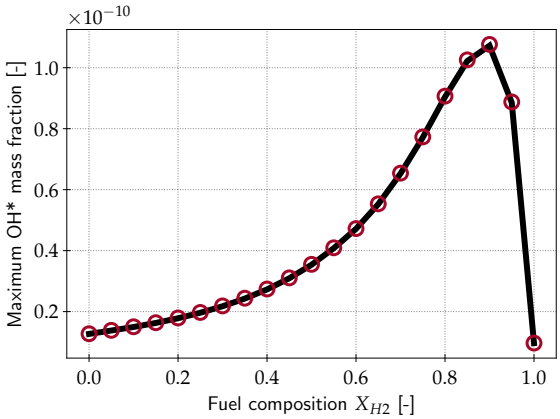

(c) Maximum OH^* mass fraction

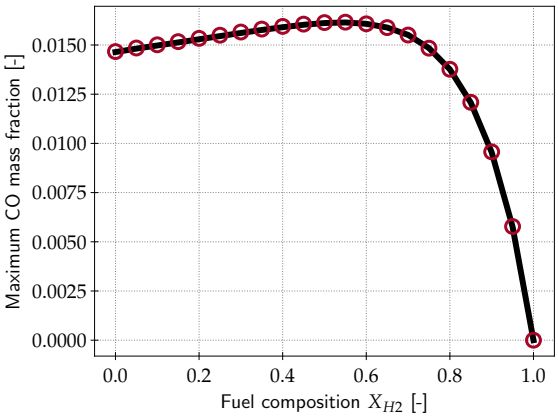

(d) Maximum CO mass fraction

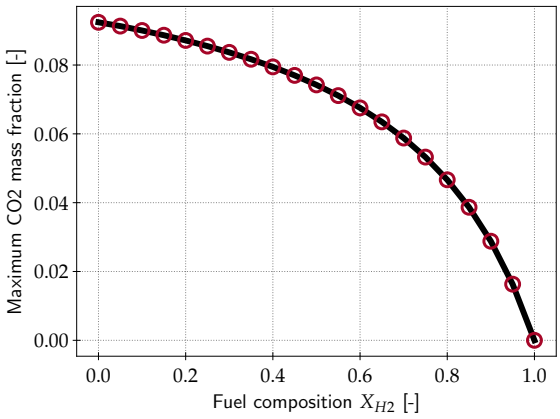

(e) Maximum CO_2 mass fraction

Figure C.0.3: Validation of the reduced mechanism for a range of hydrogen enrichment of methane laminar premixed flames with T_{inlet} = 300 K and 1 bar at ϕ = 0.6. The black solid line stand for the detailed mechanism (POLIMI_C1C3_NOx_Chemlum) and red circles stand for the reduced mechanism (Cazères27)

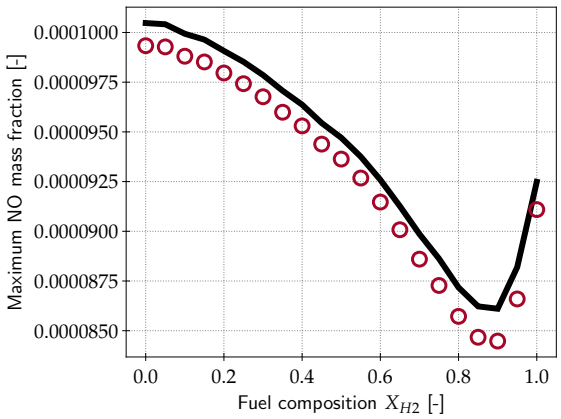

(a) Maximum NO mass fraction

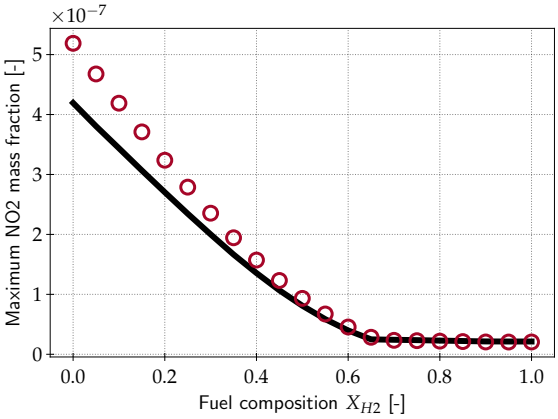

(b) Maximum NO_2 mass fraction

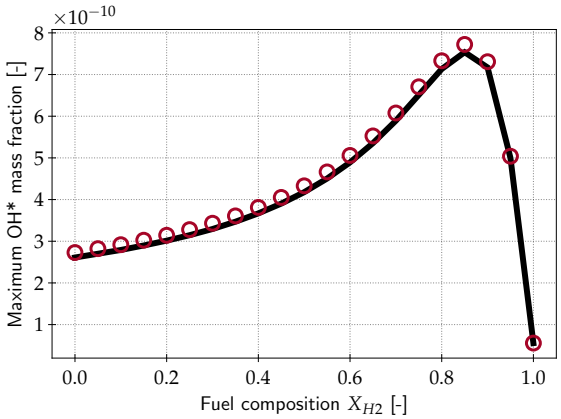

(c) Maximum OH* mass fraction

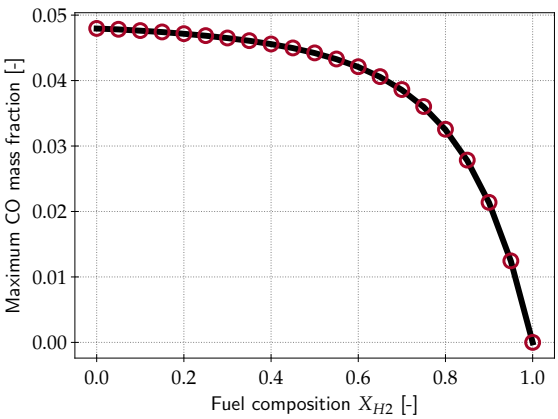

(d) Maximum CO mass fraction

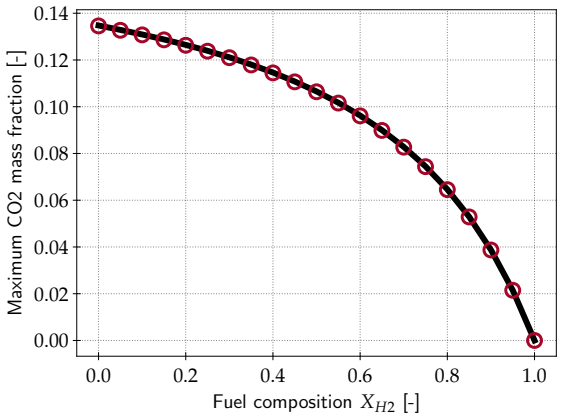

(e) Maximum CO_2 mass fraction

Figure C.0.4: Validation of the reduced mechanism for a range of hydrogen enrichment of methane laminar premixed flames with $T_{inlet} = 300$ K and 1 bar at $\phi = 1$. The black solid line stand for the detailed mechanism (POLIMI_C1C3_NOx_Chemlum) and red circles stand for the reduced mechanism (Cazères27)

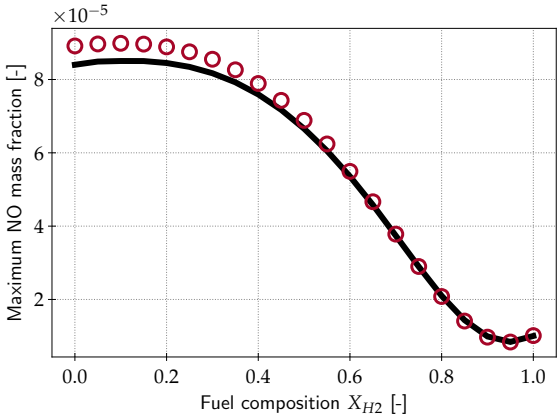

(a) Maximum NO mass fraction

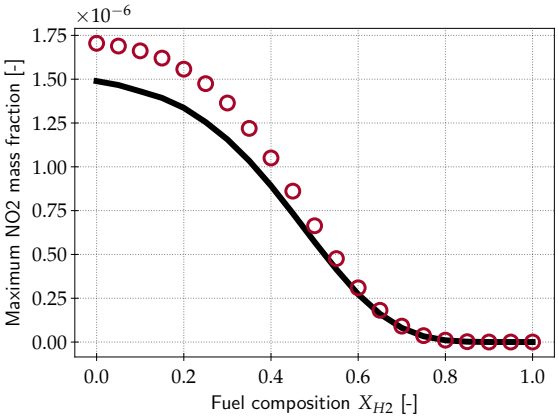

(b) Maximum NO_2 mass fraction

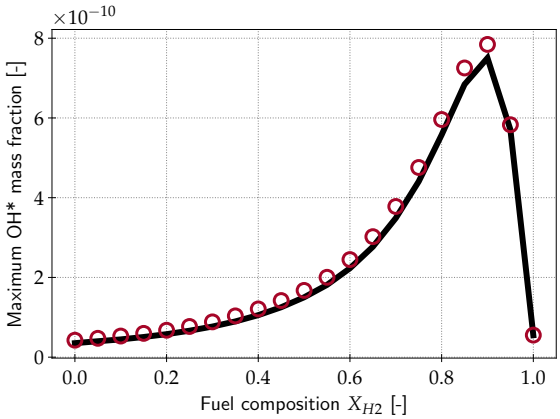

(c) Maximum OH^* mass fraction

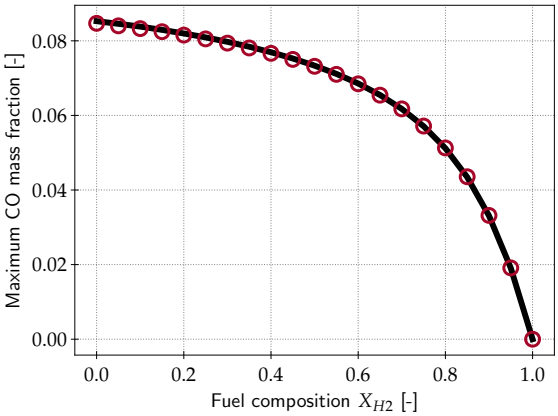

(d) Maximum CO mass fraction

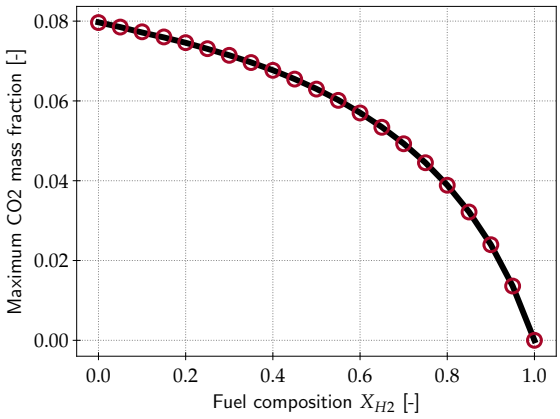

(e) Maximum CO_2 mass fraction

Figure C.0.5: Validation of the reduced mechanism for a range of hydrogen enrichment of methane laminar premixed flames with T_{inlet} = 300 K and 1 bar at ϕ = 1.4. The black solid line stand for the detailed mechanism (POLIMI_C1C3_NOx_Chemlum) and red circles stand for the reduced mechanism (Cazères27)

Appendix D

Full paper: Numerical study of multicomponent spray flame propagation

Introduction

Spray formation and combustion have been extensively studied due to the wide ranging applications in propulsion and power generation[Sirignano, 2010]. The various mechanisms involved, occurring at different length and time scales lead to a very complex combustion process with multiple flame structures and combustion regimes [Sánchez et al., 2015]. Large Eddy Simulations (LES) coupled with detailed chemistry descriptions have been recently performed to get an insight into these highly coupled systems. However a single component representation of the liquid fuel has been mostly utilised [Felden et al., 2018b, Giusti and Mastorakos, 2017, Noh et al., 2018].

Real fuels used in these combustion systems contain a large number of components belonging to a range of hydrocarbon families. Differences in their volatilities cause a spatio-temporal variation of the reactive gas phase mixture as the spray evolves. Additionally, preferential evaporation significantly affects the mixture reactivity specially when vaporisation and autoignition time-scales are comparable and in the presence of turbulent structures [Stagni et al., 2017, Govindaraju et al., 2019].

To address these, a detailed study of multicomponent spray flame structure and propagation is thus necessary in understanding turbulent combustion of fuel blends and developing corresponding models in addition to the existing LES studies [Eckel et al., 2019].

To the authors knowledge, little literature exists on multicomponent laminar spray flames and the parameters influencing it. The one dimensional laminar premixed spray flame configuration using a single component fuel has been studied to understand the main propagation mechanisms. For lean and stoichiometric mixtures, [Ballal and Lefebvre, 1981] experimentally showed that compared to a gaseous premixed laminar flame at the same overall equivalence ratio, increasing droplet diameter reduces the laminar spray flame speed. This is due to the vapourisation of smaller droplets before reaching the flamefront, which increases the equivalence ratio seen by the flame. For rich mixtures, [Hayashi et al., 1977] observed an enhanced flame speed over a specific range of droplet diameters. Here the partial evaporation causes the mixture to burn at stoichiometric conditions enhancing the flame speed. Based on detailed chemistry simulations, [Neophytou and Mastorakos, 2009] marginally correlated the laminar spray flame speed trends with an effective equivalence ratio ϕ_{eff} seen by the flame. All of these studies were performed for zero relative velocity between the liquid and the gas phases. However recently, [Rochette et al., 2019] performed one dimensional n-heptane laminar spray flame simulations using a two-step chemistry and showed that the relative velocity between the liquid phase and the carrier gas phase also has significant impact on ϕ_{eff} and hence the propagation speed. They also derived correlations for the estimation of ϕ_{eff} and the laminar spray flame speed as a function of the spray parameters.

This work aims to analyse the effect of a multicomponent fuel on spray flames, including evaporation and chemistry effects. It is the first attempt to include both Analytically Reduced Chemistry (ARC) and multicomponent evaporation in one dimensional numerical simulations to understand the effect of various spray parameters (diameter, liquid loading, relative velocity and equivalence ratio) on the structure and propagation of a multicomponent spray flame.

Numerical setup

Computations are performed using the CFD code AVBP with a Lagrangian point particle formulation to represent the spray. Source terms for transfer of mass, momentum and energy from the liquid to gaseous phase are distributed to the closest nodes in the Eulerian gas phase in a two-way coupling approach (http://cerfacs.fr/avbp7x/).

Chemical Mechanism

In this work, the surrogate for Jet-A proposed by [Narayanaswamy et al., 2016a] is reduced. The three components of the surrogate are n-dodecane (NDC), methyl-cyclohexane (MCH) and a xylene (XYL) species that represents the three possible isomers (ortho-, para- and meta-xylene). The mole fractions of each component in the fuel are $X_{NDC} = 0.451$, $X_{MCH} = 0.268$ and $X_{XYL} = 0.281$. The detailed mechanism with 230 species and 4868 reversible reactions of [Ranzi et al., 2012b] has been reduced with the reduction code ARCANE (https://chemistry.cerfacs.fr/en/arcane/) based on YARC [Pepiot, 2008]. The resulting mechanism, **JetA_3Comp_45_686_16_QC**, comprising of 45 transported species, 16 Quasi-Steady State species and 686 irreversible reactions is provided in the supplementary material. The **JetA_3Comp_45_686_16_QC** scheme for the surrogate is in very good agreement with the detailed mechanism for premixed flames on the whole equivalence ratio range at 400 K and 1 bar as shown in Fig. D.0.1.

Droplet Evaporation Model

The droplet evaporation is modelled using a quasi steady state assumption. It was shown in [Rauch et al., 2012] that including the liquid phase diffusion did not lead to significant difference of the evaporation rate in comparison with infinite liquid diffusivity (as used here). Time scales for droplet heating (τ_{heat}) and mass diffusion inside the liquid (τ_{diff}) for a droplet of radius R are:

$$\tau_{heat} = \mathbf{O}\left(\frac{R^2}{\alpha_{liq}}\right) \; ; \quad \tau_{diff} = \mathbf{O}\left(\frac{R^2}{D_{liq}}\right) \tag{D.1}$$

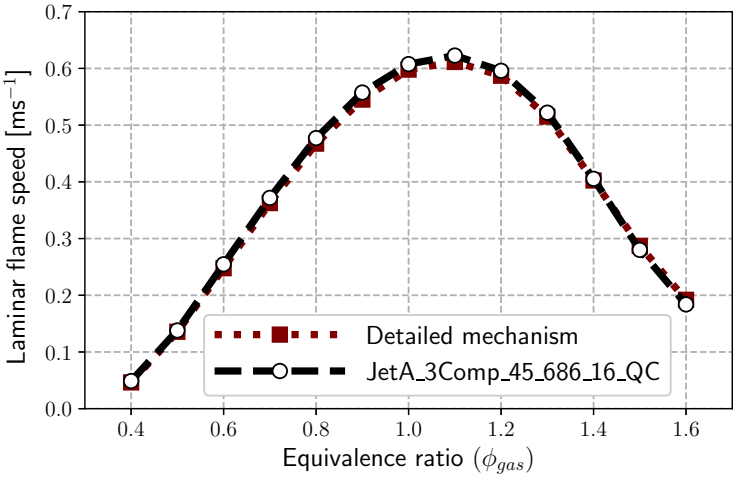

Figure D.0.1: Laminar flame speed for gaseous mixture of Jet-A surrogate/Air at 400 K and 1 bar

where α_{liq} and D_{liq} are the thermal and mass diffusivity in the liquid phase. For small droplets of diameter less than 100μm, $\tau_{heat}, \tau_{diff} \ll \tau_{ev}$ (evaporation timescale). Detailed description of the evaporation model can be found in earlier studies [Rochette et al., 2019, Felden et al., 2018b]. The multicomponent extension is discussed here. The Spalding mass transfer number B_M and the fraction of vapour ϵ^i for an individual component i are calculated as [Sirignano, 2010]:

$$B_M = \frac{\sum_{i=1}^{k} Y^i_{surf} - \sum_{i=1}^{k} Y^i_{\infty}}{1 - \sum_{i=1}^{k} Y^i_{surf}} = \frac{Y^i_{surf} - Y^i_{\infty}}{\epsilon^i - Y^i_{surf}} \tag{D.2}$$

where Y^i is the mass fraction of the individual component i and the subscripts $surf$ and ∞ denote the droplet surface and far-field locations respectively. Only the components present in the liquid phase are considered in Eq. D.2. Vapour liquid equilibrium Eq. D.3 is used to obtain the mole fractions of the fuel components at the droplet surface ($X_{i,surf}$) using the liquid mole fractions ($X_{i,liq}$) and the vapour pressure ($P_{sat,i}(T)$) of the different components. Calculating the surface mass fractions Y^i_{surf} to be used in Eq. D.2 is then straightforward.

$$X_{i,surf} P_{gas} = X_{i,liq} P_{sat,i} \tag{D.3}$$

Using the above equations, the evaporation rate m^i_p of an individual component can be calculated using the total evaporation rate of the droplet $\dot{m}_p$ and the fraction of

vapour ϵ_i as:

$$\dot{m}_p^i = \epsilon^i \dot{m}_p \quad \text{with} \sum_{i=1}^{k} \epsilon^i = 1 \tag{D.4}$$

The evaporation model is validated against experiments in Fig. D.0.2 showing the evolution of Normalised Diameter (ND) and temperature for a single evaporating droplet. After an initial heating phase, the droplet surface area reduces linearly following the D^2, agreeing well with the experimental data of [Javed et al., 2013]. The highly volatile MCH dominates the composition initially. As MCH and XYL completely evaporate, the liquid and vapour composition in the latter part is composed of only NDC.

Configuration

The one-dimensional domain shown in Fig. D.0.3 is $0.02m$ long and is discretised using 500 equally spaced elements. To avoid the influence of droplet residence time and to better control of the liquid and gaseous fluxes into the reaction zone, fuel droplets are injected just in front of the flame. Interaction of the fuel droplets and the premixed flame causes a change in flame speed and position. The inlet velocity (u_g) must be adjusted to a new value of the two-phase laminar flame speed $S_{L_{TP}}$ to stabilize the flame. The simulated cases are summarised in Tab. D.0.1 . Cases A and B represent overall lean and rich cases. Case C is overall lean and only liquid fuel is provided to the flame. These cover a wide range of typical burning regimes observed in real combustors where preferential concentration may lead to a variety of both local liquid loadings and gaseous equivalence ratios with varying relative velocities between the two phases. Total equivalence ratio describes the overall fuel (gaseous and liquid)-to-oxidizer ratio, hence is represented as the sum of gaseous and liquid equivalence ratios ($\phi_{\text{tot}} = \phi_{\text{gas}} + \phi_{\text{liq}}$).

Inlet gas temperature is 400K and droplets are injected at 300K. The flame speeds and structures are computed over a range of droplet diameters ranging from $d_{p_0} = 5\mu m$ to $80\mu m$. For a given droplet diameter, the number of injected droplets is adjusted to fulfil the targeted equivalence ratio. Under saturated conditions and in flame regions it is possible to encounter isolated droplet combustion. The diameter of flame (d_f) around a droplet of size (d_p) can be calculated as $d_f \approx 12 d_p$ [Sirignano, 2010]. Droplets are injected such that the inter-droplet distance $S < d_f$ and the

isolated burning regime is not activated. The relative velocity between the phases is taken into account by introducing a velocity ratio $u^* = u_{liq}/u_{gas}$ [Rochette et al., 2019].

Case name	ϕ_{tot}	$\phi_{gas,liq}$	u^*	d_{p_0} (μm)
A	0.9	$\phi_{gas} = 0.8$ $\phi_{liq} = 0.1$	1, 30	5-80
B	1.3	$\phi_{gas} = 0.8$ $\phi_{liq} = 0.5$	1, 30	5-80
C	0.9	$\phi_{gas} = 0.0$ $\phi_{liq} = 0.9$	1, 30	5-80

Table D.0.1: Conditions of simulated cases

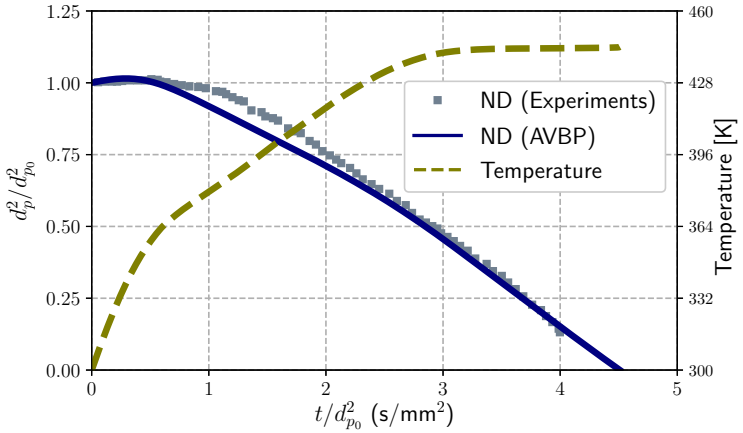

(a) Evolution of ND and temperature

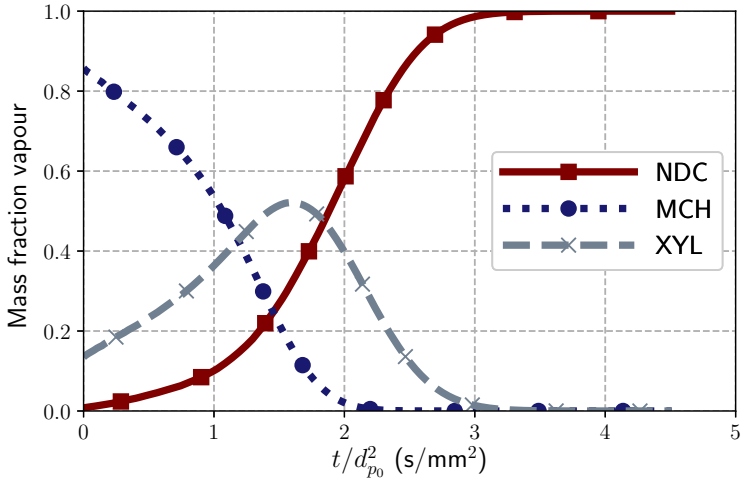

(b) Composition of the evaporating flux

Figure D.0.2: Single Jet-A droplet evaporation. d_{p0} =1000 μm at 300 K in a quiescent air at 773 K

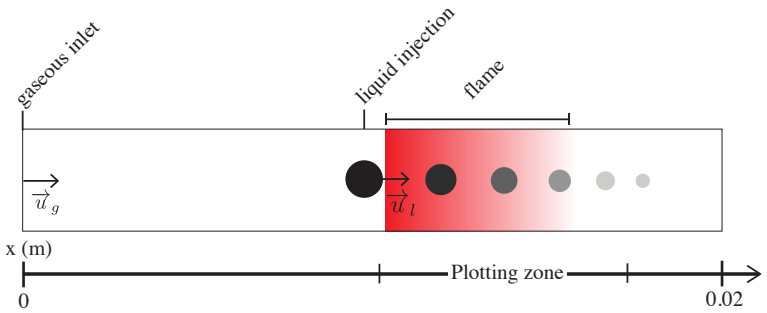

Figure D.0.3: Computational configuration [Rochette et al., 2019]

Results

Multicomponent spray flame structure

Flame structures for the cases in Tab. D.0.1 are compared for $d_{p_0} = 20\mu m$, $u^* = 1$ and 30. The heat release (HR) profiles are plotted with the evaporation source terms (Γ_F) and the volumetric consumption ($-\dot{\omega}_F$) speed of the components. Droplets injected just before the flamefront begin to release vapour in the reacting zone and the evaporation zone extends beyond the main flame region.

In Fig. D.0.4 for Case A and $u^* = 1$ MCH is shown to evaporate completely in the main flame region followed by XYL and finally NDC. The preferential evaporation of MCH and its complete consumption within the main premixed flame zone shown in Fig. D.0.4b causes a slight increase in ϕ_{eff} compared to ϕ_{gas}. As the droplets move through the main flamefront gradually they contain only XYL and NDC, and finally only NDC, whose evaporation rate reaches a maximum in the post-flame high temperature region. Due to the lower volatility and longer evaporation distance of NDC, a secondary consumption zone with very low but non-zero reaction rates exists as seen in Fig. D.0.4c.

Increasing the droplet velocity so that $u^* = 30$ shifts the evaporation zone behind the main flamefront as shown in Fig. D.0.5. The dominant flame structure is that of the premixed gaseous flame at $\phi_{gas} = 0.8$ and the contribution of the liquid phase towards ϕ_{eff} is negligible. An extended secondary combustion zone behind the main reaction zone exists where the evaporating droplets react with the excess oxygen. This zone for NDC is shown in Fig. D.0.5b, and similar ones for MCH and XYL are observed (not shown).

In Case A two limiting regimes may be encountered. The first corresponds to droplets small or slow enough to evaporate completely in the main reaction zone leading to $\phi_{eff} = \phi_{tot}$ while in the second limit large or fast droplets contribute very little to the flame propagation and $\phi_{eff} = \phi_{gas}$. As the flame is overall lean, this leads to the spray flame speed limits for Case A to lie between $S_{L_{\phi_{gas}}} \leq S_{L_{TP}} \leq S_{L_{\phi_{tot}}}$.

The spatial profiles of HR, Γ_F and $-\dot{\omega}_F$ for Case B are shown in Fig. D.0.6 and Fig. D.0.7. The evaporation trends are very similar to Case A, however due to the high liquid loading the amount of vapour released is significantly higher. For the condition $u^* = 1$ the evaporation and consumption profiles of MCH (not shown)

are similar to that observed in Fig. D.0.4b. NDC shows a strong and prominent secondary reaction zone behind the main premixed flamefront where the remaining oxidiser is consumed in long droplet burning regime highlighted in Fig. D.0.6b. As in Case A, this secondary reaction zone does not affect the propagation speed but contributes towards the overall heat release.

For $u^* = 30$, a distinct secondary reaction zone away from the premixed flamefront is observed for NDC. Since the main premixed flame is lean with $\phi_{\text{gas}} = 0.8$, the remaining oxidiser is consumed as the evaporation progresses. Multiple reaction pathways are possible for the consumption of fuel components due to the ARC mechanism used. Some vapour released in this region also undergoes pyrolysis producing new smaller fuel species which diffuse back to burn with oxygen. This complex diffusion flame structure is illustrated with two components formed by NDC pyrolysis (H_2, C_2H_2) having a slope of opposite sign compared to the oxygen (O_2) profile, shown in Fig. D.0.7b. Burnt gas composition contains the standard combustion products CO_2, H_2O, CO together with smaller components.

As in Case A, the upper and lower limits of ϕ_{eff} for Case B are ϕ_{tot} (fast evaporation) and ϕ_{gas} (slow evaporation). However, with $\phi_{tot} = 1.3$ it is possible to find conditions for which $\phi_{eff} \approx 1.0$ leading to $S_{L_{TP}} > S_{L_{\phi_{tot}}}$.

Results for Case C where all the fuel is in the liquid phase are shown in Fig. D.0.8 and Fig. D.0.9. For $u^* = 1$, the faster evaporation of MCH initiates the flame. Significant amounts of XYL and NDC also vaporise before the location of peak heat release. Energy from the reactions provides the latent heat of evaporation needed to sustain the flame. This causes significantly lower heat release rates and flame speeds compared to a purely gaseous flame or spray flame with lower liquid loading as Case A. For higher droplet velocities $u^* = 30$, the reaction zone develops later after significant amount of liquid fuel has vaporised. For the purely liquid controlled Case C, the HR zone extends across the entire evaporation zone of the droplets with $-\dot{\omega}_F$ and Γ_F superimposed in this region.

Laminar two-phase flame speeds for multicomponent droplets

The laminar two-phase flame speed is controlled by ϕ_{eff} which is a function of the gaseous equivalence ratio and the evaporation of liquid inside the flamefront of thickness δ_L^0. The distance over which the droplets evaporate, compared against δ_L^0 can

be used to estimate the contribution of evaporation to ϕ_{eff}. Previously laminar flame speed correlations have been developed and validated for a single component n-heptane case [Rochette et al., 2019]. To extend these correlations to the present case, it is necessary to consider the varying evaporation rates (Fig. D.0.2) and contributions of the liquid fuel components.

The different evaporation time scales (τ^i_{ev}), of the liquid components are calculated using the fraction of each component ϵ_i averaged over the lifetime of i in the liquid state. In Eq. D.5 the Spalding mass transfer number B_M is calculated at the mean of liquid injection and wet bulb temperatures, $(T_{inj} + T_{wb})/2$ (using the T_{wb} of NDC in this case because it is the last remaining component) for a droplet evaporating in flame conditions.

$$\tau^i_{ev} = \frac{\rho_{liq} d^2_{p_0}}{12 \rho_{gas} D_F \epsilon_i \ln(1+B_M)} \underbrace{\left[1 + \frac{k Sc^{1/3} Re_p^{1/2}}{2 \dfrac{(1+B_M)^{0.7} \ln(1+B_M)}{B_M}}\right]^{-1}}_{\text{accounts for droplet velocity}} \tag{D.5}$$

where d_{p_0}, ρ_{liq} and ρ_{gas} are the initial droplet diameter, liquid and gas density respectively. D_F is the diffusion coefficient of the fuel vapour, Sc is the Schmidt number of the surrounding gas and Re_p is the Reynolds number of the droplet. k is a factor whose value is taken as 0.6. [Sirignano, 2010].

For droplets with high relative velocity, it is important to take into account drag force acting on them. Using the droplet relaxation time $\tau_p = \rho_{liq} d^2_{p0}/18\mu_{gas}$ (μ_{gas} is the dynamic viscosity of the surrounding gas) and the flame time $\tau_f = \delta^0_{S_L}/S^0_L$, a flame Stokes number is identified as $St_f = \tau_p/\tau_f$. A droplet injected with a velocity u_{p_0} reaches after crossing the flame thickness the velocity u_p:

$$u_p = u_{gas}\left(1 - e^{-1/St_f}\right) + u_{p_0} e^{-1/St_f} \tag{D.6}$$

The evaporation length for each component i is then given by $\delta^i_{ev} = u_p \tau^i_{ev}$. Following [Rochette et al., 2019] and using the above expressions, ϕ_{eff} is

$$\phi_{eff} = \sum_i \left(\frac{\delta^0_L}{max\left(\delta^0_L, \delta^i_{ev}\right)}\right)^{\frac{2}{3}} \left(\frac{s_i}{s_{Jet\text{-}A}}\right) \phi_{liq} + \phi_{gas} \tag{D.7}$$

In Eq. D.7, s is the stoichiometric ratio. For a hydrocarbon fuel C_xH_y, $s = x + y/4$. The term $s_i/s_{Jet\text{-}A}$ accounts for the varying contribution of each component present

in the liquid fuel to ϕ_{eff}. For small droplets which evaporate fast, Eq. D.7 yields $\phi_{eff} = \phi_{tot}$. For larger droplets having non-negligible evaporation times, Eq. D.7 gives $\phi_{gas} < \phi_{eff} < \phi_{tot}$. Similarly, volatile components with $\delta^i_{ev} \leq \delta^0_L$ contribute completely to ϕ_{eff} whereas less volatile components with large evaporation thickness only partially contribute to the flame.

For flames controlled by evaporation (Case C), the flame speed correlations from [Rochette et al., 2019] considering the smallest evaporation timescale of MCH (τ^{MCH}_{ev}) is used.

$$S_{L_{TP}} = \frac{\delta_{S_{L_{\phi_{gas}}}}}{\tau^{MCH}_{ev}} \tag{D.8}$$

The correlations are compared with the simulation results for all cases in Tab. D.0.1 and overall a good agreement with the trends are observed. Comparison for Case A is shown in Fig. D.0.10 . The laminar flame speed is less than $S_{L_{\phi_{tot}}} = 0.56\,\mathrm{m}s^{-1}$ for all droplet sizes. For large droplets the contribution of evaporation to ϕ_{eff} is negligible. Increasing the droplet velocity reduces the residence time in the reactive zone, reducing further the liquid phase contribution leading to $\phi_{eff} = \phi_{gas}$ and $S_{L_{TP}} = S_{L_{\phi_{gas}}} = 0.48\,\mathrm{m}s^{-1}$. For Case B (Fig. D.0.11), an optimum diameter exists at which the two phase flame burns close to stoichiometry. For $u^* = 1$ it is found at $20\,\mu$m and for $u^* = 30$ at $10\,\mu$m. Due to the varying volatilities of the multicomponent fuel, such an optimum diameter exists even when the droplets move very quickly across the flame. For the evaporation controlled flames of Case C (Fig. D.0.13), correlation follows the trend but with some deviation from the simulation results. It is observed in Fig. D.0.13 that a flame can be sustained for gaseous equivalence ratios lower than the flammability limit if droplets have low or zero relative velocities. As was observed in Fig. D.0.8 and Fig. D.0.9, significant amounts of liquid components evaporate before a stable flame can be sustained. This leads to multiple reaction pathways involving all components, hence τ^{MCH}_{ev} cannot be used alone for the estimation of the flame speed. A detailed comparison between the evaporation and chemical timescales is needed to obtain a better agreement with the simulated data for Case C.

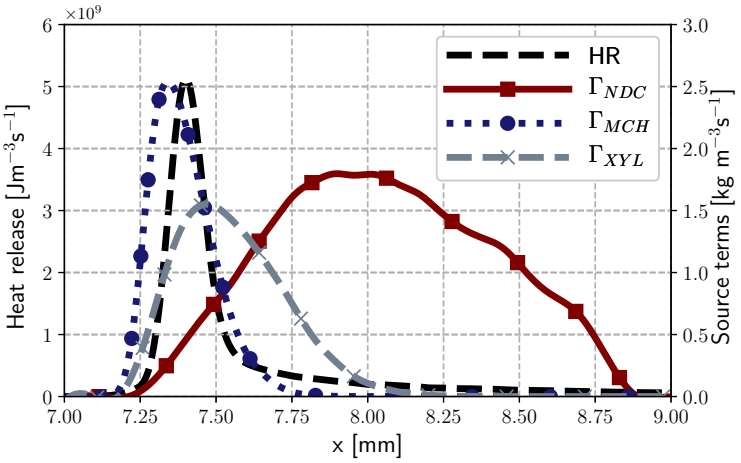

(a) Heat release and evaporation source terms

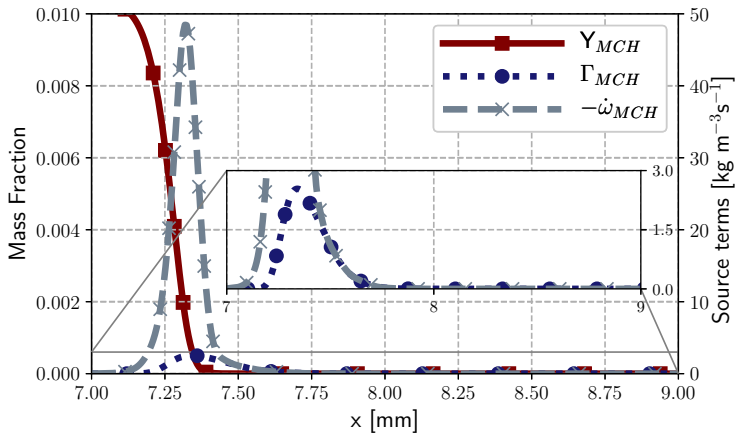

(b) Mass fractions and consumption rates of MCH

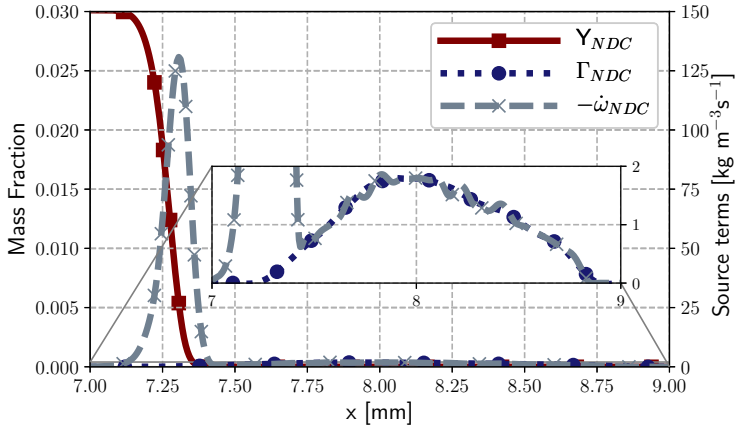

(c) Mass fractions and consumption rates of NDC

Figure D.0.4: Profiles of heat release, mass fractions, evaporation and consumption rates for Case A, $d_{p_0} = 20\mu m$ and $u^* = 1$

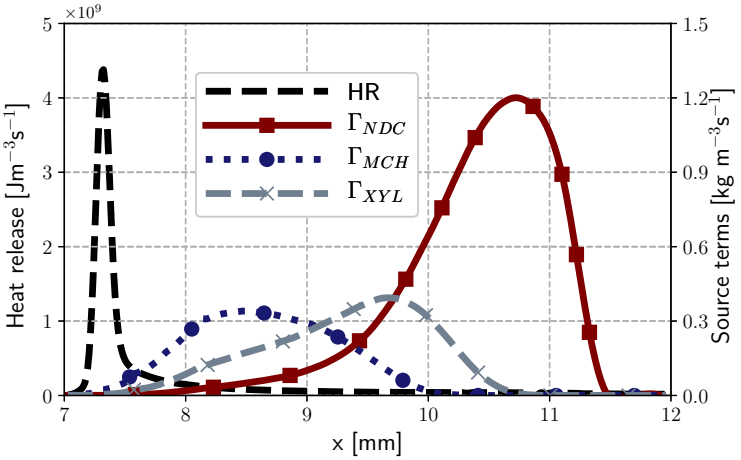

(a) Heat release and evaporation source terms

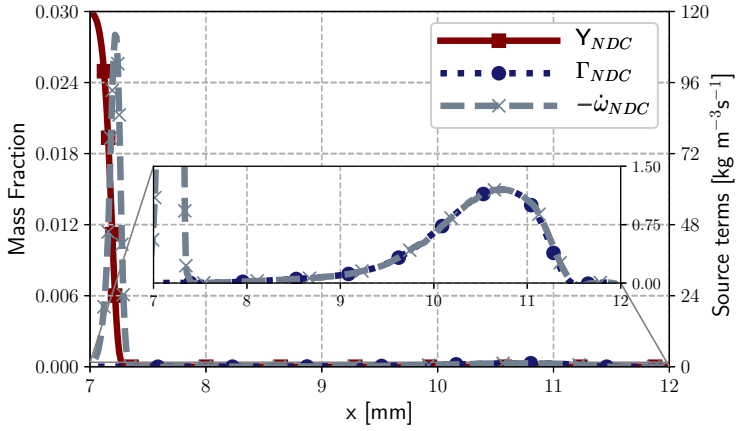

(b) Mass fractions and consumption rates of NDC

Figure D.0.5: Profiles of heat release, mass fractions, evaporation and consumption rates for Case A, $d_{p_0} = 20\mu m$ and $u^* = 30$

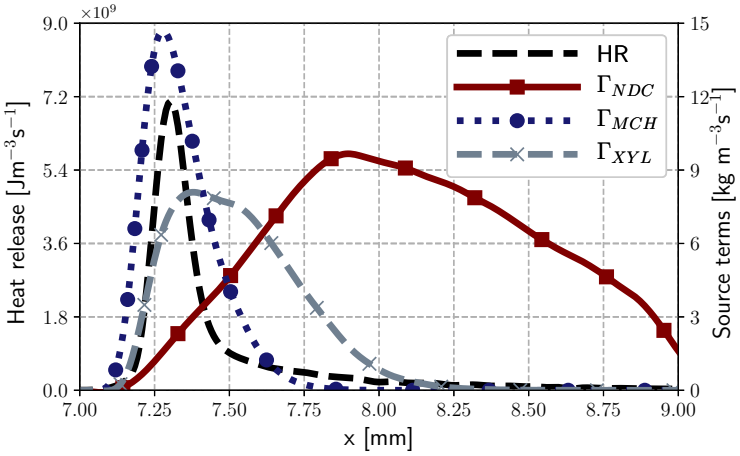

(a) Heat release and evaporation source terms

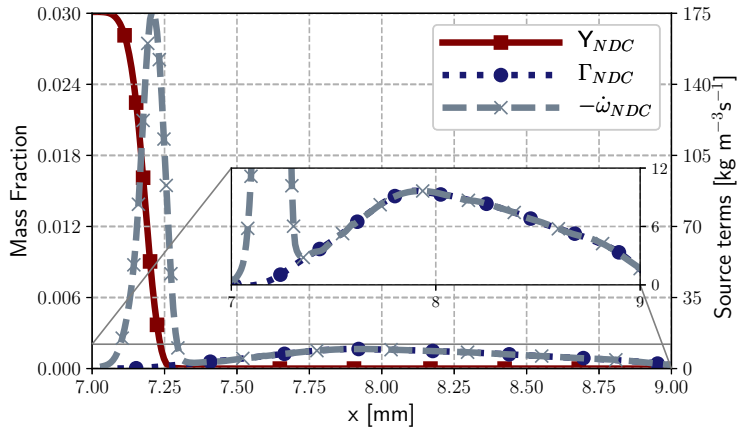

(b) Mass fractions and consumption rates of NDC

Figure D.0.6: Profiles of heat release, mass fractions, evaporation and consumption rates for Case B, $d_{p_0} = 20\mu m$ and $u^* = 1$

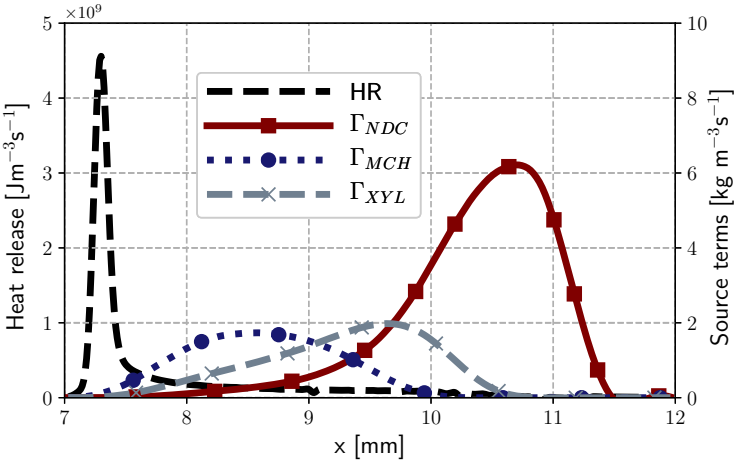

(a) Heat release and evaporation source terms

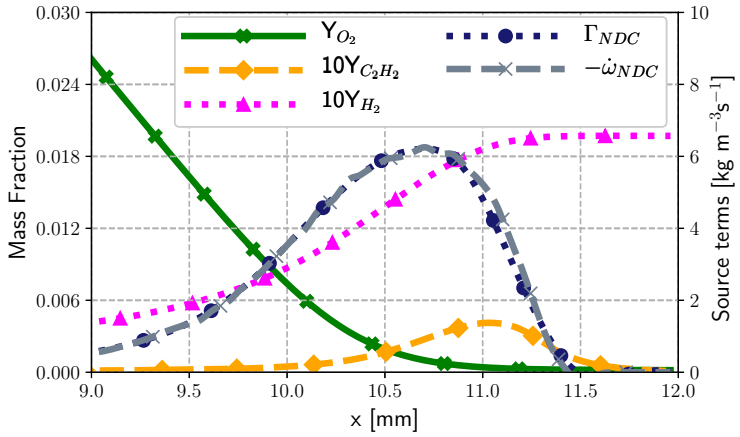

(b) Diffusion flame structure for NDC

Figure D.0.7: Profiles of heat release, mass fractions, evaporation and consumption rates for Case B, $d_{p_0} = 20\mu m$ and $u^* = 30$

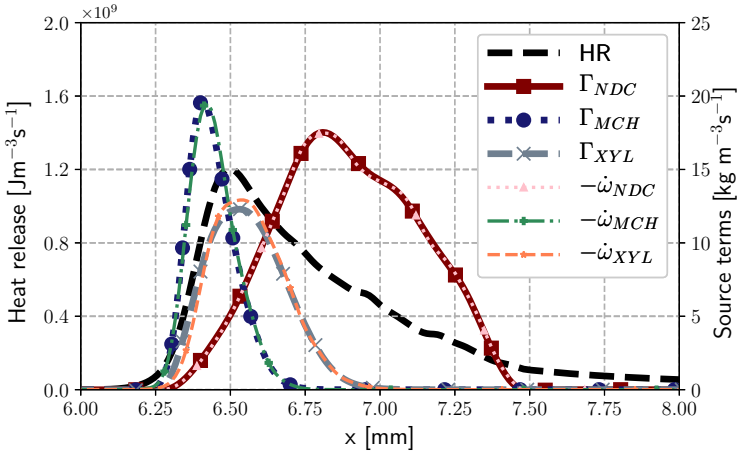

Figure D.0.8: Profiles of heat release, evaporation and consumption rates for Case C, $d_{p_0} = 20\mu m$ and $u^* = 1$

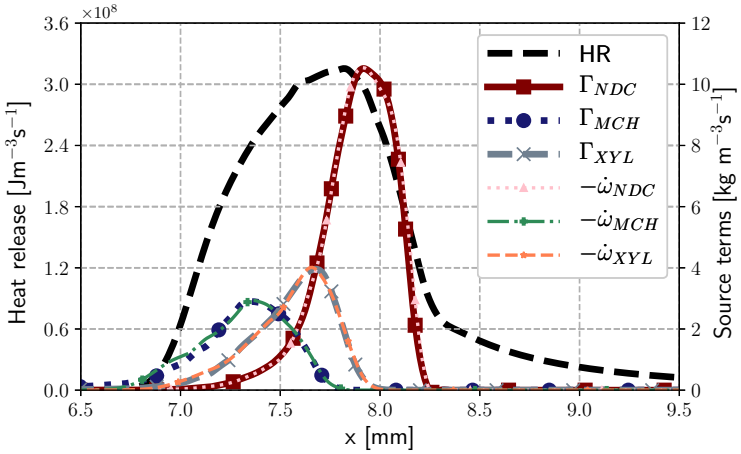

Figure D.0.9: Profiles of heat release, evaporation and consumption rates for Case C, $d_{p_0} = 20\mu m$ and $u^* = 30$

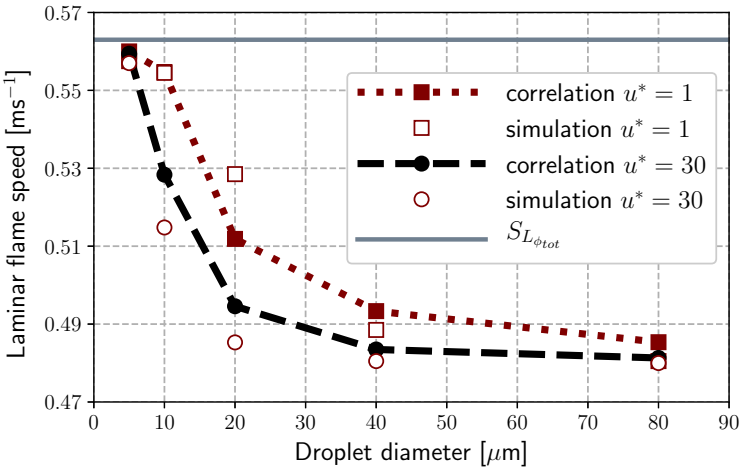

Figure D.0.10: Two-phase flame speed of Jet-A vs initial droplet diameter. Comparison between simulations and correlations (Eq. D.7) for Case A

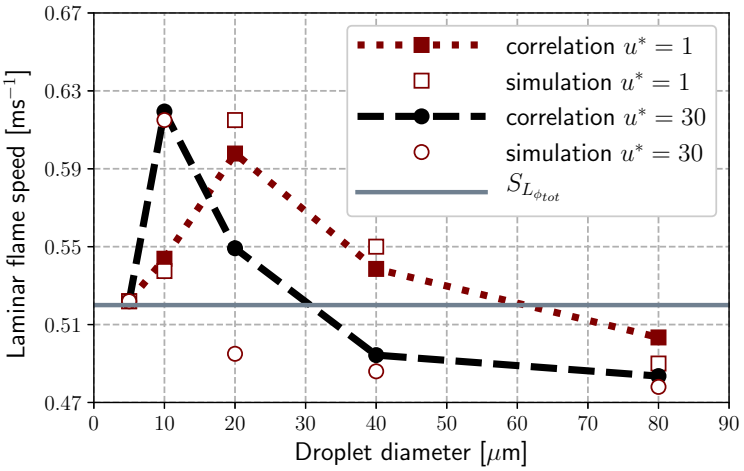

Figure D.0.11: Two-phase flame speed of Jet-A vs initial droplet diameter. Comparison between simulations and correlations (Eq. D.7) for Case B

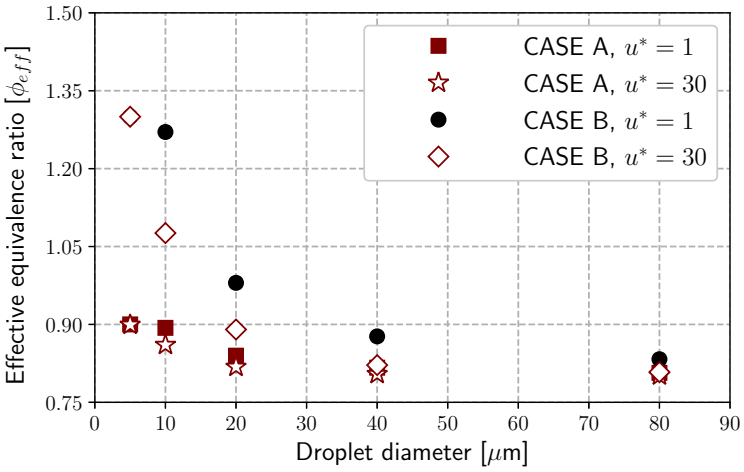

Figure D.0.12: Effective equivalence ration calculated by Eq. D.7

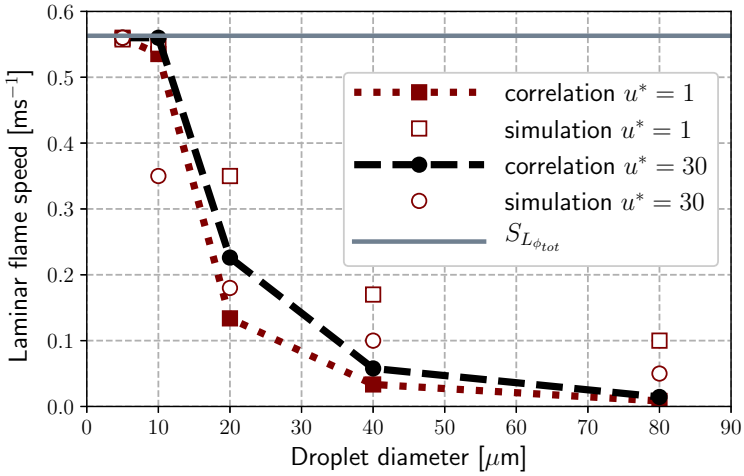

Figure D.0.13: Two-phase flame speed of Jet-A vs initial droplet diameter. Comparison between simulations and correlations (Eq. D.8) for Case C

Conclusions

Multicomponent one-dimensional spray flame simulations were performed for a Jet-A surrogate composed of n-dodecane (NDC), methyl-cyclohexane (MCH) and xylene (XYL). Flame structure and spray flame speed have been examined for a wide range of equivalence ratios, droplet diameters and droplet velocities. Due to the varying volatilities of these components, a staged evaporation behaviour was observed as the droplets move through the reactive flamefront. MCH being the most volatile component enhances the effective equivalence ratio and this effect is more pronounced for low relative velocities. NDC being the least volatile component leads to an extended secondary reaction zone following the primary flame zone. For rich cases with high relative velocity, a separated secondary diffusion flame of NDC can even be observed. For purely liquid fuels the heat release zone extends over the entire evaporation zone. Correlations were proposed to estimate laminar spray flame speeds considering the varying vapour fluxes and contributions of the different liquid components as well as the drag effect. These correlations are in very good agreement with numerical results, except for purely liquid flames which demand an accurate comparison of the various evaporation and chemical timescales and will be the focus of future work. Overall the various mechanisms controlling the laminar spray flame speed for multicomponent droplets have been identified and may be used in turbulent combustion modelling of multicomponent sprays.

Acknowledgments

This project has received funding from the EU Horizon 2020 research and innovation programme under Agreement 723525 (JETSCREEN) and the Marie Sklodowska-Curie Agreement 766264 (MAGISTER). HPC resources from GENCI-CINES (Grant 2020-A0052B10157) were utilised.

Appendix E

Complementary data on spray flames with 60 μm droplets

60 μm droplets cases counterparts of the Figures presented in 14 can be found hereafter with the reaction rates profiles of CO-producing reactions helping identify the reactions taking place.

B1 with 60 μm droplets

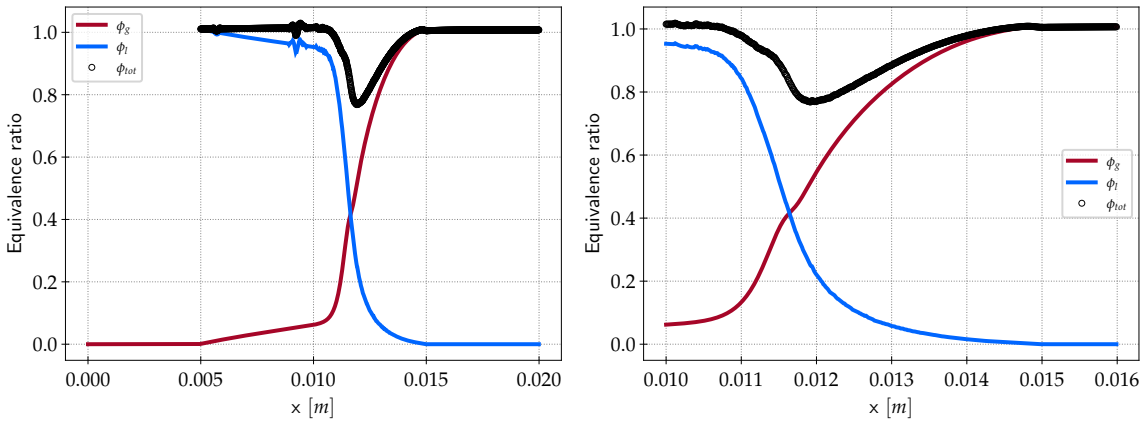

(a) Full domain (b) Zone of interest

Figure E.0.1: Spatial profile of the gaseous equivalence ratio ϕ_g (solid red line), the liquid equivalence ratio ϕ_l (solid blue line) and the total equivalence ratio ϕ_{tot} (black circles) on (a) the fuel domain and (b) the zone of interest for B1 with 60 μm droplets.

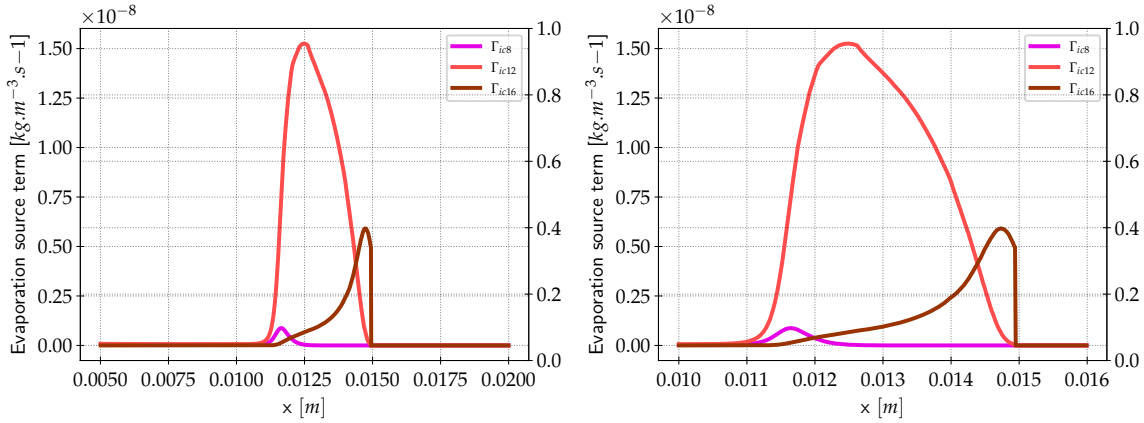

(a) Full domain (b) Zone of interest

Figure E.0.2: Spatial profile of the evaporation mass flow rate for each fuel species iso-octane, iso-dodecane and iso-cetane (respectively in pink, red and maroon) and the heat release rate (black) on (a) the fuel domain and (b) the zone of interest for B1 with 60 μm droplets.

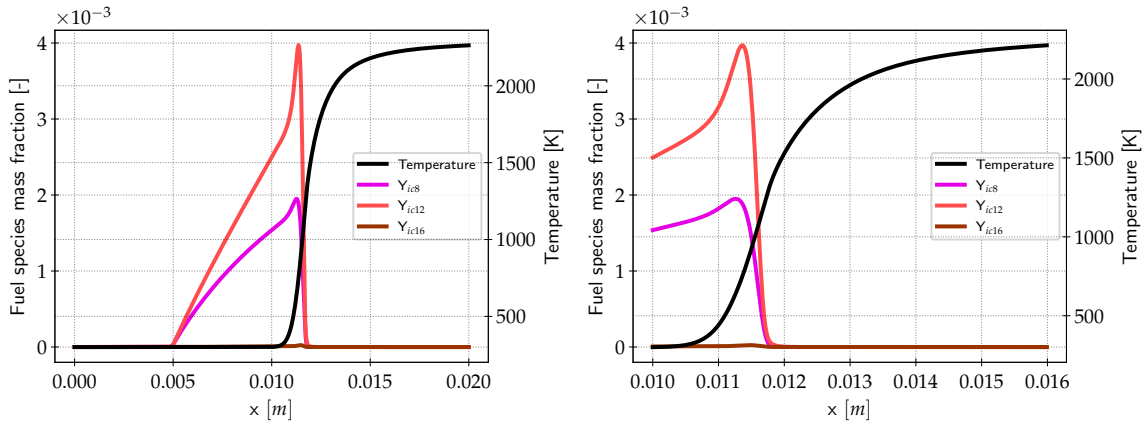

(a) Full domain (b) Zone of interest

Figure E.0.3: Spatial profile of the fuel species mass fractions iso-octane, iso-dodecane and iso-cetane (respectively in pink, red and maroon) and temperature (black) on (a) the fuel domain and (b) the zone of interest for B1 with 60 μm droplets.

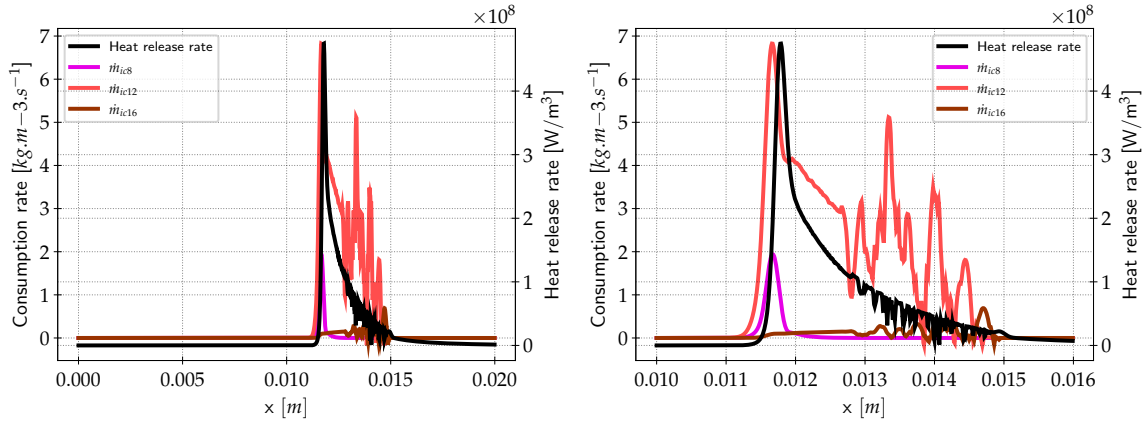

(a) Full domain (b) Zone of interest

Figure E.0.4: Spatial profile of the fuel species consumption rates iso-octane, iso-dodecane and iso-cetane (respectively in pink, red and maroon) and the heat release rate (black) on (a) the fuel domain and (b) the zone of interest for B1 with 60 μm droplets.

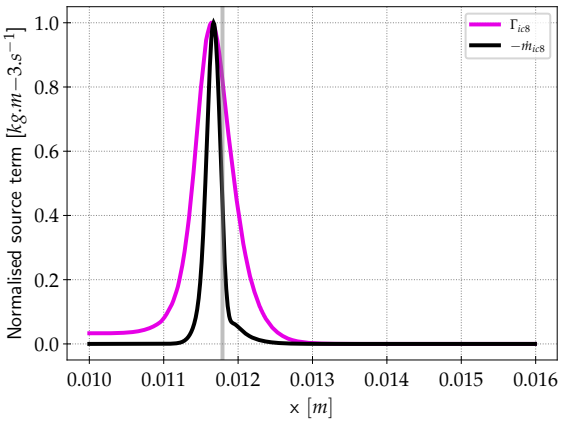

Figure E.0.5: Spatial profile of the normalised evaporation source term (pink) and the normalised consumption rate (black) of iso-octane on the zone of interest for B1 with 60 μm droplets.

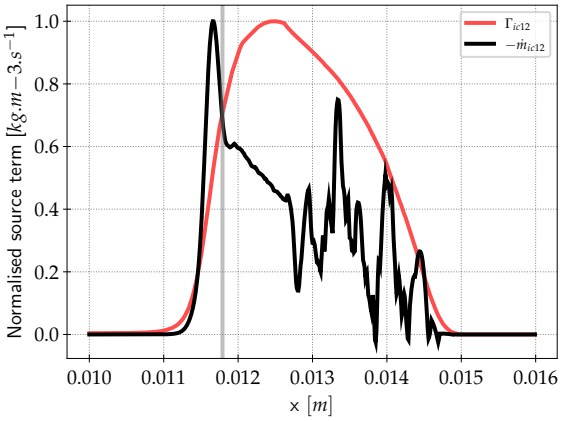

Figure E.0.6: Spatial profile of the normalised evaporation source term (red) and the normalised consumption rate (black) of iso-dodecane on the zone of interest for B1 with 60 μm droplets.

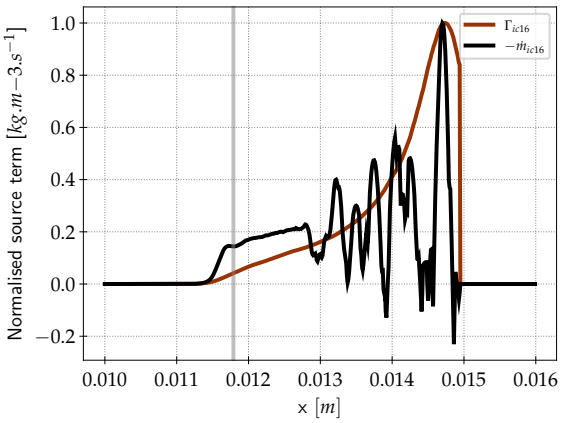

Figure E.0.7: Spatial profile of the normalised evaporation source term (maroon) and the normalised consumption rate (black) of iso-cetane on the zone of interest for B1 with 60 μm droplets.

C1 with 60 μm droplets

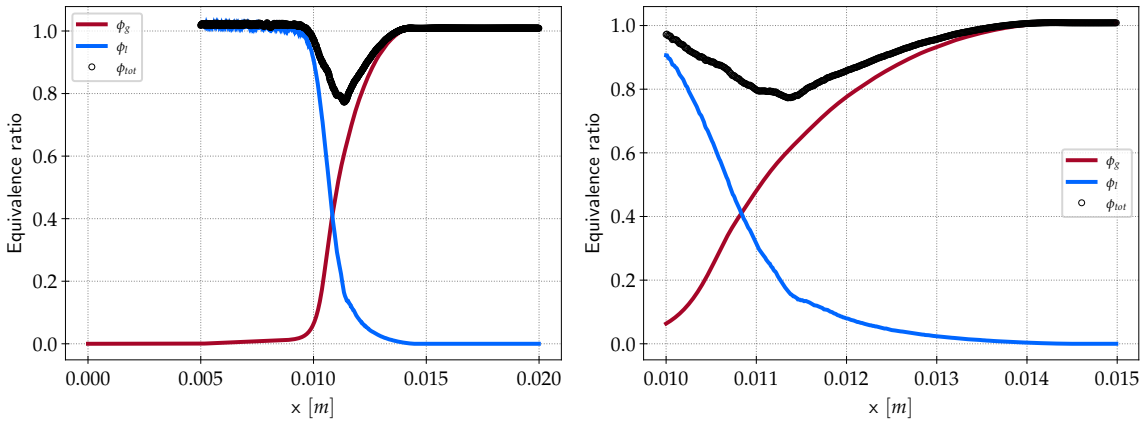

(a) Full domain (b) Zone of interest

Figure E.0.8: Spatial profile of the gaseous equivalence ratio ϕ_g (solid red line), the liquid equivalence ratio ϕ_l (solid blue line) and the total equivalence ratio ϕ_{tot} (black circles) on (a) the fuel domain and (b) the zone of interest for C1 with 60 μm droplets.

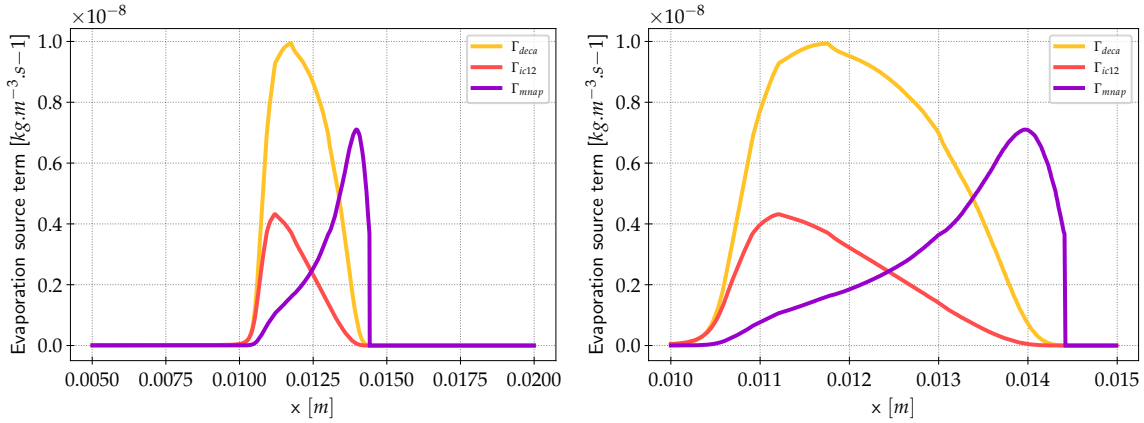

(a) Full domain (b) Zone of interest

Figure E.0.9: Spatial profile of the evaporation mass flow rate for each fuel species decalin, iso-dodecane and methyl-naphtalene (respectively in yellow, red and purple) and the heat release rate (black) on (a) the fuel domain and (b) the zone of interest for C1 with 60 μm droplets.

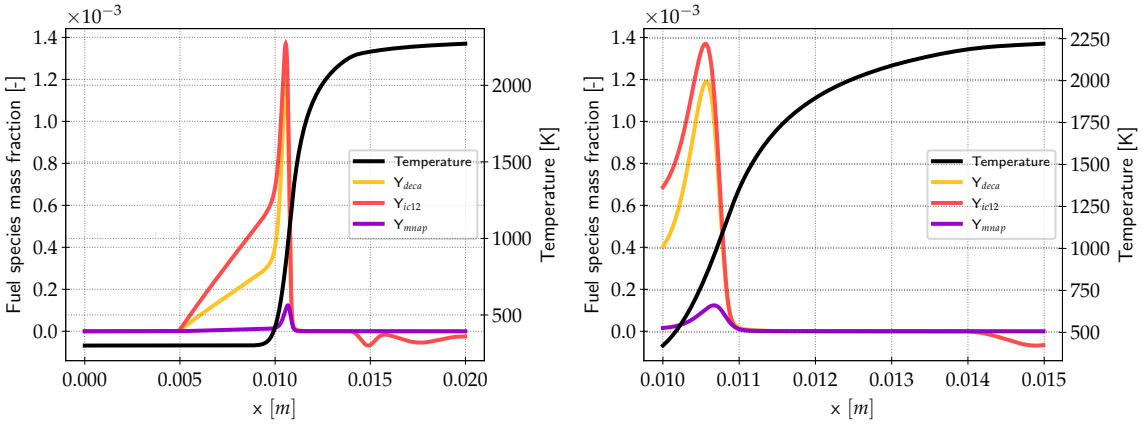

(a) Full domain (b) Zone of interest

Figure E.0.10: Spatial profile of the fuel species mass fractions decalin, iso-dodecane and methyl-naphtalene (respectively in yellow, red and purple) and temperature (black) on (a) the fuel domain and (b) the zone of interest for C1 with 60 μm droplets.

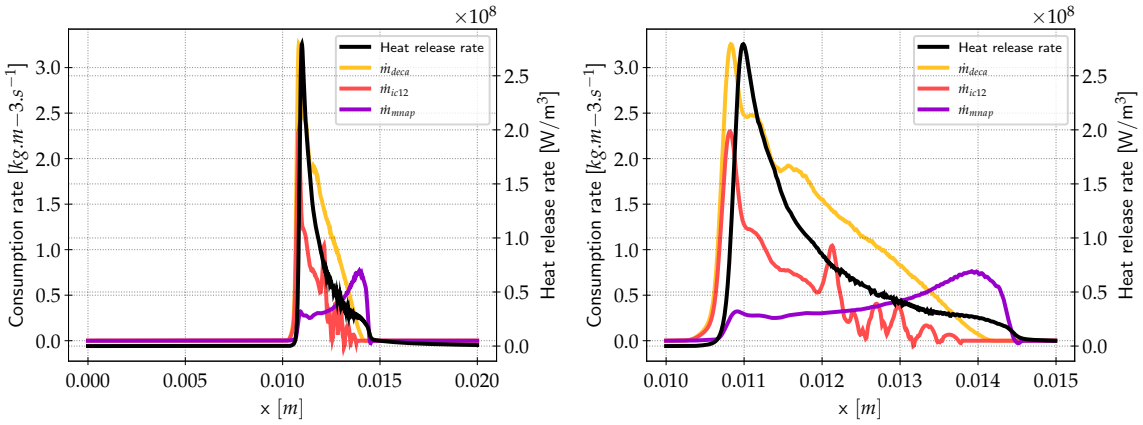

(a) Full domain (b) Zone of interest

Figure E.0.11: Spatial profile of the fuel species consumption rates decalin, iso-dodecane and methyl-naphtalene (respectively in yellow, red and purple)) and the heat release rate (black) on (a) the fuel domain and (b) the zone of interest for C1 with 60 μm droplets.

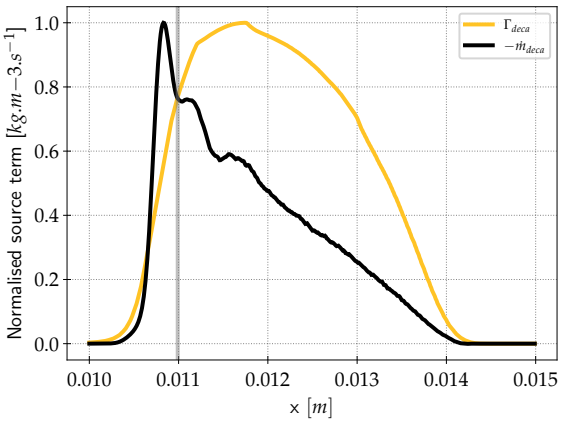

Figure E.0.12: Spatial profile of the normalised evaporation source term (yellow) and the normalised consumption rate (black) of decalin on the zone of interest for C1 with 60 μm droplets.

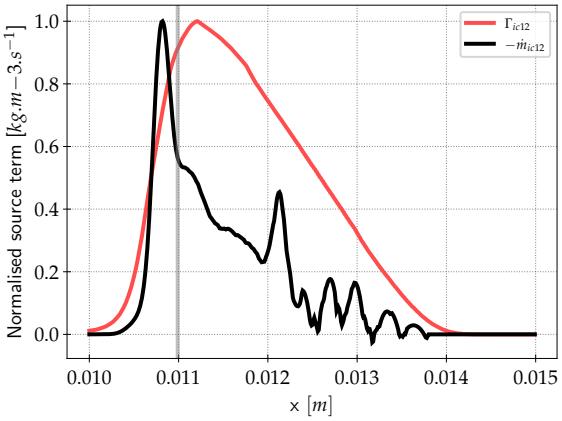

Figure E.0.13: Spatial profile of the normalised evaporation source term (red) and the normalised consumption rate (black) of iso-dodecane on the zone of interest for C1 with 60 μm droplets.

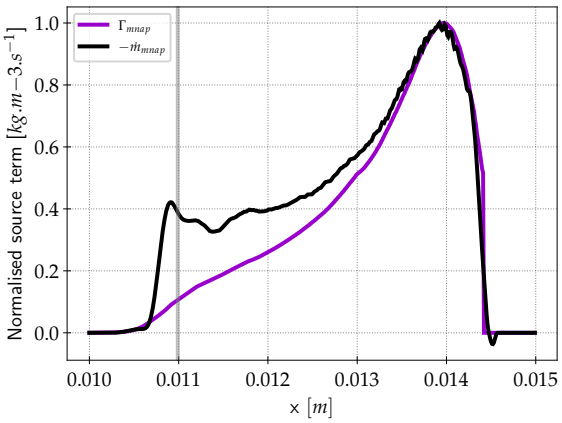

Figure E.0.14: Spatial profile of the normalised evaporation source term (purple) and the normalised consumption rate (black) of methyl-naphtalene on the zone of interest for C1 with 60 μm droplets.

CO-producing reactions

Figures E.0.15 to E.0.22, present the reaction rates of the reactions common to the three mechanisms that are producing CO.

The secondary peak highlighted in 14.4 is seen here to result from H-abstraction on the HCO species with various species. For A1 and B1, a smaller contribution from the reaction $HCCO + OH => 2CO + H_2$ can also be observed (Fig E.0.21.

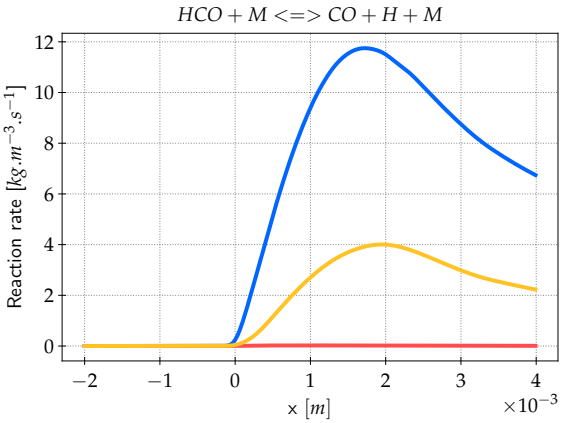

Figure E.0.15: Reaction rate of the reaction $HCO + M <=> CO + H + M$ for A1 (blue), B1 (red) and C1 (yellow) two-phase flames with 60 μm droplets. The x-coordinate has been shifted for an easier comparison.

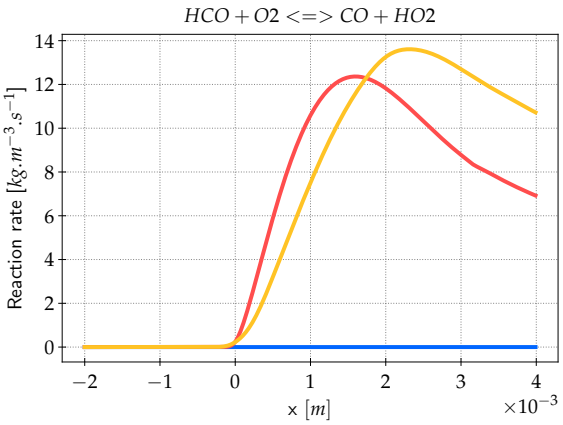

Figure E.0.16: Reaction rate of the reaction $HCO + O_2 <=> CO + HO_2$ for A1 (blue), B1 (red) and C1 (yellow) two-phase flames with 60 μm droplets. The x-coordinate has been shifted for an easier comparison.

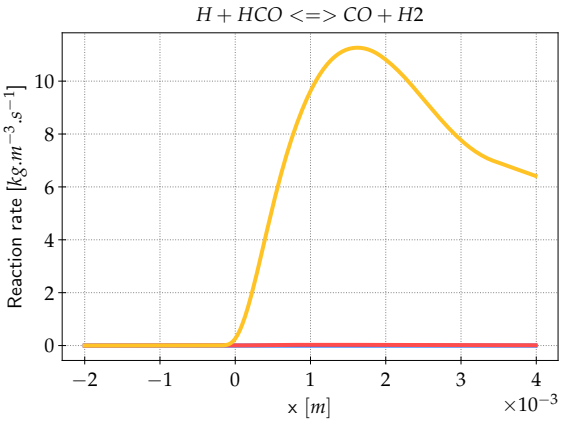

Figure E.0.17: Reaction rate of the reaction $H + HCO <=> CO + H2$ for A1 (blue), B1 (red) and C1 (yellow) two-phase flames with 60 μm droplets. The x-coordinate has been shifted for an easier comparison.

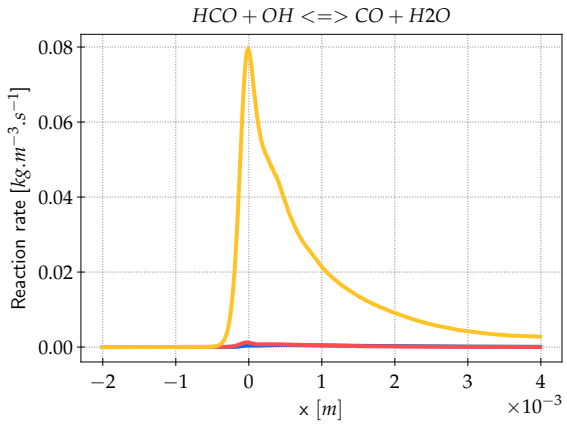

Figure E.0.18: Reaction rate of the reaction $HCO + OH <=> CO + H_2O$ for A1 (blue), B1 (red) and C1 (yellow) two-phase flames with 60 μm droplets. The x-coordinate has been shifted for an easier comparison.

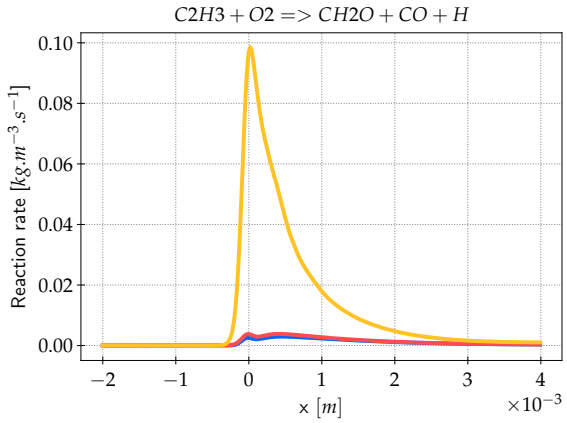

Figure E.0.19: Reaction rate of the reaction $C_2H_3 + O_2 => CH_2O + CO + H$ for A1 (blue), B1 (red) and C1 (yellow) two-phase flames with 60 μm droplets. The x-coordinate has been shifted for an easier comparison.

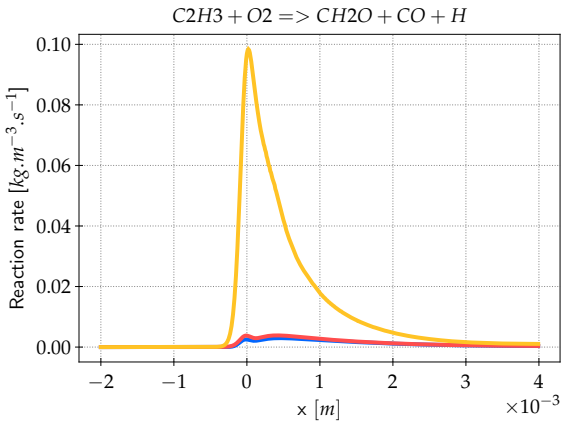

Figure E.0.20: Reaction rate of the reaction $C_2H_3 + O_2 => CH_2O + CO + H$ for A1 (blue), B1 (red) and C1 (yellow) two-phase flames with 60 μm droplets. The x-coordinate has been shifted for an easier comparison.

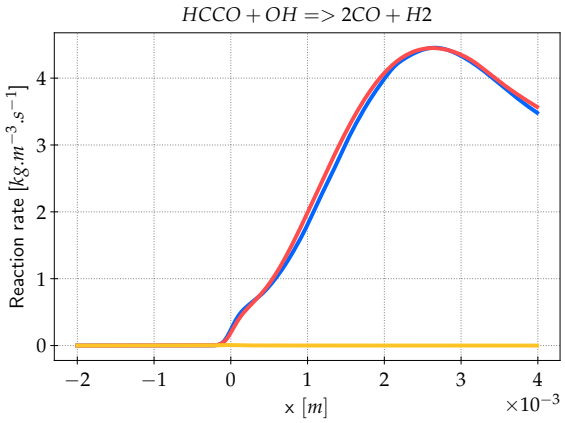

Figure E.0.21: Reaction rate of the reaction $HCCO + OH => 2CO + H_2$ for A1 (blue), B1 (red) and C1 (yellow) two-phase flames with 60 μm droplets. The x-coordinate has been shifted for an easier comparison.

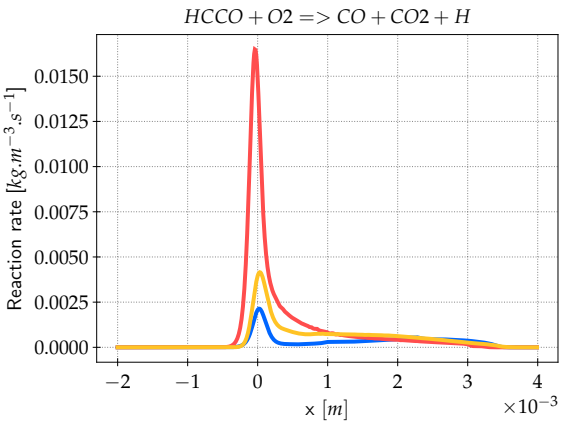

Figure E.0.22: Reaction rate of the reaction $HCCO + O_2 => CO + CO_2 + H$ for A1 (blue), B1 (red) and C1 (yellow) two-phase flames with 60 μm droplets. The x-coordinate has been shifted for an easier comparison.